# Modelling magnetic diffusion and decadal geomagnetic secular variation

**Maurits Cornelis Metman**

Submitted in accordance with the requirements for the degree of
Doctor of Philosophy

The University of Leeds
School of Earth and Environment

September 2019

*To Alette and Paul*

The candidate confirms that the work submitted is his own, except where work which has formed part of jointly authored publications has been included. The contribution of the candidate and the other authors to this work has been explicitly indicated below. The candidate confirms that appropriate credit has been given within the thesis where reference has been made to the work of others.

The work in Chapter 2 of the thesis has appeared in publication as follows:
**Metman, M. C.**, Livermore, P. W., and Mound, J. E. (2018), *The reversed and normal flux contributions to axial dipole decay for 1880-2015*, Physics of Earth and Planetery Interiors, 276: 106-117, doi:10.1016/j.pepi.2017.06.007.

MM designed the magnetic equator algorithm, ran and wrote the code associated with the work, analysed the results, made the figures, and wrote the text. JM devised the integral quantities in equations (2.4) to (2.6). The work benefitted from discussions with PL and JM, and from reviews by Hagay Amit, Vincent Lesur and Michael Le Bars, which resulted in its overall improvement.

The work in Chapter 3 of the thesis has appeared in publication as follows:
**Metman, M. C.**, Livermore, P. W., Mound, J. E., and Beggan, C. D. (2019), *Modelling decadal secular variation with only magnetic diffusion*, Geophysical Journal International, doi:10.1093/gji/ggz089.

MM designed the experiments, made the derivations, ran and wrote the code associated with the work, analysed the results, made the figures, and wrote the text. PL proposed the use of the Galerkin scheme, and supplied the associated Jacobi polynomials. The work benefitted from discussions with PL, JM, and CB, and from reviews by Hagay Amit and another anonymous reviewer, which resulted in its overall improvement.

Chapter 4 is a manuscript draft ready to be submitted for publication. As such, the format of this thesis is in compliance with the requirements for thesis submission with the use of published material.

# Acknowledgements

First and foremost, I would like to express my indebtness to Phil Livermore, Jon Mound, and Ciarán Beggan for their continuous support and for the countless hours we have spent discussing my work — I could not have asked for more knowledgeable and attentive supervisors.

I also thank Ciarán for the incredibly enjoyable time spent in Edinburgh, and for our many musical pub trips there, which played no small part in it becoming my all-time favourite city.

I would like to say thanks to everyone within the Deep Earth research group for giving me the opportunity to present my work regularly on our Friday afternoon sessions, and for the constructive feedback I received then.

I thank also Nicholas Gillet for his continuous support regarding the use of the COV-OBS.x1 field model.

I am also grateful to Tim Taylor and Chris Turbitt for our pleasant and instructive excursion to the Eskdalemuir observatory, and for their demonstration of making geomagnetic measurements. In addition, I thank Juliane Hübert for taking me along during a pleasant (and sunny!) field trip through Lothian.

I also thank the many friends I have made within the School for making my time at Leeds so memorable, for example by enjoying the occasional pint at various pubs, or by playing a Sunday afternoon board game or two. I acknowledge also that the betrayal by Josh Williams within a particular Game of Thrones session will never be forgotten.

I thank my brother Bas for his seemingly endless supply of high-energy music, which often allowed me to keep going when caffeine failed.

Lastly, but certainly not least, I am eternally grateful to Loes for her undying support, for giving me the opportunity to explore this country together, and for believing in me even at times I could not.

# Abstract

Changes in the magnetic field generated within Earth's core that occur over years to centuries are known as geomagnetic secular variation (SV). These temporal variations arise from motions of the electrically conducting outer core fluid, and magnetic diffusion. Diffusive field changes are often considered much slower than those associated with fluid flow. For yearly to decadal SV, diffusion is therefore neglected in the widely adopted frozen-flux approximation.

However, several studies have stressed the incompatibility of frozen flux with the SV observed over the 20th century. In particular, the approximation conflicts with the emergence of reversed-flux patches (RFPs) on the core-mantle boundary (CMB), which are regions where the sign of radial magnetic field differs from the otherwise prevalent dipole field aligned with Earth's rotation axis (i.e. the axial dipole field). In this thesis, we first introduce a method to characterise RFPs and their evolution. Subsequently, we show how these features have proliferated, strengthened, and migrated towards the geographic poles, matching the observed weakening of the axial dipole.

We introduce a formalism allowing the inversion of the observed SV for an initial magnetic field throughout the core, assuming purely diffusive SV. With this method we demonstrate that pure diffusion is consistent with the SV over several decades, and can reproduce fundamental SV characteristics such as westward drift, recent North Magnetic Pole acceleration, and reversed-flux emergence.

We also use our inverse formalism to augment frozen-flux models for core fluid motion by including magnetic diffusion. This hybrid scheme is shown to more accurately predict yearly SV than steady core flow, in particular that of South Atlantic RFPs. Finally, we use this hybrid forecasting method to compute a candidate model for the 2020.0 International Geomagnetic Reference Field. Our predictions also show how future axial dipole decay is no longer due to poleward migration of RFPs.

# Contents

# List of Figures

# List of Tables

# Nomenclature

**List of acronyms**

| | |
|---|---|
| CMB | Core-mantle boundary |
| GAD | Geocentric axial dipole |
| ICB | Inner-core boundary |
| IGRF | International Geomagnetic Reference Field |
| MHD | Magnetohydrodynamics |
| NMP | North Magnetic Pole |
| RFP | Reversed-flux patches |
| RMS | Root-mean-square |
| SAA | South Atlantic Anomaly |
| SV | Secular variation |
| WMM | World Magnetic Model |

# Chapter 1

# Introduction

## 1.1 A historical perspective

*'Extraordinary claims require extraordinary evidence.'*

**Carl Sagan**

It was *Gilbert* (1600) who was first to consider our planet Earth as one (giant) magnet — an extraordinary claim indeed, considering the lack of knowledge of Earth's interior at the time. His idea was supported by experiments involving the use of a spherical magnet (a *terella*), and his work therefore remains one of the earliest examples of experiment-based science in general.

However, the discovery and study of naturally occuring magnets, historically referred to as *lodestones*, predates *Gilbert*'s (1600) seminal work by several centuries. For instance, the Ancient Greek philosopher Thales of Miletus reported the ability of these rocks to remotely attract or repel other physical bodies, which was then attributed to the soul that resides inside them (*Mitchell*, 1946). In addition, the Ancient Greeks are accredited with the etymology of the word 'magnet', a reference to the region of Magnesia where such lodestones were found.

The magnetic properties of lodestones have also independently been documented by the Chinese of the 1st century, who were first to note that these rocks tend to align themselves (roughly) along the north-south direction (*Needham*, 1962). Almost a millennium later, that is in the 11th century, it is again in China where the use of this aligning property is introduced for the purpose of navigation, and also where the first magnetic compass is manufactured (*Wang*, 1948). The use of these compasses subsequently led to the observation that their needle does not strictly point towards the geographic north, marking the first notion of *magnetic declination*, i.e. the angular distance between the compass needle and geographic north (*Needham*, 1962).

By the 17th century, the concept of magnetic declination had reached Western Europe. At this time, it was understood that this quantity can vary significantly around the globe and in time, and it was widely acknowledged that these spatial variations in declination are useful for the purposes of naval navigation, as these allow an estimation of geographic longitude.

Motivated by this practical use, the end of the 17th century saw the first large-scale mapping of magnetic declination, focused in particular at the Atlantic Ocean. This expedition was ordered and captained by Sir Edmund Halley, who also was first to interpret the temporal variation among declination measurements in terms of a *westward drift*. He hypothesised that this drift resulted from the rotation of concentric shells of magnetised material inside the Earth (*Halley*, 1692), a suggestion consistent with the proposition by *Gilbert* (1600). Despite the fact that this theory has since been disproven, in part because the Earth's interior is generally too hot to sustain such remnant magnetism (the ambient temperature at these depths are above the Curie temperature, see e.g. *Tauxe* (2010)), the westward drift remains a widely studied property of the Earth's magnetic field to this day (e.g. *Bullard et al.*, 1950, *Finlay and Jackson*, 2003).

## 1.2 Earth's core

At present, *Halley*'s hypothesis can be considered at least partially true. Namely, it is now widely accepted that our approximately spherical Earth (with a mean radius of 6371 km) is indeed layered. Specifically, it has a predominantly metallic *core* (which will be the main region of interest for this thesis), surrounded by a rocky *mantle*, which is subsequently overlain by a thin *crust* ($\approx$ 5-50 km thick). The interface between the core and mantle, residing at a depth of approximately 2,886 km, is the *core-mantle boundary* (CMB). This separation is clearly manifest in seismological observations (*Oldham*, 1906, *Gutenberg*, 1912), which are consistent with marked discontinuities in the properties of Earth's constituents at this boundary. For example, when crossing from the mantle to the core the density increases from 5.6 to 10 g cm$^{-3}$, and the velocity of seismic P-waves (i.e. longitudinal pressure waves discharged by earthquakes) decreases from 13.7 to 8.1 km s$^{-1}$ (*Dziewonski and Anderson*, 1981) (Fig. 1.1). Compositional differences between the two regions explain these differences: the mantle is predominantly rich in silicates, whereas the core consists mostly of liquid iron (e.g. *Fowler*, 2005). In addition, the core itself is partitioned into an *inner* and *outer core*. Their separation at a radius of roughly 1220 km is known as the *inner-core boundary* (ICB), and has originally been observed from reflections of seismic P-waves (*Lehmann*, 1936) (Fig. 1.1). While the CMB also reflects a material change, the ICB predominantly marks the phase difference of a solid inner and liquid outer core.

Ultimately, this large-scale layered structure results from the differentiation of the initial bulk composition Earth acquired during its formation approximately 4.5 Gyr ago (e.g. *Wood et al.*, 2006). This formation event, driven by gravitational accretion, has allowed large amounts of potential energy to be converted to thermal energy (heat). This heat is still continuously radiated into space, and the current total heat transfer at Earth's surface is estimated at 43-49 TW (*Pollack et al.*, 1993, *Lay et al.*, 2008).

To constrain the dynamics of the fluid that comprises the outer core, it is crucial to know what portion of this global heat budget is transferred through the CMB. Unfortunately, the total CMB heat flux remains poorly constrained, and typical estimates range between 3 to 15

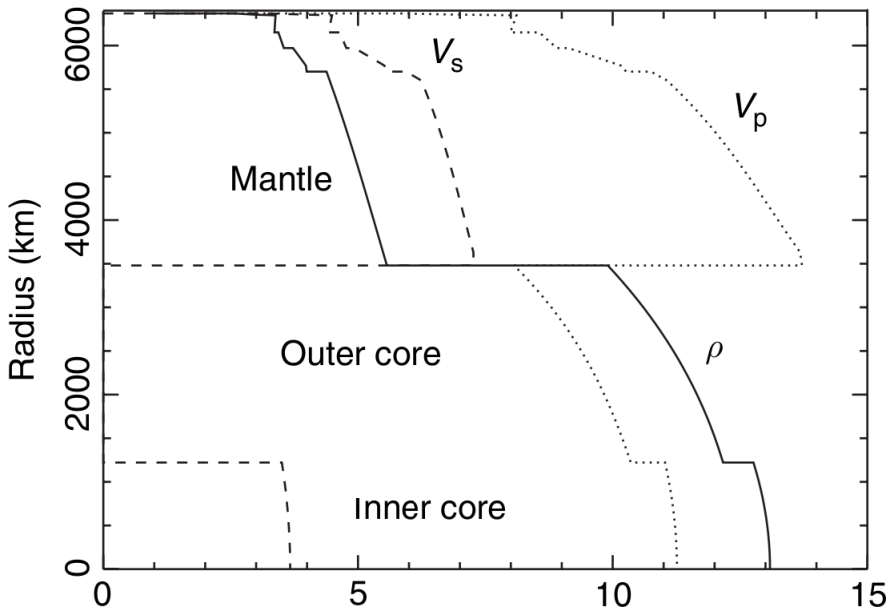


**Figure 1.1:** The one-dimensional global-scale structure of the Earth in terms of density $\rho$ (in g cm$^{-3}$) and seismic shear and pressure wave velocities $V_S$ and $V_P$ (both in km s$^{-1}$), respectively (*Dziewonski and Anderson*, 1981). Notable interfaces within this structure include the core-mantle boundary (CMB) at a radius of 3480 km, and the inner-core boundary (ICB) at a radius of 1220 km (image adapted from *Olson* (2007)).

TW (*Sleep*, 1990, *Lay et al.*, 2008). Nevertheless, it is thought to exceed the conductive heat transport inside the outer core due to adiabatic decompression, which is roughly 0.3 and 6 TW near the ICB and CMB respectively (*Roberts et al.*, 2003, *Stacey and Loper*, 2007). Thermal *convection* must therefore take place within the core, through which thermally buoyant core fluid rises upward and subsequently cools, thereby contributing to the overall transport of heat towards the CMB.

As the core has cooled over time, the ambient pressures at large depth have caused it to freeze radially outward, and this process is widely believed to have formed the solid inner core (e.g. *Sumita and Bergman*, 2015). However, the inner core age remains a subject for debate, and based on energetic, chemical, and magnetic considerations, estimates of the inner core age exist of 0.5-2.5 Ga (*Labrosse et al.*, 2001, *Lassiter*, 2006, *Aubert et al.*, 2009, *Biggin et al.*, 2015, *Davies et al.*, 2015). Because the core continues to cool, inner core freezing is ongoing, and these inner core ages imply an average growth rate of the ICB radius of roughly 0.5-2.5 mm yr$^{-1}$. The outer core fluid is an iron alloy, a property consistent with the observation that the outer core density is roughly 10% lighter than that of pure iron (*Birch*, 1964). As a result, freezing of the inner core is associated with the release of light (non-iron) elements into the outer core. However, it remains difficult to establish the exact composition of the outer core; candidate light elements include silicon, oxygen, sulphur, hydrogen, carbon, magnesium, or some mixture of these (*Poirier*, 1994, *O'Rourke and Stevenson*, 2016). Nevertheless, it is acknowledged that the presence of these light elements increases the buoyancy of the lowermost outer core, and that these compositional differences therefore contribute significantly to the

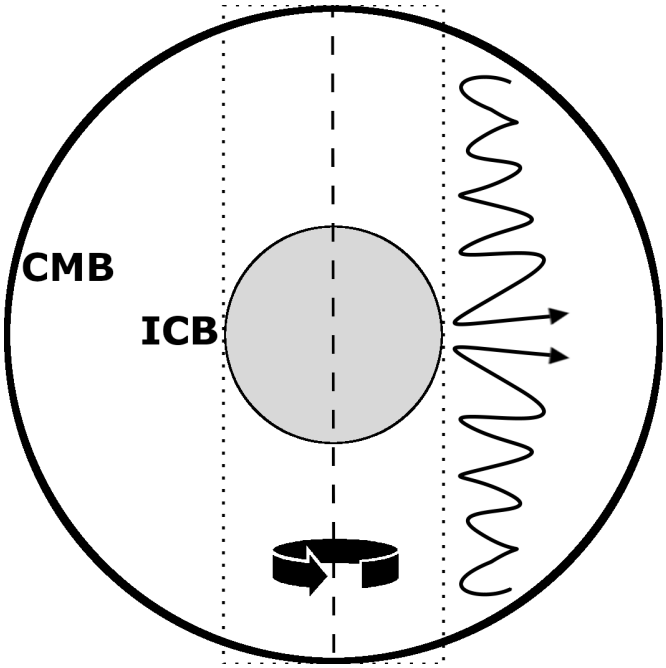


**Figure 1.2:** A schematic representation of the motions in the outer core. The dashed line marks Earth's rotation axis, and the cylinder aligned with this axis that encloses the inner core (the tangent cylinder) is shown by dotted lines. Thin arrows indicate the direction of core fluid motion outside the tangent cylinder, typically arranged in columnar vortices. The tangent cylinder dynamically separates the core fluid.

convective motion within the outer core (e.g. *Jones*, 2015).

Earth's rotation strongly affects the nature of convection within the outer core. A well-known example of such rotation-dominated fluid motion follows from the Taylor-Proudman theorem (*Proudman*, 1916, *Taylor*, 1917), which applies to some extent to the outer core. This scenario considers a steady and inviscid flow for which the Coriolis force (associated with the rotation) balances pressure (i.e. *geostrophic* balance). Then, there can exist no fluid flow variation along the direction parallel to the axis of rotation. As the inner core is impermeable, the application of this constraint to the outer core implies that the fluid outside an (imaginary) cylinder, that is one aligned with the rotation axis and containing the inner core (the *tangent cylinder*), is entirely separated from the rest of the outer core (Fig. 1.2). While such rotational effects are thought to take place in the outer core, the Taylor-Proudman scenario remains a much too simplified view of the true outer core dynamics. This theorem relies on ignoring for example thermal, viscous, and electrodynamic processes, which are frequently accounted for in (computationally demanding) numerical simulations of core convection. Still, these numerical models confirm the highly cylindrical nature of core convection, and typically render vortices within columns aligned with the rotation axis, which transport core fluid from and towards the equatorial plane (e.g. *Christensen and Wicht*, 2015) (Fig. 1.2). For example, by considering a non-magnetic and steady linearised force balance comprising thermal, rotational, and viscous effects within numerical simulations of core convection, workers have demonstrated that the

thickness of these columns generally decreases with rotation rate — extrapolation of these simulated results to Earth-like conditions yields a column thickness of no more than 300 m (e.g. *Jones*, 2015), further demonstrating that core convection is strongly rotation-controlled. However, for the real Earth non-linear and magnetic effects are expected, which are capable of significantly widening these convective rolls (e.g. *Jones*, 2015).

It is currently debated whether the core convects in its entirety. Specifically, several authors have argued for a thermally or chemically stratified layer at the top of the core, in which radial fluid motion is strongly suppressed. Constraints on the existence of this layer come from seismic waves, particularly from travel time differences between SnKS phases travelling within a thin region beneath the CMB (*Lay and Young*, 1990, *Garnero et al.*, 1993, *Helffrich and Kaneshima*, 2010, *Kaneshima*, 2018), but also from magnetic considerations (*Whaler*, 1980, *Gubbins*, 2007, *Buffett*, 2014). In addition, data from mineral physics are consistent with high thermal conductivity below the CMB, that is in excess of 90 W $m^{-1}$ $K^{-1}$ (*Pozzo et al.*, 2012, *Gomi et al.*, 2013). Such values imply that most of the CMB heat flow may be accounted for with only thermal conduction within a layer below the CMB, and barring any heat transport associated with dynamical instabilities arising from shearing between the stratified layer and the rest of the outer core (e.g. barotropic and baroclinic instabilities), this would circumvent the need for radial convective motion. However, the existence of this layer remains controversial, and estimates for its depth extent range considerably, from about 50 km (*Garnero et al.*, 1993) to possibly up to 450 km (*Kaneshima*, 2018).

## 1.3 Magnetohydrodynamic considerations

It is now widely accepted that these turbulent, convective motions of the (electrically conducting) fluid comprising the outer core generate a magnetic field that we observe at Earth's surface (the so-called *core* or *main field*). Essentially, the outer core is a dynamo, converting kinetic energy to magnetic energy — this process is therefore suitably referred to as the *geodynamo*. Such a mechanism was originally proposed by *Larmor* (1919) a century ago in an attempt to explain the Sun's magnetic field, but was considered applicable also to the Earth following further developments in the 20th century (an overview of these is given by *Olson* (2007)). The physical processes that govern the geodynamo are ultimately placed within the broader field of magnetohydrodynamics (MHD), and in this section we shall touch upon some of its aspects, allowing observations of the core field to be linked to processes operating inside the core. Accordingly, these theoretical considerations will provide the necessary physical context for the discussion on the temporal evolution of Earth's magnetic field that is given later.

In what follows, bold characters shall denote real 3-vectors (unless state otherwise). Furthermore, we assume a spherical, concentric Earth and core, with radii $a$ and $c$, respectively. Accordingly, we adopt a spherical coordinate system, with the origin in Earth's centre and the position vector $\mathbf{r} = (r, \theta, \varphi)^T$, where $r$, $\theta$, and $\varphi$ denote radius, colatitude, and longitude, respectively.

### 1.3.1 Maxwell's equations

The basis for the theory of the geodynamo (or classical electrodynamics in general) is formed by Maxwell's equations, which in differential form read

$$\nabla \cdot \mathbf{E} = \frac{\varsigma}{\varepsilon_0}, \tag{1.1}$$

$$\nabla \cdot \mathbf{B} = 0, \tag{1.2}$$

$$\nabla \times \mathbf{E} = -\frac{\partial \mathbf{B}}{\partial t}, \tag{1.3}$$

$$\nabla \times \mathbf{B} = \mu_0 \left( \mathbf{J} + \varepsilon_0 \frac{\partial \mathbf{E}}{\partial t} \right), \tag{1.4}$$

where $\mathbf{E}$ is the electric field, $\varsigma$ the electric charge density, $\mathbf{B}$ is the magnetic field (in place of the commonly used field $\mathbf{H} = \mathbf{B}/\mu_0$), $t$ is time, $\mathbf{J}$ is electric current density, and the constants $\varepsilon_0$ and $\mu_0$ are respectively the permittivity and permeability of free space. These equations represent respectively Gauss's law, Gauss's law for magnetism (corresponding to the absence of magnetic monopoles), Faraday's law of induction, and Ampere's circuital law (e.g. *Fleisch*, 2008).

MHD is generally a classical (non-relativistic) subject, and therefore it is sufficient to consider Ampere's law (eq. 1.4) without the displacement current term, i.e. the second term on the r.h.s. To illustrate this, consider first eq. (1.3), which has the order-of-magnitude relation $\mathcal{E}/\mathcal{L} \sim \mathcal{B}/\mathcal{T}$, with $\mathcal{E}, \mathcal{L}, \mathcal{B}$, and $\mathcal{T}$ characteristic scales for the electric field, length, the magnetic field and time. Combining this scaling with the ratio of the displacement current to the l.h.s. term in (1.4) then yields

$$\frac{|\mu_0 \varepsilon_0 (\partial \mathbf{E}/\partial t)|}{|\nabla \times \mathbf{B}|} \sim \frac{1}{c^2} \frac{\mathcal{E}\mathcal{L}}{\mathcal{B}\mathcal{T}} = \left( \frac{\mathcal{U}}{c} \right)^2, \tag{1.5}$$

where the velocity scale $\mathcal{U} = \mathcal{L}/\mathcal{T}$ and $c = (\mu_0 \varepsilon_0)^{-\frac{1}{2}}$ is the speed of light in vacuum. A typical estimate for the velocity of core fluid motion is $5 \times 10^{-4}$ m s$^{-1}$ (e.g. *Holme*, 2015), whereas $c \approx 3 \times 10^8$ m s$^{-1}$. Neglect of the displacement current is therefore justified for the Earth's core and is known as the *MHD approximation*.

### 1.3.2 The induction equation

This approximation has considerable advantages, and we now use it to link magnetic field variations to the Earth's core dynamically. Doing so requires another equation, that is Ohm's law for a moving conductor:

$$\mathbf{J} = \sigma(\mathbf{E} + \mathbf{u} \times \mathbf{B}) \tag{1.6}$$

with $\sigma$ the electric conductivity and $\mathbf{u}$ the fluid velocity. While we shall not further specify $\mathbf{u}$, we note that the ICB and CMB are impermeable boundaries, therefore $u_r = 0$ at these interfaces. In addition, the mantle is widely considered electrically insulating, therefore it is common to assume that $\sigma = |\mathbf{J}| = 0$ for $r > c$. Equation 1.4 implies therefore that outside the core, the magnetic field is curl-free, a property that we will be used later. Nevertheless, $\mathbf{B}$ can be shown to be continuous across the CMB (*Gubbins and Roberts*, 1987).

Combining eq. (1.3), (1.4), and (1.6) together with the MHD approximation yields

$$\frac{\partial \mathbf{B}}{\partial t} = \nabla \times (\mathbf{u} \times \mathbf{B} - \eta \nabla \times \mathbf{B}), \tag{1.7}$$

with $\eta = (\mu_0 \sigma)^{-1}$ the *magnetic diffusivity*. For the case of uniform diffusivity this equation simplifies to

$$\frac{\partial \mathbf{B}}{\partial t} = \nabla \times (\mathbf{u} \times \mathbf{B}) + \eta \nabla^2 \mathbf{B}, \tag{1.8}$$

where we have used eq. (1.2) and the identity

$$\nabla \times \nabla \times \mathbf{v} \equiv \nabla(\nabla \cdot \mathbf{v}) - \nabla^2 \mathbf{v}, \tag{1.9}$$

with $\mathbf{v}$ is any 3-vector. Equation (1.8) is known as the *induction equation* (for uniform diffusivity), which explicitly gives time changes in the magetic field as the sum of two (r.h.s.) terms: the first is the induction term representing the interaction between the fluid flow and the magnetic field, which may allow fluid motion to generate a magnetic field; the second is a diffusive term which results in an overall decay of the magnetic field. It is of note that eq. (1.1)-(1.4) and (1.6) considered both the electric and magnetic field, whereas the induction equation is entirely independent of $\mathbf{E}$ (due to the MHD approximation). This shows that for our purposes, the electric field is only of secondary importance. Still, if need be, $\mathbf{E}$ can readily be determined from eq. (1.4) and (1.6) when $\mathbf{u}$ and $\mathbf{B}$ are known.

An expanded representation of the induction term in eq. (1.8) is

$$\nabla \times (\mathbf{u} \times \mathbf{B}) = (\mathbf{B} \cdot \nabla)\mathbf{u} - (\mathbf{u} \cdot \nabla)\mathbf{B} - (\nabla \cdot \mathbf{u})\mathbf{B}, \tag{1.10}$$

which results from the application of eq. (1.2) and the vector identity

$$\nabla \times (\mathbf{v} \times \mathbf{w}) \equiv (\mathbf{w} \cdot \nabla)\mathbf{v} - (\mathbf{v} \cdot \nabla)\mathbf{w} + (\nabla \cdot \mathbf{w})\mathbf{v} - (\nabla \cdot \mathbf{v})\mathbf{w}. \tag{1.11}$$

The terms of eq. (1.10) represent different mechanisms for temporal field change due to fluid flow. The first r.h.s. term describes how fluid flow changes along magnetic field lines, and therefore represents dynamical stretching of the magnetic field; the second characterises the converse, that is how the magnetic field changes along field lines of fluid flow, i.e. advection of the magnetic field; the final term denotes field strengthening or weakening due to flow convergence or divergence, respectively.

### 1.3.3 Magnetic energy conservation

Although the temporal variabilty of the magnetic field is already given by eq. (1.8), the dynamo mechanism can also be viewed from an energetic perspective. First of all, magnetic energy is defined as $\mathbf{B}^2/(2\mu_0)$, and the temporal evolution of this quantity may be described with eq. (1.3), giving

$$\frac{1}{2\mu_0}\frac{\partial \mathbf{B}^2}{\partial t} = \frac{1}{\mu_0}\mathbf{B}\cdot\frac{\partial \mathbf{B}}{\partial t} = -\frac{1}{\mu_0}\mathbf{B}\cdot(\nabla\times\mathbf{E}). \tag{1.12}$$

Using the vector identity

$$\nabla\cdot(\mathbf{v}\times\mathbf{w}) \equiv \mathbf{w}\cdot(\nabla\times\mathbf{v}) - \mathbf{v}\cdot(\nabla\times\mathbf{w}) \tag{1.13}$$

for any 3-vectors $\mathbf{v}$ and $\mathbf{w}$, and combining it with eq. (1.12), (1.4) (under the MHD approximation), and (1.6) results in

$$\frac{1}{2\mu_0}\frac{\partial \mathbf{B}^2}{\partial t} = -\frac{1}{\mu_0}\nabla\cdot(\mathbf{E}\times\mathbf{B}) - \frac{\mathbf{J}^2}{\sigma} - \mathbf{u}\cdot(\mathbf{J}\times\mathbf{B}). \tag{1.14}$$

Finally, we integrate this equation over some (stationary) volume $\Lambda$, and by application of the divergence theorem the total magnetic energy balance becomes

$$\frac{1}{2\mu_0}\int_\Lambda \frac{\partial \mathbf{B}^2}{\partial t}\,\mathrm{d}\Lambda = -\frac{1}{\mu_0}\int_{\partial\Lambda}(\mathbf{E}\times\mathbf{B})\cdot\hat{\mathbf{n}}\,\mathrm{d}S - \int_\Lambda \frac{\mathbf{J}^2}{\sigma}\,\mathrm{d}\Lambda - \int_\Lambda \mathbf{u}\cdot(\mathbf{J}\times\mathbf{B})\,\mathrm{d}\Lambda, \tag{1.15}$$

where $\hat{\mathbf{n}}$ is the outward normal vector orthogonal to the boundary surface $\partial\Lambda$, and $\mathrm{d}S$ an infinitesimal surface element. The first term on the r.h.s. corresponds to the flux of electromagnetic energy through $\partial\Lambda$, characterised by the vector $(\mathbf{E}\times\mathbf{B})/\mu_0$ (known as the Poynting vector). The second term represents Ohmic dissipiation or Joule heating due to the core fluid's finite conductivity. Note that this term is always negative, and without sources external to $\Lambda$, dynamo action must therefore take place to sustain the field against Ohmic dissipation. Such a source of magnetic energy is given by the third term, which is the energy from the electromagnetic force on the core fluid (i.e. the Lorentz force).

### 1.3.4 The frozen-flux approximation

We have established that the temporal evolution of the magnetic field is produced by the two r.h.s. terms in the induction equation (eq. 1.8), but how important are they relative to each other? To shed light on this issue, consider their following ratio

$$\frac{||\nabla\times(\mathbf{u}\times\mathbf{B})||}{||\eta\nabla^2\mathbf{B}||} \sim \frac{\mathcal{U}\mathcal{L}}{\eta} = \frac{\tau_d}{\tau_u} = Rm, \tag{1.16}$$

where $\tau_d = \mathcal{L}^2/\eta$ and $\tau_u = \mathcal{L}/\mathcal{U}$ are characteristic time scales for field changes due to diffusion and fluid flow respectively, and $Rm$ denotes the magnetic Reynolds number (compare

for example with the more common hydrodynamic Reynolds number $Re$, defined instead by the kinematic diffusivity). In other words, the magnitude of $Rm$ characterises the disparity between the diffusive and fluid flow time scales. If we use conventional estimates for the above quantities ($\mathcal{L} = 10^6$ m, $\mathcal{U} = 5 \times 10^{-4}$ m s$^{-1}$, and $\eta = 2$ m$^2$ s$^{-1}$), we find $Rm \sim 10^2$, and the time scales $\tau_d = 16$ kyr and $\tau_u = 65$ yr. Therefore, it appears that temporal changes in $\mathbf{B}$ due to diffusion are much slower than those produced by the fluid flow. When considering field evolution over short time scales (yearly to decadal field changes, say), it seems reasonable then to ignore the diffusive contribution in the induction equation entirely, or equivalently to treat the core fluid as an electrical superconductor ($\sigma \to \infty$) (*Roberts and Scott*, 1965). Such a treatment gives the induction equation in reduced form

$$\frac{\partial \mathbf{B}}{\partial t} \approx \nabla \times (\mathbf{u} \times \mathbf{B}), \tag{1.17}$$

$$\approx (\mathbf{B} \cdot \nabla)\mathbf{u} - (\mathbf{u} \cdot \nabla)\mathbf{B}. \tag{1.18}$$

This is the *frozen-flux approximation*.

The equation above relies on the assumption that the core fluid is incompressible, i.e. it is assumed that $\nabla \cdot \mathbf{u} = 0$. Such a simplification is also widely made in for example geodynamo simulations to reduce the complexity of the associated governing equations, which are already difficult to solve numerically. It is of note, however, that the outer core mass density is believed to vary by about 20% from the ICB to the CMB, and these variations may be particularly important for the core's thermal evolution (*Anufriev et al.*, 2005).

There is an intuitive reason for the name of frozen flux: under this approximation the magnetic field evolves by moving with the flow as though it were 'frozen' into the core fluid. Let us briefly illustrate this by considering some material line element $\mathrm{d}\mathbf{l}$. Its change due to some background flow $\mathbf{u}$ is then described with a material derivative

$$\left(\frac{\partial}{\partial t} + \mathbf{u} \cdot \nabla\right)\mathrm{d}\mathbf{l} = \mathbf{u}(\mathbf{r} + \mathrm{d}\mathbf{l}) - \mathbf{u}(\mathbf{r}) = (\mathrm{d}\mathbf{l} \cdot \nabla)\mathbf{u}, \tag{1.19}$$

where the r.h.s. follows from a first-order Taylor series. It may readily be seen that this equation has the same form as eq. (1.18). As such, the magnetic field lines will subsequently evolve as though they are material lines and therefore move along with the flow. This is known as Alfvén's theorem (*Alfvén*, 1942).

### 1.3.5 Backus' conditions for frozen-flux

Along with the frozen-flux approximation (eq. 1.18) comes a set of constraints on the evolution of the radial magnetic field $B_r$, derived by *Backus* (1968). Just below the CMB core fluid flow is horizontal (recall that it is a material boundary), in which case this component of the field varies in time according to

$$\frac{\partial B_r}{\partial t} = \hat{\mathbf{r}} \cdot \nabla \times (\mathbf{u} \times \mathbf{B}), \tag{1.20}$$

$$= -\nabla_H \cdot (B_r \mathbf{u}_H), \tag{1.21}$$

where $\nabla_H := \nabla - \hat{\mathbf{r}}\partial/\partial r$ is the horizontal divergence, and $\mathbf{u}_H - u_r\hat{\mathbf{r}}$. If we integrate this equation over a spherical surface $P$ bounded by a null-flux curve (i.e. $\forall \mathbf{r} \in \partial P, B_r = 0$), we find

$$\int_P \frac{\partial B_r}{\partial t}\,\mathrm{d}S = -\int_P \nabla_H \cdot (B_r \mathbf{u}_H)\,\mathrm{d}S, \tag{1.22}$$

$$= -\int_{\partial P} (B_r \mathbf{u}_H) \cdot \hat{\mathbf{n}}\,\mathrm{d}P, \tag{1.23}$$

$$= 0, \tag{1.24}$$

where $\hat{\mathbf{n}}$ is normal to $\partial P$ and we have applied the divergence theorem. This result implies that for a perfect conductor the magnetic flux within a null-flux bounded curve is conserved. We may extend this result by considering all such curves on the CMB, which either bound a surface over which $B_r < 0$ ($P^-$) or $B_r > 0$ ($P^+$). The total flux change through all these patches is then

$$0 = \sum_i \int_{P_i^+} \frac{\partial B_r}{\partial t}\,\mathrm{d}S - \sum_j \int_{P_i^-} \frac{\partial B_r}{\partial t}\,\mathrm{d}S, \tag{1.25}$$

$$= \sum_i \int_{P_i^+} \frac{\partial |B_r|}{\partial t}\,\mathrm{d}S + \sum_j \int_{P_i^-} \frac{\partial |B_r|}{\partial t}\,\mathrm{d}S, \tag{1.26}$$

$$= \frac{d}{dt} \int_{\mathrm{CMB}} |B_r|\,\mathrm{d}S, \tag{1.27}$$

as the union of all $P_i^+$ and $P_j^-$ is the CMB. Therefore, for a perfectly conducting fluid, the total unsigned flux over the CMB is conserved. Equations (1.24) and (1.27) are *Backus*' (1968) conditions for CMB field evolution under the frozen-flux approximation, and will appear frequently throughout this work.

## 1.4 Geomagnetic measurements

Although the core field is generated thousands of kilometers below our feet, it permeates throughout the overlying mantle and crust, allowing us to measure the field at Earth's surface and above. Ultimately, these observations allows us to constrain the dynamics inside the core, using theoretical considerations such as those given in the previous section. In this section, different types of measurements are discussed, as well as how these are used to build space and time-dependent models of the core field.

First of all, it is important to note that the *geomagnetic field*, i.e. Earth's magnetic field measurable at its surface, is a superposition of several magnetic sources. We already discussed the core or main field, and based on its magnitude it forms the largest contribution to the total geomagnetic field. However, there exist other magnetic fields of internal origin, e.g. those from the permanently and inductively magnetised rocks within the lithosphere, and from electrical currents in the oceans. While these contributions are not as strong as the core field (around 1% of the core field strength (e.g. *Maus et al.*, 2002, *Maus*, 2010)), they can exhibit considerable spatial variation and need to be accounted for. Temporal variation of the internal magnetic field originates predominantly from the core. These changes typically take place over decades to centuries, hence the time derivative of the internal field is termed the *geomagnetic secular variation* (SV). It is these timescales and the associated secular variation that will be the focus of this thesis. Lastly, sources of external origin include those due to electrical current systems in the ionosphere and magnetosphere, known jointly as the *external field*. At Earth's surface, this contribution is much weaker than the internal field (around 2-5% of the internal field strength (e.g. *Hulot et al.*, 2015)), and operates on shorter (second to daily) time scales. Again, in order to be able to study the core field exclusively, geomagnetic measurements need to correct for this additional source.

Let us now briefly introduce the geomagnetic quantities that are typically measured. As noted earlier, magnetic fields are vector quantities, and have a direction and magnitude. The local field direction measured in terms of its components that point to the north, to the east, and downward, are typically denoted as the $X$, $Y$, and $Z$-components (Fig. 1.3). The horizontal components $X$ and $Y$ are associated with the horizontal intensity $H$, whereas the full length of the magnetic field vector is denoted by $F$. As mentioned in section 1.1, historical geomagnetic observations are often declination measurements, defined by the non-linear relationship $D = \tan^{-1}(Y/X)$. Similarly, the vertical angle between the horizontal and full magnetic field is referred to as inclination $I = \tan^{-1}(Z/H)$. The inclination defines the North Magnetic Pole (NMP), that is the location on the Northern Hemisphere where $I = 90^\circ$ (and similarly for the South Magnetic Pole), a commonly studied property of the field. It is of note that in contrast to declination measurements, which have been documented systematically from the 16th century onward, measuring field intensity became possible only after 1832 thanks to the work of *Gauss* (1837).

In what follows, we shall discuss several sources of geomagnetic observations, and their

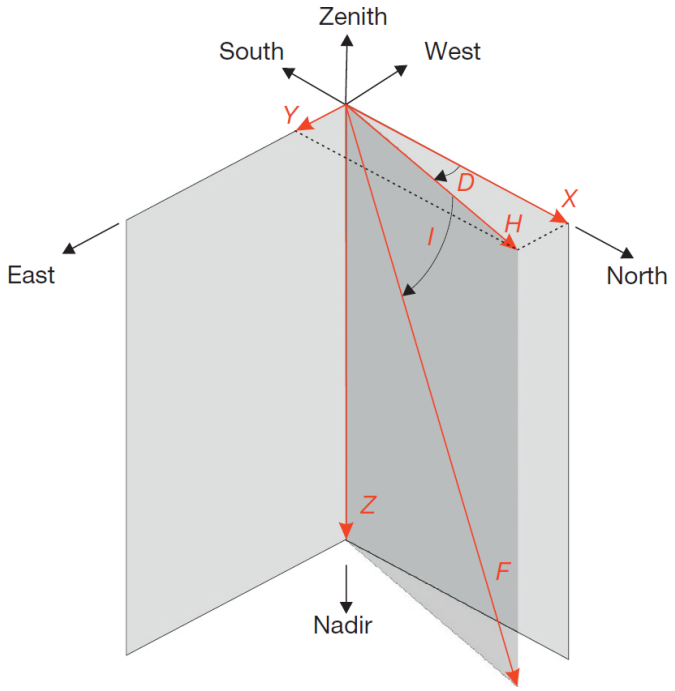


**Figure 1.3:** The local components of the magnetic field and their respective angles (image from *Hulot et al.* (2015))

strengths and weaknesses.

### 1.4.1 Geomagnetic observatories

A continuous source of geomagnetic data is those provided at *geomagnetic observatories*, where measurements of Earth's magnetic field are made at fixed time intervals. Several observatories had been set up by the early 19th century, and currently there are approximately 150 observatories spread around the globe (that is within the INTERMAGNET consortium, see `http://www.intermagnet.org/`). While observatory data has historically been provided as annual or hourly means, 1-minute means are also becoming available at an increasing rate. There is a major advantage to observatory measurements, which is that they have continuously monitored field evolution over decadal to centennial time scales with high temporal resolution. However, they are rather unevenly distributed across the Earth's surface, with most observatories situated in Western Europe, and relatively few in the Southern Hemisphere and across the oceans.

### 1.4.2 Satellite missions

For two decades (1999 — ) the observatory data have been complemented by continuous measurements made by satellites in low-orbit (typically at altitudes of several hundreds of km). These circumnavigate the entire Earth approximately every 90 minutes, and therefore provide geomagnetic measurements with unprecedented spatial coverage. However, because they

move continuously, differences among satellite measurements require additional data treatment to separate spatial and temporal field variability. Moreover, these measurements are relatively new, and can therefore not be used to investigate the field on historical time scales, in contrast to observatory data. The first global (intensity only) measurements were made by the POGO satellite series, specifically the OGO-2, OGO-4, and OGO-6 missions operating from 1965 to 1971 (*Cain*, 2007). These missions were succeeded by the MAGSAT satellite, operating from 1979 to 1980, which was the first to also provide global directional observations of the field (*Purucker*, 2007). The most recent mission is titled SWARM (*Friis-Christensen et al.*, 2006), a constellation mission launched in 2013 and led by the European Space Agency (ESA) which comprises three identical satellites, which together provide directional and intensity measurements at a sampling frequency of 1 Hz with measurement errors less than 0.5 nT. Other continuous satellite measurements have been made by CHAMP (which operated between 2000-2010, see also *Reigber et al.* (2002)) and the Danish mission Ørsted (which has operated since 1999 onward, see also *Neubert et al.* (2001)). Satellite measurements have been employed by for example *Finlay et al.* (2016a) (in addition to observatory data) to build the CHAOS-6 field model, which describes the space and time variability of the core field over approximately the past two decades.

### 1.4.3 Historical logs

A third source for geomagnetic observations are historical logs made primarily for navigational purposes, as mentioned in section 1.1. A monumental effort of cataloging these measurements, some of which date back to the 16th century, was made by *Jackson et al.* (2000) and *Jonkers et al.* (2003) to which the reader is referred for further details. However, we note here that these observations have relatively poor spatial coverage, as these were made predominantly along former trade routes in the Atlantic and Indian oceans. Additionally, most observations in these logs are declination measurements which, in absence of intensity measurements, constrain only the morphology of the magnetic field and not its strength. Nevertheless, this source of geomagnetic data has proven invaluable, and in the landmark study by *Jackson et al.* (2000) these observations have been combined to build the gufm1 field model, describing the historical secular variation of the core field from 1590 to 1990. In addition, *Gillet et al.* (2013, 2015) employed historical measurements in addition to observatory and satellite data to build the COV-OBS and COV-OBS.x1 ensemble field models for the periods 1840-2010 and 1840-2015 respectively, which comprise multiple model realisations from an optimised probability distribution (of which 100 are published).

### 1.4.4 Palaeomagnetism

Further constraints on the history of Earth's magnetic field come from *palaeomagnetism*, which may easily be regarded as a separate field of research by itself. Nevertheless, because of its valuable contributions to our understanding of Earth's magnetic field and the geodynamo, some

of its characteristics are touched upon here.

In essence, palaeomagnetism concerns the ancient magnetic field recorded by igneous or sedimentary rocks, or artificially baked materials. During their formation, and while their temperature is below the Curie temperature, magnetic minerals comprising the rock tend to align themselves along the ambient magnetic field, i.e. that of Earth (e.g. *Tauxe*, 2010). As a result, these rocks record the geomagnetic field state at the time of solidification (much like a cassette tape). Together with the absolute dating of the rocks, this magnetisation property provides us with a powerful tool, for investigating the field of up to billions of years in the past, which allows us to constrain the behaviour of the ancient geodynamo. In fact, palaeomagnetic field intensities indicate that the Earth's magnetic field (and hence the geodynamo) is at least as old as 3.5 Gyr, and that the ancient field was approximately 50% weaker than its present-day configuration (*Tarduno et al.*, 2007, 2010).

Unfortunately, palaeomagnetic data are incredibly sparsely distributed over the globe and through time. Therefore, at a single point in time they often constrain only the largest wavelength of the field, which is typically assumed to be that of a dipole field tilted with respect to Earth's rotation axis (this is known as the geocentric axial dipole (GAD) hypothesis). With the use of this approximation, which is confirmed a valid representation for the time-averaged field over at least several tens of thousands of years (*Acton et al.*, 1996, *Driscoll and Wilson*, 2018), it is evident that the dipole component has reversed polarity numerous times over the lifetime of the field (e.g. *Cox et al.*, 1963). Such polarity transitions are referred to as *geomagnetic reversals*. Despite this reversing behaviour, long-term magnetic field variation is generally characterised by stable, non-reversing periods (with a typical time scale of 100 kyr), interrupted by relatively fast reversal events (often these transitions take less than 10 kyr (*Clement*, 2004)). In any case, it is clear that the frequency at which reversals occur is far from steady: palaeomagnetic data are replete with long periods such as the Cretaceous normal superchron (84-121 Ma) during which no reversals occurred (*Cande and Kent*, 1995), but also unstable periods (e.g. 150-170 Ma) characterised by high reversal rates, possibly in excess of 12 $\mathrm{Myr}^{-1}$ (*Tominaga et al.*, 2008); estimates for the present-day reversal frequency are around 4 $\mathrm{Myr}^{-1}$ (*Biggin et al.*, 2012).

It remains unclear what exactly triggers a geomagnetic reversal. However, they are observed within numerical simulations of the geodynamo (*Kageyama and Sato*, 1995, *Glatzmaier and Roberts*, 1995), indicating that these are characteristic features of the geomagnetic field. With the use of such simulations, several authors have additionally found that reversals are more frequent when either the total CMB heat flow or its heterogeneity are increased (*Glatzmaier et al.*, 1999, *Driscoll and Olson*, 2009, *Olson et al.*, 2010, *Olson and Amit*, 2014). These variations in CMB heat flow, and therefore the reversal frequency, may reflect the thermal control of mantle convection on the geodynamo (*Biggin et al.*, 2012).

## 1.5 Core field modelling

Geomagnetic data are certainly useful to investigate the core field at a specific location or at a single point in time. However, can we use such observations to obtain better understanding of the field morphology on a global scale, including regions which are not sampled? Similarly, if we were to know the field morphology exactly at two epochs, how well can we constrain the field between those dates? Models of the core field, often simply referred to as *field models*, aid in resolving such issues. In this section, we will summarise how such observation-based models of the core field can be constructed, and comment on several characteristic features of the field manifest in these models.

### 1.5.1 Mathematical representation

To construct core field models it is necessary to choose a suitable mathematical representation of the field. Earlier we considered the magnetic field as a vector field; such a representation corresponds to three unknowns (in three-dimensional space). Computational considerations require the field to be discretised (a computer can only represent a finite numerical resolution). We therefore introduce here another representation widely used within the geomagnetism community, which reduces the number of free parameters and allows for a discrete parameterisation.

We assume that the region outside the core is an electrical insulator, in which case no electrical currents can exist there, and therefore $\nabla \times \mathbf{B} = 0$ for $r > c$ (eq. 1.4). Then, the field may be represented by a scalar potential $V$ such that

$$\mathbf{B} = -\nabla V. \tag{1.28}$$

This representation must satisfy the absence of magnetic monopoles (eq. 1.2), therefore the scalar potential is a potential field:

$$\nabla^2 V = 0. \tag{1.29}$$

Solutions to the above exist in the form of spherical harmonics, and if we exclude external sources (at $r > a$), these have the canonical form (e.g. *Hulot et al.*, 2015)

$$V(\mathbf{r}, t) = a \sum_{l=1}^{\infty} \sum_{m=0}^{l} \left(\frac{a}{r}\right)^{l+1} \left(g_l^m(t) Y_{l,0}^m(\theta, \phi) + h_l^m(t) Y_{l,1}^m(\theta, \phi)\right), \tag{1.30}$$

$$= a \sum_{l=1}^{\infty} \sum_{m=0}^{l} \left(\frac{a}{r}\right)^{l+1} \left(g_l^m(t) \cos(m\varphi) + h_l^m(t) \sin(m\varphi)\right) P_l^m(\cos\theta), \tag{1.31}$$

where $l$ and $m$ respectively denote spherical harmonic degree and order, $Y_{l,n}^m$ are the so-called

*spherical harmonics*, which have either azimuthal cosine or sine dependence (with $n$ a binary index used here to distinguish between the two types), the $P_l^m(x)$ are the associated Legendre functions, and the $g_l^m$ and $h_l^m$ are the time-dependent *Gauss coefficients*. Within geomagnetism, it is common practice to adopt Schmidt quasi-normalised $P_l^m(x)$, so that the spherical harmonics obey the orthogonality condition

$$\int_{\Omega(1)} Y_{l,n}^m Y_{i,k}^j \, \mathrm{d}S = \frac{4\pi}{2l+1} \delta_{li} \delta_{mj} \delta_{nk}, \tag{1.32}$$

with $\Omega(r)$ a spherial surface of radius $r$ (e.g. *Winch et al.*, 2005). Therefore, projecting $V$ (if known) on any of the spherical harmonics with the above norm, one may solve for the Gauss coefficient associated with that harmonic. Conversely, if the Gauss coefficients are known, then the spherical harmonic representation and eq. (1.28) allow $V$ and all vector components of the field to be straightforwardly computed at any location or time. The orthogonality of the harmonics may also be utilised to compute power spectra of the field or *Lowes-Mauerberger* spectra (*Lowes*, 1974), defined as

$$\frac{1}{4\pi} \int_{\Omega(r)} \mathbf{B}^2(r) \, \mathrm{d}S = \sum_{l=1}^{\infty} W_l(r), \tag{1.33}$$

$$:= \sum_{l=1}^{\infty} (l+1) \left( \frac{a}{r} \right)^{2l+4} \sum_{m=0}^{l} (g_l^m)^2 + (h_l^m)^2. \tag{1.34}$$

Due to practical limitations, it is necessary to truncate eq. (1.31) and (1.34) at some degree $l \leq L$, which is variable among types of models. For observation-based models it is generally necessary to set $L \leq 14$, as higher-degree core field contributions are difficult to separate from those of crustal field (*Langel and Estes*, 1982). Therefore, the horizontal resolution of such models is inherently limited. For forward numerical simulations however, truncation of the spherical harmonic series is constrained only by computational limitations, and it is typical for such models that $L > 100$ — a recent state-of-the-art geodynamo model has even been reported with $L = 1000$ (*Schaeffer et al.*, 2017).

It is important to note that the radial solution in eq. (1.31) depends on $l$. As a consequence, high degree features become much more attenuated with increasing altitude compared to low degree contributions. As we will see later, the modelled core field at the CMB ($r = c$) is therefore characterised by relatively short wavelengths compared to their corresponding representation of the field at Earth's surface ($r = a$).

Lastly, time-dependent models require also an expansion onto a time-dependent basis, which usually takes the form

$$g_l^m(t) = \sum_k {}_k g_l^m \phi_k(t), \tag{1.35}$$

where the ${}_k g_l^m$ are coefficients associated with the temporal basis functions $\phi_k(t)$. Various choices for $\phi_k(t)$ exist, although a currently popular choice is that of B-splines (e.g. *de Boor*, 1978), motivated by the reduced computational requirements associated with these functions, and the fact that they are relatively smooth functions (conforming to the idea that a simple solution is preferred over a complex one).

### 1.5.2 General inverse strategy

Models of the core field derived from geomagnetic observations (section 1.4) are generally a solution to an *ill-posed* inverse problem. Within geomagnetism, these are generally of the overdetermined type, in which case the inconsistency among data prohibits the existence of a single solution that fits all data exactly. The associated forward problem, derived using the mathematical representation given in the previous section for instance, has the discretised form

$$\mathbf{d} = \mathbf{G}(\mathbf{m}) \tag{1.36}$$

where $\mathbf{d}$ is a data vector containing all observations (e.g. field measurements at various locations and at a single point in time), $\mathbf{m}$ some model vector (e.g. the Gauss coefficients at a single point in time), and $\mathbf{G}$ the relation between the two. It should be clear that while we previously considered only 3-vectors, the data and model vectors can have any dimension. If we consider the case that $\mathbf{G}$ is linear ($\mathbf{G}(\mathbf{m}) = \mathbf{G}\mathbf{m}$), a solution for $\mathbf{m}$ could in principle be computed by multiplying the system of equations by $\mathbf{G}^{-1}$. However, for an ill-posed problem such a matrix is singular — in fact, $\mathbf{G}$ need not even be square!

A more feasible approach is therefore not to fit all data exactly, but instead find some model $\hat{\mathbf{m}}$ that minimises the overall misfit to the data, which is defined by a *cost* or *objective function*. A typical choice for this norm is the damped weighted $L_2$ or Euclidean norm, in which case

$$\Phi(\mathbf{m}) := \big(\mathbf{d} - \mathbf{G}(\mathbf{m})\big)^T \mathbf{C}_d^{-1} \big(\mathbf{d} - \mathbf{G}(\mathbf{m})\big) + \lambda \mathbf{m}^T \mathbf{C}_m^{-1} \mathbf{m}. \tag{1.37}$$

where the associated weights are provided by the data and model covariance matrices $\mathbf{C}_d$ and $\mathbf{C}_m$, respectively. The first term on the r.h.s. represents a weighted least-squares residual between the model and the data, in other words the overall fit to the data provided by the model — ideally the data is matched optimally, and this term is therefore as low as possible. However, such a small residual may be associated with large magnetic field amplitudes or gradients within the model, which may be harder to justify (for example from physical considerations). Therefore, a second *regularisation* term is often included to penalise the overall model complexity (second term on the r.h.s.). Different choices of regularisation exist, all of which result in a different weighting matrix $\mathbf{C}_m^{-1}$. The non-negative *damping parameter* $\lambda$ is then a measure for the trade-off between a good fit to the data and model complexity; choosing an appropriate value for this parameter is generally not trivial, and may require additional constraints. In any case, minimising an objective function of the form of eq. (1.37) will provide a model that fits the data, while also penalising model complexity.

A typical method of minimising the cost function is by finding $\hat{\mathbf{m}}$ for which the objective function is stationary, i.e. when

$$\nabla_{\hat{\mathbf{m}}}\Phi(\hat{\mathbf{m}}) = \mathbf{0}. \tag{1.38}$$

When $\mathbf{G}$ is linear in $\mathbf{m}$ (i.e. when $\mathbf{G}(\mathbf{m}) = \mathbf{G}\mathbf{m}$), the Euclidean cost function is quadratic in $\mathbf{m}$, and the expression above yields an explicit solution for the optimal model that minimises $\Phi$:

$$\hat{\mathbf{m}} = (\mathbf{G}^T\mathbf{C}_d^{-1}\mathbf{G} + \lambda\mathbf{C}_m^{-1})^{-1}\mathbf{G}^T\mathbf{C}_d^{-1}\mathbf{d}. \tag{1.39}$$

As mentioned earlier, while $\hat{\mathbf{m}}$ is uniquely determined in this case, it may return unrealistically large amplitudes or gradients. These may be reduced by choosing a sufficiently large $\lambda$, although increased regularisation is often associated with compromising on the fit to the data. Additional complications may arise when $\mathbf{G}$ is nonlinear in $\mathbf{m}$ (for example when $\mathbf{d}$ contains declination data), in which case the explicit solution above cannot be used. Then, the objective function needs to be minimised iteratively, for example through the use of Newton's method (see e.g. *Menke*, 2018).

### 1.5.3 Core flow models

The methods described above may be used to compute some model of the core field that best fits geomagnetic measurements, which for instance comprises a set of Gauss coefficients (eq. 1.31). A related class of models exists, which are the result of an inversion of geomagnetic observations for the motion of core fluid just below the CMB, sometimes modelled jointly with the Gauss coefficients. Such core flow models take advantage of the frozen-flux approximation, in which diffusion is negligible, and therefore a direct relation exists between the field and fluid flow (eq. 1.18). The associated discretised problem then has the form of eq. (1.36), where the data vector may contain time derivatives of Gauss coefficients, and the model coefficients could for example be spectral coefficients describing fluid flow (e.g. *Whaler*, 1986).

The solution to this problem is, however, always non-unique. This may readily be seen from equation (eq. 1.18): only one equation is employed to obtain two (horizontal) flow components. As such, the problem is strongly underdetermined, which implies that additional information or constraints on the flow should be introduced to compute a meaningful solution. Since there are several ways of doing so, there exists a variety of core flow models each with different underlying assumptions (see *Holme* (2015) for an overview). A most common method to mitigate this ill-posedness is to adopt some form of regularisation (e.g. as in eq. 1.37), for example by penalising the kinetic energy of the obtained flow (*Madden and Le Mouël*, 1982) or the flow heterogeneity (*Bloxham*, 1988). The latter method is often referred to as the use of the 'strong norm', as it penalises the small-wavelength flow more strongly compared to the former. However, for either type of regularisation the downside is that the flow is restricted to be mostly of large scale, depending on the magnitude of the damping parameter. Another

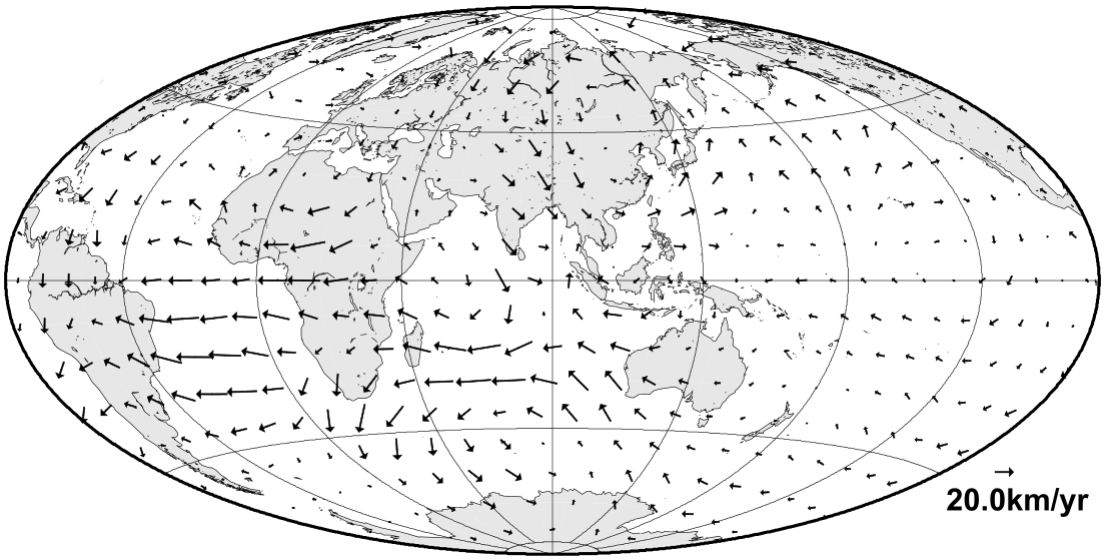


**Figure 1.4:** The steady part of a model for core fluid motion just below the CMB over 2001.0-2010.0 (image from *Whaler and Beggan* (2015)).

way of improving the conditioning of the core flow inversion is to assume the flow is purely toroidal, reducing the degrees of freedom of the solution. This type of flow is motivated by the potentially stratified layer in the outermost core, which would inhibit radial flow (*Whaler*, 1980). While the toroidal constraint improves the conditioning of the problem, the associated flows have been shown to imperfectly match the observed SV (*Lesur et al.*, 2015). A reduction in the number of free parameters of the flow model may also be accomplished by considering steady flows. Still, time-dependent flows are particularly valuable as these can be linked to length-of-day variations (*Jault et al.*, 1988), therefore providing some physical justification for core flow modelling. Finally, we comment on tangentially geostrophic flows, which are built on the assumption that the forces associated with rotation, buoyancy, and pressure gradients are in balance. Such a constraint can be shown to provide better conditioning than that of toroidal-only flows, although the assumed force balance is expected to fail near the equator (the Coriolis force is zero there) (*Backus and Le Mouël*, 1986).

As an example, Fig. 1.4 shows the steady part of a model for core flow below the CMB for the period 2001.0-2010.0, computed by *Whaler and Beggan* (2015). A characteristic feature of this flow pattern is the westward motion in the equatorial Atlantic, which is commonly used to explain the westward drift in magnetic features discussed earlier. Additionally, these models often render gyre-like circulation beneath the Southern Indian Ocean, and small-amplitude flow in the Pacific Hemisphere. These features are shared among various core flow models, even though each may be subject to other assumptions on the nature of the flow (a comparison of flow models is given by *Bloxham and Jackson*, 1991). Nonetheless, differences in such assumptions may still result in significant local variation among flow patterns.

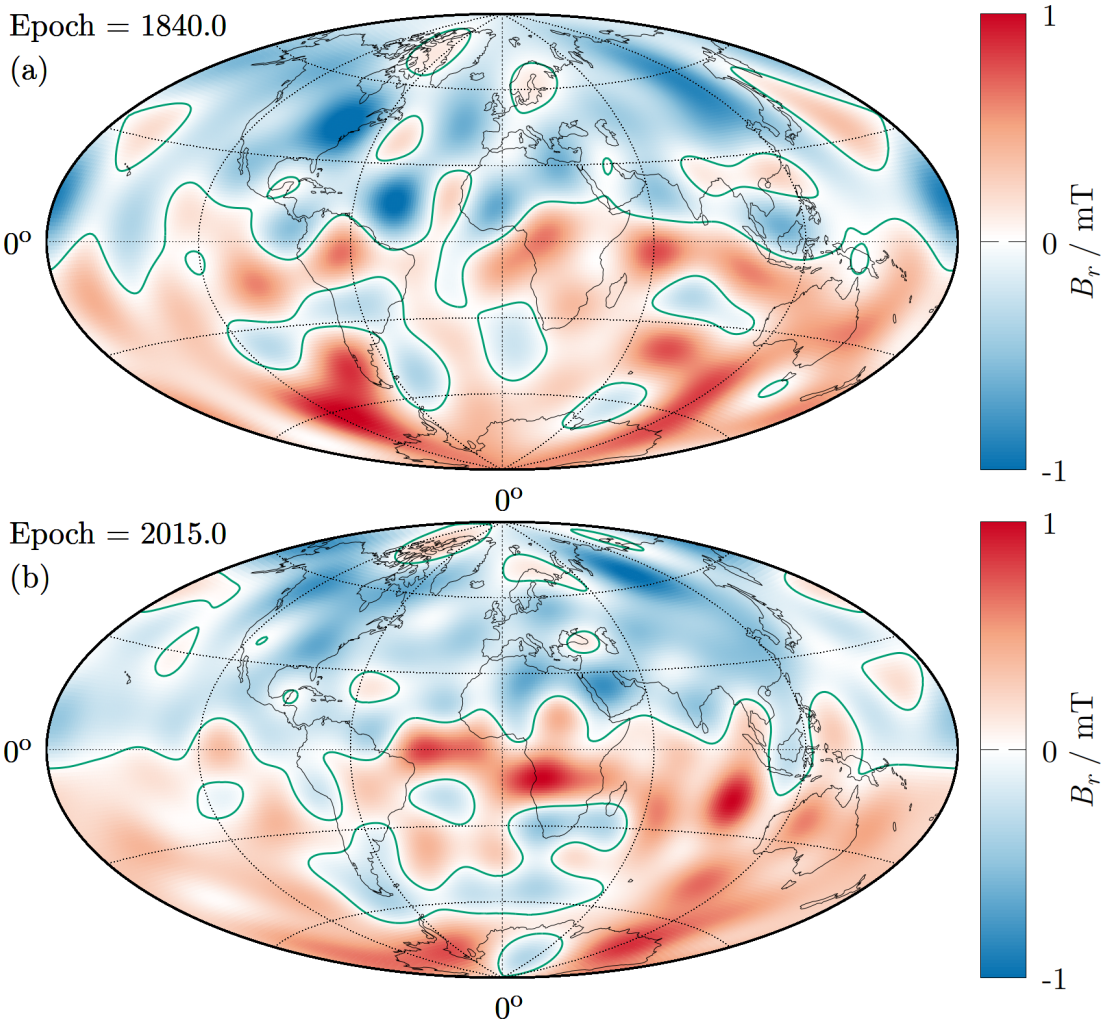


**Figure 1.5:** The radial field at the CMB and in 1840.0 (a) and 2015.0 (b) according to the COV-OBS.x1 field model (*Gillet et al.*, 2015). Null-flux curves are denoted in green.

### 1.5.4 Characteristics of secular field evolution

There exists a variety of time-dependent models of the core field, each derived with different methods, assumptions, and/or data (e.g. *Jackson et al.*, 2000, *Lesur et al.*, 2008, *Gillet et al.*, 2015, *Finlay et al.*, 2016a). Here, we will discuss some of the commonly found features of the field in these models.

Maps of the radial field at the CMB (Fig. 1.5) confirm that the field is well approximated by a dipole aligned with the axis of rotation, as the magnetic field is mainly orientated radially inwards/outwards in the Northern/Southern Hemisphere. Although this axial dipole field, defined by the $g_1^0$ coefficient (eq. 1.31), is dominant over all other multipole contributions, it has been weakening for several centuries (*Barraclough*, 1974, *Gubbins et al.*, 2006). The axial dipole decay may be expressed as a weighted integral of the radial CMB field. Then, patches of $B_r$ with a sign different to the prevalent axial dipole, often referred to as *reversed-flux patches* (RFPs), can be shown to contribute destructively to the magnitude of the axial

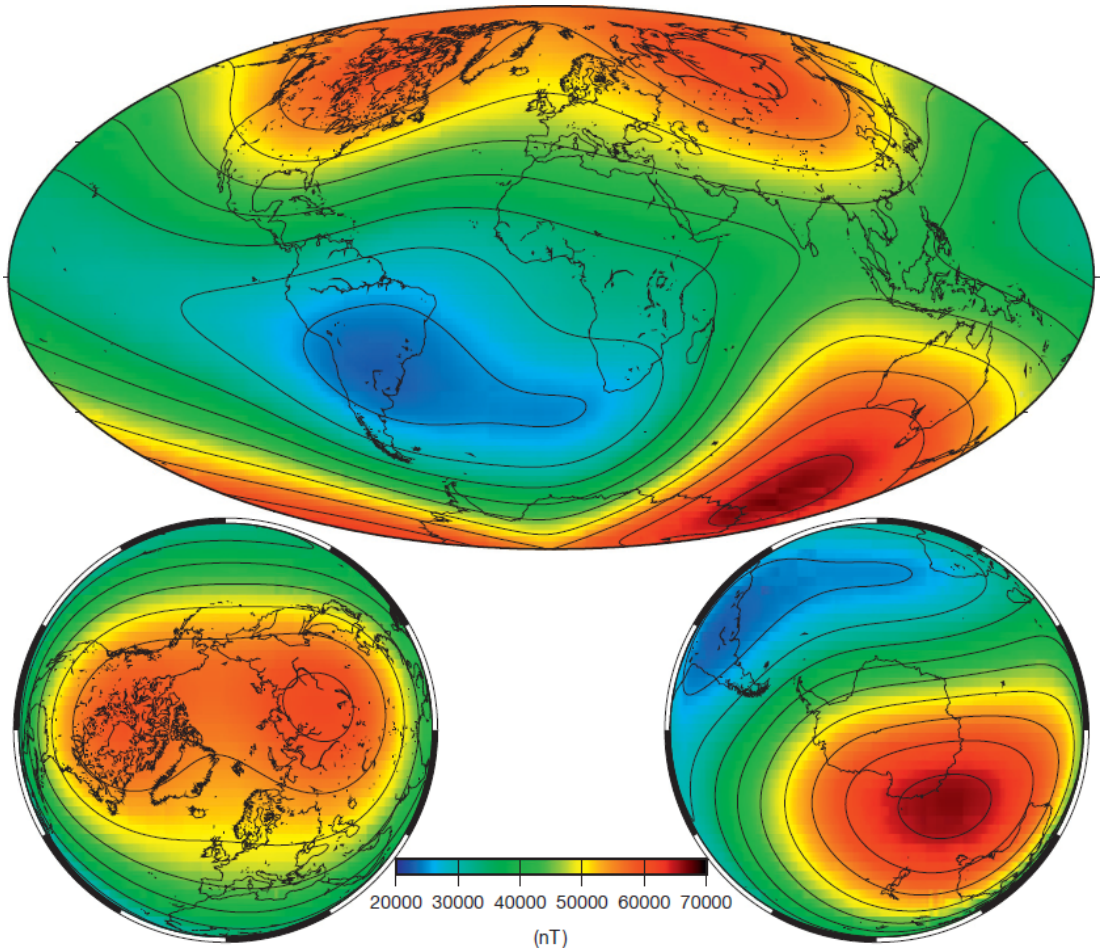


**Figure 1.6:** The field intensity $F$ at the Earth's surface in 2010.0, according to the CHAOS-4 field model (*Olsen et al.*, 2014) (image from *Hulot et al.* (2015)).

dipole field. Within the present-day field, several of such patches reside in the South Atlantic (Fig. 1.5). Therefore, several authors have linked the temporal evolution of these patches to the decaying axial dipole, and have proposed this as a potential mechanism for geomagnetic polarity reversals (*Gubbins and Roberts*, 1987, *Olson and Amit*, 2006, *Gubbins et al.*, 2006, *Terra-Nova et al.*, 2015). Specifically, it has been shown that over the 20th century RFPs have weakened the axial dipole by migrating towards the geographic poles (where the associated averaging kernel is of higher amplitude) (*Olson and Amit*, 2006, *Terra-Nova et al.*, 2015, *Finlay et al.*, 2016b), for example due to the gyre-like motion beneath the Indian Ocean (Fig. 1.4). However, such studies do not usually consider the evolution of non-reversed field, which too may be weakening and/or migrating, and could therefore play an important role in the observed axial dipole decay.

The reversed-flux patches have a clear signature on the magnetic field at the Earth's surface. These features cause a local cancellation of the radial field, resulting in reduced overall field intensity (*Terra-Nova et al.*, 2017). This is demonstrated in (Fig. 1.6), a map of the surface intensity at 2010.0. The surface field is characterised by high-intensity lobes at inter-

mediate to high-latitude (near North America, Siberia and south of Australia), corresponding to the predominantly axially dipolar nature of the field, which are classically attributed to fluid downwelling motion near the tangent cylinder (*Christensen et al.*, 1998). However, there is a distinct region covering most of South America where the field is anomalously weak, typically less than 30,000 nT. This weak-field region is known as the South-Atlantic Anomaly (SAA), and is potentially a persistent feature of the field. For example, there is evidence that this feature has existed for several centuries, and may have emerged even before 950 AD (*Hartmann and Pacca*, 2009, *Tarduno et al.*, 2015, *Hartmann et al.*, 2019). Because the non-dipole field is generally thought to change over shorter time scales (*Lhuillier et al.*, 2011), the SAA may be the result of the thermal interaction between the core and mantle (*Tarduno et al.*, 2015, *Terra-Nova et al.*, 2019), as the latter evolves comparatively slowly. Additional interest in the SAA comes from the increased radiation damage to aircraft and satellites travelling within this region, as the locally reduced intensity of the core field results in increased susceptibility to incoming charged particles (e.g. those expelled due to solar activity) (*Heirtzler*, 2002).

### 1.5.5 Appraising frozen flux

As the frozen flux approximation allows us to render core fluid motion below the CMB, it is certainly tempting to neglect diffusion in the induction equation (eq. 1.8). Still, is it actually appropriate to do so for Earth's core?

By consideration of the argument that $Rm$ is rather large for Earth's core, we may indeed be convinced that such neglect is allowed (section 1.3.4). However, the parameters used to compute this number are not necessarily well-constrained. For example, the magnetic length scale $\mathcal{L} \approx 10^3$ km is generally based on the horizontal morphology of the field, as described by observation-based field models. As such, the high-$Rm$ argument falls short of considering also the radial length of the magnetic field, which is poorly constrained. In addition, several authors have argued for much reduced radial magnetic length scales below the CMB (*Olson et al.*, 2010, *Finlay and Amit*, 2011, *Terra-Nova et al.*, 2016), which would subsequently lead to smaller $Rm$. Furthermore, earlier we used $\mathcal{U} \approx 5 \times 10^{-4}$ km s$^{-1}$, but this values is classically derived by attributing the westward drift rate to fluid flow, which therefore supports frozen-flux only in a circular manner. It seems therefore that the value of $Rm$, and its implications for the evolution of the core field, should be considered with caution.

We have already seen that for negligible diffusion, the total magnetic flux change over patches bounded by a null-flux curve is invariant with time (eq. 1.24). Therefore, this condition provides a means to test the validity of frozen flux quantitatively. Accordingly, several authors have constructed field models at different epochs and found that the frozen-flux constraint was not satisfied. For example, *Bloxham and Gubbins* (1985) and *Bloxham and Gubbins* (1986) found that the overall flux through reversed-flux patches in the South Atlantic, which are inherently bounded by $B_r = 0$ contours, increased significantly over the 20th century. Later the violation of Backus' frozen-flux constraints was confirmed also by *Chulliat and Olsen*

(2010) and *Asari et al.* (2010). However, such observation-based studies may incorporate the frozen-flux constraint (eq. 1.24) as an additional penalisation term in the minimised objective function (e.g. of the form of eq. 1.37), and considering the problem of choosing an appropriate scaling factor to this term objectively, it remains difficult to unambiguously detect violation of frozen flux with these methods. Moreover, several workers have succesfully constructed field models that are consistent with frozen flux (*Gubbins*, 1984, *Constable et al.*, 1993, *Wardinski and Lesur*, 2012).

Magnetic diffusion was first modelled together with (steady) core flow by *Voorhies* (1993), which allowed for an improved fit to geomagnetic field models compared to steady flow only. Later, *Gubbins* (1996) provided a more general method to co-estimate the fluid flow and diffusive contributions to secular variation and found that diffusion is indeed required to explain the overall intensification of an RFP below South Africa. *Bloxham* (1986) proposed a mechanism explaining the temporal evolution of RFPs physically, that of a local fluid upwelling concentrating the field below the CMB followed by radial magnetic diffusion, a process known as *flux expulsion*. Such an interaction has also been observed in numerical geodynamo simulations (*Aubert et al.*, 2008), which are often characterised by values of $Rm$ that are considered Earth-like (*Christensen et al.*, 2010). Therefore, even if $Rm$ is large, diffusion could still be capable of contributing significantly to the short-term evolution of the core field. However, such simulations have also demonstrated that the fluid flow just below the CMB can reliably be inverted for with frozen flux, although the necessary truncation of the spherical harmonic representation (e.g. by setting $L = 14$) can lead to increased uncertainty of inverted flow structures, in particular that of low-latitude motions commonly used to explain the westward drift (*Rau et al.*, 2000).

### 1.5.6 Forecasting core field evolution

Every five years sees a new release of the field models within the International Geomagnetic Reference Field (IGRF) series and the World Magnetic Model (WMM) series. These pragmatic models, used for a variety of purposes such as exploration geophysics and navigation (*Meyers and Davis*, 1990), come in the form of a set of Gauss coefficients which describe the field at a single epoch. In addition, these models also provide the estimated secular variation coefficients $\{\dot{g}_l^m, \dot{h}_l^m\}$ over the next five years. If these are assumed steady, they can be used to forecast field evolution over the next five years (until the release of a newer IGRF or WMM iteration). Note that an out-of-cycle update to the 2015 WMM model has recently been released (*Chulliat et al.*, 2019).

The last decade or so has seen the introduction of more advanced methods aimed at forecasting core field evolution. Often, these forecasts rely on *data assimilation* techniques, which are designed to correct the observed temporal core field evolution with some numerical model describing its forward evolution. Not only does such an updated trajectory provide a better fit to the data, it also allows for more accurate predictions of field evolution than the IGRF/WMM

steady SV forecasts. Data assimilation has already been applied widely over the past decades, e.g. for weather forecasting, however it is relatively recent that these techniques have been applied within the context of geomagnetism (for an overview of developments see e.g. *Fournier et al.* (2010)). Following the proof-of-concept studies by *Fournier et al.* (2007) and *Kuang et al.* (2008), a first application to geomagnetic forecasting was made by *Beggan and Whaler* (2009), in which the forward field evolution was described by the relatively simple case of steady core fluid motion. Indeed, this method provides forecasts with improved global accuracy compared to the Gauss coefficient extrapolation provided by the IGRF and WMM models: over a period of 5 years (that is the period between releases of the IGRF and WMM models) their global forecast error is less than 30 nT, while at the end of such a period the linear extrapolation of Gauss coefficients is accurate only within approximately 80 nT.

However, in reality core fluid motion is not steady. Furthermore, magnetic diffusion could also be important for short-term field change (as discussed in the previous section). The performance of these forecasts was also limited by the occurrence of *geomagnetic jerks*, i.e. jump changes in the second time derivative of the field. More elaborate (and computationally expensive) forecasts are those by *Aubert* (2015), who utilised full-sphere geodynamo simulations in a data assimilation scheme, and reported a much improved predictability with respect to the IGRF forecasts when a prediction window of several decades is considered. Additionally, *Barrois et al.* (2017) and *Barrois et al.* (2018) have constructed a data assimilation scheme that relies on the statistics derived from the same geodynamo simulation as employed by *Aubert* (2015). However, as a result their analysis appears too strongly biased towards the time-average geodynamo reference state (in which the SV approximately vanishes) to match observed trends. Morever, it is of note that as with any modern geodynamo model, their control parameters are separated from Earth-like values by several orders of magnitude, and may therefore not truly reflect the dynamics inside the core. Recently, *Bärenzung et al.* (2018) have proposed a simulation-independent frozen-flux data assimilation scheme. They report forecasts with higher accuracy than those based the IGRF SV prediction, in particular when predictions over several decades to centuries are considered. Their limit of predictability can exceed several centuries (depending on the spherical harmonic degree), consistent with the geodynamo predictability horizon of several centuries reported by *Hulot et al.* (2010). However, this approach still relies on the frozen-flux hypothesis, and if diffusion is indeed relevant for short-term SV, accounting for diffusion may improve core field predictions and possibly extend the predictability limit of purely flow-based forecasts.

## 1.6 Outline of thesis and motivation

This thesis concerns the role of magnetic diffusion in the overall geomagnetic secular variation. This diffusive contribution is often assumed to operate on time scales of tens of thousands of years, and has therefore widely been neglected when considering the yearly-to-decadal evolution of the core field. However, both observation-based and numerical studies indicate that

it may provide an important contribution to secular variation, in particular for the growth and intensification of reversed-flux patches observed over the 20th century. Therefore, our main research aim is to explore to what extent diffusion can explain the short-term SV. Such information may be valuable, for example as a means to improve forecasts of short-term core field evolution, which frequently rely on a frozen-flux description of SV. These issues are addressed in the following chapters:

- Chapter 2 concerns a characterisation of the reversed and normal-flux evolution over the past century or so using time-dependent field models, in which we describe their growth, intensification, and migration over this period.
- In Chapter 3 we introduce the purely diffusive end-member model to secular variation, and test how well it fits secular variation and several of its characteristics, such as reversed-flux emergence.
- Chapter 4 is an application to forecasting the short-term core field evolution, in which we employ purely flow-based predictions, and consider a extension based on magnetic diffusion to improve these forecasts.
- In Chapter 5 we present final concluding remarks and outline several implications associated with this work.

# References


Acton, G. D., K. E. Petronotis, C. D. Cape, S. R. Ilg, R. G. Gordon, and P. C. Bryan (1996), A test of the geocentric axial dipole hypothesis from an analysis of the skewness of the central marine magnetic anomaly, *Earth and Planetary Science Letters*, *144*(3), 337 – 346. 1.4.4

Alfvén, H. (1942), Existence of electromagnetic-hydrodynamic waves, *Nature*, *150*. 1.3.4

Anufriev, A., C. Jones, and A. Soward (2005), The Boussinesq and anelastic liquid approximations for convection in the earths core, *Physics of the Earth and Planetary Interiors*, *152*(3), 163 – 190. 1.3.4

Asari, S., V. Lesur, and M. Mandea (2010), Geomagnetic secular variation violating the frozen-flux condition at the core surface, *Earth, Planets and Space*, *62*(9), 693–709. 1.5.5

Aubert, J. (2015), Geomagnetic forecasts driven by thermal wind dynamics in the Earth's core, *Geophysical Journal International*, *203*(3), 1738–1751. 1.5.6

Aubert, J., J. Aurnou, and J. Wicht (2008), The magnetic structure of convection-driven numerical dynamos, *Geophysical Journal International*, *172*(3), 945–956. 1.5.5

Aubert, J., S. Labrosse, and C. Poitou (2009), Modelling the palaeo-evolution of the geodynamo, *Geophysical Journal International*, *179*(3), 1414–1428. 1.2

Backus, G. (1968), Kinematics of geomagnetic secular variation in a perfectly conducting core, *Philosophical Transactions of the Royal Society of London. Series A, Mathematical and Physical Sciences*, *263*(1141), 239–266. 1.3.5, 1.3.5

Backus, G. E., and J.-L. Le Mouël (1986), The region on the coremantle boundary where a geostrophic velocity field can be determined from frozen-flux magnetic data, *Geophysical Journal International*, *85*(3), 617–628. 1.5.3

Bärenzung, J., M. Holschneider, J. Wicht, S. Sanchez, and V. Lesur (2018), Modeling and predicting the short-term evolution of the geomagnetic field, *Journal of Geophysical Research: Solid Earth*, *123*(6), 4539–4560. 1.5.6

Barraclough, D. R. (1974), Spherical Harmonic Analyses of the Geomagnetic Field for Eight Epochs between 1600 and 1910, *Geophysical Journal International*, *36*(3), 497–513. 1.5.4

Barrois, O., N. Gillet, and J. Aubert (2017), Contributions to the geomagnetic secular variation from a reanalysis of core surface dynamics, *Geophysical Journal International*, *211*(1), 50–68. 1.5.6

Barrois, O., M. D. Hammer, C. C. Finlay, Y. Martin, and N. Gillet (2018), Assimilation of ground and satellite magnetic measurements: inference of core surface magnetic and velocity field changes, *Geophysical Journal International*, *215*(1), 695–712. 1.5.6

Beggan, C. D., and K. A. Whaler (2009), Forecasting change of the magnetic field using core surface flows and ensemble Kalman filtering, *Geophysical Research Letters*, *36*(18). 1.5.6

Biggin, A. J., B. Steinberger, J. Aubert, N. Suttie, R. Holme, T. H. Torsvik, D. G. van der Meer, and D. J. J. van Hinsbergen (2012), Possible links between long-term geomagnetic variations and whole-mantle convection processes, *Nature Geoscience*, *5*, 526533. 1.4.4

Biggin, A. J., E. J. Piispa, L. J. Pesonen, R. Holme, G. A. Paterson, T. Veikkolainen, and L. Tauxe (2015), Palaeomagnetic field intensity variations suggest Mesoproterozoic inner-core nucleation, *Nature*, *526*, 245–248. 1.2

Birch, F. (1964), Density and composition of mantle and core, *Journal of Geophysical Research*, *69*(20), 4377–4388. 1.2

Bloxham, J. (1986), The expulsion of magnetic flux from the Earth's core, *Geophysical Journal of the Royal Astronomical Society*, *87*(2), 669–678, doi:10.1111/j.1365-246X.1986.tb06643.x. 1.5.5

Bloxham, J. (1988), The dynamical regime of fluid flow at the core surface, *Geophysical Research Letters*, *15*(6), 585–588. 1.5.3

Bloxham, J., and D. Gubbins (1985), The secular variation of Earth's magnetic field, *Nature*, *317*(6040), 777. 1.5.5

Bloxham, J., and D. Gubbins (1986), Geomagnetic field analysis — IV. Testing the frozen-flux hypothesis, *Geophysical Journal International*, *84*(1), 139–152. 1.5.5

Bloxham, J., and A. Jackson (1991), Fluid flow near the surface of Earth's outer core, *Reviews of Geophysics*, *29*(1), 97–120. 1.5.3

Buffett, B. (2014), Geomagnetic fluctuations reveal stable stratification at the top of the Earth's core, *Nature*, *507*, 484–487. 1.2

Bullard, E. C., C. Freeman, H. Gellman, and J. Nixon (1950), The westward drift of the Earth's magnetic field, *Philosophical Transactions of the Royal Society of London A: Mathematical, Physical and Engineering Sciences*, *243*(859), 67–92. 1.1

Cain, J. C. (2007), *POGO (OGO2, 4 and 6 Spacecraft)*, pp. 828–829, Springer Netherlands. 1.4.2

Cande, S. C., and D. V. Kent (1995), Revised calibration of the geomagnetic polarity timescale for the late cretaceous and cenozoic, *Journal of Geophysical Research: Solid Earth*, *100*(B4), 6093–6095. 1.4.4

Christensen, U., and J. Wicht (2015), Numerical dynamo simulations, in *Treatise on Geophysics*, vol. 8, 2 ed., chap. 10, pp. 245–277, Elsevier, Oxford. 1.2

Christensen, U., P. Olson, and G. A. Glatzmaier (1998), A dynamo model interpretation of geomagnetic field structures, *Geophysical Research Letters*, *25*(10), 1565–1568. 1.5.4

Christensen, U. R., J. Aubert, and G. Hulot (2010), Conditions for Earth-like geodynamo models, *Earth and Planetary Science Letters*, *296*(3), 487–496. 1.5.5

Chulliat, A., and N. Olsen (2010), Observation of magnetic diffusion in the Earth's outer core from Magsat, Ørsted, and CHAMP data, *Journal of Geophysical Research: Solid Earth*, *115*(B5). 1.5.5

Chulliat, A., W. Brown, P. Alken, S. Macmillan, M. Nair, C. Beggan, A. Woods, B. Hamilton, B. Meyer, and R. Redmon (2019), Out-of-cycle update of the us/uk world magnetic model for 2015-2020: Technical note, *National Centers for Environmental Information, NOAA*. 1.5.6

Clement, B. M. (2004), Dependence of the duration of geomagnetic polarity reversals on site latitude, *Nature*, *428*, 637640. 1.4.4

Constable, C. G., R. L. Parker, and P. B. Stark (1993), Geomagnetic field models incorporating frozen-flux constraints, *Geophysical Journal International*, *113*(2), 419–433. 1.5.5

Cox, A., R. R. Doell, and G. B. Dalrymple (1963), Geomagnetic polarity epochs and Pleistocene geochronometry, *Nature*, *198*, 1049–1051. 1.4.4

Davies, C., M. Pozzo, D. Gubbins, and D. Alfè (2015), Constraints from material properties on the dynamics and evolution of Earths core, *Nature Geoscience*, *8*, 678–685. 1.2

de Boor, C. (1978), *A practical guide to splines*, vol. 27, Springer-Verlag New York. 1.5.1

Driscoll, P., and P. Olson (2009), Effects of buoyancy and rotation on the polarity reversal frequency of gravitationally driven numerical dynamos, *Geophysical Journal International*, *178*(3), 1337–1350. 1.4.4

Driscoll, P. E., and C. Wilson (2018), Paleomagnetic biases inferred from numerical dynamos and the search for geodynamo evolution, *Frontiers in Earth Science*, *6*, 113. 1.4.4

Dziewonski, A. M., and D. L. Anderson (1981), Preliminary reference Earth model, *Physics of the Earth and Planetary Interiors*, *25*(4), 297 – 356. (document), 1.2, 1.1

Finlay, C. C., and H. Amit (2011), On flow magnitude and field-flow alignment at Earth's core surface, *Geophysical Journal International*, *186*(1), 175–192. 1.5.5

Finlay, C. C., and A. Jackson (2003), Equatorially dominated magnetic field change at the surface of Earth's core, *Science*, *300*(5628), 2084–2086. 1.1

Finlay, C. C., N. Olsen, S. Kotsiaros, N. Gillet, and L. Tøffner-Clausen (2016a), Recent geomagnetic secular variation from Swarm and ground observatories as estimated in the CHAOS-6 geomagnetic field model, *Earth, Planets and Space*, *68*(1), 112. 1.4.2, 1.5.4

Finlay, C. C., J. Aubert, and N. Gillet (2016b), Gyre-driven decay of the Earth's magnetic dipole, *Nature Geoscience*, *7*. 1.5.4

Fleisch, D. A. (2008), *A student's guide to Maxwell's equations*, Cambridge University Press. 1.3.1

Fournier, A., C. Eymin, and T. Alboussière (2007), A case for variational geomagnetic data assimilation: insights from a one-dimensional, nonlinear, and sparsely observed MHD system, *Nonlinear Processes in Geophysics*, *14*(2), 163–180. 1.5.6

Fournier, A., G. Hulot, D. Jault, W. Kuang, A. Tangborn, N. Gillet, E. Canet, J. Aubert, and F. Lhuillier (2010), An introduction to data assimilation and predictability in geomagnetism, *Space Science Reviews*, *155*(1-4), 247–291. 1.5.6

Fowler, C. M. R. (2005), *The Solid Earth: An Introduction to Global Geophysics*, 2 ed., Cambridge University Press, Cambridge, United Kingdom. 1.2

Friis-Christensen, E., H. Lühr, and G. Hulot (2006), Swarm: A constellation to study the Earth's magnetic field, *Earth, Planets and Space*, *58*(4), 351–358. 1.4.2

Garnero, E. J., D. V. Helmberger, and S. P. Grand (1993), Constraining outermost core velocity with SmKS waves, *Geophysical Research Letters*, *20*(22), 2463–2466. 1.2

Gauss, K. F. (1837), Intensitas vis magneticæ terrestris ad mensuram absolutam revocata, *Abstracts of the Papers Printed in the Philosophical Transactions of the Royal Society of London*, *3*, 166–174. 1.4

Gilbert, W. (1600), *De Magnete, Magneticisque Corporibus, et de Magno Magnete Tellure*, Peter Short, London. 1.1

Gillet, N., D. Jault, C. Finlay, and N. Olsen (2013), Stochastic modeling of the Earth's magnetic field: Inversion for covariances over the observatory era, *Geochemistry, Geophysics, Geosystems*, *14*(4), 766–786. 1.4.3

Gillet, N., O. Barrois, and C. C. Finlay (2015), Stochastic forecasting of the geomagnetic field from the COV-OBS.x1 geomagnetic field model, and candidate models for IGRF-12, *Earth, Planets and Space*, *67*(1), 71. (document), 1.4.3, 1.5, 1.5.4

Glatzmaier, G. A., and P. H. Roberts (1995), A three-dimensional self-consistent computer simulation of a geomagnetic field reversal, *Nature*, *377*, 203–209. 1.4.4

Glatzmaier, G. A., R. S. Coe, L. Hongre, and P. H. Roberts (1999), The role of the Earth's mantle in controlling the frequency of geomagnetic reversals, *Nature*, *401*, 885–890. 1.4.4

Gomi, H., K. Ohta, K. Hirose, S. Labrosse, R. Caracas, M. J. Verstraete, and J. W. Hernlund (2013), The high conductivity of iron and thermal evolution of the Earth's core, *Physics of the Earth and Planetary Interiors*, *224*, 88 – 103. 1.2

Gubbins, D. (1984), Geomagnetic field analysis — II. Secular variation consistent with a perfectly conducting core, *Geophysical Journal of the Royal Astronomical Society*, *77*(3), 753–766. 1.5.5

Gubbins, D. (1996), A formalism for the inversion of geomagnetic data for core motions with diffusion, *Physics of the Earth and Planetary Interiors*, *98*(3), 193–206. 1.5.5

Gubbins, D. (2007), Geomagnetic constraints on stratification at the top of Earth's core, *Earth, Planets and Space*, *59*(7), 661–664. 1.2

Gubbins, D., and P. H. Roberts (1987), Magnetohydrodynamics of the Earth's Core, in *Geomagnetism*, vol. 2, chap. 1, Academic Press. 1.3.2, 1.5.4

Gubbins, D., A. L. Jones, and C. C. Finlay (2006), Fall in Earth's magnetic field is erratic, *Science*, *312*(5775), 900–902. 1.5.4

Gutenberg, B. (1912), Über Erdbebenwellen. V. Konstitution des Erdinnern, erschlossen aus dem Bodenverruckungsverhltnis der einmal reflektierten zu den direkten longitudinalen Erdbebenwellen, und einige andere Beobachtungen ueber E, *Nachrichten von der Gesellschaft der Wissenschaften zu Göttingen, Mathematisch-Physikalische Klasse*, pp. 121–206. 1.2

Halley, E. (1692), An account of the cause of the change of the variation of the magnetical needle. with an hypothesis of the structure of the internal parts of the Earth: as it was proposed to the Royal Society in one of their late meetings, *Philosophical Transactions*, *17*(195), 563–578. 1.1, 1.2

Hartmann, G. A., and I. G. Pacca (2009), Time evolution of the South Atlantic Magnetic Anomaly, *Anais da Academia Brasileira de Ciências*, *81*, 243 – 255. 1.5.4

Hartmann, G. A., W. Poletti, R. I. Trindade, L. M. Ferreira, and P. L. Sanches (2019), New archeointensity data from South Brazil and the influence of the South Atlantic Anomaly in South America, *Earth and Planetary Science Letters*, *512*, 124 – 133. 1.5.4

Heirtzler, J. (2002), The future of the South Atlantic Anomaly and implications for radiation damage in space, *Journal of Atmospheric and Solar-Terrestrial Physics*, *64*(16), 1701 – 1708. 1.5.4

Helffrich, G., and S. Kaneshima (2010), Outer-core compositional stratification from observed core wave speed profiles, *Nature*, *468*, 807–810. 1.2

Holme, R. (2015), Large-Scale Flow in the Core, in *Treatise on Geophysics*, vol. 8, chap. 4, pp. 91–113, Elsevier. 1.3.1, 1.5.3

Hulot, G., F. Lhuillier, and J. Aubert (2010), Earth's dynamo limit of predictability, *Geophysical Research Letters*, *37*(6). 1.5.6

Hulot, G., T. Sabaka, N. Olsen, and A. Fournier (2015), The present and future geomagnetic field, in *Treatise on Geophysics*, vol. 5, 2 ed., chap. 2, pp. 33 – 78, Elsevier, Oxford. (document), 1.4, 1.3, 1.5.1, 1.6

Jackson, A., A. R. T. Jonkers, and M. R. Walker (2000), Four centuries of geomagnetic secular variation from historical records, *Philosophical Transactions of the Royal Society of London. Series A: Mathematical, Physical and Engineering Sciences*, *358*(1768), 957–990. 1.4.3, 1.5.4

Jault, D., C. Gire, and J.-L. Le Mouël (1988), Westward drift, core motions and exchanges of angular momentum between core and mantle, *Nature*, *333*, 353356. 1.5.3

Jones, C. A. (2015), Thermal and compositional convection in the outer core, in *Treatise on Geophysics*, vol. 8, chap. 5, pp. 131–185, Elsevier. 1.2, 1.2

Jonkers, A. R. T., A. Jackson, and A. Murray (2003), Four centuries of geomagnetic data from historical records, *Reviews of Geophysics*, *41*(2). 1.4.3

Kageyama, A., and T. Sato (1995), Computer simulation of a magnetohydrodynamic dynamo. ii, *Physics of Plasmas*, *2*(5), 1421–1431. 1.4.4

Kaneshima, S. (2018), Array analyses of SmKS waves and the stratification of Earth's outermost core, *Physics of the Earth and Planetary Interiors*, *276*, 234 – 246. 1.2

Kuang, W., A. Tangborn, W. Jiang, D. Liu, Z. Sun, J. Bloxham, and Z. Wei (2008), MoSST-DAS: the first generation geomagnetic data assimilation framework, *Commun. Comput. Phys*, *3*, 85–108. 1.5.6

Labrosse, S., J.-P. Poirier, and J.-L. Le Mouël (2001), The age of the inner core, *Earth and Planetary Science Letters*, *190*(3), 111–123. 1.2

Langel, R. A., and R. H. Estes (1982), A geomagnetic field spectrum, *Geophysical Research Letters*, *9*(4), 250–253. 1.5.1

Larmor, J. (1919), How could a rotating body such as the Sun become a magnet, *Report of the British Association for the Advancement of Science 87th Meeting*, pp. 159–160. 1.3

Lassiter, J. (2006), Constraints on the coupled thermal evolution of the Earth's core and mantle, the age of the inner core, and the origin of the $^{186}Os/^{188}Os$ core signal in plume-derived lavas, *Earth and Planetary Science Letters*, *250*(1), 306–317. 1.2

Lay, T., and C. J. Young (1990), The stably-stratified outermost core revisited, *Geophysical Research Letters*, *17*(11), 2001–2004. 1.2

Lay, T., J. Hernlund, and B. A. Buffett (2008), Core-mantle boundary heat flow. 1.2

Lehmann, I. (1936), P', *Publications du Bureau Central Seismologique International, Série A, Travaux Scientifique*, *14*, 87115. 1.2

Lesur, V., I. Wardinski, M. Rother, and M. Mandea (2008), GRIMM: The GFZ reference internal magnetic model based on vector satellite and observatory data, *Geophysical Journal International*, *173*(2), 382–394. 1.5.4

Lesur, V., K. Whaler, and I. Wardinski (2015), Are geomagnetic data consistent with stably stratified flow at the coremantle boundary?, *Geophysical Journal International*, *201*(2), 929–946. 1.5.3

Lhuillier, F., A. Fournier, G. Hulot, and J. Aubert (2011), The geomagnetic secular-variation timescale in observations and numerical dynamo models, *Geophysical Research Letters*, *38*(9). 1.5.4

Lowes, F. J. (1974), Spatial power spectrum of the main geomagnetic field, and extrapolation to the core, *Geophysical Journal International*, *36*(3), 717–730. 1.5.1

Madden, T., and J.-L. Le Mouël (1982), The recent secular variation and the motions at the core surface, *Philosophical Transactions of the Royal Society of London. Series A, Mathematical and Physical Sciences*, *306*(1492), 271–280. 1.5.3

Maus, S. (2010), An ellipsoidal harmonic representation of earth's lithospheric magnetic field to degree and order 720, *Geochemistry, Geophysics, Geosystems*, *11*(6). 1.4

Maus, S., M. Rother, R. Holme, H. Lhr, N. Olsen, and V. Haak (2002), First scalar magnetic anomaly map from CHAMP satellite data indicates weak lithospheric field, *Geophysical Research Letters*, *29*(14), 45–1–47–4. 1.4

Menke, W. (2018), *Geophysical data analysis: Discrete inverse theory*, Academic Press. 1.5.2

Meyers, H., and W. M. Davis (1990), A profile of the geomagnetic model user and abuser, *Journal of Geomagnetism and Geoelectricity*, *42*(9), 1079–1085. 1.5.6

Mitchell, A. C. (1946), Chapters in the history of terrestrial magnetism, *Terrestrial Magnetism and Atmospheric Electricity*, *51*(3), 323–351. 1.1

Needham, J. (1962), Physics and Physical Technology Part 1, in *Science and Civilisation in China*, vol. 4, Cambridge University Press, Cambridge. 1.1

Neubert, T., M. Mandea, G. Hulot, R. von Frese, F. Primdahl, J. L. Jørgensen, E. Friis-Christensen, P. Stauning, N. Olsen, and T. Risbo (2001), Ørsted satellite captures high-precision geomagnetic field data, *Eos, Transactions American Geophysical Union*, *82*(7), 81–88. 1.4.2

Oldham, R. D. (1906), The constitution of the interior of the Earth as revealed by earthquakes, *Nature*, *92*, 684–685. 1.2

Olsen, N., H. Lühr, C. C. Finlay, T. J. Sabaka, I. Michaelis, J. Rauberg, and L. Tøffner-Clausen (2014), The CHAOS-4 geomagnetic field model, *Geophysical Journal International*, *197*(2), 815–827. (document), 1.6

Olson, P. (2007), Overview, in *Treatise on Geophysics*, vol. 8, chap. 1, pp. 1–30, Elsevier, Amsterdam. (document), 1.1, 1.3

Olson, P., and H. Amit (2006), Changes in Earth's dipole, *Naturwissenschaften*, *93*(11), 519–542. 1.5.4

Olson, P., and H. Amit (2014), Magnetic reversal frequency scaling in dynamos with thermo-chemical convection, *Physics of the Earth and Planetary Interiors*, *229*, 122–133. 1.4.4

Olson, P. L., R. S. Coe, P. E. Driscoll, G. A. Glatzmaier, and P. H. Roberts (2010), Geodynamo reversal frequency and heterogeneous coremantle boundary heat flow, *Physics of the Earth and Planetary Interiors*, *180*(1), 66 – 79. 1.4.4, 1.5.5

O'Rourke, J. G., and D. J. Stevenson (2016), Powering Earth's dynamo with magnesium precipitation from the core, *Nature*, *529*, 387–389. 1.2

Poirier, J.-P. (1994), Light elements in the Earth's outer core: A critical review, *Physics of the Earth and Planetary Interiors*, *85*(3), 319 – 337. 1.2

Pollack, H. N., S. J. Hurter, and J. R. Johnson (1993), Heat flow from the Earth's interior: Analysis of the global data set, *Reviews of Geophysics*, *31*(3), 267–280. 1.2

Pozzo, M., C. Davies, D. Gubbins, and D. Alfè (2012), Thermal and electrical conductivity of iron at Earths core conditions, *Nature*, *485*, 355–358. 1.2

Proudman, J. (1916), On the motion of solids in a liquid possessing vorticity, *Proceedings of the Royal Society of London. Series A, Containing Papers of a Mathematical and Physical Character*, *92*(642), 408–424. 1.2

Purucker, M. E. (2007), *Magsat*, pp. 673–674, Springer Netherlands. 1.4.2

Rau, S., U. Christensen, A. Jackson, and J. Wicht (2000), Core flow inversion tested with numerical dynamo models, *Geophysical Journal International*, *141*(2), 485–497. 1.5.5

Reigber, C., H. Lühr, and P. Schwintzer (2002), CHAMP mission status, *Advances in Space Research*, *30*(2), 129 – 134. 1.4.2

Roberts, P. H., and S. Scott (1965), On analysis of the secular variation, *Journal of Geomagnetism and Geoelectricity*, *17*(2), 137–151. 1.3.4

Roberts, P. H., C. A. Jones, and A. Calderwood (2003), Energy fluxes and Ohmic dissipation in the Earth's core, in *Earth's Core and Lower Mantle*, chap. 5, pp. 135–169, CRC Press. 1.2

Schaeffer, N., D. Jault, H.-C. Nataf, and A. Fournier (2017), Turbulent geodynamo simulations: a leap towards Earth's core, *Geophysical Journal International*, *211*(1), 1–29. 1.5.1

Sleep, N. H. (1990), Hotspots and mantle plumes: Some phenomenology, *Journal of Geophysical Research: Solid Earth*, *95*(B5), 6715–6736. 1.2

Stacey, F., and D. Loper (2007), A revised estimate of the conductivity of iron alloy at high pressure and implications for the core energy balance, *Physics of the Earth and Planetary Interiors*, *161*(1), 13 – 18. 1.2

Sumita, I., and M. Bergman (2015), Inner core dynamics, in *Treatise on Geophysics*, vol. 8, 2 ed., chap. 12, pp. 297 – 316, Elsevier, Amsterdam, The Netherlands. 1.2

Tarduno, J. A., R. D. Cottrell, M. K. Watkeys, and D. Bauch (2007), Terrestrial nitrogen and noble gases in lunar soils, *Nature*, *446*, 657–660. 1.4.4

Tarduno, J. A., R. D. Cottrell, M. K. Watkeys, A. Hofmann, P. V. Doubrovine, E. E. Mamajek, D. Liu, D. G. Sibeck, L. P. Neukirch, and Y. Usui (2010), Geodynamo, solar wind, and magnetopause 3.4 to 3.45 billion years ago, *Science*, *327*(5970), 1238–1240. 1.4.4

Tarduno, J. A., M. K. Watkeys, T. N. Huffman, R. D. Cottrell, E. G. Blackman, A. Wendt, C. A. Scribner, and C. L. Wagner (2015), Antiquity of the South Atlantic Anomaly and evidence for top-down control on the geodynamo, *Nature Communications*, *6*, 7865. 1.5.4

Tauxe, L. (2010), *Essentials of Paleomagnetism*, University of California Press, London. 1.1, 1.4.4

Taylor, G. I. (1917), Motion of solids in fluids when the flow is not irrotational, *Proceedings of the Royal Society of London. Series A, Containing Papers of a Mathematical and Physical Character*, *93*(648), 99–113. 1.2

Terra-Nova, F., H. Amit, G. A. Hartmann, and R. I. F. Trindade (2015), The time dependence of reversed archeomagnetic flux patches. 1.5.4

Terra-Nova, F., H. Amit, G. A. Hartmann, and R. I. Trindade (2016), Using archaeomagnetic field models to constrain the physics of the core: robustness and preferred locations of reversed flux patches, *Geophysical Journal International*, *206*(3), 1890–1913. 1.5.5

Terra-Nova, F., H. Amit, G. A. Hartmann, R. I. Trindade, and K. J. Pinheiro (2017), Relating the South Atlantic Anomaly and geomagnetic flux patches, *Physics of the Earth and Planetary Interiors*, *266*, 39–53. 1.5.4

Terra-Nova, F., G. Choblet, and H. Amit (2019), Preferred locations of weak surface field in numerical dynamos with heterogeneous core-mantle boundary heat flux: Consequences for the South Atlantic Anomaly, *Geophysicsl Journal International*. 1.5.4

Tominaga, M., W. W. Sager, M. A. Tivey, and S.-M. Lee (2008), Deep-tow magnetic anomaly study of the pacific jurassic quiet zone and implications for the geomagnetic polarity reversal timescale and geomagnetic field behavior, *Journal of Geophysical Research: Solid Earth*, *113*(B7). 1.4.4

Voorhies, C. V. (1993), *Geomagnetic Estimates of Steady Surficial Core Flow and Flux Diffusion: Unexpected Geodynamo Experiments*, pp. 113–125, American Geophysical Union (AGU). 1.5.5

Wang, C. (1948), Discovery and application of magnetic phenomena in China. 1. The lodestone spoon of the Han, *Chinese Journal of Archaeology*, *3*, 119. 1.1

Wardinski, I., and V. Lesur (2012), An extended version of the C$^3$FM geomagnetic field model: application of a continuous frozen-flux constraint, *Geophysical Journal International*, *189*(3), 1409–1429. 1.5.5

Whaler, K. A. (1980), Does the whole of the Earth's core convect?, *Nature*, *287*, 528–530. 1.2, 1.5.3

Whaler, K. A. (1986), Geomagnetic evidence for fluid upwelling at the core-mantle boundary, *Geophysical Journal of the Royal Astronomical Society*, *86*(2), 563–588. 1.5.3

Whaler, K. A., and C. D. Beggan (2015), Derivation and use of core surface flows for forecasting secular variation, *Journal of Geophysical Research: Solid Earth*, *120*(3), 1400–1414. (document), 1.4, 1.5.3

Winch, D. E., D. J. Ivers, J. P. R. Turner, and R. J. Stening (2005), Geomagnetism and Schmidt quasi-normalization, *Geophysical Journal International*, *160*(2), 487–504. 1.5.1

Wood, B. J., M. J. Walter, and J. Wade (2006), Accretion of the Earth and segregation of its core, *Nature*, *441*, 825–833. 1.2

# Chapter 2

# The reversed and normal flux contributions to axial dipole decay for 1880-2015

**M. C. Metman**[1], P. W. Livermore[1], and J. E. Mound[1]

[1]*School of Earth and Environment, University of Leeds, Leeds LS2 9JT, United Kingdom*

*'Gotta have opposites, light and dark, dark and light, continually in a painting. If you have light on light, you have nothing. If you have dark on dark, you basically have nothing. It's like in life.'*

**Bob Ross**

## Abstract

The axial dipole component of Earths internal magnetic field has been weakening since at least 1840, an effect widely believed to be attributed to the evolution of reversed flux patches (RFPs). These are regions on the core-mantle boundary (CMB) where the sign of radial flux deviates from that of the dominant sign of hemispheric radial flux. We study dipole change over the past 135 years using the field models gufm1, COV-OBS.x1 and CHAOS-6; we examine the impact of the choice of magnetic equator on the identification of reversed flux, the contribution of reversed and normal flux to axial dipole decay, and how reversed and normal field evolution has influenced the axial dipole. We show that a magnetic equator defined as a null-flux curve of the magnetic field truncated at spherical harmonic degree 3 allows us to robustly identify reversed flux, which we demonstrate is a feature of at least degree 4 or 5. Additionally, our results indicate that the evolution of reversed flux accounts for approximately two-thirds of

the decay of the axial dipole, while one third of the decay is attributed to the evolution of the normal field. We find that the decay of the axial dipole over the 20th century is associated with both the expansion and poleward migration of reversed flux patches. In contrast to this centennial evolution, changes in the structure of secular variation since epoch 2000 indicate that poleward migration currently plays a much reduced role in the ongoing dipole decay.

## 2.1 Introduction

Observations of Earth's internal magnetic field reveal that its largest component is that of the axial dipole, which has been in decline since at least 1840 at a rate of approximately 15 nT yr$^{-1}$ (*Barraclough*, 1974, *Gubbins*, 1987, *Gubbins et al.*, 2006) (see also Fig. 2.1). The strength of this component is measured by the degree one, order zero spherical harmonic or Gauss coefficient $g_1^0$ (e.g. *Backus et al.*, 1996). A determination of this component has been possible since Gauss' work in the 1830's and estimates have been refined by modern observatory and satellite data (e.g. *Finlay et al.*, 2016a).

The coefficient $g_1^0$ can be computed with knowledge of the radial magnetic field $B_r$ on the core-mantle boundary (CMB) through evaluation of the integral:

$$g_1^0(t) = \frac{3c}{8\pi a^3} \int_S B_r(\mathbf{r}, t) \cos\theta \, \mathrm{d}S \tag{2.1}$$

where $t$ is time, $\mathbf{r}$ is the position vector, $a$ and $c$ are the radii of the Earth and its outer core respectively, $\theta$ is colatitude and $S$ is the area of the CMB (*Gubbins*, 1987). Figure 2.1 shows the integrand of Eq. (2.1) evaluated at the CMB at epochs 1840.0 and 2015.0. The integral is negative and therefore so is $g_1^0$. However, there are regions on the CMB where the integrand is positive, which therefore contribute destructively towards $|g_1^0|$. These regions may be referred to as reversed flux patches (RFPs).

Temporal variation in $B_r$, and therefore in $|g_1^0|$, ultimately results from the convection of the electrically conducting iron-alloy that comprises the outer core. However, Eq. (2.1) illustrates that the secular variation of $|g_1^0|$ may be expressed mathematically in terms of $B_r$ at the CMB only. With this in mind, the observed decay of $|g_1^0|$ has most often been attributed to the secular evolution of RFPs (*Gubbins*, 1987, *Gubbins et al.*, 2006). In particular, various authors have stressed the importance of the evolution of the Southern Hemisphere RFPs underneath the southern tips of South America and Africa (*Bloxham and Gubbins*, 1985, *Gubbins*, 1987, *Bloxham et al.*, 1989, *Olson and Amit*, 2006, *Terra-Nova et al.*, 2016). For example, *Olson and Amit* (2006) and *Finlay et al.* (2016b) employed geomagnetic secular variation models to determine core flow at the CMB, and combined these flow and field models to map the associated contributions to axial dipole decay. *Olson and Amit* (2006) show that as much as roughly 80% of the instantaneous change in the axial dipole for 1980 may be the result of meridional advection of the field. Over archeomagnetic timescales (in particular the past 3 ka) *Terra-Nova et al.* (2015) found that RFPs have existed and that they contribute to axial dipole decay, this

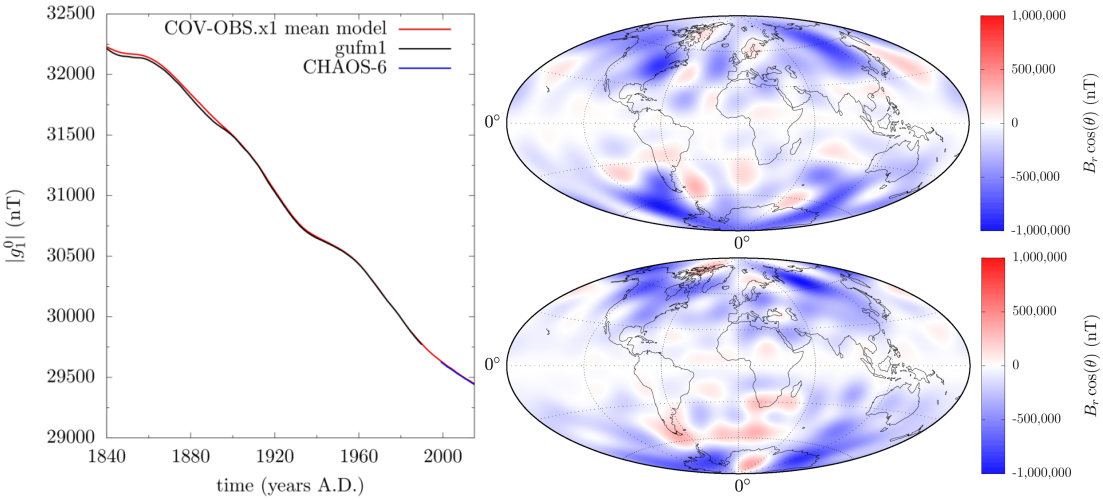


**Figure 2.1:** The magnitude of the axial dipole coefficient $g_1^0$ for the period 1840.0 to 2015.0 (left), and the spatial distribution of $B_r \cos(\theta)$ on the CMB for the COV-OBS.x1 mean model at epochs 1840.0 (top right) and 2015.0 (bottom right).

signal being clearer especially over the past several centuries when resolution of field models is greater. In particular, by using a null-flux line (where $B_r = 0$) as a magnetic equator in place of the geographic equator, they showed that spherical harmonic field components of degree 4 and higher are important in describing RFP evolution. They were able to partition the flux patches into a variety of types and quantified the contribution of each to the decay of $|g_1^0|$.

Models of Earth's internal field can generally be divided in two types: those that adopt the frozen-flux approximation (*Roberts and Scott*, 1965), that is they neglect diffusive contributions to secular variation (e.g. *Bloxham and Gubbins*, 1986, *Constable et al.*, 1993, *Lesur et al.*, 2010, *Wardinski and Lesur*, 2012); and those that do not (e.g. *Jackson et al.*, 2000, *Gillet et al.*, 2013, 2015, *Finlay et al.*, 2016a). In frozen-flux models field evolution is rather restricted, there can be no net change in magnetic flux through a given RFP and RFPs are not allowed to merge or divide (*Backus*, 1968). This may be a problem as the intensification of reversed flux may well be the result of flux expulsion (*Bloxham*, 1986), a diffusive process that is absent from frozen-flux field models. Some models additionally conserve radial vorticity (e.g. *Jackson et al.*, 2007, *Asari and Lesur*, 2011), so that poleward migration of RFPs is allowed only if there is an associated change in the morphology of that patch (*Jackson*, 1996). With such constraints, RFPs are then expected to contribute to axial dipole decay only by growing in surface area or by migrating towards the geographic poles. In what follows, we will therefore refrain from using frozen-flux models.

In this study, we build upon this previous work to address three objectives. Firstly, we evaluate the impact of the choice of the magnetic equator on RFP characteristics. As we will show later, the use of a magnetic equator with a relatively complex morphology can hamper the robust characterisation of reversed flux evolution, and a spatially smooth equator is therefore more appropriate for our analysis. The second objective is to quantify the importance of the reversed portion of the field for axial dipole decay, relative to the unreversed or normal part of

the CMB field. Finally, we evaluate what characteristics of the RFP secular evolution contribute to this decay, specifically their intensification, migration, and growth in combined surface area.

This work is outlined as follows: section 2.2 specifies the field models used for our analysis, followed by our means of RFP identification in section 2.3. Sections 2.4 and 2.5 present respectively how the reversed and normal contributions to axial dipole decay are computed, and how this decay is interpreted in terms of RFP evolution. Our results are discussed in more detail in section 2.6 which also concludes our work.

## 2.2 Field models

We employed the field models gufm1 (*Jackson et al.*, 2000), COV-OBS.x1 (*Gillet et al.*, 2015), and CHAOS-6 (*Finlay et al.*, 2016a) for the time periods 1840-1990, 1840-2015, and 1999-2015 respectively. The first model has been used in earlier works concerning reversed flux evolution (e.g. *Gubbins et al.*, 2006, *Olson and Amit*, 2006, *Terra-Nova et al.*, 2015) and the use of COV-OBS.x1 and CHAOS-6 allows us to extend their analysis by 25 years. Additionally, the lengths of the investigated periods for gufm1 and COV-OBS.x1 are larger than all non-dipole secular variation timescales (*Lhuillier et al.*, 2011), such that significant temporal variation of the non-dipole field (and therefore that of reversed flux) is captured.

Among these field models there are similarities in terms of the data they are built upon. For example, the models gufm1 and COV-OBS.x1 rely on the compilation made by *Jackson et al.* (2000) (described in detail by *Jonkers et al.*, 2003), which includes observations of marine and land surveys, observatory annual means (OAMs), and satellite data from the POGO and Magsat missions. Also, COV-OBS.x1 and CHAOS-6 both incorporate recent directional and intensity observations from the missions Ørsted, CHAMP, SAC-C, and Swarm, as well as OAMs up to the years 2013.5 and 2015 respectively. Moreover, the three models are constructed without the use of the frozen-flux approximation, so that the temporal evolution of RFPs is not further restricted.

The field models use different underlying modelling strategies, which result in different spatial and temporal behaviour, even at times when the same data are used. The models gufm1 and CHAOS-6 employ regularisation that ensures convergence of the spatial and temporal field spectra, while satisfactorily fitting the data. By contrast, COV-OBS.x1 is the result of a Bayesian (stochastic) inference obtained with *a priori* means and covariance information (for details see *Gillet et al.*, 2013). This model comprises an ensemble of members, all of which fit the data satisfactorily and none of which are regularised. This ensemble enables us to determine uncertainties in field structure and derived quantities.

For all models we computed $B_r$ for yearly intervals using a spherical harmonic expansion up to degree 14 on a $0.45^\circ \times 0.45^\circ$ latitude-longitude grid (i.e., $400 \times 800$ grid points). Several integral quantities (discussed in the following sections) were computed on the same grid for gufm1, the COV-OBS.x1 mean model, all 100 COV-OBS.x1 ensemble members, and CHAOS-6. The use of a higher resolution grid was tested (up to double the resolution) and did not yield

significantly different results.

## 2.3 Identification of RFPs using a magnetic equator

### 2.3.1 Choice of magnetic equator

The first step in describing reversed flux is selecting a magnetic equator that partitions the CMB into two magnetic hemispheres (which may not be of equal surface area), each characterised by its dominant sign of radial flux. Reversed flux patches are then regions where the sign of $B_r$ is opposite to the dominant sign of flux of the magnetic hemisphere in which they reside. The choice of the magnetic equator is non-unique; previous studies have employed both low (*Olson and Amit*, 2006) and high morphological complexity (*Terra-Nova et al.*, 2015). It is sensible to define the magnetic equator according to a null-flux curve of a field truncated to a certain spherical harmonic degree $l_{\text{max}}^{\text{eq}}$. For example, truncating to the axial dipole component alone gives the geographic equator, a full degree 1 expansion yields a great circle tilted with respect to the geographic equator, and a higher degree multipole expansion yields an undulating curve. Note that a magnetic equator constructed using a degree of truncation $l_{\text{max}}^{\text{eq}} < 14$ will in general not align with null-flux curves of the degree 14 magnetic field used in this study.

### 2.3.2 Construction of a discrete magnetic equator

Any definition of the magnetic equator that depends on the morphology of the CMB field will evolve through time. *Terra-Nova et al.* (2015) presented and employed an algorithm that allows the determination of the magnetic equator for any given field morphology. Their algorithm finds an initial longitude along which there is only one location where $B_r = 0$ (strictly speaking where there is only one change in sign of $B_r$) and then repeatedly selects the closest grid location to this point at which $B_r = 0$ as the next point on the equator. Joining these grid points together then defines a discretised magnetic equator.

Our method of defining the magnetic equator is based on the algorithm of *Terra-Nova et al.* (2015), although we extended it in two ways. Firstly, it can not always be guaranteed that there exists an initial longitude along which there is only one location where $B_r = 0$. This can for example be the case when a RFP resides on the geographic North Pole. As an alternative approach, we chose an arbitrary initial longitude and selected the latitude at which $B_r = 0$ closest to the geographic equator. We do this by searching for a change in sign of $B_r$ on our grid and then use a linear interpolation between grid points to find the location where $B_r = 0$. This location is then taken as the starting point of the discrete magnetic equator.

Secondly, we found that the magnetic equator constructed by the algorithm of *Terra-Nova et al.* (2015) was very sensitive to the structure of the magnetic field, particularly near the geographic equator when multiple null-flux curves were relatively close. There were cases where the iterative construction of the equator incorrectly joined nearby but separate null-flux curves, manifest by a local jump in the curvature of the magnetic equator. In order to enforce

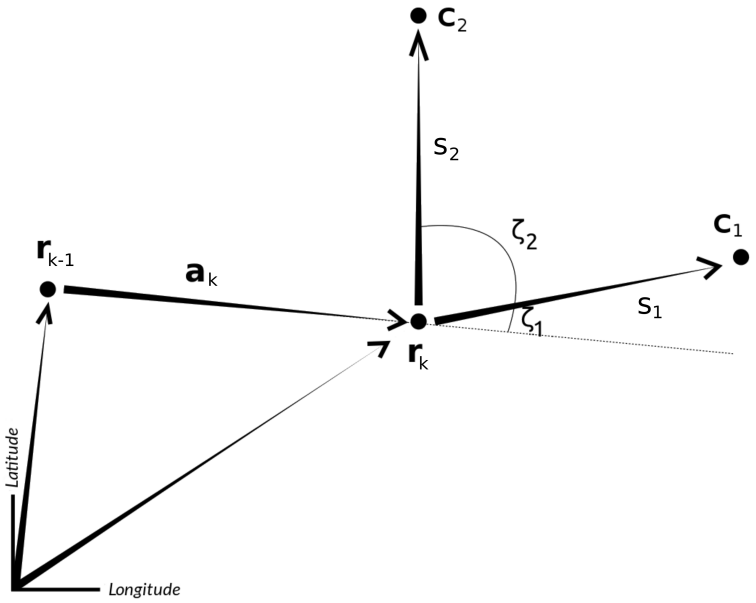


**Figure 2.2:** A visual representation in longitude-latitude space of the quantities involved in the magnetic equator construction algorithm. Locations already classified as part of the discrete equator at some iteration $k$ are $\mathbf{r}_{k-1}$ and $\mathbf{r}_k$. For this iteration, we find the candidate locations $\mathbf{c}_i$, each with an associated distance $s_i$ and tangential angle $\zeta_i$ with respect to the current candidate location $\mathbf{r}_k$. The next candidate location $\mathbf{r}_{k+1}$ is then chosen such that it minimises the norm $\chi_i$ among all candidates. Therefore for this iteration $\mathbf{r}_{k+1} = \mathbf{c}_1$, as this candidate has a smaller tangential angle compared to $\mathbf{c}_2$ but an equal distance to $\mathbf{r}_k$.

smoothness in the magnetic equator we scan along nearby lines of equal longitude for locations which have a change of sign in $B_r$, constructing a set of candidate locations defining the next point on our discrete magnetic equator. Then, we compute an unsuitability norm $\chi_i = \alpha s_i + \beta\zeta_i$ for every $i^{\text{th}}$ candidate location, which involves both distance ($s_i$) and the change in tangential angle ($\zeta_i$) between the current and candidate locations.

As an example, consider Fig. 2.2 which shows for some iteration $k$ the locations $\mathbf{r}_k$ and $\mathbf{r}_{k-1}$ comprising the (incomplete) discrete equator. Now, the task at hand is to identify a set of candidate locations (where $B_r = 0$) by scanning along the line of longitude that meets with $\mathbf{r}_k$ and those lines adjecent to it. In this example case, the operation returned the candidate locations $\mathbf{c}_i$ in Fig. 2.2 (locations already part of the discretised magnetic equator are not considered candidates). Both of these candidates have an associated distance to the current location $\mathbf{r}_k$ ($s_i$) and describe an angular distance between $\mathbf{r}_k - \mathbf{r}_{k-1}$ ($\zeta_i$). We finally select the next equator location $\mathbf{r}_{k+1}$ as the candidate that best minimises both distance to $\mathbf{r}_k$ and smoothness of the equator, that is

$$\mathbf{r}_{k+1} = \arg\min_{\mathbf{c}_i} \chi(\mathbf{c}_i). \tag{2.2}$$

For our example in Fig. 2.2 $s_1 = s_2$ and $\zeta_2 > \zeta_1$, therefore we would obtain $\mathbf{r}_{k+1} = \mathbf{c}_1$.

This procedure only leaves us with an appropriate choice for the coefficients $\alpha$ and $\beta$ de-

scribing the importance of distance and smoothness respectively. We fix the value of $\alpha$ and select $\beta$ in a number of steps. Initially, we set $\beta = 0$ and select the candidate locations which minimise $\chi_i$ (this mimics the algorithm of *Terra-Nova et al.* (2015)). If at some iteration we find a new equator location for which $\zeta_i > 3\pi/4$, we deem this point unacceptable, as such a large change in tangential angle often indicates the magnetic equator connects to a different null-flux curve. Subsequently, we restart the equator construction algorithm with an increased $\beta$. This process is repeated until no candidate points which minimise $\chi_i$ have an associated $\zeta_i > 3\pi/4$.

Having defined the magnetic equator we assign the dominant radial magnetic flux in the northern magnetic hemisphere to have negative sign and positive for the southern magnetic hemisphere. Within each magnetic hemisphere any grid point at which the sign of $B_r$ is different from the dominant sign is assigned to be reversed. This defines the distribution of reversed flux in a point-wise manner.

### 2.3.3 Quantifying reversed flux

Any choice of magnetic equator presents problems for the identification of reversed flux. Using the geographic equator as the magnetic equator is undesirable as the Earth's dipole field is tilted; consideration of this component alone fragments individual low-latitude features into separate reversed and normal regions (Fig. 2.3a and 2.3b). This results in a substantial increase in the number of reversed flux regions which would otherwise not be considered as reversed. Conversely, an $l^{\text{eq}}_{\text{max}} = 14$ multipole expansion results in diversions of the equator to high latitudes encompassing large geographic areas. For example, for the year 1900 there is a large intrusion of the magnetic equator into the southern geographic hemisphere, caused by the connection of the reversed flux beneath the South Atlantic to the northern magnetic hemisphere (Fig. 2.3i and 2.3j). We assert that for the field models considered in this work this region should be considered a reversed flux patch in the southern magnetic hemisphere, because there are times when this region is present but is not connected to the northern magnetic hemisphere.

This effect is quantified in Figure 2.4a where we show the combined reversed flux area $A_R$ (see section 2.5 for details) normalised by the total CMB area $S$ as a function of time, using a magnetic equator obtained with $l^{\text{eq}}_{\text{max}} = 14$. There are clear discontinuities in $A_R$ which occur when null-flux curves defining the boundaries of reversed flux disconnect from or connect to the magnetic equator. Of further note is that the spread among the COV-OBS.x1 ensemble members is relatively large near the end of the 20$^{\text{th}}$ century, precisely when data quality and quantity is relatively high. The change in ensemble spread during this period reflects how for this type of magnetic equator the identification of reversed flux is particularly sensitive to small-scale features of the field. For example, a very small temporal change in the morphology of the field may yield the merging of a RFP and the opposing magnetic hemisphere, which will strongly affect the secular variation of $A_R$. On the other hand, similar change in field structure elsewhere that does not result in such a merge, will have little effect on $A_R$. Therefore, the

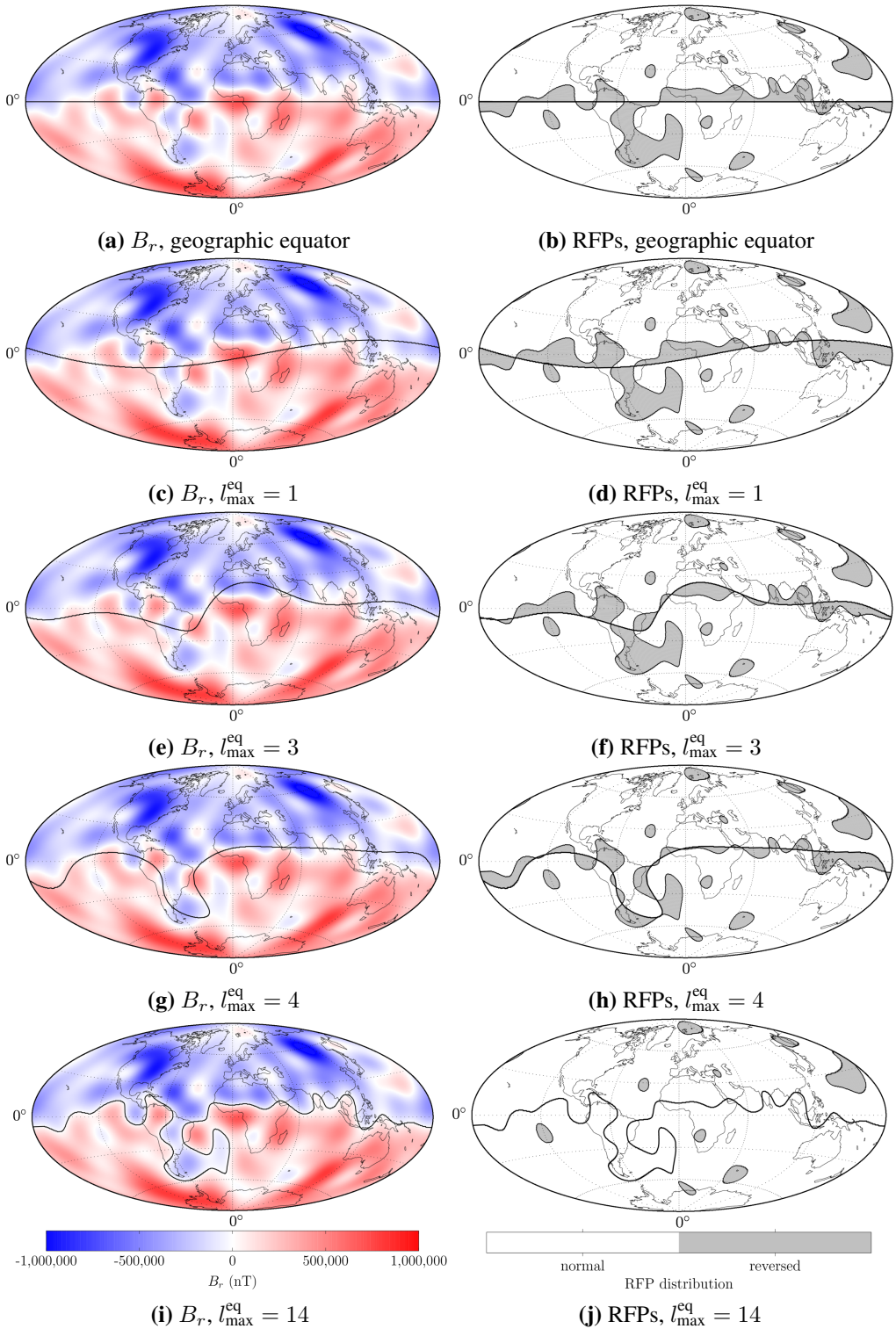


**(a)** $B_r$, geographic equator **(b)** RFPs, geographic equator

**(c)** $B_r$, $l^{\text{eq}}_{\text{max}} = 1$ **(d)** RFPs, $l^{\text{eq}}_{\text{max}} = 1$

**(e)** $B_r$, $l^{\text{eq}}_{\text{max}} = 3$ **(f)** RFPs, $l^{\text{eq}}_{\text{max}} = 3$

**(g)** $B_r$, $l^{\text{eq}}_{\text{max}} = 4$ **(h)** RFPs, $l^{\text{eq}}_{\text{max}} = 4$

**(i)** $B_r$, $l^{\text{eq}}_{\text{max}} = 14$ **(j)** RFPs, $l^{\text{eq}}_{\text{max}} = 14$

**Figure 2.3:** The radial field $B_r$ on the CMB (left) and the associated distribution of RFPs (right) for epoch 1900.0 and several configurations of the magnetic equator (solid black line).

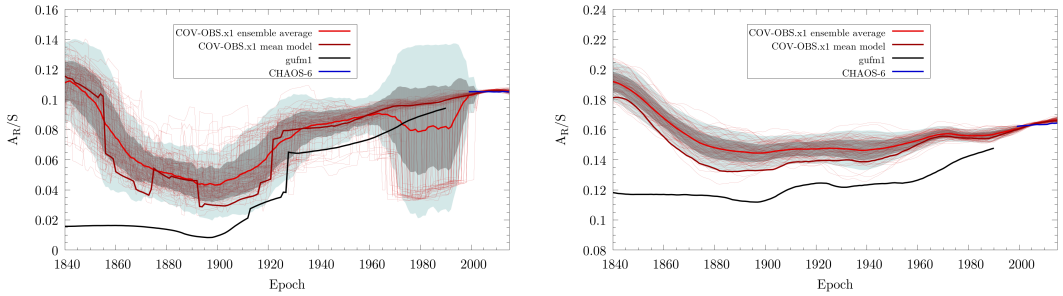


**(a)** $l^{\text{eq}}_{\text{max}} = 14$ **(b)** $l^{\text{eq}}_{\text{max}} = 3$

**Figure 2.4:** The combined reversed to CMB surface area ratio $A_R/S$ as a function of time for all COV-OBS.x1 ensemble members, using a magnetic equator with $l^{\text{eq}}_{\text{max}} = 14$ (a) and $l^{\text{eq}}_{\text{max}} = 3$ (b). Shown are the results for gufm1 (black curve), the COV-OBS.x1 mean model (dark red curve), and all COV-OBS.x1 ensemble members (thin red curves). The thick light red curve is the average among the results for the ensemble members, and the dark and light gray areas correspond to confidence intervals of one and two times the standard deviation, respectively.

use of a magnetic equator defined with $l^{\text{eq}}_{\text{max}} = 14$ makes it difficult to robustly quantify the temporal evolution of reversed flux, and we therefore deem it unacceptable for our analysis. Of additional interest in this figure is that although the results for COV-OBS.x1 and CHAOS-6 appear to be consistent, there is an apparent disagreement between COV-OBS.x1 and gufm1 during the first four decades of the time period shown: $A_R$ according to gufm1 shows an almost constant value, whilst $A_R$ according to COV-OBS.x1 exhibits rapid decline. This time period coincides with the start-up period for the COV-OBS.x1 model, and is likely to be a manifestation of an end effect (N. Gillet, personal communication, 2016). For this reason, we focus attention on the period 1880-2015 for the remainder of this work.

A magnetic equator that is defined using a low degree of truncation will limit the occurrence of large intrusions, whereas increasing $l^{\text{eq}}_{\text{max}}$ reduces the combined surface area of divided low-latitude reversed flux. Figures 2.3c to 2.3h show the effect of the choosing of $l^{\text{eq}}_{\text{max}} \in \{1, 3, 4\}$ on the identification of reversed flux. The choice of $l^{\text{eq}}_{\text{max}} = 1$ is undesirable as it still fragments low-latitude features particularly underneath the Pacific. Conversely, for $l^{\text{eq}}_{\text{max}} = 4$ the equator assumes a shape that resembles the hemispherical intrusion of $l^{\text{eq}}_{\text{max}} = 14$. The choice $l^{\text{eq}}_{\text{max}} = 3$ gives the most structured magnetic equator, such that the combined surface area of divided low-latitude reversed flux is acceptable, while avoiding the problematic intrusion.

The sensitivity of reversed flux identification to magnetic equator complexity has also been quantified by computing time series of $A_R/S$ for various $l^{\text{eq}}_{\text{max}}$ (Fig. 2.5). It appears that decreasing $l^{\text{eq}}_{\text{max}}$ generally yields a larger value of $A_R/S$, due to the associated inclusion of divided low-latitude RFPs. However, the trends among all continuous curves remain similar. It is also of note that the apparent lowest degree of complexity for the magnetic equator we can employ before any discontinuities develop is $l^{\text{eq}}_{\text{max}} = 4$. Nevertheless, this is not a robust choice for the magnetic equator, as it still yields jumps in magnetic equator morphology. These jumps can not be detected from the $A_R$ time series (Fig. 2.5); however, they can be seen in other quantities. For example, the change in magnetic equator morphology between 1946 and 1947 yields neg-

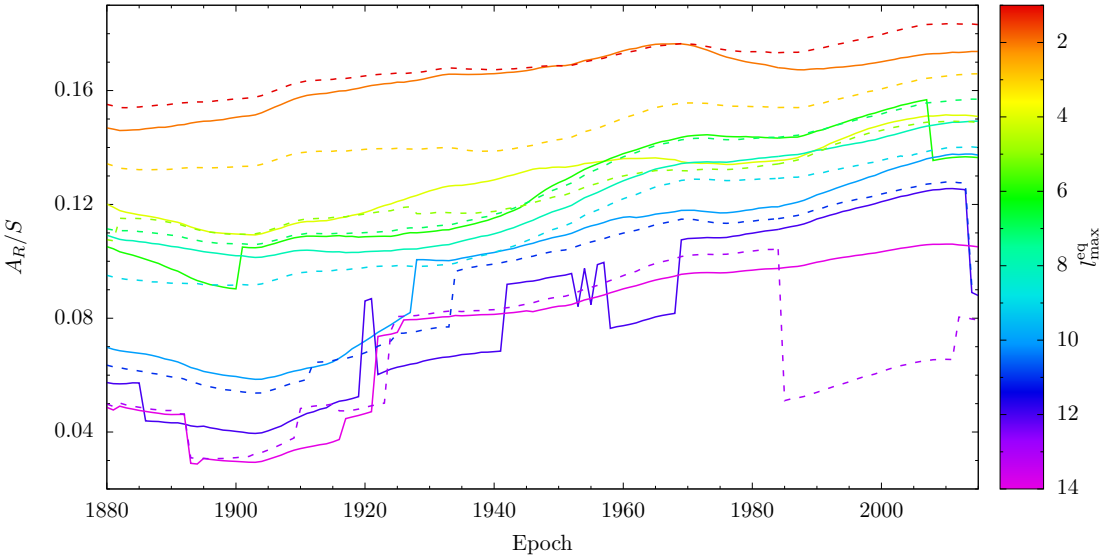


**Figure 2.5:** The combined reversed to CMB surface area ratio $A_R/S$ as a function of time and for various $l^{eq}_{max}$. Solid and dashed curves represent even and uneven $l^{eq}_{max}$ respectively.

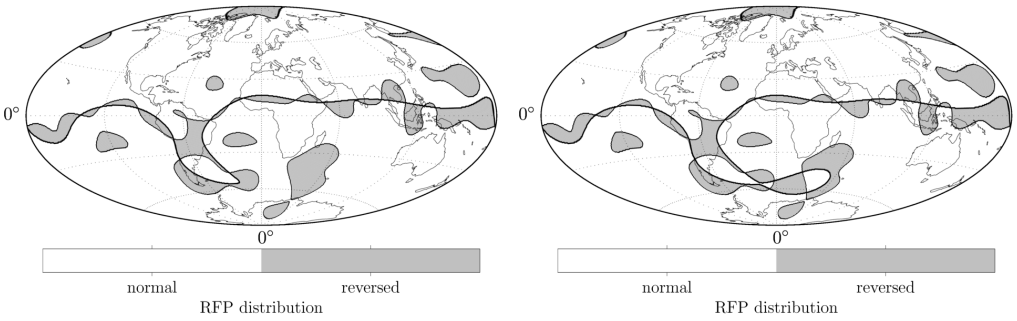


**(a)** **(b)**

**Figure 2.6:** The distribution of reversed flux for epochs 1946.0 (a) and 1947.0 (b).

ligible overall change in $A_R$ (Fig. 2.6), whereas the classification of $B_r$ within the magnetic hemispheres has changed abruptly. Also, these maps illustrate the unrealistic identification of normal flux, with normal features in the Southern Hemisphere completely detached from the Northern Hemisphere. Considering these difficulties with $l^{eq}_{max} = 4$, we instead adopt $l^{eq}_{max} = 3$ for the remainder of this work, and to maintain consistency among our results we do so for all field models. Under this definition of the magnetic equator, for the COV-OBS.x1 model Fig. 2.4b shows an initial fall in the total flux patch area, a stable period between 1880 and 1920 when $A_R/S$ is constant, and a gradual increase in $A_R/S$ to the present day. This behaviour is largely parallelled by gufm1, although it has no initial decay and for all times $A_R/S$ is less than that calculated from COV-OBS.x1. Moreover, we again find agreement among CHAOS-6 and COV-OBS.x1 results, although the former model appears to yield a slightly lower rate of change in $A_R/S$. Lastly, Fig. 2.4b shows that over the time periods investigated RFPs do not cover more than 20% of the CMB.

An alternative characterisation of RFPs, in addition to their area, is by their typical spherical

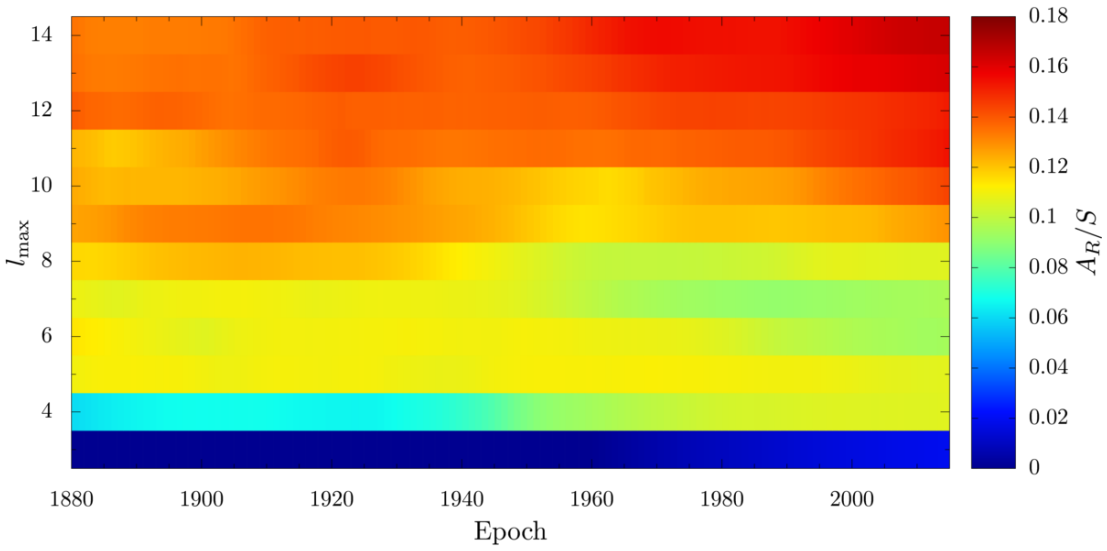


**(a)** $l_{\max}^{\text{eq}} = 3$

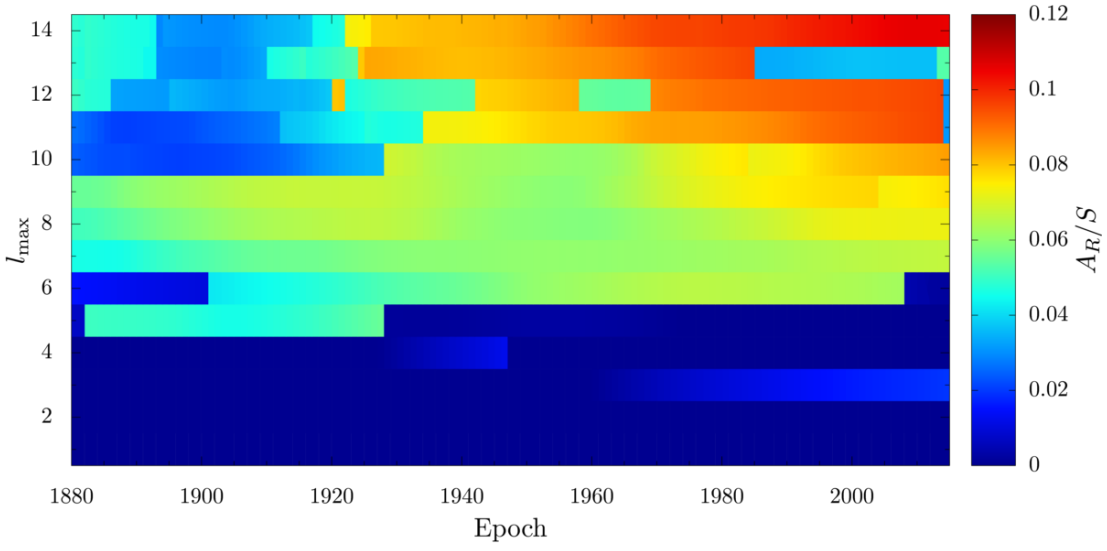


**(b)** $l_{\max}^{\text{eq}} = 14$

**Figure 2.7:** The ratio of the combined RFP area relative to the CMB surface area $A_R/S$ as a function of time and degree of truncation $l_{\max}$ for the COV-OBS.x1 mean model, using either a magnetic equator obtained with $l_{\max}^{\text{eq}} = 3$ (a) or $l_{\max}^{\text{eq}} = 14$ (b).

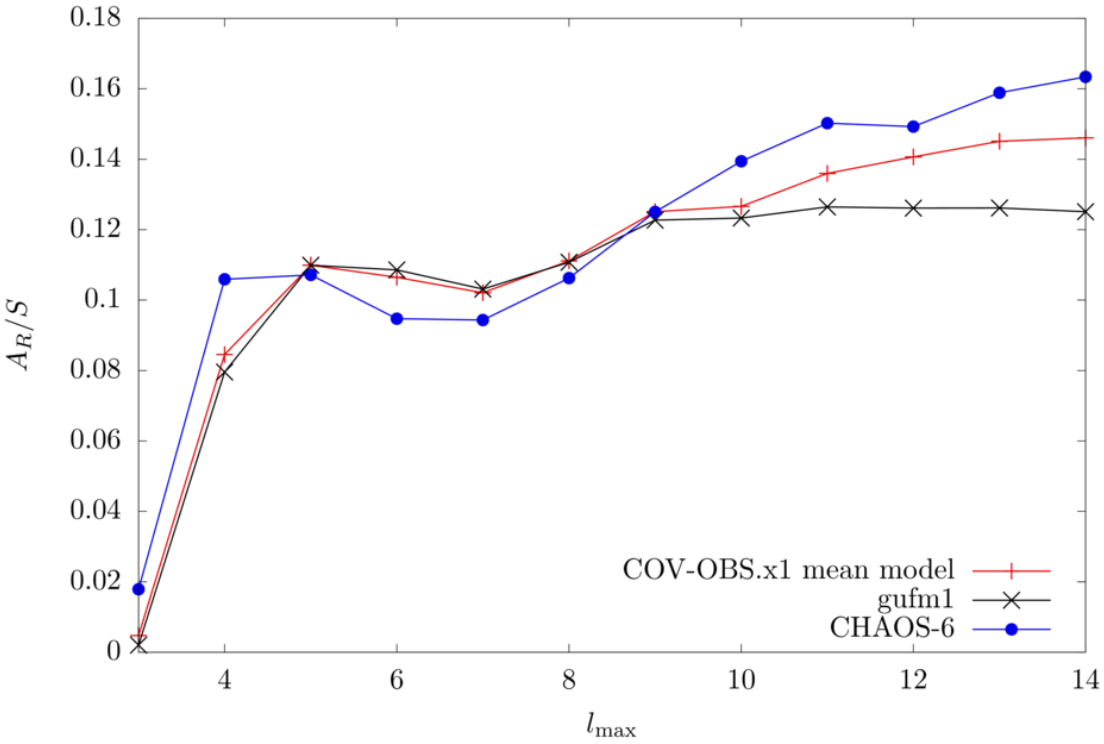


**Figure 2.8:** The ratio of the combined reversed flux area relative to the CMB surface area $A_R/S$ averaged over the investigated periods with $l^{eq}_{max} = 3$ and as a function of $l_{max}$.

harmonic degrees. For our choice of magnetic equator $l^{eq}_{max} = 3$, figure 2.7a shows the effect of truncating the field to degree $l_{max}$ by its flux patch area $A_R/S$ as a function of time. There appears to exist a minimum degree of truncation required to resolve RFPs, which is time-dependent. For example, during the second half of the investigated period there are almost no RFPs for $l_{max} \leq 3$; however, setting $l_{max} = 4$ yields a marked increase in RFP area. In earlier times, setting $l_{max} = 4$ resolves relatively less reversed flux and it appears that $l_{max} = 5$ is required to resolve the majority of RFPs for that period. Also, Fig. 2.7a shows that $l_{max}$ and $A_R$ are not strictly positively correlated, as $A_R/S$ exhibits a decline within the ranges $l_{max} = 9$ to 11 and $l_{max} = 5$ to 8 for the approximate periods 1880-1910 and 1950-2015, respectively.

To assess the robustness of the above characterisation of reversed flux we briefly consider the effect of applying the same analysis using a magnetic equator defined using $l^{eq}_{max} = 14$. Figure 2.7b shows two key features: first is the signature of the intrusion which is particularly noticeable between 1880 and 1920 for $l_{max} \geq 10$. Second is that we find a clearer signature of the characteristic spherical harmonic degree defining RFPs of least 5. This matches the results presented in Fig. 2.7a as in both cases an $l_{max}$ of at least 5 is required to resolve a significant portion of the reversed field. Lastly, Figure 2.8 shows the total flux patch area for $l^{eq}_{max} = 3$ and as a function of $l_{max}$ when time averaged. It shows for gufm1 and the COV-OBS.x1 mean model that there is no single characteristic minimum degree for the whole of the period and that the inclusion of degrees 4 and 5 yields the greatest increases in $A_R/S$. This illustrates the particular importance of these degrees for resolving reversed flux over the corresponding

time periods. However, the CHAOS-6 results demonstrate that for approximately the past two decades that RFPs are predominantly degree 4 features, and that there is also a small contribution from degree 3, reflecting a change in the typical wavelength of these features.

## 2.4 Contributions to the axial dipole

Having defined RFPs we are now in a position to compute the contributions from the combined area of RFPs, $S_R$, and the combined area of normal field (i.e. the remaining regions), $S_N$, to the axial dipole coefficient $g_1^0$. Following Eq. (2.1) we can partition these contributions as follows

$$\begin{aligned} g_1^0(t) &= \frac{3c}{8\pi a^3}\left( \int_{S_R(t)} B_r(\mathbf{r},t)\cos\theta \,\mathrm{d}S + \int_{S_N(t)} B_r(\mathbf{r},t)\cos\theta \,\mathrm{d}S \right) \\ &= g_{1,R}^0(t) + g_{1,N}^0(t) \end{aligned} \tag{2.3}$$

The above expression explictly shows how $g_1^0$ may be expressed in terms of the reversed and normal flux distribution. Using the grid specified in section 2.2, $g_{1,R}^0$ and $g_{1,N}^0$ are computed through 2-D trapezoidal integration at yearly intervals, where only quadrilaterals with four nodal points that are designated reversed contribute to $g_{1,R}^0$, while the remaining quadrilaterals contribute to $g_{1,N}^0$.

The time-dependence of the contributions $g_{1,R}^0$ and $g_{1,N}^0$ is shown in Fig. 2.9a and 2.9b, respectively. Both gufm1 and the ensemble mean of COV-OBS.x1 show a monotonic increase in $g_{1,R}^0$ from about 1900 onwards. According to either model, the increase in $g_{1,R}^0$ over the 20$^{\text{th}}$ century amounts to approximately $1.3\cdot10^3$ nT: this is roughly two-thirds of the decay in $|g_1^0|$ (of about $1.8\cdot10^3$ nT, see Fig. 2.1) over that time. However, it should be noted that our estimate of the reversed axial dipole contribution is likely to be a lower bound due to differences in the magnetic equator we consider and the geographic equator which defines the axial dipole. For example, by employing our magnetic equator there exist field features that are considered reversed and still enforce the actual dipole.

Figure 2.9b shows the time dependence of $g_{1,N}^0$, which is an important but a less frequently considered contribution to the axial dipole. Its increase since 1900 parallels that of $g_{1,R}^0$, although to a lesser extent. Indeed, the change in $g_{1,N}^0$ is one third of the decay in $|g_1^0|$ over the 20$^{\text{th}}$ century. Comparing figures 2.4b and 2.9a we see that, compared with COV-OBS.x1, gufm1 provides a lower value for $A_R$ and its corresponding $g_{1,R}^0$.

## 2.5 Characterisation of reversed flux patch evolution

In this section we focus on characterising the increases in $g_{1,R}^0$ and $g_{1,N}^0$ over the 20$^{\text{th}}$ century in terms of reversed- and normal-flux evolution respectively, which have jointly contributed to

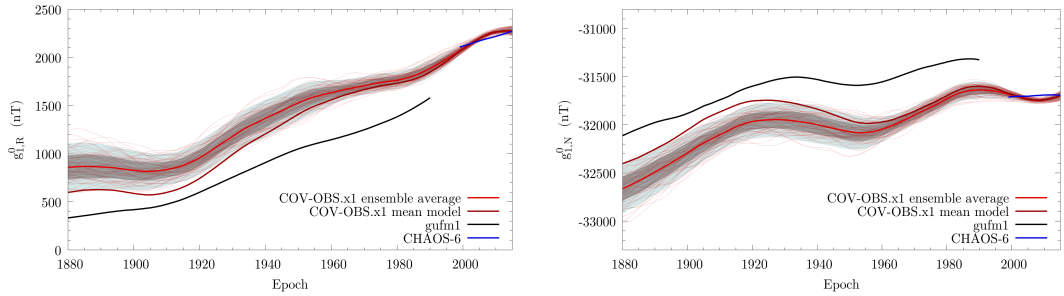


**(a)** **(b)**

**Figure 2.9:** The reversed (a) and normal contributions (b) to the axial dipole field over the investigated periods (the same colouring as in Fig. 2.4 applies).

the decline of $|g_1^0|$ over this period. Inspection of Eq. (2.3) shows that secular increases in $g^0_{1,R/N}$ can be due to a change in one or more of $S_{R/N}$ (growth/reduction of combined area), the latitude-weighted area (poleward/equatorward migration), or $B_r$ (flux (de)intensification). We test which of these effects have importance for the evolution of $g^0_{1,R/N}$ by computing the quantities:

$$A_R(t) = \int_{S_R(t)} \mathrm{d}S\,, \tag{2.4}$$

$$\Phi_{R/N}(t) = \frac{1}{A_{R/N}(t)} \int_{S_{R/N}(t)} |B_r(\mathbf{r},t)|\,\mathrm{d}S\,, \tag{2.5}$$

$$\Theta_{R/N}(t) = \frac{1}{A_{R/N}(t)} \int_{S_{R/N}(t)} |\cos\theta|\,\mathrm{d}S\,, \tag{2.6}$$

which represent, respectively, the combined reversed surface area (note that $A_N(t) + A_R(t) = S$), the average unsigned $B_r$ over $S_{R/N}$, and the average unsigned cosine latitude weighting factor average over $S_{R/N}$.

The time-dependency of $A_R$ has already been shown in Fig. 2.4b. As mentioned above it shows a gradual growth over the 20$^{\text{th}}$ century which amounts to a relative increase of about 11% for the COV-OBS.x1 ensemble average and more than 30% for gufm1. The correlation between these increases and those in $g^0_{1,R}$ (Fig. 2.9a) suggests that the decay in $|g_1^0|$ may be linked to an increase in RFP area. However, this takes no account of where RFPs are located. Figure 2.10a shows that $\Theta_R$ has increased by 27% according to COV-OBS.x1 and 51% according to gufm1 over the 20$^{\text{th}}$ century. This indicates that in these models RFPs show a significant average poleward migration. Of further note is that since 2000, $\Theta_R$ has been approximately constant and therefore has not contributed itself to any recent change in $g_1^0$, in contrast to its significant role over the past century. Lastly, Fig. 2.10b shows that the average radial flux through RFPs has increased significantly over the 20$^{\text{th}}$ century by approximately 14% and 21% for COV-OBS.x1 and gufm1, respectively. In common with previous figures, the estimates for

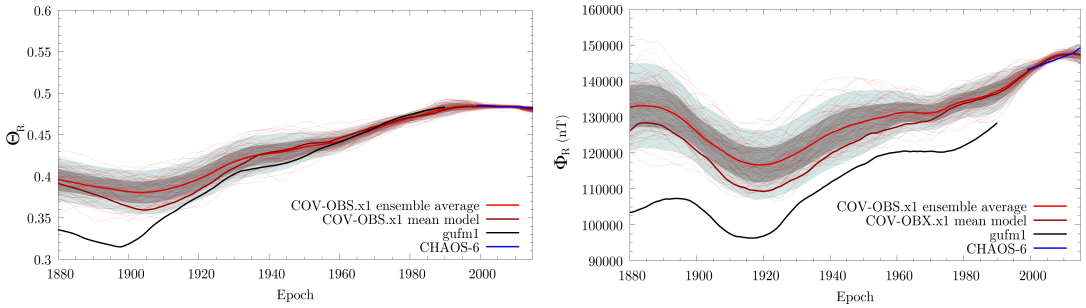


**(a)** **(b)**

**Figure 2.10:** The average over the combined RFP area of $|\cos\theta|$ (a) and $|B_r|$ (b) as a function of time (the same colouring as in Fig. 2.4 applies).

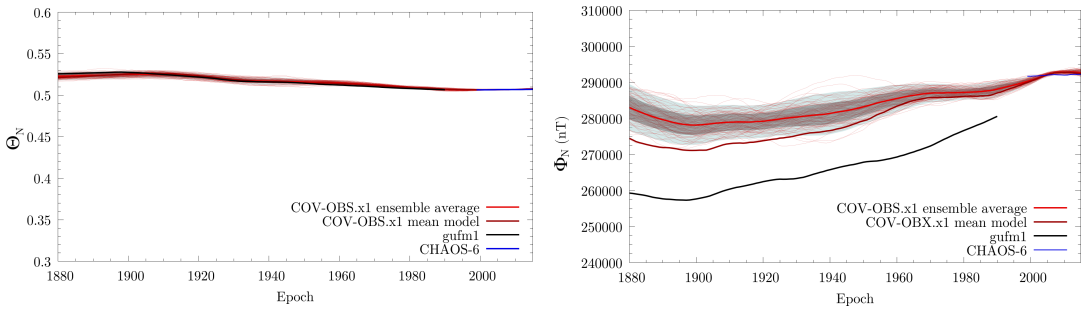


**(a)** **(b)**

**Figure 2.11:** The average over the combined normal area of $|\cos\theta|$ (a) and $|B_r|$ (b) as a function of time (the same colouring as in Fig. 2.4 applies).

$\Phi_R$ from gufm1 are lower than those from COV-OBS.x1.

Taken together, the relative increases of $A_R$, $\Theta_R$ and $\Phi_R$ suggest that the decay in $|g_1^0|$ over the past century is manifest at the CMB as a combination of growth of RFP area, poleward migration, and flux intensification within RFPs over that period. Comparing the magnitudes of the increases in the quantities we consider, the relative increase in $\Theta_R$ is roughly twice that of $A_R$ and $\Phi_R$, such that more than half of the increase in $g_{1,R}^0$ over the 20$^{\text{th}}$ century may be attributed to poleward migration and the remaining increase may be equally ascribed to each of reversed flux expansion and intensification (Table 2.1).

The evolution of the normal field is characterised by the time-series of the quantities $\Theta_N$ and $\Phi_N$, shown in Fig. 2.11a and 2.11b, respectively. It is clear that $\Theta_N$ has remained relatively constant over the 20$^{\text{th}}$ century with a relative change of less than 5% over this period for both COV-OBS.x1 and gufm1. The average intensity of normal-flux, $\Phi_N$, has undergone a relative increase of approximately 10% over the investigated period, a change that strengthens the axial dipole. The overall influence of the changes in the normal-field quantities is to weaken the axial dipole, mainly due to the change in $A_N$, with the impact of changes in $\Theta_N$ and $\Phi_N$ on $g_1^0$ approximately cancelling (Table 2.1).

| | $A$ | $\Theta$ | $\Phi$ | total |
|---|---|---|---|---|
| $g^0_{1,R}$ | 0.3 | 0.7 | 0.3 | 1.3 |
| $g^0_{1,N}$ | 0.6 | 0.2 | -0.3 | 0.5 |

**Table 2.1:** The approximate impact of changes in the integral quantities $A$, $\Theta$ and $\Phi$ over the 20$^{\text{th}}$ century on the axial dipole contributions $g^0_{1,R/N}$ in units of $10^3$ nT.

## 2.6 Discussion and conclusions

We set out to address three issues in the determination of RFP evolution and their influence on the decay of the axial dipole. First, we needed to define a magnetic equator enabling the identification of RFPs. We investigated the use of null-flux curves for different degrees of truncation of the magnetic field. We found that the use of a degree three field provided a robust method of identifying RFPs, and that RFPs are features of at least degree 5. Our choice of magnetic equator contrasts with that of *Terra-Nova et al.* (2015) who used a null-flux curve of the total field (in this case of degree 10) as the magnetic equator, and with *Olson and Amit* (2006) who used the geographic equator. As we show, neither of these are effective for our time period: setting $l^{\text{eq}}_{\text{max}}$ to be $l_{\text{max}}$ of the total field produces a large intrusion of the magnetic equator into the southern hemisphere during approximately 1880-1920, while the use of a geographic equator fragments low-latitude features. Over a longer archeomagnetic timescale (about the past three millennia), *Terra-Nova et al.* (2015) showed that RFPs are features of degree at least 4, which is consistent with our results.

The second issue we addressed was to quantify the contribution of the reversed and normal flux regions on the CMB to the decay of the axial dipole. The $g^0_1$ coefficient can be altered by changes in the area of reversed or normal flux ($A_R$ and $A_N$), the latitudinal migration of flux patches (as characterised by $\Theta_R$ and $\Theta_N$), or changes in flux intensity within the patches (as characterised by $\Phi_R$ and $\Phi_N$); first-order estimates of each of these effects are given in Table 2.1. We found that roughly two-thirds of the decay over the 20$^{\text{th}}$ century may be attributed to RFPs and one-third to the evolution of the normal field. Although normal field provides a smaller contribution, it is sufficiently significant such that the decay of the axial dipole can not exclusively be attributed to the reversed part of the field (*Gubbins*, 1987). However, given that the total reversed surface area relative to the area of the CMB is 20% at most, the axial dipole appears to be particularly sensitive to changes in the reversed portion of the field compared to the normal field.

Third, we find that in the field models considered, the most important contributions to the decrease in $|g^0_1|$ arise from the changed partitioning of reverse and normal field area at the CMB, and the poleward migration of RFPs. It is interesting to note that these dominant contributions over the past century may not continue to reflect the current (or future) secular variation of the axial dipole. For example, the contribution to dipole decay arising from the average poleward migration of RFPs plateaued at around epoch 2000 (Fig. 2.10a); the continuing decrease of $g^0_1$ since that time is primarily due to increases in the average amplitude of reversed flux within

the RFPs (Fig. 2.10b).

Our results are consistent with the work of *Terra-Nova et al.* (2015) who find a similar time dependence over the 20$^{\text{th}}$ century for the contribution of the reversed field to the axial dipole, although this is to be expected as they employ the CALS3k.4b field model which is constrained by gufm1 for the years 1840 to 1990 (*Korte and Constable*, 2011). Additionally, by using gufm1 for the same period as in this study, *Olson and Amit* (2006) find that the fall in $|g_1^0|$ is mostly due to secular variation in the Southern Hemisphere. This is again consistent with ou/ results as we find that the evolution of RFPs, which reside predominantly in the Southern Hemisphere, account for most of the $|g_1^0|$ decay. Our results also demonstrate the significance of poleward migration of RFPs for axial dipole decay, similar to the studies of *Olson and Amit* (2006) and *Finlay et al.* (2016b). However, both studies highlight the importance of equatorward flow of intense normal flux beneath the southern Indian Ocean, which contrasts with our finding that the reversed flux contribution to axial dipole decay is more than twice as large as its normal counterpart. We find evidence for equatorward advection of normal field, but its contribution to axial dipole decay appears to be relatively small. It is possible that these discrepancies can be explained by the fact that the flow models from the previous studies are constrained by the frozen-flux approximation, unlike our approach.

In this study we compared results from COV-OBS.x1 and gufm1; although based on similar data the models show a marked difference in the RFP identification from 1840 to 1880. The major difference during this period is in the representation of small scale magnetic features. Whereas gufm1 has relatively strong temporal and spatial damping that penalises small scales, by contrast COV-OBS.x1 has no damping, and apparently has anomalously strong small scale features between 1840 and 1880 that is likely due to an end effect (N. Gillet, personal communication, 2016). For this reason we restrict attention to the period of 1880 onwards. As the investigated quantities (Eq. 2.3-2.6) are particularly sensitive to the distribution and intensity of the short-wavelength reversed field, the relatively strong regularisation inherent in gufm1 has a signature in all of our plots that characterise the area and magnitude of RFPs, by having markedly lower estimates of our descriptive quantities than COV-OBS.x1 (Fig. 2.4, 2.9a and 2.10). Despite these differences, the general trends agree and therefore both models support the conclusions that we have reached.

Both gufm1 and COV-OBS.x1 are constructed without frozen-flux constraints on RFP evolution. The use of models that employ such constraints (e.g. *Bloxham and Gubbins*, 1986, *Constable et al.*, 1993, *Lesur et al.*, 2010, *Wardinski and Lesur*, 2012) may yield significantly different results than those presented in this work. This is especially the case for the quantities $A_R$ and $\Phi_R$ that respectively represent RFP surface area and intensity. If models that additionally conserve radial vorticity were to be applied in our analysis (e.g. *Jackson et al.*, 2007, *Asari and Lesur*, 2011), then this may also yield different results for the evolution of $\Theta_R$, as in that case poleward migration of an RFP is allowed only if there is an associated change in the morphology of that patch (*Jackson*, 1996). Thus, for these models the decay of the axial dipole remains to be explained and further work will be required to determine how it may be

attributed to different aspects of CMB field evolution. Within the models we have analysed, poleward migration of RFPs is an important contributor to $20^{th}$ century dipole decay; however, this process contributes little to the ongoing decay after the year 2000.

## Acknowledgments

We thank Vincent Lesur and Hagay Amit for reviewing our work and their constructive criticism. Additionally, we are grateful to Nicolas Gillet, Chris Finlay and Ciarán Beggan for their useful comments, which further improved this work. Lastly, we thank the National Space Institute of the Technical University of Denmark for their open-access repository of magnetic field models. M. C. Metman is supported by a studentship awarded as part of the Leeds-York NERC Doctoral Training Partnership (NE/L002574/1) and by the BGS University Funding Initiative PhD studentship (S305).

# References


Asari, S., and V. Lesur (2011), Radial vorticity constraint in core flow modeling, *Journal of Geophysical Research: Solid Earth*, *116*(11). 2.1, 2.6

Backus, G., R. Parker, and C. Constable (1996), *Foundations of Geomagnetism*, Cambridge University Press, Cambridge. 2.1

Backus, G. E. (1968), Kinematics of geomagnetic secular variation in a perfectly conducting core, *Philosophical Transactions of the Royal Society of London A: Mathematical, Physical and Engineering Sciences*, *263*(1141), 239–266. 2.1

Barraclough, D. R. (1974), Spherical harmonic analyses of the geomagnetic field for eight epochs between 1600 and 1910, *Geophysical Journal of the Royal Astronomical Society*, *36*(3), 497–513. 2.1

Bloxham, J. (1986), The expulsion of magnetic flux from the Earth's core, *Geophysical Journal International*, *87*(2), 669–678. 2.1

Bloxham, J., and D. Gubbins (1985), The secular variation of Earth's magnetic field, *Nature*, *317*, 777–781. 2.1

Bloxham, J., and D. Gubbins (1986), Geomagnetic field analysis − IV. Testing the frozen-flux hypothesis, *Geophysical Journal of the Royal Astronomical Society*, *84*(1), 139–152. 2.1, 2.6

Bloxham, J., D. Gubbins, and A. Jackson (1989), Geomagnetic secular variation, *Philosophical Transactions of the Royal Society of London*, *329*, 415–502. 2.1

Constable, C. G., R. L. Parker, and P. B. Stark (1993), Geomagnetic field models incorporating frozen-flux constraints, *Geophysical Journal International*, *113*, 419–433. 2.1, 2.6

Finlay, C. C., N. Olsen, S. Kotsiaros, N. Gillet, and L. Tøffner-Clausen (2016a), Recent geomagnetic secular variation from Swarm and ground observatories as estimated in the CHAOS-6 geomagnetic field model, *Earth, Planets and Space*, *68*(1), 112. 2.1, 2.1, 2.2

Finlay, C. C., J. Aubert, and N. Gillet (2016b), Gyre-driven decay of the Earth's magnetic dipole, *Nature Communcations*, *7*(10422). 2.1, 2.6

Gillet, N., D. Jault, C. C. Finlay, and N. Olsen (2013), Stochastic modeling of the Earth's magnetic field: Inversion for covariances over the observatory era, *Geochemistry, Geophysics, Geosystems*, *14*(4), 766–786. 2.1, 2.2

Gillet, N., O. Barrois, and C. Finlay (2015), Stochastic forecasting of the geomagnetic field from the COV-OBS.x1 geomagnetic field model, and candidate models for IGRF-12 International Geomagnetic Reference Field - The Twelfth generation, *Earth, Planets and Space*, *67*(1). 2.1, 2.2

Gubbins, D. (1987), A mechanism for geomagnetic polarity reversals, *Nature*, *326*, 167–169. 2.1, 2.1, 2.1, 2.6

Gubbins, D., A. L. Jones, and C. C. Finlay (2006), Fall in Earth's magnetic field is erratic, *Science*, *312*, 900–902. 2.1, 2.1, 2.2

Jackson, A. (1996), Kelvin's theorem applied to the Earth's core, *Proceedings of the Royal Society of London A: Mathematical, Physical and Engineering Sciences*, *452*(1953), 2195–2201. 2.1, 2.6

Jackson, A., A. R. T. Jonkers, and M. R. Walker (2000), Four centuries of geomagnetic secular variation from historical records, *Philosophical Transactions of the Royal Society of London*, *358*, 957–990. 2.1, 2.2

Jackson, A., C. Constable, M. Walker, and R. Parker (2007), Models of Earth's main magnetic field incorporating flux and radial vorticity constraints, *Geophysical Journal International*, *171*(1), 133–144. 2.1, 2.6

Jonkers, A. R. T., A. Jackson, and A. Murray (2003), Four centuries of geomagnetic data from historical records, *Reviews of Geophysics*, *41*(2). 2.2

Korte, M., and C. Constable (2011), Improving geomagnetic field reconstructions for 0-3 ka, *Physics of the Earth and Planetary Interiors*, *188*(34), 247 – 259. 2.6

Lesur, V., I. Wardinski, S. Asari, B. Minchev, and M. Mandea (2010), Modelling the Earth's core magnetic field under flow constraints, *Earth, Planets and Space*, *62*(6), 503–516. 2.1, 2.6

Lhuillier, F., A. Fournier, G. Hulot, and J. Aubert (2011), The geomagnetic secular-variation timescale in observations and numerical dynamo models, *Geophysical Research Letters*, *38*(9). 2.2

Olson, P., and H. Amit (2006), Changes in Earth's dipole, *Naturwissenschaften*, *93*(11), 519–542. 2.1, 2.2, 2.3.1, 2.6

Roberts, P. H., and S. Scott (1965), On Analysis of the Secular Variation. 1. A Hydromagnetic Constraint: Theory, *Journal of Geomagnetism and Geoelectricity*, *17*(2), 137–151. 2.1

Terra-Nova, F., H. Amit, G. A. Hartmann, and R. I. F. Trindade (2015), The time dependence of reversed archeomagnetic flux patches, *Journal of Geophysical Research: Solid Earth*, *120*, 691–704. 2.1, 2.2, 2.3.1, 2.3.2, 2.3.2, 2.6

Terra-Nova, F., H. Amit, G. A. Hartmann, and R. I. Trindade (2016), Using archaeomagnetic field models to constrain the physics of the core: robustness and preferred locations of reversed flux patches, *Geophysical Journal International*, *206*(3), 1890–1913. 2.1

Wardinski, I., and V. Lesur (2012), An extended version of the $C^3$FM geomagnetic field model: Application of a continuous frozen-flux constraint, *Geophysical Journal International*, *189*(3), 1409–1429. 2.1, 2.6

# Addendum: Chapter 2 — The reversed and normal flux contributions to axial dipole decay for 1880-2015

Before moving on to the next chapter, we further discuss the characterisation of historical axial dipole decay made in the previous chapter, and draw some additional conclusions.

First of all, this chapter focused on several global integral quantities, i.e. those defined in eq. (2.3)-(2.6). By considering time series of these quantities over decadal to centennial time scales, we determined how axial dipole decay is manifest, in a global sense, in the evolution of the radial field at the CMB. Since the global quantities depend on the distribution of reversed and normal magnetic flux on the CMB, this analysis required a choice for the magnetic equator. If this equator is of short wavelength, or equally if the largest spherical harmonic degree defining the magnetic equator (denoted by $l^{\text{eq}}_{\text{max}}$) is high, large jump discontinuities will occur in the time series of the integral quantities (compare for example Fig. 2.4a and 2.4b). We have demonstrated that with such discontinuities, a meaningful interpretation of these time series is impossible. Setting $l^{\text{eq}}_{\text{max}}$ well below the largest degree of the field model analysed (in our case, setting $l^{\text{eq}}_{\text{max}} < l_{\text{max}} = 14$) is also preferred because such a choice ensures that the mapping of reversed and normal flux does not depend on knowledge of the small-wavelength field, which is relatively uncertain. Thus, a sufficiently small $l^{\text{eq}}_{\text{max}}$ is preferable.

Conversely, we also provided motivation to allow for at least some curvature in the magnetic equator by setting $l^{\text{eq}}_{\text{max}}$ not 'too low' either. Namely, while a small value for this parameter will prevent the occurrence of jump discontinuities in the time series of our global quantities, it will also result in increased fragmentation of field patches bounded by null-flux curves at low latitude (Fig. 2.3). Still, to what extent is an intermediate choice for the magnetic equator actually better? For example, due to the latitude-dependent averaging kernel associated with $g^0_1$ (eq. 2.1), field features near the geographic equator already provide a relatively small contribution to the axial dipole. Therefore, reversed-flux fragmentation is likely of little influence when computing the normal and reversed contributions to axial dipole decay (e.g. through eq. 2.3). Additionally, while in chapter 2 our preferred choice was to set $l^{\text{eq}}_{\text{max}} = 3$, it is clear that for this choice there is still a considerable amount of fragmentation (compare Fig. 2.3e and 2.3f with 2.3i and 2.3j). In other words, an intermediate choice for the magnetic equator does not

eliminate low-latitude flux fragmentation completely. Moreover, while we have shown for the field models used in chapter 2 that setting $l^{\mathrm{eq}}_{\mathrm{max}} = 3$ yields continuous time series of our integral quantities, strictly speaking this can not be guaranteed when this choice of equator is applied to other field models. This compatibility issue does for example not arise when using the magnetic equator with minimal curvature, that is the geographic equator, as it is independent of the morphology of the field. This choice has additional value since it is much easier to discretise, and circumvents the need for the algorithm described in section 2.3.2. With the considerations above in mind, the geographic equator should then also be regarded as a reasonable choice for the magnetic equator, if not better than one defined by $l^{\mathrm{eq}}_{\mathrm{max}} = 3$.

In our work we considered the magnetic field described by observation-based models, which can not be resolved for spherical harmonic degrees larger than 14 due to lithospheric contamination (*Langel and Estes*, 1982). The situation is different for numerically simulated core fields: for these models horizontal resolution of the field is limited only by computational resources, and therefore allows the resolution of core field features of much smaller wavelength (often $l_{\mathrm{max}} > 100$). With this in mind, what is an appropriate choice for the largest degree of the magnetic equator $l^{\mathrm{eq}}_{\mathrm{max}}$ when analysing such simulated magnetic fields? As the field is well resolved at all wavelengths, there is no need for a conservative choice for this parameter, i.e. one that prevents the reversed-flux distribution to depend on the small-wavelength field. It is also possible that when the field is expanded up to such high spherical degrees that hemispherical intrusions such as those in Fig. 2.3i and 2.3j do not occur and with that prevents the occurrence of jump discontinuities of the integral quantities we study. In this case, for numerically simulated fields setting $l^{\mathrm{eq}}_{\mathrm{max}}$ much larger than 3, and perhaps $l^{\mathrm{eq}}_{\mathrm{max}} = l_{\mathrm{max}}$, would define a magnetic equator that allows for time-series analysis of our integral quantities, while also producing minimal fragmentation of patches bounded by null-flux curves at low latitudes. However, if these conditions apply for geodynamo simulations is difficult to confirm *a priori*, and an appropriate choice of $l^{\mathrm{eq}}_{\mathrm{max}}$ for these models therefore requires further study.

A magnetic equator allows us to map the distribution of reversed and normal field at the CMB, and therefore to compute the integral quantities which depend on these distributions (eq. 2.3-2.6). But how well-defined are such integral quantities? For example, inspection of Fig. 2.8 leads to the conclusion that the total reversed-flux surface area (eq. 2.4) increases with the degree of truncation of the field, even for relatively high $l_{\mathrm{max}}$. In other words, the mapping of reversed-flux on the CMB is possibly not converged with spherical harmonic degree. Therefore, while we state in chapter 2 that reversed-flux is of degree 4-5 (as field features of these degrees give relatively large contributions to the total reversed surface area), this should by no means be interpreted as a hard bound. In fact, Fig. 2.8 gives the impression that if we were to know the field up to a degree much larger than $l_{\mathrm{max}} = 14$, then distribution of reversed and normal flux could be different. This property of reversed flux is particularly problematic for models depending on archeomagnetic and paleomagnetic data, which are resolved well only up to spherical harmonic degree 4 or so (e.g. *Korte et al.*, 2011). For such models, a reliable mapping of reversed flux is therefore difficult. This is in accordance with the results of *Terra-Nova*

*et al.* (2015) who found relatively few RFPs over archeomagnetic periods, and a significant increase in the number of RFPs over the past four centuries when geomagnetic data became less sparsely distribution over the globe. Still, since the strength of the axial dipole decay is ongoing, higher degree features (such as RFPs) will inevitably become more prominent. The reversed-flux proliferation observed by *Terra-Nova et al.* (2015) may therefore well be a true property of the temporal evolution of the core field over these time scales, and would then be indicative of the untenability of frozen flux over such periods.

Another, yet similar, issue with the analysis of global integral quantities which depend on field morphology has been presented by *Holme and Olsen* (2006), and later by *Holme et al.* (2011). They demonstrate with a field model derived from modern satellite data that the SV spectrum is 'blue' (the power in the SV increases with spherical harmonic degree). As such, there is more power in the wavelengths of SV which are relatively uncertain. *Holme and Olsen* (2006) point out an important consequence of this property of the field, namely that the change in the global frozen-flux condition (eq. 1.27) is not converged up to $l_{\max} = 14$. Although we have found in chapter 2 that the radial field has globally intensified, and that the total reversed-flux surface area has increased, with the considerations presented above we arrive at the conclusion that observation-based field models do likely not contain sufficient information to test the frozen-flux hypothesis with the use of global integral quantities. Therefore, one should be cautious of interpreting our results in the previous chapter as a failure of frozen flux over the historical period.

A key point of the previous chapter that also requires addressing revolves around our characterisation of axial dipole decay in terms of field evolution at the CMB (section 2.5). More specifically, we partitioned the decay in three parts associated with the (re)distribution of reversed flux on the CMB, flux (de)intensification, and meridional migration of the field (eq. 2.4-2.6). For example, we found that approximately half of the decay of the reversed field over the 1880-2015 period was due to poleward migration of RFPs (Table 2.1). However, by making such estimations, we have implicitly assumed that these processes are independent; generally speaking this is not the case. For instance, the surface area of a single RFP (in which $B_r$ is constant, say) could expand towards the equator, and while this would increase and decrease the integral quantities $A_R$ and $\Theta_R$ respectively, these variations may cancel and generate little effective change in the axial dipole strength. Conversely, the same patch could also have expanded towards the poles, in which case variation in the variable $A_R$ underestimates the effect of this morphological change on the axial dipole. Therefore, attributing axial dipole decay to changes in these integral quantities, as has been done to compute the values in Table 2.1, is not straightforward, and a meaningful interpretation of these variations in terms of core processes is therefore even more difficult.

That brings us to the next chapter. We have highlighted here considerable difficulties of using observation-based models of the core field to analyse temporal variation of global integral quantities which depend on field morphology, and with that to assess to what extent the frozen-flux approximation is appropriate for Earth's core over the centennial to decadal time scales.

Furthermore, we have not physically explained the dipole decay in terms of core processes, only characterised it in a mathematical sense in terms of CMB field evolution. In the following chapter, we shall therefore appraise frozen flux using a different strategy, as well as introduce some physical considerations. More specifically we shall determine to what extent magnetic diffusion alone can explain historical field evolution — if this is for example not the case, then we may state with more confidence that SV is well described by the frozen-flux approximation.

# References

Holme, R., and N. Olsen (2006), Core surface flow modelling from high-resolution secular variation, *Geophysical Journal International*, *166*(2), 518–528. 2.6

Holme, R., N. Olsen, and F. L. Bairstow (2011), Mapping geomagnetic secular variation at the core-mantle boundary, *Geophysical Journal International*, *186*(2), 521–528. 2.6

Korte, M., C. Constable, F. Donadini, and R. Holme (2011), Reconstructing the Holocene geomagnetic field, *Earth and Planetary Science Letters*, *312*(3), 497–505. 2.6

Langel, R. A., and R. H. Estes (1982), A geomagnetic field spectrum, *Geophysical Research Letters*, *9*(4), 250–253. 2.6

Terra-Nova, F., H. Amit, G. A. Hartmann, and R. I. F. Trindade (2015), The time dependence of reversed archeomagnetic flux patches. 2.6

# Chapter 3

# Modelling decadal secular variation with only magnetic diffusion

**M. C. Metman**[1], P. W. Livermore[1], J. E. Mound[1], and C. D. Beggan[2]

[1]*School of Earth and Environment, University of Leeds, Leeds LS2 9JT, United Kingdom*
[2]*British Geological Survey, Edinburgh EH14 4AP, United Kingdom*

*'Even a broken clock is right twice a day.'*

**English proverb**

## Abstract

Secular variation (SV) of Earth's internal magnetic field is the sum of two contributions, one resulting from core fluid flow and the other from magnetic diffusion. Based on the millenial diffusive timescale of global-scale structures, magnetic diffusion is widely perceived to be too weak to significantly contribute to decadal SV, and indeed is entirely neglected in the commonly adopted end-member of frozen-flux. Such an argument however lacks consideration of radially fine-scaled magnetic structures in the outermost part of the liquid core, whose diffusive timescale is much shorter. Here we consider the opposite end-member model to frozen flux, that of purely diffusive evolution associated with the total absence of fluid flow. Our work is based on a variational formulation, where we seek an optimised full-sphere initial magnetic field structure whose diffusive evolution best fits, over various time windows, a time-dependent magnetic field model. We present models which are regularised based on their magnetic energy, and consider how well they can fit the COV-OBS.x1 ensemble mean using a global error bound based on the standard deviation of the ensemble. With these regularised models, over time periods of up to 30 years, it is possible to fit COV-OBS.x1 within one standard deviation at all times. For time windows up to 102 years we show that our models can fit COV-OBS.x1 when

adopting a time-averaged global uncertainty. Our modelling is sensitive only to magnetic structures in approximately the top 10% of the liquid core, and show an increased surface area of reversed flux at depth. The diffusive models recover fundamental characteristics of field evolution including the historical westward drift, the recent acceleration of the North Magnetic Pole and reversed-flux emergence. Based on a global time-averaged residual, our diffusive models fit the evolution of the geomagnetic field comparably, and sometimes better than, frozen-flux models within short time windows.

## 3.1 Introduction

The magnetic field generated within the Earth's fluid outer core exhibits continuous change in time over yearly to decadal timescales, termed secular variation (SV). Global geomagnetic field models constructed from ground-based observatories, satellites and other data sources are often expressed in terms of time-dependent Gauss coefficients $\{g_l^m, h_l^m\}$, each of degree $l$ and order $m$, which correspond to a spherical harmonic partitioning of the field; decadal changes of selected spherical harmonic components are shown in Fig. 3.1.

Secular variation results from two processes within the liquid core: interaction between outer core fluid flow and the magnetic field, and magnetic diffusion (e.g. *Jackson and Finlay*, 2015). The general balance between these two processes is quantified by the magnetic Reynolds number

$$Rm = \frac{\mathcal{U}\mathcal{L}}{\eta} = \frac{\tau_d}{\tau_u}, \tag{3.1}$$

with $\mathcal{U}$ and $\mathcal{L}$ characteristic fluid velocity and magnetic length scales respectively, $\eta$ the magnetic diffusivity, and typical time scales for diffusion and advection denoted by $\tau_d$ and $\tau_u$ respectively. Estimates of these quantities ($\mathcal{L} = 10^3$ km, $\mathcal{U} = 20$ km yr$^{-1}$, and $\eta = 63$ km$^2$ yr$^{-1}$, e.g. *Jackson and Finlay*, 2015) yield the time scales $\tau_d = 16$ kyr and $\tau_u = 63$ yr, and $Rm \sim 10^2$ (where the tilde denotes order of magnitude). The disparity between these time scales implies that for decadal SV diffusion may be neglected, an approximation commonly referred to as that of frozen flux as introduced by *Roberts and Scott* (1965).

This assertion has proven extremely valuable over the past decades. Not only have several authors demonstrated a mathematical consistency between geomagnetic observations and frozen-flux constraints on core field evolution (e.g. *Gubbins*, 1984, *Constable et al.*, 1993, *Wardinski and Lesur*, 2012), the approximation has also allowed the inversion of SV observations on the Earth's surface and above for core fluid motions along the core-mantle boundary (CMB) (e.g. *Vestine et al.*, 1967, *Whaler*, 1980, *Bloxham*, 1988). In addition, frozen flux has been utilised to further constrain the space and time-variability of core fluid flow (*Olsen and Mandea*, 2008, *Aubert*, 2012, *Livermore et al.*, 2017), to forecast SV over periods of less than a decade (*Beggan and Whaler*, 2009, *Whaler and Beggan*, 2015, *Bärenzung et al.*, 2018, *Beggan and Whaler*, 2018), and to explain length-of-day variations resulting from core-mantle

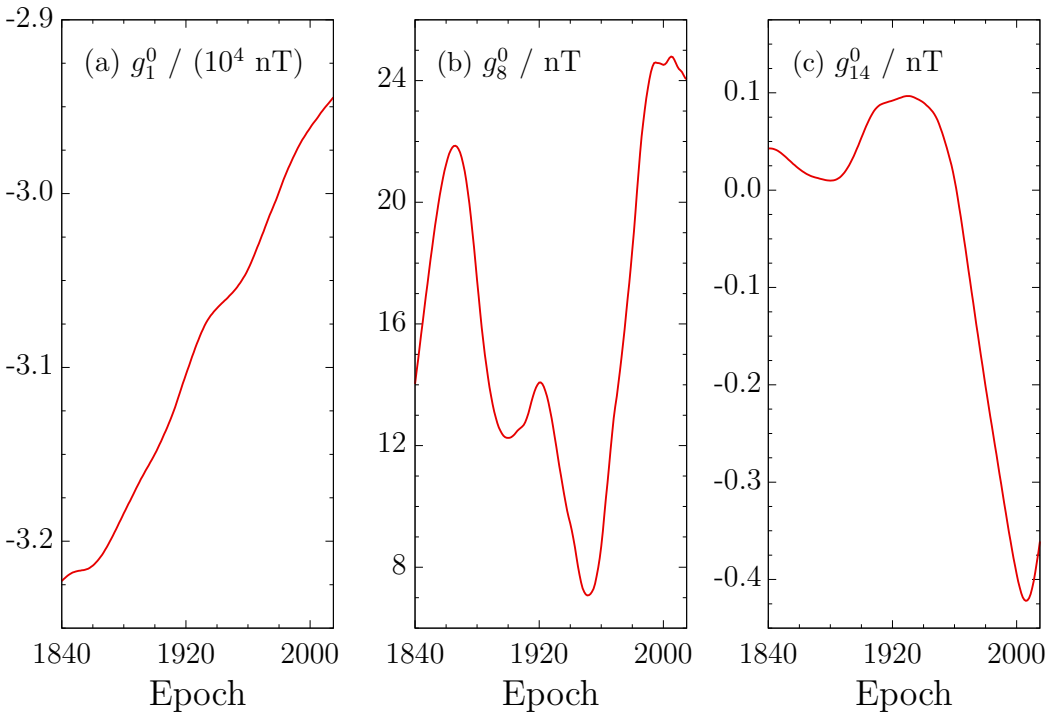


**Figure 3.1:** Time series of the Gauss coefficients $g_1^0$ (a), $g_8^0$ (b), and $g_{14}^0$ (c) obtained from the mean COV-OBS.x1 field model for the period 1840.0-2015.0 (*Gillet et al.*, 2015b).

coupling (*Jault et al.*, 1988, *Jackson et al.*, 1993, *Gillet et al.*, 2015a).

Although frozen flux has been shown to be a useful approximation, there is ongoing discussion regarding what part of the observed SV can truly be attributed to magnetic diffusion, which relates to the parameters that define $Rm$ (Eq. 3.1). Firstly, typical estimates for $\mathcal{L}$ are based only on horizontal CMB field morphology, and a typical magnetic length scale in the radial direction remains poorly constrained (e.g. *Holme*, 2015), although for the region just below the CMB it has been estimated at several tens to hunderds of km (*Amit and Christensen*, 2008, *Chulliat and Olsen*, 2010, *Terra-Nova et al.*, 2016). In light of this, several authors have stressed the inevitable failure of the approximation if magnetic features are indeed of sufficiently small radial scale, for example due to the concentration of toroidal field beneath the CMB through fluid upwelling, a process known as flux expulsion (*Bloxham*, 1986, *Gubbins and Kelly*, 1996). Secondly, the velocity scale $\mathcal{U}$ is usually estimated by directly attributing the observed secular westward drift of equatorial magnetic features (*Halley*, 1692, *Finlay and Jackson*, 2003) to fluid flow, showing only (in a circular argument) that the frozen-flux approximation is consistent with high-$Rm$. What this argument does not consider, however, are alternative processes that may explain the westward drift (such as waves (*Hide*, 1966) or diffusion) which would require smaller magnitude flows to explain the residual SV and thus have a smaller associated $Rm$.

Aside from these theoretical considerations, the importance of diffusion has also been highlighted with numerical simulations of the geodynamo. Such models can yield observable dif-

fusion through flux expulsion (*Aubert et al.*, 2008, *Aubert*, 2014), despite the fact that these models are typically characterised by Earth-like $Rm$ (*Christensen et al.*, 2010). Furthermore, the special geodynamo case of steady core fluid motion has been demonstrated to be incompatible with frozen flux (*Gubbins and Kelly*, 1996, *Love*, 1999). More recently, *Barrois et al.* (2017) employed statistics derived from geodynamo simulations to demonstrate that even on short time scales diffusion contributes up to approximately 10% of the overall SV at the core-mantle boundary, although separating this diffusive signal from errors related to finite horizontal resolution remains non-trivial (*Barrois et al.*, 2018).

Local failure of frozen flux has also been inferred from observations of the core magnetic field, using the constraint that without diffusion the total magnetic flux through patches bounded by null-flux curves should remain steady (*Backus and Bullard*, 1968). For instance, recent rapid change of the north Magnetic Pole and of the radial magnetic field under St. Helena have been attributed to flux expulsion (*Chulliat et al.*, 2010, *Chulliat and Olsen*, 2010). *Gubbins* (1996) made an initial attempt to invert for core motion with the explicit inclusion of diffusion, and estimated a considerable radial gradient of toroidal field of 20 nT $\mathrm{m}^{-1}$ beneath the South Atlantic, sufficient to explain the local intensification of magnetic flux of 500 MWb. However, it remains difficult to unambiguously detect such expulsion patches and hence a signature of magnetic diffusion in the core (*Amit*, 2014). Furthermore, it is challenging to distinguish magnetic diffusion from energy transfer between unresolved small scale flow and the observed large-scale magnetic field (*Roberts and Glatzmaier*, 2000).

In this paper, we will test whether magnetic diffusion is capable of generating decadal SV that matches the observation-based model COV-OBS.x1 (*Gillet et al.*, 2015b). To do this, we use a variational formulation, where we seek the 3D structure of an initial magnetic field whose subsequent evolution best explains SV over a defined time window. Variational data assimilation has been implemented successfully in several nonlinear geodynamo models (*Fournier et al.*, 2007, *Li et al.*, 2014) but here, owing to the lack of any coupling through the absent flow, the optimal initial field can be found in a particularly simple way as a solution to a linear system. We consider various time windows to assess whether a purely diffusive model is consistent with SV on yearly, decadal, and centennial time scales. This approach allows us to explore a new end-member model of the secular variation, that of pure diffusion, and compare it against models of the more traditional frozen-flux type. Our purely diffusive model is not intended to fully represent the mechanism responsible for SV, but rather to test whether it is sufficient to reconstruct the observed SV and to probe the field below the core-mantle boundary using the inherent assumptions of the model. While the formalism by *Gubbins* (1996) permits diffusion as a correction term for frozen flux, and could be utilised to jointly invert observed field evolution for the frozen-flux and diffusive contributions to SV, we present here a new scheme which considers diffusion as the sole contribution to SV.

This work is structured as follows: we first describe in Section 3.2 how we optimise the initial full-sphere magnetic field to match SV through its diffusive evolution; the resultant diffusive models along with their general and local characteristics are presented in Section 3.3;

Section 3.4 discusses the geophysical implications of our results. Four appendices describe technical details including depth-sensitivity and numerical convergence.

## 3.2 Methods

In this section we present our variational formalism for a diffusing 3D magnetic field. Assuming that the solid inner core has the same electrical conductivity as the liquid core, the same diffusion equation is obeyed everywhere in the core by the magnetic field and we therefore seek full-sphere solutions, which are also therefore valid in a spherical shell. We begin by briefly introducing the associated forward problem and its canonical solutions: the decay modes. These functions are used in Appendix A.1 to determine the resolving power of our methodology as a function of depth. We also present an alternative representation of the forward model using Galerkin polynomials, which turns out to be numerically much better conditioned than that based on decay modes. Finally, we consider a means of regularising the inverse solution by penalising the total magnetic energy.

### 3.2.1 Decay modes

Here, a set of analytical (forward) solutions to the (dimensional) magnetic diffusion equation are given (*Gubbins and Roberts*, 1987). If we were provided with the structure of the magnetic field throughout the entire core, these solutions would describe the temporal evolution of that field in the absence of fluid flow. We start with the three-dimensional magnetic diffusion equation for uniform magnetic diffusivity, which reads

$$\left(\frac{\partial}{\partial t} - \eta\nabla^2\right)\mathbf{B} = \mathbf{0}, \tag{3.2}$$

where $t$ is time, and $\mathbf{B}$ denotes the core field. Because the field is solenoidal, it may be partitioned into its toroidal and poloidal parts:

$$\mathbf{B} = \mathbf{B}_T + \mathbf{B}_S = \nabla \times (T\mathbf{r}) + \nabla \times \nabla \times (S\mathbf{r}), \tag{3.3}$$

with $\mathbf{B}_T$ and $\mathbf{B}_S$ the toroidal and poloidal field respectively, and $T$ and $S$ their respective defining potentials. Applying this decomposition simplifies the diffusion problem to the scalar equations

$$\left(\frac{\partial}{\partial t} - \eta\nabla^2\right)T = \left(\frac{\partial}{\partial t} - \eta\nabla^2\right)S = 0. \tag{3.4}$$

Both of these equations may be solved to obtain a diffusive description for all vector components of the field. However, the toroidal field inside the core is unobservable (the field outside the core is purely poloidal) and we therefore restrict attention to the poloidal diffusion problem by setting $T = 0$. The scalar $S$ is then expanded in real-valued Schmidt quasi-normalised spherical harmonics $Y_\alpha(\theta, \phi)$ ($\theta$ and $\phi$ denote colatitude and longitude, respectively), the index

$\alpha$ corresponding to the harmonic of degree $1 \leq l_\alpha \leq L$ for some $L$, and order $0 \leq m_\alpha \leq l_\alpha$, which has either azimuthal sine or cosine dependence. This representation then requires

$$\left(\frac{\partial}{\partial t} - \eta D_{l_\alpha}^2\right) r s_\alpha(r,t) = 0, \tag{3.5}$$

with $r$ radius, $s_\alpha$ the spherical harmonic coefficients of $S$, and where we have defined the operator

$$D_{l_\alpha}^2 f(r) = \left(\frac{\partial^2}{\partial r^2} - \frac{l_\alpha(l_\alpha+1)}{r^2}\right) f(r). \tag{3.6}$$

This equation has the solution

$$\begin{aligned} s_\alpha(r,t) &= \sum_{n=1}^{N} q_\alpha^n d_{l_\alpha}^n(r,t), \\ &= \sum_{n=1}^{N} q_\alpha^n j_{l_\alpha}\left(\frac{k_{l_\alpha}^n r}{c}\right) \exp\left[-\eta\left(\frac{k_{l_\alpha}^n}{c}\right)^2 (t-t_0)\right], \end{aligned} \tag{3.7}$$

where $d_{l_\alpha}^n(r,t)$ denotes the $n^{\text{th}}$ decay mode of degree $l_\alpha$, the $q_\alpha^n$ a set of constants, $j_{l_\alpha}(z)$ the spherical Bessel function of the first kind, $k_{l_\alpha}^n$ the $n^{\text{th}}$ root of $j_{l_\alpha+1}(z)$, and $c$ the core radius. The initial state is given by the expression evaluated at the initial time $t_0$. The decay modes form an orthonormal set in terms of an all-space energy norm (*Backus*, 1958). This solution allows us to express the radial field $B_r$ up to degree $L$ satisfying the diffusion equation as:

$$\begin{aligned} B_r(\mathbf{r},t) &= \frac{1}{r}\sum_{\alpha=1}^{L(L+2)} l_\alpha(l_\alpha+1) s_\alpha(r,t) Y_\alpha(\theta,\phi), \\ &= \frac{1}{r}\sum_{\alpha=1}^{L(L+2)}\sum_{n=1}^{N} q_\alpha^n l_\alpha(l_\alpha+1) j_{l_\alpha}\left(\frac{k_{l_\alpha}^n r}{c}\right) \\ &\qquad \times \exp\left[-\eta\left(\frac{k_{l_\alpha}^n}{c}\right)^2 (t-t_0)\right] Y_\alpha(\theta,\phi). \end{aligned} \tag{3.8}$$

Using this decay mode expansion, we may already describe our following inverse approach qualitatively. Consider for example Fig. 3.2, showing the time dependence of the first five modes for $l_\alpha = 1$ (a) and $l_\alpha = 14$ (b), where their initial amplitude has been normalised to unity. It can readily be seen that all individual modes decay monotonically with time, and that their respective rate of decay increases with $l_\alpha$ and $n$. However, a linear combination of modes need not always decay, as is the case for the difference $d_{l_\alpha}^3 - d_{l_\alpha}^5$ (solid black curve), which exhibits transient growth (e.g. *Livermore and Jackson*, 2006). Although the modes are formally

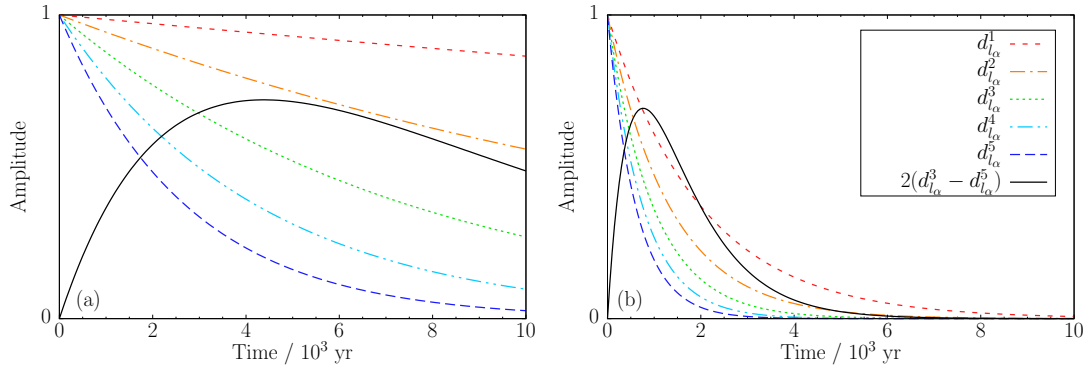


**Figure 3.2:** Time dependence of the first five decay modes $d^n_{l_\alpha}$ for (a) $l_\alpha = 1$ and (b) $l_\alpha = 14$, normalised to have initial positive unit amplitude. While a single mode always decays monotonically, a linear combination of these functions may exhibit transient strengthening (solid curve).

orthogonal in a global sense, they are not orthogonal when evaluated at a single value of $r = c$ and thus transient effects can readily occur. In the same way, there may exist a combination of modes that describes an initial field configuration whose evolution matches the observed SV (which shows in general both transient decay and growth) over some time window.

We also use the decay modes a priori to estimate the sensitivity of the CMB field evolution to magnetic diffusion within different regions of the core. It may be expected that the core is not sampled uniformly; we consider diffusion only over time intervals of decades to centuries, and bearing in mind the slow 16 kyr timescale of global modes, the diffusive evolution of deep magnetic structures may not have a signature in CMB SV within such time intervals. In Appendix A.1, we show that for pure diffusion the CMB field evolution can only constrain the magnetic structure within a region close to the CMB. This layer spans approximately the top 80 km when one decade of diffusion is considered (Fig. A.2a); for 175 years, which matches the full COV-OBS.x1 time window, this region extends to roughly the upper 400 km (Fig. A.2b). Therefore, even though we shall seek an optimal full-sphere magnetic structure, structures below the sensitivity depth should not be interpreted geophysically.

### 3.2.2 A Galerkin discretisation

While the decay modes solve the magnetic diffusion equation exactly, the series in Eq. (3.8) is characterised by slow (algebraic) convergence in $N$ (e.g. *Boyd*, 2000), associated with poor numerical conditioning of the inverse problem. In the following, as an expedient alternative, we solve the radial diffusion problem (Eq. 3.5) with a Galerkin polynomial basis set in radius, yielding faster (spectral) convergence and much better conditioning. To do so, we approximate

$$rs_\alpha(r,t) = \sum_{n=1}^{N} \xi^n_\alpha(r)\varphi^n_\alpha(t)q^n_\alpha, \tag{3.9}$$

with $\varphi_\alpha^n(0) = 1$. We choose the radially dependent basis functions to be built from weighted Jacobi polynomials (*Livermore*, 2010) of the form

$$\xi_\alpha^n(r) = A_\alpha^n \psi_\alpha^n(r/c), \tag{3.10}$$

where $A_\alpha^n$ is a normalisation constant and

$$\psi_\alpha^n(r) = r^{l_\alpha+1}\left[n(2l+2n-1)P_n^{(0,l_\alpha+1/2)}(2r^2-1) - (n+1)(2l+2n+1)P_{n-1}^{(0,l_\alpha+1/2)}(2r^2-1)\right], \tag{3.11}$$

with $P_n^{(\alpha,\beta)}(z)$ a Jacobi polynomial. The poloidal vector modes $\mathbf{B}_\alpha^n = \nabla\times\nabla\times(\xi_\alpha^n Y_\alpha \hat{\mathbf{r}})$ have the property of orthogonality over all space (*Chen et al.*, 2018, *Li et al.*, 2018), through the integral (see also Appendix A.4)

$$\begin{aligned}\int_{\mathbb{R}^3} \mathbf{B}_\alpha^n \cdot \mathbf{B}_\beta^p \,\mathrm{d}V &= \frac{4\pi l_\alpha(l_\alpha+1)}{2l_\alpha+1} \qquad (3.12)\\ &\quad\times\left[\int_0^c \left(\frac{\partial \xi_\alpha^n}{\partial r}\right)\left(\frac{\partial \xi_\beta^p}{\partial r}\right) + \frac{l_\alpha(l_\alpha+1)}{r^2}\xi_\alpha^n\xi_\beta^p\,\mathrm{d}r + \frac{l_\alpha}{c}\xi_\alpha^n(c)\xi_\beta^p(c)\right],\\ &:= \langle \xi_\alpha^n, \xi_\beta^p\rangle_{l_\alpha}, \qquad (3.13)\end{aligned}$$

which may be used to find the constant $A_\alpha^n$. Such orthogonality is identical to that satisfied by the decay modes, but the Galerkin modes are much better numerically conditioned as they show asymptotic spectral convergence. The radial dependence of these functions is visualised in Fig. 3.3, which are not only regular at the origin, but also obey the matching conditions appropriate to an external potential field.

Through substitution of the approximation (Eq. 3.9) in the radial diffusion equation (Eq. 3.5), and by projecting the result on $\xi_\alpha^j(r)$ using Eq. (3.13), we obtain the system of equations:

$$\frac{\partial}{\partial t}\boldsymbol{\varphi}_\alpha = \eta \mathbf{H}_\alpha \boldsymbol{\varphi}_\alpha, \tag{3.14}$$

where $\boldsymbol{\varphi}_\alpha := (\varphi_\alpha^1, \varphi_\alpha^2, \ldots, \varphi_\alpha^N)^T$ is the time-dependent solution for a given $\alpha$ and $H_{\alpha,ij} := \langle D_{l_\alpha}^2[\xi_\alpha^i], \xi_\alpha^j\rangle_{l_\alpha}$. The total solution, exact within the truncation specified, can be written

$$rs_\alpha(r,t) = \boldsymbol{\xi}_\alpha^T(r)\mathrm{expm}\left[\eta\mathbf{H}_\alpha(t-t_0)\right]\mathbf{q}_\alpha, \tag{3.15}$$

where expm$[\cdot]$ denotes the matrix exponential. When $t = t_0$, the given matrix exponential is the identity matrix, in which case one recovers the initial magnetic structure. Note also that for the particular case of using the decay modes in place of the Galerkin polynomials, the matrix $\mathbf{H}_\alpha$ and so $\mathrm{expm}[\mathbf{H}_\alpha]$ are diagonal, and so the above representation is equivalent to the solution given in Eq. (3.7).

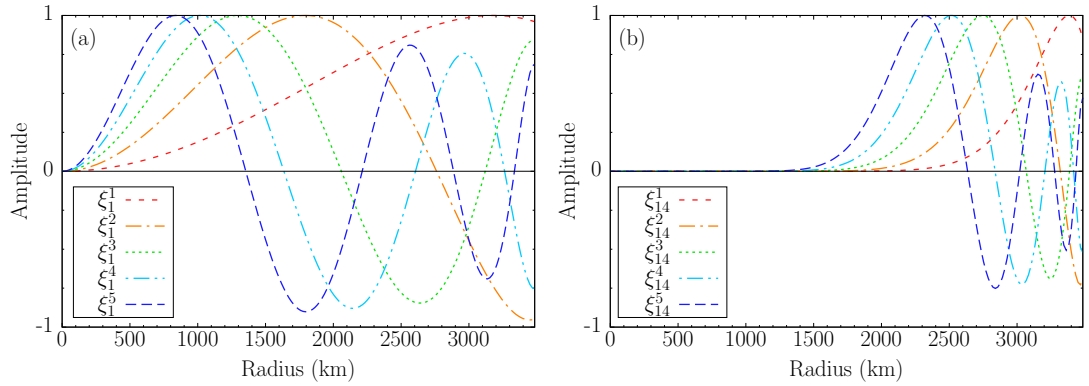


**Figure 3.3:** The Jacobi polynomials $\xi_{l_\alpha}^n$ as a function of radius, for $l_\alpha = 1$ (a) and $l_\alpha = 14$ (b), here normalised such that their extremum is of positive unit amplitude.

### 3.2.3 Unregularized inverse strategy

#### A least-squares variational analysis

With this discretisation of the diffusive forward problem, we are now in a position to define the variational scheme. Accordingly, we consider the objective function

$$R_{\text{unreg}} = \int_T \int_{\text{CMB}} \left( B_r^{\text{obs}}(t) - \hat{B}_r(t) \right)^2 \, \mathrm{d}S \, \mathrm{d}t, \tag{3.16}$$

where the time period is $T = [t_0, t_e]$, $B_r^{\text{obs}}$ is the radial field prescribed by a time-dependent geomagnetic field model, and $\hat{B}_r(t)$ denotes the radial component of our modelled field. We seek an initial structure of the magnetic field that minimises $R_{\text{unreg}}$.

Discretising the temporal integrals, and expressing $R_{\text{unreg}}$ in terms of the model coefficients gives the reduced form

$$R_{\text{unreg}} = (\mathbf{g} - \mathbf{D}\hat{\mathbf{q}})^T \mathbf{W} (\mathbf{g} - \mathbf{D}\hat{\mathbf{q}}), \tag{3.17}$$

with $\mathbf{g}$ and $\hat{\mathbf{q}}$ vectors containing all Gauss coefficients (which are known) evaluated at a set of time points and all model coefficients (which are to be found) respectively, the matrix $\mathbf{D}$ a blockwise-diagonal (one block per spherical harmonic mode) forward mapping describing purely diffusive SV, and $\mathbf{W}$ a diagonal weighting matrix related to the scheme of numerical time integration. Adopting decay modes in place of Galerkin polynomials results in a comparable form but with different $\mathbf{D}$. For the derivation and exact definition of these quantities, the reader is referred to Appendix A.2. Key here is the fact that the objective function depends only quadratically on $\hat{\mathbf{q}}$, in contrast to much more complex schemes that include nonlinear feedback from the core flow (e.g. *Li et al.*, 2014). Taking variations to find the minimum of $R_{\text{unreg}}$, with respect to $\hat{\mathbf{q}}$, then directly gives the optimal set of coefficients

$$\hat{\mathbf{q}} = (\mathbf{D}^T \mathbf{W} \mathbf{D})^{-1} \mathbf{D}^T \mathbf{W} \mathbf{g}. \tag{3.18}$$

In this paper we will consider only using this variational technique with the geomagnetic field model given by the mean of the COV-OBS.x1 ensemble (*Gillet et al.*, 2015b). This model of spherical harmonic degree $L = 14$ spans 175 years (1840.0-2015.0) that is sufficient to cover our range of time window lengths, and extends (almost) to the present day using modern satellite data.

It is worthwhile briefly considering our inversion scheme in the landscape of other mathematical inverse problems associated with diffusion. A well known example is the backwards heat conduction problem (e.g. *Miranker*, 1961) in which complete knowledge of a temperature profile is assumed at some final time $t = t_e$, and the task is to find the initial temperature profile at $t = t_0$ that evolves through heat diffusion (conduction) to match the final state; such a problem is in general tractable but ill-posed. The problem that we consider here is quite different: as described above, the structure of the evolving magnetic field is known only at $r = c$ (rather than everywhere), but for all times in $[t_0, t_e]$ (rather than at a single time). We have therefore traded complete information of structure at a single time, for partial structural information at all times. A solution of the backwards conduction problem requires two boundary conditions, as it is a second order equation like the magnetic diffusion equation. In our case we also supply two sets of information at the boundary. Firstly we constrain the poloidal scalar through matching to the field model. Secondly, we constrain the radial derivative of the poloidal scalar by virtue of the matching condition associated with the electrically insulating mantle at $r = c$. Our problem is therefore fully specified and optimal solutions exist, although we may not be able to fit the data exactly ($R_{\mathrm{unreg}} > 0$, see e.g. Appendix A.3).

**Matrix conditioning and choice of radial basis functions**

In order for our inverse approach to be viable, it is necessary that the solution of Eq. (3.18) is numerically realisable. Of particular concern is whether the numerical inverse of the weighted Gramian matrix $\mathbf{D}^T\mathbf{W}\mathbf{D}$ is computationally tractable, which can be quantified by its two-norm condition number

$$\kappa(\mathbf{A}) = ||\mathbf{A}||_2||\mathbf{A}^{-1}||_2 = \frac{\sigma_{\max}}{\sigma_{\min}}, \tag{3.19}$$

where $\mathbf{A}$ is any matrix, $||\cdot||_2$ denotes the $L_2$ matrix norm, and $\sigma_{\min/\max}$ are the smallest and largest singular value of $\mathbf{A}$ respectively. One can derive for any linear system $\mathbf{A}\mathbf{x} = \mathbf{b}$ that

$$\frac{||\delta\mathbf{x}||}{||\mathbf{x}||} \leq \kappa(\mathbf{A})\frac{||\delta\mathbf{b}||}{||\mathbf{b}||}. \tag{3.20}$$

where $\delta\mathbf{x}$ and $\delta\mathbf{b}$ are respectively some perturbation in $\mathbf{x}$ and $\mathbf{b}$. In other words, the relative change in $\mathbf{x}$ (in our case the model vector $\mathbf{q}$ representing the initial magnetic field structure), is bounded by the relative change in the vector $\mathbf{b}$ (in our case the vector $\mathbf{g}$ containing all Gauss coefficients) multiplied with the condition number. A large condition number therefore signifies an ill-posed problem associated with non-uniqueness of the solution.

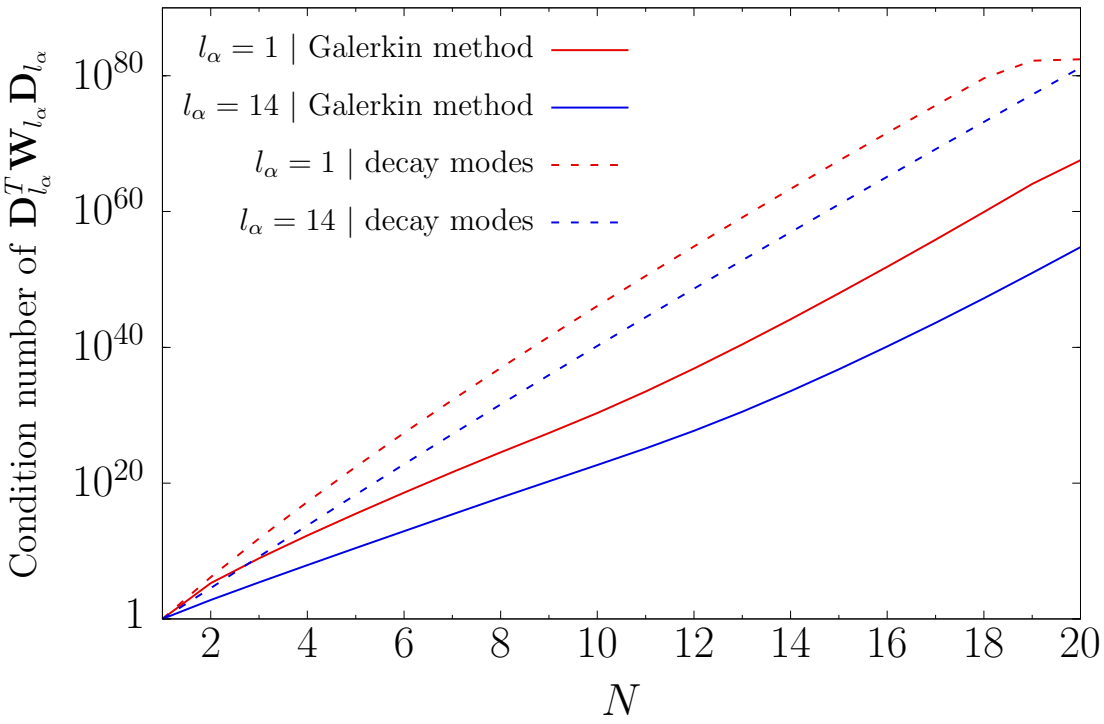


**Figure 3.4:** The condition number of the weighted Gramian block matrices, for $l_\alpha = 1$ (red) and $l_\alpha = 14$ (blue), as a function of $N$, the number of basis functions used, and using either decay modes (dashed) or the Galerkin polynomials (solid).

Moreover, as an approximate rule of thumb, if our matrix $\mathbf{D}^T\mathbf{W}\mathbf{D}$ (which is to be inverted in eq. 3.18) has a condition number $10^a$, the number of inaccurate trailing digits of $\hat{\mathbf{q}}$ is $a$ when the solution is expressed numerically with floating-point representation (e.g. *Cheney and Kincaid*, 2008). Thus in standard double-precision (about 16 digits), with a condition number of $10^{12}$, $\hat{\mathbf{q}}$ can be expected correct to about 4 significant figures; matrices with condition numbers in excess of $10^{16}$ or so cannot be inverted in double precision.

Fig. 3.4 shows the condition numbers (measured in the standard 2-norm) for the diagonal blocks of $\mathbf{D}$ associated with $l_\alpha = 1$ and $l_\alpha = 14$, representing the extreme cases, as a function of the number of basis functions (either polynomial or decay modes). Here, we used 201 time points (this ensures a numerically converged solution, see Appendix A.3), and sextuple (256-digit) precision in place of the more commonly used double (16-digit) precision to ensure that all calculations shown were accurate.

The condition numbers, many of which are far in excess of $10^{16}$, highlight the ill-posedness of the inverse problem. Physically, this may be understood by the difficulty of constraining the magnitude of initially fine scales because they diffuse very rapidly: this is a problem for both the decay mode and Jacobi polynomial representations. In practice, the large condition numbers mean that in double precision the radial resolution available for this method is extremely limited.

However, there are two ways in which we can mitigate these effects. First, it should be noted that the Galerkin scheme has a much lower condition number than the decay modes for

fixed $N$, an effect particularly noticeable for block matrices of high spherical harmonic degree. This means that for any given condition number threshold the Galerkin method allows more radial modes and therefore increased resolution. The better conditioning achieved with the Galerkin method therefore motivates us to apply it to our inverse approach. Second, we can use very high precision in our calculations (we have used up to 256 digits using the symbolic toolbox for Matlab), making possible a resolution of 30 radial polynomial modes (with typical condition numbers of $10^{95}$ and $10^{70}$ for the decay modes and Galerkin polynomials, respectively). However, as will be pointed out in the next section, we will end up adopting a means of regularising the solution, thereby ameliorating the ill-conditioning of the diffusive inverse problem without the need of such high-precision variables.

### 3.2.4 Regularised inverse strategy

#### A penalised variational approach

Minimising an objective function of the form of $R_{\text{unreg}}$ (Eq. 3.16) ensures an optimal fit to SV without consideration of the spatial complexity of the initial optimal magnetic field. It may therefore be unsurprising that the initial ($t = t_0$) magnetic structures can show large spatial fluctuations in amplitude. For example, if we consider the optimisation over the time window 2005.0-2015.0, and the associated initial field over the upper 80 km of the core (its sensitivity depth: the field below this depth is likely poorly resolved, see Appendix A.1), we find a root-mean-square (RMS) average $|\mathbf{B}|$ of about $10^{25}$ mT. Similarly, for the period 1840.0-2015.0, the optimal model has an RMS field strength in excess of $10^{29}$ mT over its sensitivity depth of 400 km. Such huge amplitudes cannot be reconciled with the RMS field strength for the core, which has been estimated at 2.5 to 4 mT (*Gillet et al.*, 2010, *Buffett*, 2010). It is likely that the ill-posedness of the unregularised inverse diffusion problem leads to these extreme solutions, and possibly the rule of thumb which specifies the number of accurate floating-point digits mentioned in the previous section does not hold for the large condition numbers computed here.

Therefore, we consider also the minimisation of an associated regularised objective function

$$R_{\text{reg}} = \int_T \int_{\text{CMB}} (B_r^{\text{obs}} - \hat{B}_r)^2 \, \mathrm{d}S \, \mathrm{d}t + \lambda \int_{\mathbb{R}^3} \hat{\mathbf{B}}_0^2 \, \mathrm{d}V, \tag{3.21}$$

where the second term corresponds to penalising the energy of the initial magnetic field $\hat{\mathbf{B}}_0$ over all space, scaled with a damping parameter $\lambda$. Note that for purely diffusive SV the total magnetic energy monotonically decays with time (e.g. *Gubbins and Roberts*, 1987) and this regularisation term will therefore penalise magnetic energy over the entire time period. Nevertheless, this constraint still permits any local exchange of magnetic energy, such as the overall energetic growth at the CMB observed for the $20^{\text{th}}$ century (*Huguet et al.*, 2018). The choice of this regularisation differs from that adopted elsewhere, e.g. the dissipation norm

of *Gubbins and Bloxham* (1985), and is motivated by the fact that it directly penalises our modelled RMS field amplitudes, therefore reconciling these with the estimates by *Gillet et al.* (2010), *Buffett* (2010). In addition, it is easily expressed in terms of our model coefficients by the very simple structure (see Appendix A.4 for a derivation):

$$\int_{\mathbb{R}^3} \hat{\mathbf{B}}_0^2 = \hat{\mathbf{q}}^T \hat{\mathbf{q}}. \tag{3.22}$$

The discretised regularised objective function is then

$$R_{\text{reg}} = (\mathbf{g} - \mathbf{D}\hat{\mathbf{q}})^T \mathbf{W} (\mathbf{g} - \mathbf{D}\hat{\mathbf{q}}) + \lambda \hat{\mathbf{q}}^T \hat{\mathbf{q}}, \tag{3.23}$$

whose minimum with respect to $\hat{\mathbf{q}}$ then yields

$$\hat{\mathbf{q}} = (\mathbf{D}^T \mathbf{W} \mathbf{D} + \lambda \mathbf{I}_{NL(L+2)})^{-1} \mathbf{D}^T \mathbf{W} \mathbf{g}, \tag{3.24}$$

where $\mathbf{I}_p$ is the $p \times p$ identity matrix, with $p = NL(L+2)$.

### Choosing the damping parameter

The solutions (Eq. 3.24) parametrise a one-dimensional family of solutions that minimise the associated objective function $R_{\text{reg}}$. We now address which solution we should choose. Ultimately, we are interested only in the solution that best describes secular variation with realistic amplitudes in the modelled core magnetic structure. In the following we shall find values for this parameter we consider optimal, based on how $\lambda$ affects the trade-off between the residual and the regularisation term.

Figure 3.5 shows a tradeoff curve for $\lambda$, showing the RMS residual in $B_r$ (i.e. the square root of $R_{\text{unreg}}$ (Eq. 3.16) averaged over the CMB and $T$) as a function of the associated initial magnetic energy (defined over all space) for various time windows, where every datum represents a choice of $\lambda$. These models have been calculated using double (16-digit) precision, 30 basis functions, and 201 time points (these values ensure a numerically converged solution, see Appendix A.3). We note that for the data plotted, the regularisation term ensures that double-precision is sufficient: clearly as $\lambda \to 0$ (and in fact for values of the energy in excess of roughly $10^{32}$ J) we recover approximately the unregularised problem for which much higher precision is needed. For all time windows, there appears to exist a regime in which the solutions do not contain enough energy to allow an adequate fit to the observations, typically when the energy is below $10^{27}$ J. Decreasing $\lambda$, and so increasing the energy beyond this point to roughly $10^{29}$ J, yields a significant reduction in the residual. This is particularly noticeable for short time windows; allowing increased energy in the longer time windows results in a relatively low improvement in the residual.

For all time windows, we consider $\lambda$ optimal if it is on the "knee" of the trade-off curve, after the initially rapid decline of the residual (diamonds in Fig. 3.5). This knee is difficult to define quantitatively for time windows spanning several decades, therefore all preferred values

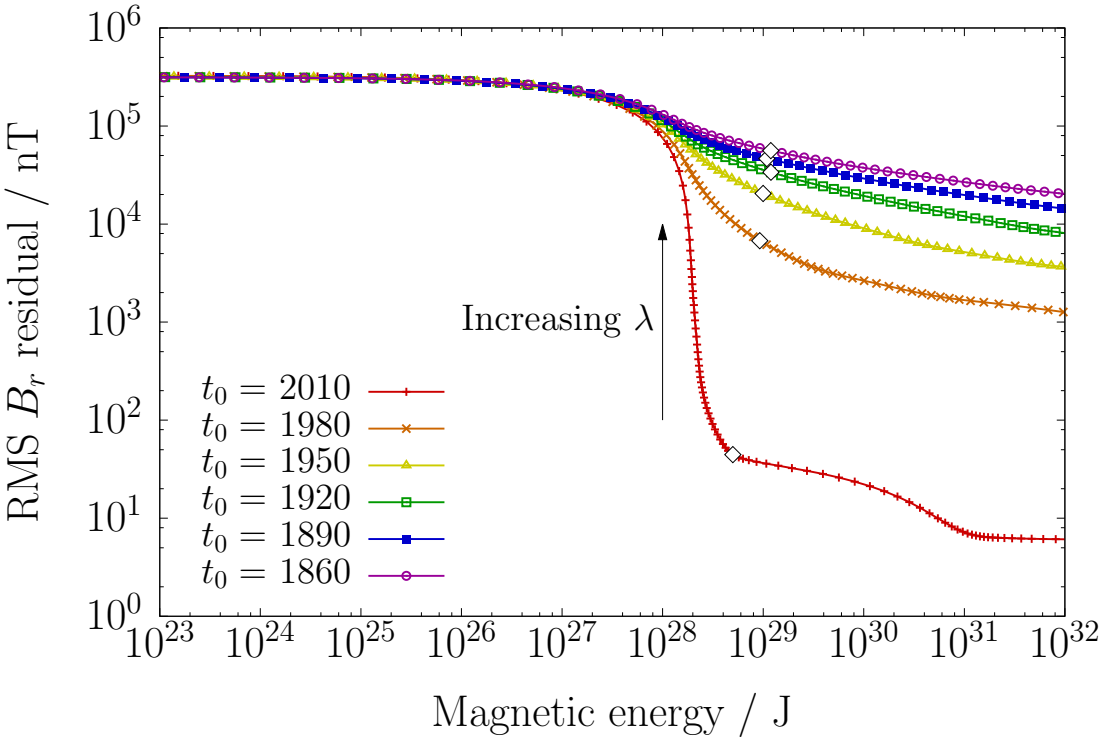


**Figure 3.5:** The RMS residual of $B_r$ as a function of the initial magnetic energy of the solution, for several time windows (from $t_0$ to 2015.0). Every datum represents a choice for the damping parameter $\lambda$. Diamonds indicate our preferred trade-off between the residual and regularisation term.

for $\lambda$ have been picked by eye, which range between $10^{-18}$ and $10^{-3}$ (supplementary data file 1 lists these values). Lastly, we note that all our preferred models have a full-core RMS field strength between 0.6 and 1.3 mT, and are therefore consistent with the 2.5 or 4 mT estimates provided by *Gillet et al.* (2010) and *Buffett* (2010).

## 3.3 Optimised purely diffusive models

### 3.3.1 Regularised models

Here we present a set of purely diffusive models, comprising regularised inversions for an initial magnetic structure whose subsequent evolution is described by the mean COV-OBS.x1 model. These solutions have been obtained for varying time windows terminating at 2015.0, and have been computed with 30 basis functions, 201 time points (ensuring a numerically converged solution, Appendix A.3), and optimal $\lambda$ values which have been selected using the criteria presented in section 3.2.4. For these models, we show a number of results. First, we compare time series of selected Gauss coefficients over a single time window. Secondly, we present $B_r$ residual error spectra for several time windows. We also demonstrate how the total residual changes as a function of the window length. Finally, we map $B_r$ and $\dot{B}_r$ residuals at the CMB and at selected epochs.

Figure 3.6 shows time series of the Gauss coefficients $g_1^0$, $g_8^0$, and $g_{14}^0$, for the period 1990.0-

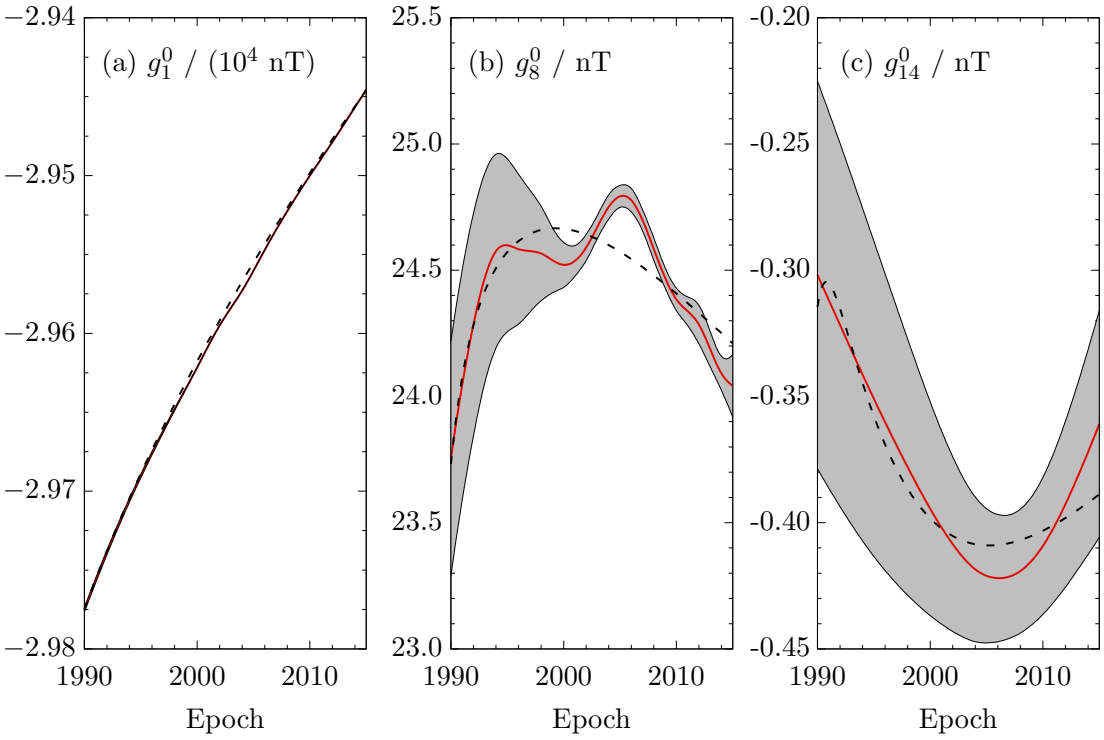


**Figure 3.6:** Comparison between time series of selected Gauss coefficients from the regularised diffusion model for 1990.0-2015.0 (black dashed), and the mean COV-OBS.x1 model (solid red). Gray shaded areas represent the mean COV-OBS.x1 model ± one standard deviation.

2015.0, from the COV-OBS.x1 mean (solid red) and diffusive model (dashed black). Gray shaded areas correspond to the time-dependent one standard deviation error bounds. Despite the correct qualitative behaviour of the diffusive model, only the high-degree coefficients are fit within the COV-OBS.x1 uncertainty. For instance, while the regularised diffusion model captures the overall decay of $g_1^0$, the diffusive time series is generally outside the COV-OBS.x1 error budget. Conversely, the regularised fit to $g_{14}^0$ is well within the COV-OBS.x1 error budget at all times. This effect is in part driven by the relative increase in the COV-OBS.x1 error budget with degree: for degree 1 the relative uncertainty is small, typically $< 0.1\%$ for this period, whereas for degree 14 it may be as large as 25%. Nevertheless, the diffusive fits to $g_1^0$ and $g_8^0$ also lack the short-term variability required to fit COV-OBS.x1 within the uncertainty at all times.

That diffusion captures higher degree features of the field more easily is quantified with spherical harmonic error spectra (Fig. 3.7), which have been computed for various time windows using

$$E(l_\alpha) = \frac{(l_\alpha+1)^2}{2l_\alpha+1}\left(\frac{a}{c}\right)^{2l_\alpha+4} \sum_{m_\alpha=0}^{l_\alpha} \frac{1}{T}\int_T \left(g_\alpha(t) - \hat{g}_\alpha(t)\right)^2 \mathrm{d}t. \tag{3.25}$$

This spectrum relates to the residual in Eq. (3.16): the sum of $E(l_\alpha)$ over $l_\alpha$ is the mean squared error in $B_r$ averaged over $T$ and the CMB. Shown as solid curves Fig. 3.7 are also the

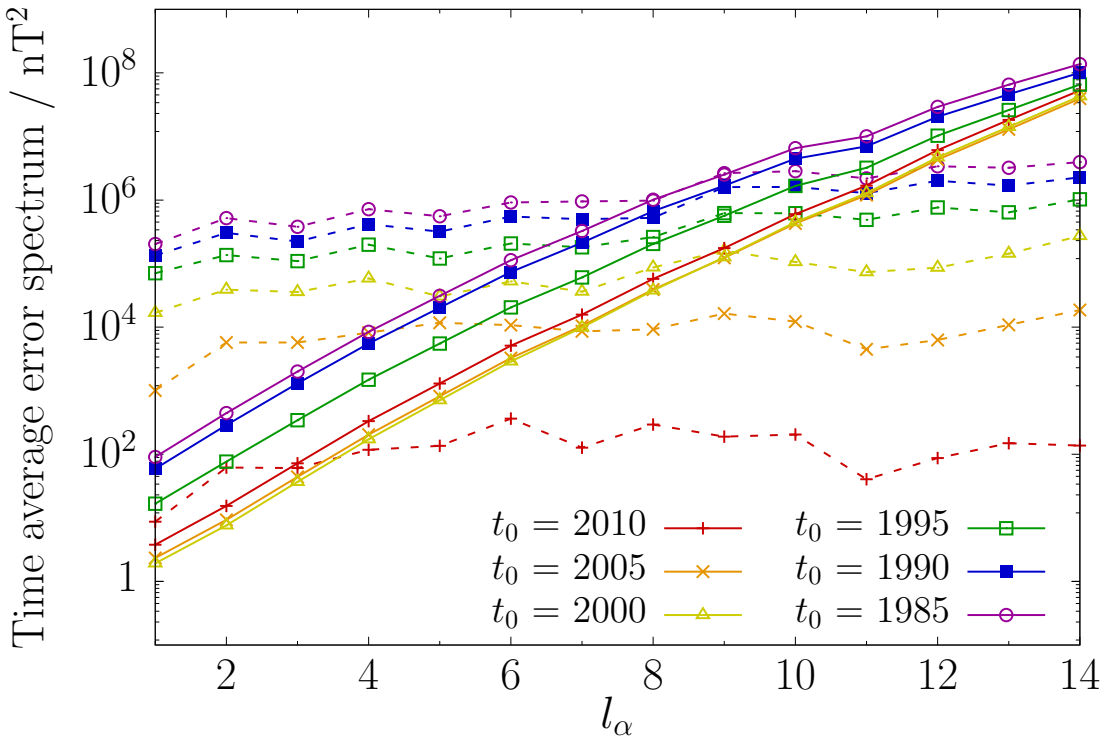


**Figure 3.7:** Time-averaged spectra of the residual $B_r$ at the CMB for the regularised diffusion models (dashed), and the time-dependent standard deviation of COV-OBS.x1 (solid). Line colours and symbols represent different time windows spanning from $t_0$ to 2015.0.

COV-OBS.x1 uncertainty spectra, computed with Eq. (3.25) and with the integrand taken to be the variance; the total mean squared uncertainty is then the sum of the uncertainty spectrum. Readily noticeable is the contrast of rather flat diffusion error spectra, and the COV-OBS.x1 uncertainty spectra increasing monotonically with $l_\alpha$, demonstrating that high degree features are more likely to be fit within the uncertainty. Also, for all degrees, the average error increases when a longer time window is considered, therefore for longer periods only relatively high degree features are captured well: for 2010.0-2015.0 degrees 3 to 14 are within the uncertainty bounds; for 1985.0-2015.0 only degrees 10 to 14 are within these bounds.

While for most degrees the regularised 1985.0-2015.0 error spectrum is orders of magnitude larger than the COV-OBS.x1 uncertainty, the total residual is actually smaller than the total uncertainty based on a single standard deviation. We confirm this by showing for the complete set of diffusion models the time-averaged RMS residual as a function of time window length, together with this uncertainty (Fig. 3.8). It then becomes evident that with our regularised diffusion models, we may fit SV over 102 years, without producing a time-averaged residual greater than the COV-OBS.x1 error budget based on one standard deviation. Additionally, we find 30 years to be the longest time window for which regularised diffusion fits SV while the total residual is smaller than the total uncertainty at all points in time. Nevertheless, it is of note that if we consider the 1913.0-2015.0 (102 year) diffusive model and compute the associated time-averaged residual over a shorter period (here taken as 1990.0-2015.0), we find it

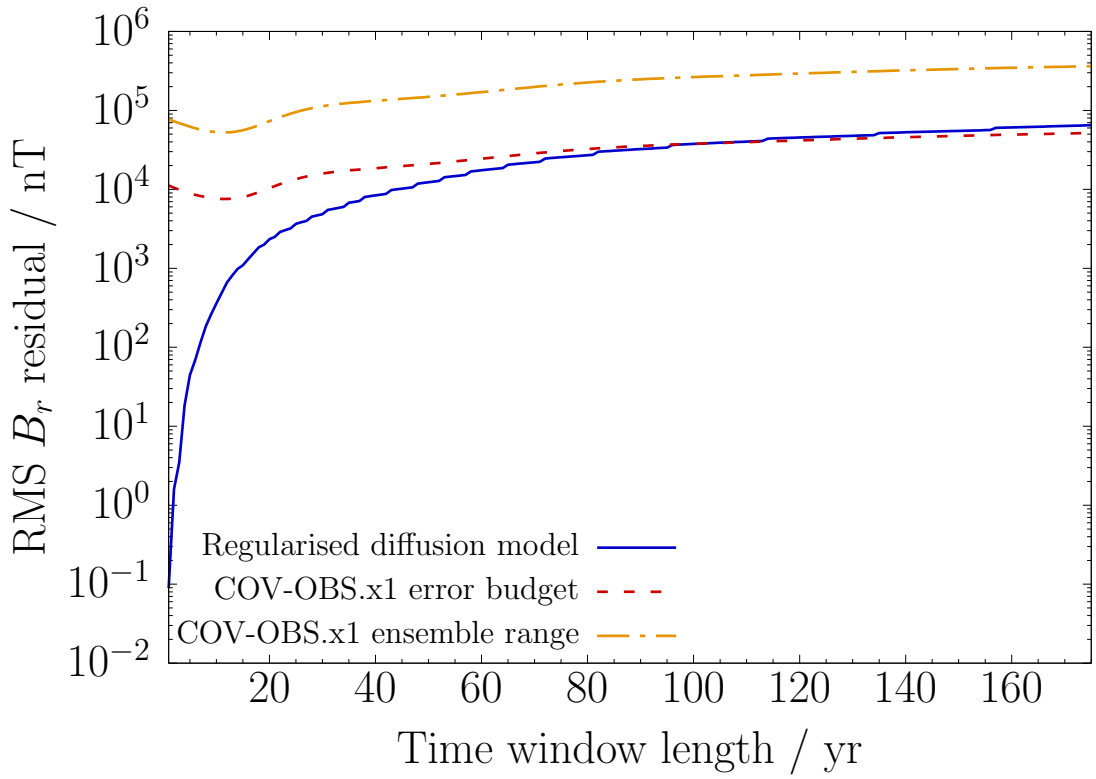


**Figure 3.8:** The time average of the RMS $B_r$ residual over the CMB as a function of time window length, for the regularised diffusion models (solid blue). Also shown are two time-average global uncertainties for COV-OBS.x1, one computed with one standard deviation among Gauss coefficients (dashed red), and the other from maximum differences between the 100 published ensemble members and the ensemble mean (dot-dashed yellow).

amounts to $4.78 \cdot 10^4$ nT - now roughly 2.5 times as large as the total COV-OBS.x1 uncertainty for the 1990.0-2015.0 period. A similar procedure but with these residuals evaluated at the Earth's surface yields an average of 810.5 nT for the full period; when averaged over the 1990.0-2015.0 period with the use of the same model, this residual equals approximately 1162 nT. These differences are indicative of an overall temporal growth of the residual, which we find for almost any choice of $T$. Shown in Fig. 3.8 is also a more generous global uncertainty measure computed using Eq. (3.25) based on the maximum difference between the 100 published COV-OBS.x1 ensemble members and the ensemble mean. It can readily be seen that the regularised diffusion models fit COV-OBS.x1 within this uncertainty bound over the full 1840.0-2015.0 period.

As the total error and its associated spectrum describe how well diffusion fits only in an average sense, we illustrate also how the residual varies spatio-temporarily. In Fig. 3.9 the radial field is shown at the CMB and at selected epochs, as prescribed by COV-OBS.x1 and the regularised 1990.0-2015.0 model (a,d,g and b,e,h respectively; see also supplementary animation 1). Also shown at these epochs is the corresponding unsigned difference between these two models (Fig. 3.9c, f, and i; see also supplementary animation 2). We find good global agreement between the models through visual comparison; this is also reflected by the associated

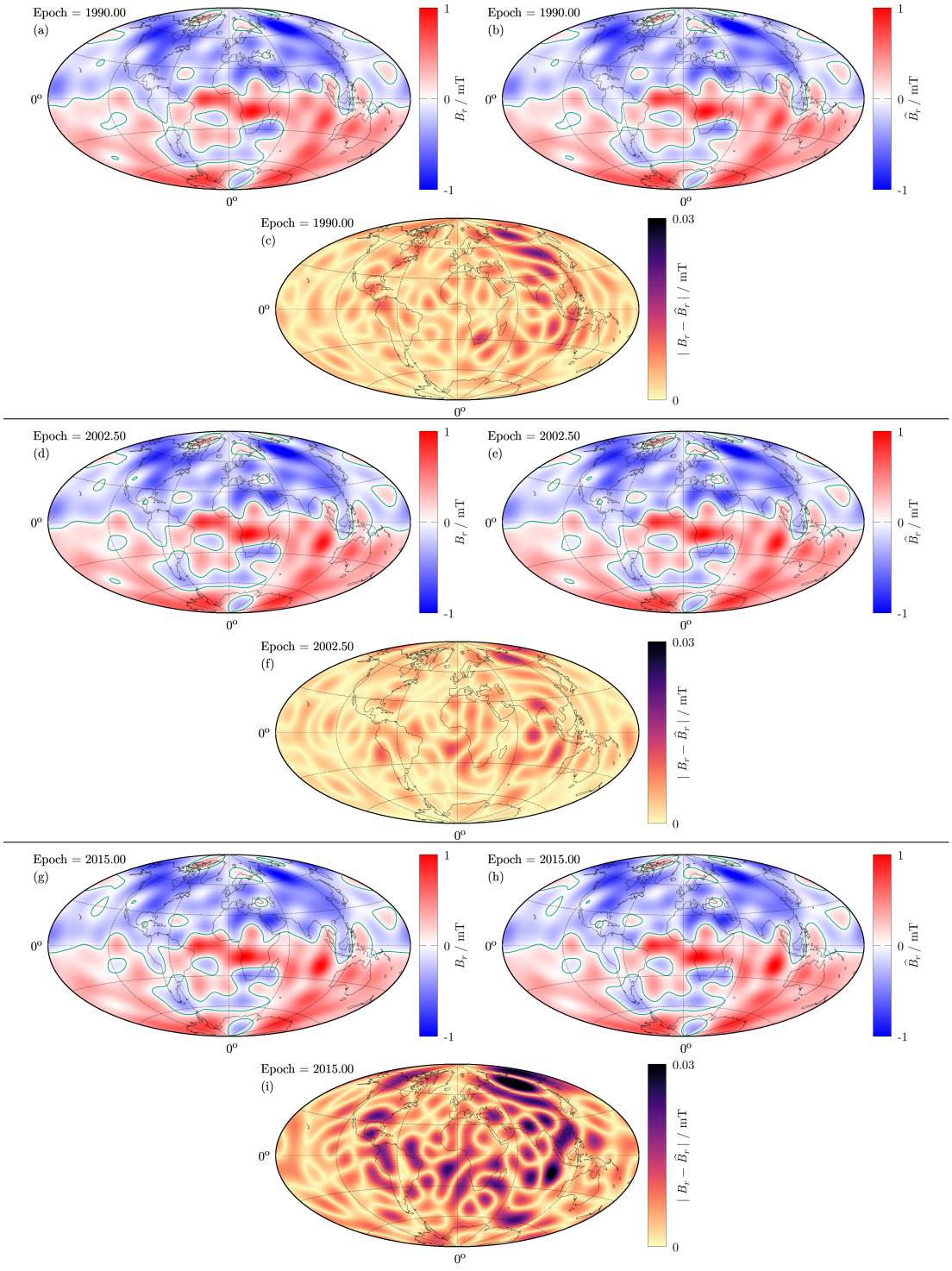


**Figure 3.9:** The radial field at the CMB and at selected epochs, as described by COV-OBS.x1 (a,d,g) and the regularised 1990.0-2015.0 diffusion model (b,e,h); figures c, f, and i show the corresponding unsigned difference between the two models. Null-flux curves are represented in green.

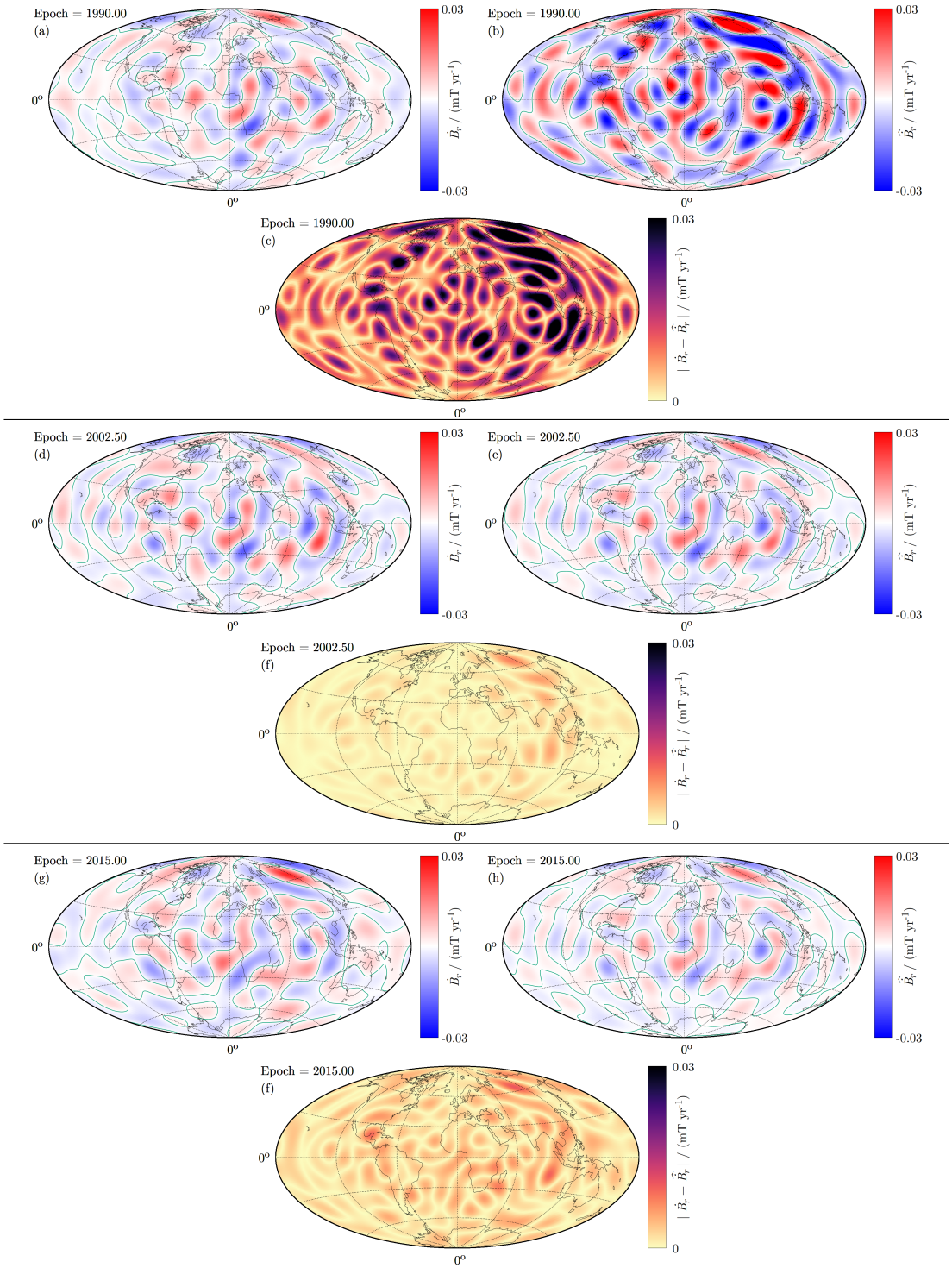


**Figure 3.10:** As Fig. 3.9, but for the time derivative of the radial field.

error amplitudes, which are low compared to the radial field itself. Still, we observe an overall growth of the unsigned residuals with time, these errors being the largest towards the end of the period. Spatially, the residuals describe a pattern where the largest amplitudes reside in the Indo-Atlantic Hemisphere, in particular under Siberia, and the Pacific generally accommodating lower amplitudes. These high error amplitudes beneath the southern Indian Ocean and Asia correlate with regions for which significant secular acceleration has been reported (*Olsen and Mandea*, 2008). As such, Fig. 3.9 demonstrates that it is more difficult for the diffusion model to replicate COV-OBS.x1 where it locally describes relatively fast field change.

We confirm this statement by investigating the fit of SV on the CMB. Figure 3.10 shows $\dot{B}_r$ on the CMB and at selected epochs for COV-OBS.x1 and the regularised 1990.0-2015.0 diffusion model (a, d, g, and b, e, h, respectively; see also supplementary animation 3); the associated unsigned SV differences are given in c, f, and i (see also supplementary animation 4). The residual patterns in Fig. 3.9 bear resemblance to the SV described by COV-OBS.x1, as both are characterised by relatively large amplitudes under Siberia, the South Atlantic, and the Indian Ocean, in particular at 2015.0. Furthermore, the residual SV amplitudes are relatively large compared to $\dot{B}_r$, although it is of note that we do not explicitly minimise the SV residual. Particularly striking is the initially high amplitude SV described by the diffusion model, which is associated with large residuals at 1990.0. However, these amplitudes diminish quickly, and we find reasonable global agreement midway through the time period. The diffusion models tend to produce higher SV initially, which diminishes through time, such that they best explain the rate of change near the centre of the modelling period. The SV residuals increase in magnitude towards the end of the period, and by 2015.0 it is particularly difficult for the diffusion model to match the SV amplitudes beneath Siberia.

### 3.3.2 Comparison with core field characteristics and evolution

The results presented above, and in particular Fig. 3.8, suggest that a globally optimised field structure with an associated diffusive time dependence is consistent with core field evolution on yearly to decadal time scales. In this section, we focus on how certain local features of the field are represented by these diffusive models.

#### Depth extent of reversed flux patches

Figure 3.11 shows the initial ($t = t_0$) radial field for the regularised 1990.0-2015.0 diffusive model, at selected depths inside the core (see also supplementary animation 5). Because this model is expected to be poorly resolved below roughly 3400 km radius (see Appendix A.1), we only highlight the modelled field structure between this depth and the CMB. In general, the field is found to contain more structure and to be of higher amplitude at greater depth. Additionally, the axial dipole is less prevalent within deeper regions of the core, as reversed-flux patches (RFPs) (*Gubbins*, 1987, *Olson and Amit*, 2006, *Terra-Nova et al.*, 2015, *Metman et al.*, 2018), i.e. areas horizontally bounded by null-flux curves where the sign of $B_r$ is opposite to the one

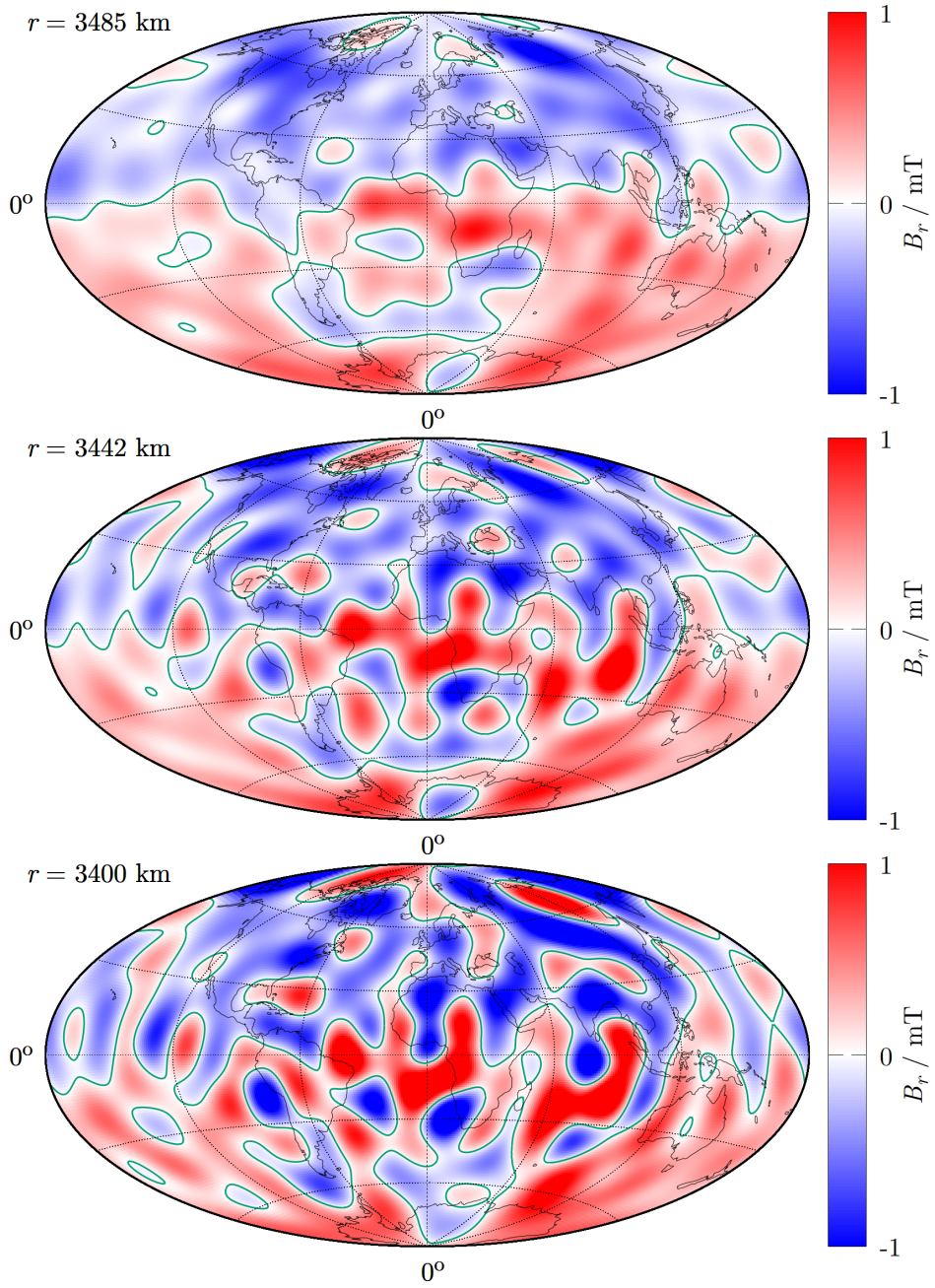


**Figure 3.11:** The radial field $B_r$ from the regularised 1990.0-2015.0 diffusion model at $t = t_0$ and selected depths inside the core. Null-flux curves are represented in green.

expected from the dipole component of the field, show a marked expansion and proliferation with increasing depth. We find in our regularised inversions that some of the RFPs on the CMB extend down to the limit of our resolving depth of 85 km inside the core; indeed, patches can merge or separate as depth increases.

### Westward drift

One of the most characteristic features of historical field evolution is the secular drift of the field towards the west, prevalent particularly within the Atlantic equatorial region. This overall westward movement of the low-latitude field is also manifest in COV-OBS.x1, as may readily be observed by evaluating the associated radial field at the equator as a function of time and longitude (Fig. 3.12a and c). The regularised 1913.0-2015.0 diffusion model, which fits COV-OBS.x1 within its uncertainty based on the global time-averaged metric, is able to locally reproduce the 0.2° drift rate (Fig. 3.12b). However, this model only provides realistic drift rates during approximately the first forty years of the modelling period, after which the model's diffusive azimuthal field motion decelerates. Nevertheless, the total westward displacement of the low-longitude field is matched reasonably. If we consider a shorter time window (e.g. 1990.0-2015.0), the corresponding regularised diffusion model gives the correct drift rates at all times (Fig. 3.12d).

### Recent North Magnetic Pole acceleration and Arctic emergence of reversed flux

The North Magnetic Pole (NMP), i.e. the location on Earth's surface where the magnetic field vector points vertically downwards, has been shown to have accelerated over the past three decades (e.g. *Mandea and Dormy*, 2003). The 1913.0-2015.0 regularised diffusion model appears incompatible with this trend, as the NMP moves relatively slowly for this model, and ultimately stalls almost entirely (Fig. 3.13a, contoured circles). However, if we focus on the period during which pole acceleration occurred, e.g. for the period 1990.0-2015.0, the regularised diffusion model shows an NMP trajectory with much improved agreement with COV-OBS.x1 (Fig. 3.13b). However, there remains some discrepancy between the two models at the end of the period, with the NMP from the diffusive model decelerating and unable to match the COV-OBS.x1 pole location at 2015.0.

*Chulliat et al.* (2010) attribute the NMP acceleration to growth and intensification of a patch of reversed flux under the New Siberian Islands. The recent evolution of this patch is shown in Fig. 3.14, an equal area projection of $B_r$ at selected epochs according COV-OBS.x1 (a, c, and e) and the 1990.0-2015.0 diffusion model (b, d, and, f). Both field models highlight in almost identical fashion how the New Siberian Islands patch expands and intensifies. Additionally, for both models we observe a net migration of this patch towards the southwest. For the diffusion model, the evolution of the patch can be linked to field morphology at greater depth (Fig. 3.11): it should be noted that the patch extends to our sensitivity depth limit of 85 km, where it is of higher amplitude and displaced towards the southwest compared to the field configuration at

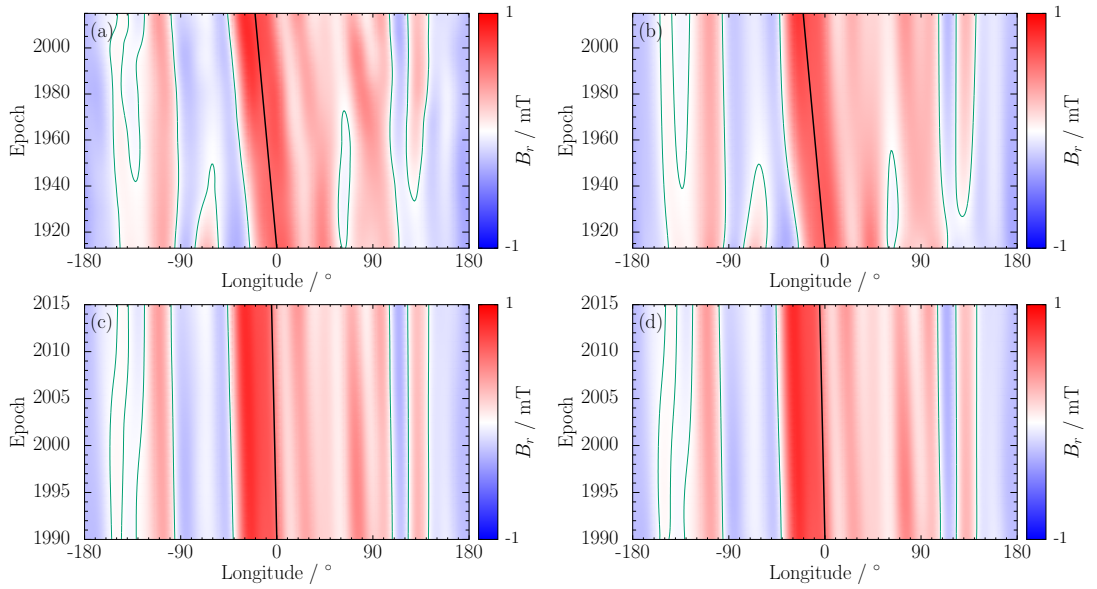


**Figure 3.12:** Time-longitude plots of the radial field at the equator according to COV-OBS.x1 (a and c), and the regularised 1913.0-2015.0 and 1990.0-2015.0 diffusion models (b and d, respectively). The black line corresponds to a drift rate of 0.2° yr$^{-1}$ towards the west. Null-flux longitudes are represented in green.

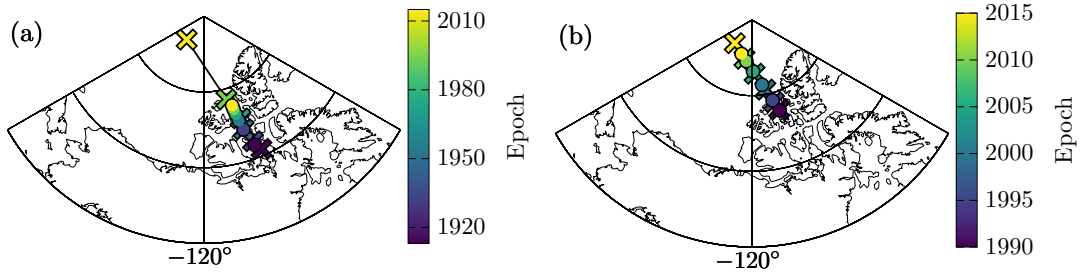


**Figure 3.13:** The position of the North Magnetic Pole on the Earth's surface as a function of time, according to COV-OBS.x1 (crosses; a and b) and the regularised diffusion models for 1913.0-2015.0 and 1990.0-2015.0 (circles; a and b, respectively). The colour of the crosses and circles denotes time.

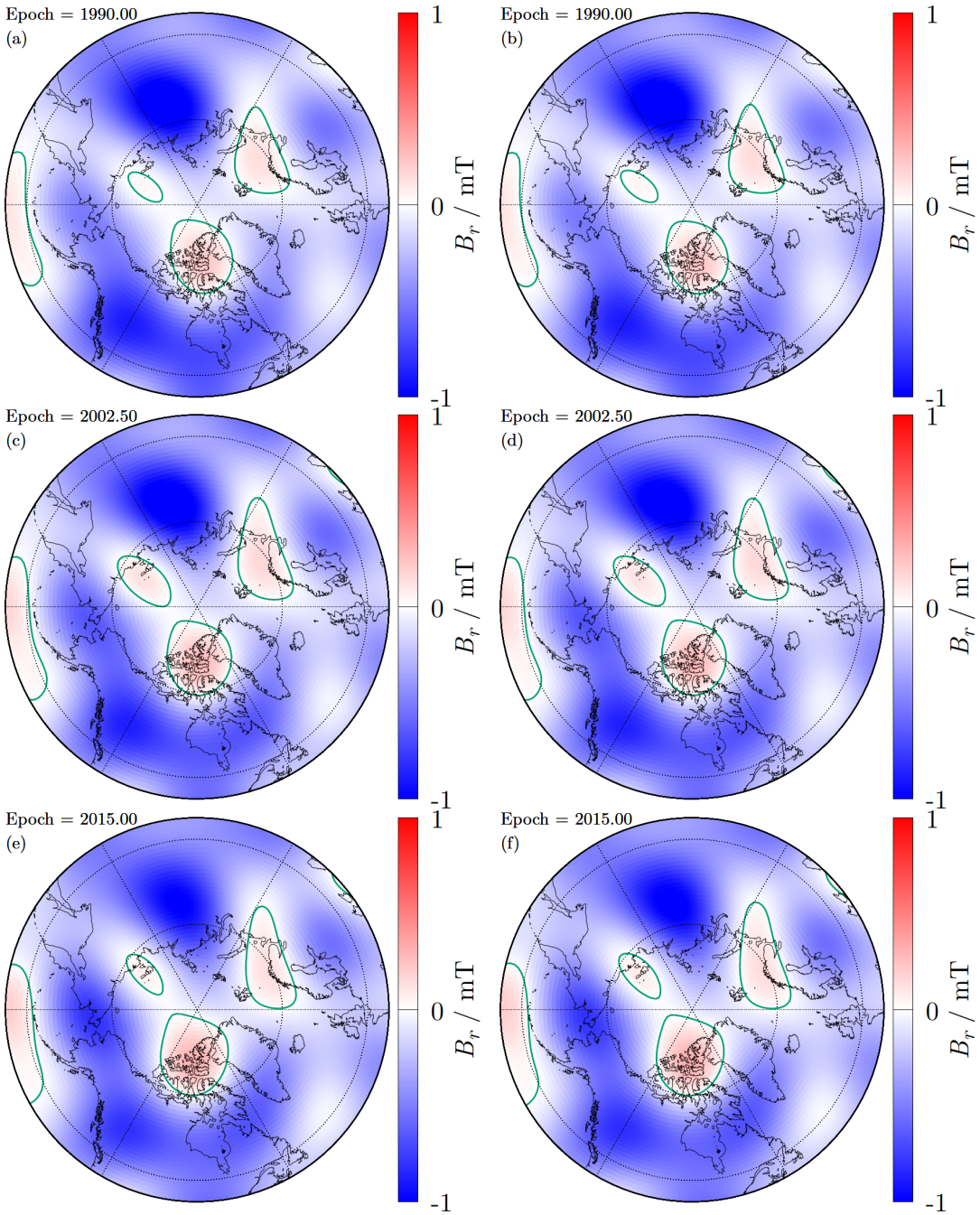


**Figure 3.14:** Polar projection of $B_r$ at the CMB and selected epochs, for COV-OBS.x1 (a, c, and e) and the 1990.0-2015.0 diffusion model (b, d, and f). Null-flux curves are represented in green.

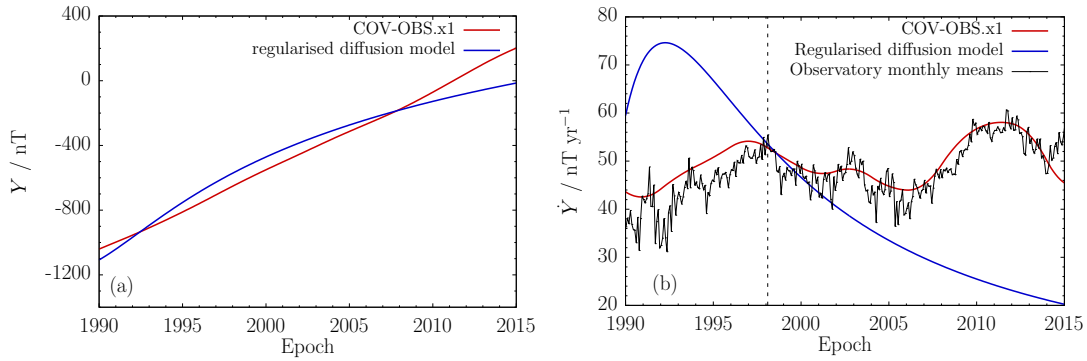


**Figure 3.15:** Time series of the eastward magnetic component $Y$ (a) and its time derivative (b) at the Chambon La Forêt (CLF) observatory, according to COV-OBS.x1 (red), the regularised 1990.0-2015.0 diffusion model (blue), and first differences of observatory monthly means (black). The dashed line denotes the approximate timing of a geomagnetic jerk.

the CMB, so that subsequent diffusive evolution of this initial state will yield the intensification and migration displayed in Fig. 3.14.

### Surface geomagnetic time series and the late 20$^{\text{th}}$ century jerk

Finally, we examine how well a globally optimised diffusion model may capture the local time series of a single field component at the Earth's surface. Specifically, we consider once more the regularised 1990.0-2015.0 diffusion model and the COV-OBS.x1 mean, and its representation of the eastward field component $Y$ at the Chambon La Forêt (CLF) observatory (Fig. 3.15a). Our interest is focussed on a geomagnetic jerk, i.e. a stepwise change in the second time derivative of a magnetic field component, which has been observed at this station at approximately 1999.0 (*Mandea et al.*, 2000). We therefore compare also the time derivative $\dot{Y}$ (Fig. 3.15b). The diffusive model captures the magnitude and growth of $Y$ in a general sense, although the two curves clearly diverge towards the end of the time period. However, the time derivatives for both models show little agreement; COV-OBS.x1 has more short-term variability with no significant overall trend, whereas the diffusive model has generally smoother behaviour and an overall decay. Although the diffusive model renders an abrupt change in $\dot{Y}$ during the first 2 years, it is too early and of significantly different magnitude to resemble the late 20$^{\text{th}}$ century jerk.

## 3.4 Discussion

We have introduced new, purely diffusive, end-member models for geomagnetic secular variation, which are obtained by minimising a global residual objective function with respect to the magnetic field structure at the start of the given time window. For chosen time periods up to 102 years, these states are found to be globally consistent with the COV-OBS.x1 field model, as their associated time-averaged residual is smaller than the time-averaged COV-OBS.x1 uncertainty based on a single standard deviation. Additionally, for a 30 year time window, we

find the global diffusive residual to be within the COV-OBS.x1 uncertainty at all times. Although these diffusive models are designed to fit COV-OBS.x1 on a global scale, they exhibit consistency with regional-scale field evolution. For instance, diffusion appears capable of reproducing much of the secular westward drift of the equatorial field over the 1913.0-2015.0 period. As such, it demonstrates that westward drift can not be uniquely attributed to fluid flow along the CMB, although this is the most common interpretation (*Bullard et al.*, 1950, *Jault et al.*, 1988, *Aubert et al.*, 2013). Moreover, our diffusive models recover both the recent shift of the North Magnetic Pole and the strengthening of reversed flux in the Arctic region, in agreement with the idea that these two phenomena may be linked dynamically (*Chulliat et al.*, 2010).

However, we considered also the local fit of our models at a single location on the Earth's surface. In particular, we showed that our models could not reproduce the signature of a late $20^{\text{th}}$ century jerk. While jerks remain poorly understood, we consider it unlikely that these are generated through regional-scale magnetic diffusion. However, it should be noted that within our formalism, observatory time series are not fit directly; indeed, it may be possible to fit a local time series of SV at the expense of large global residuals. Another issue is that we minimise a global residual with respect to the field model COV-OBS.x1, that is already a spatio-temporarily smoothed representation of the true core field and its time evolution. The models presented here are therefore the result of an indirect inversion, and have accordingly undergone additional (implicit) regularisation. This secondary smoothing may explain how the models fit well globally but still produce a large misfit to field evolution at one particular location. A potential modification of our formalism is to directly minimise the misfit to ground and/or virtual satellite observatory (*Mandea and Olsen*, 2006) data instead of an intermediate spherical harmonic field model, which may confirm with more confidence how well magnetic diffusion alone can fit local geomagnetic time series.

Let us briefly compare how well field evolution is described by both SV end members, which relate to either frozen flux or magnetic diffusion. *Whaler and Beggan* (2015) and *Beggan and Whaler* (2018) report frozen-flux fluid flow and acceleration models with associated RMS hindcast errors in $|\mathbf{B}|$ at the Earth's surface on the order of tens of nT, over a period of 5 years. Evaluating our 5-year (2010.0-2015.0) regularised diffusion model at the surface, we find the respective diffusive error is only 1.3 nT. It is important to recognise however that our diffusive models have more degrees of freedom compared to these particular frozen-flux models. Choosing a coarse radial resolution for the diffusive models ($N = 2$) in order that the number of degrees of freedom are the same produces a 5-year time-averaged RMS error in $|\mathbf{B}|$ at the Earth's surface of almost 93 nT. However, there is no physical reason why we should deliberately penalise our diffusive models in such a comparison. Furthermore, the simple measure of global misfit does not take into account how well either method captures the evolution of local features: either method could be superior in describing SV within a specific geographic area. Assuming the models by *Whaler and Beggan* (2015), *Beggan and Whaler* (2018) are illustrative of the broader suite of core flow models that have been developed (see

*Holme* (2015) for an overview), we conclude that the diffusive end-member model of secular variation provides an equally acceptable mathematical description of decadal field evolution. Additionally, our results confirm that diffusion need not be restricted to the global time scale of $\tau_d \approx 16$ kyr. Furthermore, the effective $Rm$ near the top of the core could be much lower than canonical estimates, because fine radial magnetic field structure reduces the typical length scale and when diffusion explains a significant amount of the SV large-magnitude flows are not required. Hence, for our purely diffusive models $Rm$ is much closer to estimates of a local $Rm \sim 1$ that apply just below the CMB (e.g. *Amit and Christensen*, 2008, *Finlay and Amit*, 2011).

Although both frozen-flux and purely diffusive models may adequately describe field evolution, neither end member of secular variation should be considered fully representative of the physical processes that govern the geodynamo. For example, while fluid flow can (re)generate the magnetic field, diffusion enters only as a sink term in the description of total magnetic energy evolution (e.g. *Gubbins and Roberts*, 1987). Nevertheless, in the absence of fluid flow there may still be a local energetic exchange, as demonstrated by the regularised 1840.0-2015.0 diffusion model, for which we find an overall threefold increase of the magnetic energy on the CMB. This result also contrasts with a previous suggestion that time variability in the CMB magnetic energy relates only to fluid flow (*Huguet et al.*, 2018). However, it should be noted that such local purely diffusive field growth is inherently transient, which explains the observed overall increase of modelling errors with time (e.g. in Fig. 3.6, 3.9, 3.12, and 3.15a), and the increased difficulty of using diffusion to explain field evolution over relatively long time windows (Fig. 3.8).

The dissipative nature of diffusion may also be illustrated with a comparison of field states, e.g. the regularised 2000.0-2015.0 model evaluated at 2010.0 and the initial state for the regularised 2010.0-2015.0 model: over the sensitivity region we find that the overall relative difference in $\mathbf{B}$ between these states amounts to roughly 72%, and this large temporal discontinuity between field states may suggest that one decade is sufficient to dissipate a significant part of the initial state. As such, on longer (geological) time scales diffusion alone could not have sustained the field throughout the core's lifetime, estimated to be on the order of billions of years (e.g. *Tarduno et al.*, 2010, *Biggin et al.*, 2015). The evolution of the field over these geological time scales highlights a further limitation of pure diffusion, namely its inability to explain the numerous global polarity reversals that have occurred over the field's lifespan (e.g. *Glatzmaier and Coe*, 2015). We therefore underline once more that pure magnetic diffusion is not a self-sustainable process physically capable of explaining SV indefinitely. Furthermore, as diffusion is entirely unrelated to core fluid motion, it can not explain the observed decadal length-of-day variations due to angular momentum exchange between the core and mantle, while the frozen-flux hypothesis has allowed these to be linked to SV (*Jault et al.*, 1988, *Jackson et al.*, 1993, *Gillet et al.*, 2010). Likewise, frozen-flux does not capture magnetic field evolution completely and without diffusion it would allow small scale features of the field to grow indefinitely, leading to its failure to match the observed field. Nevertheless, while neither

SV end member can explain field evolution completely, both descriptions may be utilised to fit SV on yearly to decadal time scales.

Naturally, a more complete model would consider the combined effects of both fluid flow and diffusion, which could for example be envisaged by considering diffusion as a correction term to frozen flux (*Gubbins*, 1996). Alternatively, one could envisage a scheme where diffusion is not strictly corrective, but where it is instead made an arbitrary part of the SV at the CMB. Together with the methods presented here, such a partitioning of the SV would allow the frozen-flux and diffusive parts to be fit individually. By subsequently varying the amount of SV that is attributed to diffusion, a hybrid model (incorporating frozen-flux and diffusion) which best explains the total SV could be obtained.

Lastly, we comment on the relevance of our work to the proposed stratified layer at the top of the liquid core with a possible depth of several hundreds of km (e.g. *Whaler*, 1980, *Lay and Young*, 1990, *Gubbins*, 2007, *Buffett*, 2014). Within such a layer, core fluid flow would be principally horizontal with radial flow suppressed. If this layer is indeed persistent over several hundreds of km, it is then not straightforward to physically justify the large radial magnetic gradients manifest within the sensitivity region comprising only approximately the top 80 km of the core. On the contrary, for the case of whole-core convection these gradients could more easily be linked to flux expulsion driven by upwelling. Nevertheless, our work demonstrates a mathematical consistency between diffusion and observed SV that holds in the presence or absence of such a stratified layer. The short-term evolution of the field can therefore not be used as evidence for or against a stratified layer.

To conclude, we have presented a purely diffusive description of geomagnetic secular variation. Our diffusive SV end-member models have been obtained through the global optimisation of an initial magnetic field and have a subsequent diffusive evolution that fits the COV-OBS.x1 field model over various time windows with a given uncertainty. While purely diffusive SV is described analytically by the decay modes, we use a Galerkin method which yields a much better conditioned inverse problem. We find that diffusion alone can adequately describe historical field evolution over time windows ranging up to 102 years, and can reproduce characteristic aspects of SV such as westward drift, recent North Magnetic Pole movement and emergence of reversed-flux patches.

## Acknowledgments

We thank Hagay Amit and another anonymous reviewer for their thorough reviews, and Kathryn Whaler for her constructive remarks. M. C. Metman is supported by a studentship awarded as part of the Leeds-York NERC Doctoral Training Partnership (NE/L002574/1) and by the BGS University Funding Initiative PhD studentship (S305).

# References


Amit, H. (2014), Can downwelling at the top of the Earth's core be detected in the geomagnetic secular variation?, *Physics of the Earth and Planetary Interiors*, *229*, 110 – 121, doi:10.1016/j.pepi.2014.01.012. 3.1

Amit, H., and U. R. Christensen (2008), Accounting for magnetic diffusion in core flow inversions from geomagnetic secular variation, *Geophysical Journal International*, *175*(3), 913–924. 3.1, 3.4

Aubert, J. (2012), Flow throughout the Earth's core inverted from geomagnetic observations and numerical dynamo models, *Geophysical Journal International*, *192*(2), 537–556. 3.1

Aubert, J. (2014), Earth's core internal dynamics 1840–2010 imaged by inverse geodynamo modelling, *Geophysical Journal International*, *197*(3), 1321–1334, doi:10.1093/gji/ggu064. 3.1

Aubert, J., J. Aurnou, and J. Wicht (2008), The magnetic structure of convection-driven numerical dynamos, *Geophysical Journal International*, *172*(3), 945–956. 3.1

Aubert, J., C. C. Finlay, and A. Fournier (2013), Bottom-up control of geomagnetic secular variation by the Earth's inner core, *Nature*, *502*, 219–223. 3.4

Backus, G. (1958), A class of self-sustaining dissipative spherical dynamos, *Annals of Physics*, *4*(4), 372 – 447. 3.2.1

Backus, G., and E. C. Bullard (1968), Kinematics of geomagnetic secular variation in a perfectly conducting core, *Philosophical Transactions of the Royal Society of London. Series A, Mathematical and Physical Sciences*, *263*(1141), 239–266. 3.1

Bärenzung, J., M. Holschneider, J. Wicht, S. Sanchez, and V. Lesur (2018), Modeling and predicting the short-term evolution of the geomagnetic field, *Journal of Geophysical Research: Solid Earth*, *123*(6), 4539–4560. 3.1

Barrois, O., N. Gillet, and J. Aubert (2017), Contributions to the geomagnetic secular variation from a reanalysis of core surface dynamics, *Geophysical Journal International*, *211*(1), 50–68, doi:10.1093/gji/ggx280. 3.1

Barrois, O., N. Gillet, J. Aubert, O. Barrois, M. D. Hammer, C. C. Finlay, Y. Martin, and N. Gillet (2018), Erratum: Contributions to the geomagnetic secular variation from a reanalysis of core surface dynamics and Assimilation of ground and satellite magnetic measurements: inference of core surface magnetic and velocity field changes, *Geophysical Journal International*, *216*(3), 2106–2113. 3.1

Beggan, C. D., and K. A. Whaler (2009), Forecasting change of the magnetic field using core surface flows and ensemble Kalman filtering, *Geophysical Research Letters*, *36*(18). 3.1

Beggan, C. D., and K. A. Whaler (2018), Ensemble Kalman filter analysis of magnetic field models during the CHAMP-Swarm gap, *Physics of the Earth and Planetary Interiors*, *281*, 103–110. 3.1, 3.4

Biggin, A. J., E. J. Piispa, L. J. Pesonen, R. Holme, G. A. Paterson, T. Veikkolainen, and L. Tauxe (2015), Palaeomagnetic field intensity variations suggest Mesoproterozoic inner-core nucleation, *Nature*, *526*, 245–248. 3.4

Bloxham, J. (1986), The expulsion of magnetic flux from the Earth's core, *Geophysical Journal of the Royal Astronomical Society*, *87*(2), 669–678, doi:10.1111/j.1365-246X.1986.tb06643.x. 3.1

Bloxham, J. (1988), The dynamical regime of fluid flow at the core surface, *Geophysical Research Letters*, *15*(6), 585–588. 3.1

Boyd, J. P. (2000), *Chebyshev and Fourier Spectral Methods*, second ed., Dover Publications. 3.2.2

Buffett, B. (2010), Tidal dissipation and the strength of the earths internal magnetic field, *Nature*, *468*, 952–954. 3.2.4, 3.2.4, 3.2.4

Buffett, B. (2014), Geomagnetic fluctuations reveal stable stratification at the top of the Earth's core, *Nature*, *507*, 484–487. 3.1

Bullard, E. C., C. Freeman, H. Gellman, and J. Nixon (1950), The westward drift of the Earth's magnetic field, *Philosophical Transactions of the Royal Society of London A: Mathematical, Physical and Engineering Sciences*, *243*(859), 67–92. 3.4

Chen, L., W. Herreman, K. Li, P. W. Livermore, J. W. Luo, and A. Jackson (2018), The optimal kinematic dynamo driven by steady flows in a sphere, *Journal of Fluid Mechanics*, *839*, 132. 3.2.2

Cheney, E. W., and D. Kincaid (2008), *Numerical mathematics and computing*, 6th ed., Brooks/Cole Pub. Co., Belmont, CA. 3.2.3

Christensen, U. R., J. Aubert, and G. Hulot (2010), Conditions for Earth-like geodynamo models, *Earth and Planetary Science Letters*, *296*(3), 487–496. 3.1

Chulliat, A., and N. Olsen (2010), Observation of magnetic diffusion in the Earth's outer core from Magsat, Ørsted, and CHAMP data, *Journal of Geophysical Research: Solid Earth*, *115*(B5). 3.1, 3.1

Chulliat, A., G. Hulot, and L. R. Newitt (2010), Magnetic flux expulsion from the core as a possible cause of the unusually large acceleration of the north magnetic pole during the 1990s, *Journal of Geophysical Research: Solid Earth*, *115*(B7), B007,143, doi:10.1029/2009JB007143. 3.1, 3.3.2, 3.4

Constable, C. G., R. L. Parker, and P. B. Stark (1993), Geomagnetic field models incorporating frozen-flux constraints, *Geophysical Journal International*, *113*(2), 419–433. 3.1

Finlay, C. C., and H. Amit (2011), On flow magnitude and field-flow alignment at Earth's core surface, *Geophysical Journal International*, *186*(1), 175–192. 3.4

Finlay, C. C., and A. Jackson (2003), Equatorially dominated magnetic field change at the surface of earth's core, *Science*, *300*(5628), 2084–2086. 3.1

Fournier, A., C. Eymin, and T. Alboussière (2007), A case for variational geomagnetic data assimilation: insights from a one-dimensional, nonlinear, and sparsely observed MHD system, *Nonlinear Processes in Geophysics*, *14*(2), 163–180. 3.1

Gillet, N., D. Jault, E. Canet, and A. Fournier (2010), Fast torsional waves and strong magnetic field within the earths core, *Nature*, *465*, 74–77. 3.2.4, 3.2.4, 3.2.4, 3.4

Gillet, N., D. Jault, and C. C. Finlay (2015a), Planetary gyre, time-dependent eddies, torsional waves, and equatorial jets at the Earth's core surface, *Journal of Geophysical Research: Solid Earth*, *120*(6), 3991–4013. 3.1

Gillet, N., O. Barrois, and C. C. Finlay (2015b), Stochastic forecasting of the geomagnetic field from the COV-OBS.x1 geomagnetic field model, and candidate models for IGRF-12, *Earth, Planets and Space*, *67*(1), 71. (document), 3.1, 3.2.3

Glatzmaier, G., and R. S. Coe (2015), Magnetic polarity reversals in the core, in *Treatise on Geophysics*, vol. 8, second ed., chap. 9, Elsevier, Oxford. 3.4

Gubbins, D. (1984), Geomagnetic field analysis - II. Secular variation consistent with a perfectly conducting core, *Geophysical Journal of the Royal Astronomical Society*, *77*(3), 753–766. 3.1

Gubbins, D. (1987), Mechanism for geomagnetic polarity reversals, *Nature*, *326*, 167169. 3.3.2

Gubbins, D. (1996), A formalism for the inversion of geomagnetic data for core motions with diffusion, *Physics of the Earth and Planetary Interiors*, *98*(3), 193–206, doi:10.1016/S0031-9201(96)03187-1. 3.1, 3.1

Gubbins, D. (2007), Geomagnetic constraints on stratification at the top of Earth's core, *Earth, Planets and Space*, *59*(7), 661–664. 3.1

Gubbins, D., and J. Bloxham (1985), Geomagnetic field analysisIII. Magnetic fields on the coremantle boundary, *Geophysical Journal International*, *80*(3), 695–713. 3.2.4

Gubbins, D., and P. Kelly (1996), A difficulty with using the frozen flux hypothesis to find steady core motions, *Geophysical Research Letters*, *23*(14), 1825–1828, doi:10.1029/96GL01392. 3.1, 3.1

Gubbins, D., and P. H. Roberts (1987), Magnetohydrodynamics of the Earth's Core, in *Geomagnetism*, vol. 2, chap. 1, Academic Press. 3.2.1, 3.2.4, 3.4

Halley, E. (1692), An account of the cause of the change of the variation of the magnetical needle. with an hypothesis of the structure of the internal parts of the earth: as it was proposed to the royal society in one of their late meetings, *Philosophical Transactions*, *17*(195), 563–578. 3.1

Hide, R. (1966), Free hydromagnetic oscillations of the earth's core and the theory of the geomagnetic secular variation, *Philosophical Transactions of the Royal Society of London A: Mathematical, Physical and Engineering Sciences*, *259*(1107), 615–647. 3.1

Holme, R. (2015), Large-Scale Flow in the Core, in *Treatise on Geophysics*, vol. 8, chap. 4, pp. 91–113, Elsevier. 3.1, 3.4

Huguet, L., H. Amit, and T. Alboussière (2018), Geomagnetic dipole changes and upwelling/downwelling at the top of the Earth's core, *Frontiers in Earth Science*, *6*, 170. 3.2.4, 3.4

Jackson, A., and C. Finlay (2015), Geomagnetic secular variation and its applications to the core, in *Treatise on Geophysics*, vol. 5, second ed., chap. 5, Elsevier, Oxford. 3.1, 3.1

Jackson, A., J. Bloxham, and D. Gubbins (1993), Time-dependent flow at the core surface and conservation of angular momentum in the coupled core-mantle system, in *Dynamics of Earth's Deep Interior and Earth Rotation*, pp. 97–107, American Geophysical Union (AGU). 3.1, 3.4

Jault, D., C. Gire, and J.-L. Le Mouël (1988), Westward drift, core motions and exchanges of angular momentum between core and mantle, *Nature*, *333*, 353356. 3.1, 3.4

Lay, T., and C. J. Young (1990), The stably-stratified outermost core revisited, *Geophysical Research Letters*, *17*(11), 2001–2004. 3.1

Li, K., A. Jackson, and P. W. Livermore (2014), Variational data assimilation for a forced, inertia-free magnetohydrodynamic dynamo model, *Geophysical Journal International*, *199*(3), 1662–1676. 3.1, 3.2.3

Li, K., A. Jackson, and P. W. Livermore (2018), Taylor state dynamos found by optimal control: axisymmetric examples, *Journal of Fluid Mechanics*, *853*, 647697. 3.2.2

Livermore, P. W. (2010), Galerkin orthogonal polynomials, *Journal of Computational Physics*, *229*(6), 2046 – 2060. 3.2.2

Livermore, P. W., and A. Jackson (2006), Transient magnetic energy growth in spherical stationary flows, *Proceedings of the Royal Society of London A: Mathematical, Physical and Engineering Sciences*, *462*(2072), 2457–2479, doi:10.1098/rspa.2005.1644. 3.2.1

Livermore, P. W., R. Hollerbach, and C. C. Finlay (2017), An accelerating high-latitude jet in Earth's core, *Nature Geoscience*, *10*, 62–68. 3.1

Love, J. J. (1999), A critique of frozen-flux inverse modelling of a nearly steady geodynamo, *Geophysical Journal International*, *138*(2), 353–365. 3.1

Mandea, M., and E. Dormy (2003), Asymmetric behavior of magnetic dip poles, *Earth, Planets and Space*, *55*(3), 153–157. 3.3.2

Mandea, M., and N. Olsen (2006), A new approach to directly determine the secular variation from magnetic satellite observations, *Geophysical Research Letters*, *33*(15). 3.4

Mandea, M., E. Bellanger, and J.-L. Le Mouël (2000), A geomagnetic jerk for the end of the 20th century?, *Earth and Planetary Science Letters*, *183*(3), 369 – 373. 3.3.2

Metman, M., P. Livermore, and J. Mound (2018), The reversed and normal flux contributions to axial dipole decay for 1880-2015, *Physics of the Earth and Planetary Interiors*, *276*, 106 – 117. 3.3.2

Miranker, W. L. (1961), A well posed problem for the backward heat equation, *Proceedings of the American Mathematical Society*, *12*(2), 243–247. 3.2.3

Olsen, N., and M. Mandea (2008), Rapidly changing flows in the Earth's core, *Nature Geoscience*, *1*, 390–394, doi:10.1038/ngeo203. 3.1, 3.3.1

Olson, P., and H. Amit (2006), Changes in Earth's dipole, *Naturwissenschaften*, *93*(11), 519–542. 3.3.2

Roberts, P. H., and G. A. Glatzmaier (2000), A test of the frozen-flux approximation using a new geodynamo model, *Philosophical Transactions of the Royal Society of London. Series A: Mathematical, Physical and Engineering Sciences*, *358*(1768), 1109–1121. 3.1

Roberts, P. H., and S. Scott (1965), On analysis of the secular variation, *Journal of Geomagnetism and Geoelectricity*, *17*(2), 137–151. 3.1

Tarduno, J. A., R. D. Cottrell, M. K. Watkeys, A. Hofmann, P. V. Doubrovine, E. E. Mamajek, D. Liu, D. G. Sibeck, L. P. Neukirch, and Y. Usui (2010), Geodynamo, Solar Wind, and Magnetopause 3.4 to 3.45 Billion Years Ago, *Science*, *327*(5970), 1238–1240. 3.4

Terra-Nova, F., H. Amit, G. A. Hartmann, and R. I. F. Trindade (2015), The time dependence of reversed archeomagnetic flux patches, *Journal of Geophysical Research: Solid Earth*, *120*(2), 691–704. 3.3.2

Terra-Nova, F., H. Amit, G. A. Hartmann, and R. I. Trindade (2016), Using archaeomagnetic field models to constrain the physics of the core: robustness and preferred locations of reversed flux patches, *Geophysical Journal International*, *206*(3), 1890–1913. 3.1

Vestine, E. H., R. H. Ball, and A. B. Kahle (1967), Nature of surface flow in the Earth's central core, *Journal of Geophysical Research*, *72*(19), 4927–4936, doi:10.1029/JZ072i019p04927. 3.1

Wardinski, I., and V. Lesur (2012), An extended version of the $C^3$FM geomagnetic field model: application of a continuous frozen-flux constraint, *Geophysical Journal International*, *189*(3), 1409–1429. 3.1

Whaler, K. (1980), Does the whole of the Earth's core convect?, *Nature*, *287*, 528–530. 3.1, 3.1

Whaler, K. A., and C. D. Beggan (2015), Derivation and use of core surface flows for forecasting secular variation, *Journal of Geophysical Research: Solid Earth*, *120*(3), 1400–1414, doi:10.1002/2014JB011697. 3.1, 3.4

# Addendum: Chapter 3 — Modelling decadal secular variation with only magnetic diffusion

To what extent can magnetic diffusion alone explain the temporal evolution of the core magnetic field over yearly to decadal time scales? In the previous chapter we set out to answer this question, and introduced a formalism to construct purely diffusive models which best fit an observation-based core field model. It is possible that after reading this chapter, the reader feels convinced that magnetic diffusion provides a description of field evolution that is at least as 'good' as frozen-flux end-member models of SV. In fact, following a comparison with (frozen-flux) core flow models, we too have stated: '[...], we conclude that the diffusive end-member model of secular variation provides an equally acceptable mathematical description of decadal field evolution.'

Perhaps, in retrospect, the question above is ill-posed. Namely, while both end-members models of SV (i.e. frozen-flux and pure diffusion) have been shown to be *mathematically* consistent with the observed field evolution on yearly to decadal time scales, a diffusive description of SV nevertheless contains less realism on *physical* grounds. For instance, and as already stated in section 3.4, fluid motion is required to generate a magnetic field through dynamo action to counter Ohmic dissipation, and can therefore sustain SV over longer periods. This signifies a fundamental difference between diffusion and fluid motion: the former acts to diminish existing field gradients, while the latter can also enhance these. As such, fitting the observed field evolution with pure diffusion over extended periods of time is problematic. This limitation of diffusion is also apparent from our results in Chapter 3: we find a general increase of the diffusive residual with time (e.g. Fig. 3.15a), while the SV produced by diffusion exhibits overall decay (e.g. Fig. 3.15b). Similarly, by comparing Fig. 3.12a and 3.12b we find that our diffusive models reproduce the westward drift for a period of only 50 yr or so, while in fact it has been ongoing for at least 400 yr (e.g. *Halley*, 1692, *Finlay and Jackson*, 2003). In contrast, core flow models have been shown to be able to match the field evolution at historical epochs (*Whaler and Holme*, 2011). But perhaps it is most important to note that core flow models allow a prediction of angular momentum exchange between the core and mantle that correlates with observed variations in length-of-day (e.g. *Jault et al.*, 1988). As such, there

is *independent* verification that core flow models contain realism. For purely diffusive models of SV, confirmation that these models are meaningful is (at this stage) lacking, and as such we stress that these should not be considered as a realistic alternative to frozen-flux descriptions of the field.

Let us also briefly revisit the goodness-of-fit described by our diffusive models. In Chapter 3 we state that pure diffusion fits the field evolution described by the COV-OBS.x1 field model over several decades, and even over a century. However, it must be noted that this assertion is ultimately based on the error budget provided by this field model. As can be noted from Fig. 3.6 and 3.7, the posterior uncertainties provided by COV-OBS.x1 increase rapidly with spherical harmonic degree. Consequently, whether or not diffusion fits COV-OBS.x1 within the global error budget (as discussed in Fig. 3.8) depends strongly on these high-degree uncertainties, and therefore also on the spherical harmonic degree of truncation of the field. How well would the diffusive models then perform if the degree of truncation $L < 14$? Figure 3.7 demonstrates that with decreasing $L$ the total error budget decreases much more rapidly than the total diffusive residual. As such, the largest time window we could fit with diffusion before our global residual (eq. 3.16) exceeds the global error budget would most likely be much shorter when $L < 14$. While we state that diffusion can explain field evolution over 102 yr, this bound should therefore be adopted with caution. Also, since the conclusions reached in Chapter 3 rely strongly on the uncertainties assigned to the field model used, it would be interesting to investigate how pure diffusion can reproduce the field evolution described by other field models. However, we emphasise again that a more meaningful approach is to make use of geomagnetic data directly, instead of field models that already give a smoothed representation of observed core field evolution.

Nevertheless, difficulties of fitting COV-OBS.x1 due to a reduced error budget could (at least partially) be mitigated by setting the damping parameter $\lambda$ (eq. 3.21) smaller, effectively putting more magnetic energy in our modelled structure of the core field. The RMS field amplitudes of our modelled fields (a quantity proportional to the square root of the associated magnetic energy) is always less than 1.3 mT, and therefore well below the estimates of 2.5 to 4 mT for the RMS field strength inside the core (*Buffett*, 2010, *Gillet et al.*, 2010). Such a choice for assigning a smaller value to the damping parameter would therefore be perfectly reasonable, and may allow diffusion to fit COV-OBS.x1 globally even when $L < 14$.

To summarise, we have shown that our purely diffusive models are mathematically consistent with historical field evolution. However, this assertion likely depends strongly on the spherical harmonic degree of truncation, such that the length of the time window over which we can fit field evolution with diffusion is reduced by setting a lower degree of truncation. In addition, we lack independent verification that these diffusive models are physically realistic, in contrast to flow models derived from frozen flux. A meaningful interpretation of geomagnetic secular variation is therefore still (primarily) in terms of core fluid motion just below the CMB. For this reason, we propose in the following chapter a means of combining our purely diffusive formalism with core flow modelling. Specifically, we shall employ our diffusive for-

malism to augment core flow models, resulting in an improved fit to the SV described by some field model, and we will also use both end-member models to give improved forecasts of field evolution over yearly time scales.

# References


Buffett, B. (2010), Tidal dissipation and the strength of the Earth's internal magnetic field, *Nature*, *468*, 952–954. 3.1

Finlay, C. C., and A. Jackson (2003), Equatorially dominated magnetic field change at the surface of Earth's core, *Science*, *300*(5628), 2084–2086. 3.1

Gillet, N., D. Jault, E. Canet, and A. Fournier (2010), Fast torsional waves and strong magnetic field within the Earth's core, *Nature*, *465*, 74–77. 3.1

Halley, E. (1692), An account of the cause of the change of the variation of the magnetical needle. with an hypothesis of the structure of the internal parts of the Earth: as it was proposed to the Royal Society in one of their late meetings, *Philosophical Transactions*, *17*(195), 563–578. 3.1

Jault, D., C. Gire, and J.-L. Le Mouël (1988), Westward drift, core motions and exchanges of angular momentum between core and mantle, *Nature*, *333*, 353356. 3.1

Whaler, K., and R. Holme (2011), The axial dipole strength and flow in the outer core, *Physics of the Earth and Planetary Interiors*, *188*(3), 235 – 246. 3.1

# Chapter 4

# Forecasting secular variation through sequential estimation of core fluid flow and magnetic diffusion

**M. C. Metman**[1], C. D. Beggan[2], P. W. Livermore[1], and J. E. Mound[1], and

[1]*School of Earth and Environment, University of Leeds, Leeds LS2 9JT, United Kingdom*
[2]*British Geological Survey, Edinburgh EH14 4AP, United Kingdom*

*'I think we agree, the past is over.'*

**George W. Bush**

## Abstract

The Earth's internal magnetic field is generated through motion of the electrically conductive iron-alloy fluid comprising Earth's outer core. Temporal variability of this field, termed secular variation, resuls from two processes: one is the interaction between core fluid motion and the magnetic field, the other is magnetic diffusion. Because diffusion is widely thought to take place over relatively long, millenial time scales, it is common to disregard it when considering short-term field changes (the frozen-flux approximation), which allows a mapping of the core fluid motion along the CMB using observations of SV at Earth's surface. Subsequently, such flow models have been used to predict variation in the magnetic field. However, recent work suggests that diffusion may contribute significantly also on short time scales, manifest for example by the evolution of areas on the CMB where the sign of the radial field is different to the prevalent axial dipole (i.e. reversed-flux patches), suggesting that diffusion may need to be accounted for when considering short-term SV. Therefore, we introduce here a hybrid method to forecast field evolution which considers field changes due to fluid flow and diffusion. These

predictions rely on fitting the SV described by the CHAOS-6 field model with steady core fluid motion, and subsequently using the associated residual to model magnetic diffusion. With this approach, we find that including diffusion yields a reduction in the global forecast error at Earth's surface, which can be as large as 25% at the end of a 5-year forecasting period; at the CMB the this error reduction can be in excess of 77%. These differences are explained by the fact that diffusion acts predominantly to reduce forecast errors of spherical harmonic degree 8 and above. Moreover, we demonstrate that including magnetic diffusion represents the evolution of reversed-flux patches more accurately, and that their predicted movement will cease to weaken the axial dipole field. Lastly, we predict the movement of the North Magnetic Pole up to 2025.0, which has a trajectory and displacement rate similar to that observed over the the past two decades.

## 4.1 Introduction

Earth's time-dependent internal magnetic field, commonly referred to as the core or main field, is generated through turbulent motion of the fluid and electrically conducting iron alloy comprising Earth's outer core. Although this field is generated within the core, it permeates the core-mantle boundary (CMB) and the overlying solid mantle, allowing it to be observed at the Earth's surface and above. Downwards continuation of surface observations allow models of the core field to be constructed, which describe its spatial variability as well as its time-dependence over the past decades to centuries (e.g. *Jackson et al.*, 2000, *Lesur et al.*, 2008, *Sabaka et al.*, 2015, *Gillet et al.*, 2015, *Finlay et al.*, 2016a). While temporal variation of the field, referred to as secular variation (SV), is ultimately the result of core fluid motion and magnetic diffusion (e.g. *Jackson and Finlay*, 2015), the latter contribution is often neglected under the frozen-flux assumption (*Roberts and Scott*, 1965). This approximation has allowed various workers to use geomagnetic observations to also model core fluid motion along the CMB (e.g *Vestine et al.*, 1967, *Whaler*, 1980, *Le Mouël*, 1984, *Bloxham*, 1988, *Lesur et al.*, 2010, *Kloss and Finlay*, 2019).

More recently, that is over the past decade or so, several workers have utilised such flow models to predict field evolution on yearly to decadal time scales, for example by calculating the field change that is expected when these fluid motions persist in time (*Beggan and Whaler*, 2009, *Whaler and Beggan*, 2015). In contrast, *Aubert* (2015) utilised full-sphere simulations of the geodynamo to forecast field evolution, an approach that is computationally more expensive, but does allow both core fluid flow and magnetic diffusion to be accounted for. Another forecasting method is given by *Barrois et al.* (2017), who do not employ geodynamo simulations directly, but instead predict field change using the statistical properties of the so-called Coupled Earth simulation (*Aubert*, 2013). Various authors have also implemented the use of an (ensemble) Kalman filter aimed at geomagnetic forecasting (*Beggan and Whaler*, 2009, *Barrois et al.*, 2017, 2018, *Bärenzung et al.*, 2018, *Beggan and Whaler*, 2018), an approach that also allows for a prediction of the uncertainties associated with the core field, and for the forecast to be

updated rather easily when new data becomes available.

There are several benefits to estimating the future state of the core field. For instance, such knowledge can contribute to our understanding of the physical processes governing SV, by retrospectively comparing field forecasts with geomagnetic observations (referred to as hindcasting). More practical advantages relate to naval and aerial navigation and orientation. For example, airport runway names correspond to the magnetic field configuration at the runway locations, and the non-steady nature of the field has required several runways to be renamed, a costly operation that field forecasts could help mitigate. In addition, forecasts allow the mapping of future hazardous regions, e.g. those where low-orbit spacecraft are more prone to damage from cosmic radiation (*Heirtzler*, 2002). Such a region is the South Atlantic Anomaly (SAA), where field intensities on the Earth's surface are anomalously low (typically less than 30,000 nT or so) (e.g. *Hartmann and Pacca*, 2009), currently covering parts of South Brazil and Uruguay (*Thébault et al.*, 2015).

In this work, we introduce a novel hybrid method for forecasting field evolution on yearly time scales, by combining the work of *Whaler and Beggan* (2015) and *Metman et al.* (2019). While magnetic diffusion is often considered negligible on short time intervals, we model it alongside core fluid motion, motivated by the fact that diffusion (like core fluid motion) can explain field evolution over several decades (*Metman et al.*, 2019), and that a description of both physical processes governing SV (i.e. fluid flow and diffusion) could return forecasts of increased accuracy. Several authors have already forecast field evolution by accounting for magnetic diffusion (*Aubert*, 2015, *Barrois et al.*, 2017), however our methods are fully independent of numerical geodynamo simulations (and therefore computationally inexpensive), and independent from the parameter space associated with such simulations, which typically deviates strongly from Earth-like values (e.g. *Christensen et al.*, 2010). This work is structured as follows: section 4.2 contains our forecasting strategy, in which we first consider the special case of negligible magnetic diffusion, and subsequently extend that formalism by modelling diffusion; section 4.3 contains several forecasting results, and demonstrations of how diffusion improves forecast performance; in the final section 4.4 we reflect on our results and their implications.

## 4.2 Methods

Here, we present our two-step method of forecasting core field evolution over yearly timescales. The first step consists of choosing a time window, hereafter referred to as the modelling period, and matching the SV over this period by modelling the processes governing the temporal evolution of the field. We then select a second time window over which we forecast field evolution by continuing these models forward in time. In what follows, this general approach is first applied together with the widely adopted frozen-flux limit of negligible diffusion, so that we may attribute SV to the motion of core fluid along the CMB only. This allows us to demonstrate that the spatial complexity of core fluid flow does not yield a significant global improvement of

field forecasts when it is increased beyond a certain level. While this result may be attributed to our disregard of processes such as flow acceleration and radial flow, or to our means of regularisation, we consider here the case of accounting for magnetic diffusion to further reduce forecast errors. Accordingly, we propose an extended forecasting approach, for which we use models which separately describe flow and diffusion to provide a more complete description of SV.

### 4.2.1 Field forecasts driven by core fluid flow only

We present in this section a method of forecasting field changes for the special case of negligible magnetic diffusion, largely based on the formalism by *Whaler and Beggan* (2015). We start with the radial part of the induction equation in the frozen-flux limit, describing time variability of the radial core magnetic field for a perfectly conducting fluid, which reads for the region immediately below the CMB as

$$\dot{B}_r = -\nabla_H \cdot (\mathbf{u} B_r) := \dot{B}_r^u. \tag{4.1}$$

Here, $\nabla_H \cdot = (\nabla - \hat{\mathbf{r}}\partial_r)\cdot$, $\mathbf{u}$ is the core fluid velocity (assumed horizontal and steady) , and $r$ is radius. It is clear that in this end-member case of secular variation, SV has only one contribution entirely governed by fluid flow, which we denote by $\dot{B}_r^u$.

As mentioned earlier, we proceed by first considering a modelling period $T$, which is regularly discretised with one-month time steps. Then, we find a steady $\mathbf{u}$ that best describes $\dot{B}_r$ over this period, by employing the formalism by *Whaler and Beggan* (2015). Specifically, we fit $\dot{B}_r$ as prescribed by the CHAOS-6-x7 field model (*Finlay et al.*, 2016b), which is expanded up to spherical harmonic degree $L = 14$. Additionally, $\mathbf{u}$ is assumed solenoidal (conforming to an incompressible fluid) allowing its partitioning into its toroidal and poloidal parts, each of which is also expanded by spherical harmonics up to degree $L_u$ (see e.g. *Whaler*, 1986). To circumvent the ill-posedness associated with this flow inversion we adopt the 'strong' norm by *Bloxham* (1988) penalising flow complexity, in place of explicitly assuming flow morphology (e.g. purely toroidal (*Whaler*, 1980) or tangentially geostrophic flow (*Le Mouël*, 1984); see *Holme* (2015) for an overview). Our modelled flow then minimises an unweighted quadratic cost function through

$$\mathbf{u} = (\mathbf{A}^T\mathbf{A} + \gamma\mathbf{D})^{-1}\mathbf{A}^T\dot{\mathbf{g}}, \tag{4.2}$$

where the matrix $\mathbf{A}$ corresponds to the equations of condition, $\dot{\mathbf{g}}$ is the vector containing the time derivative of all Gauss coefficients each evaluated at a set of time points, and $\mathbf{D}$ is the regularisation matrix scaled with a damping paramter $\gamma = 5 \times 10^{-5}$ (see for more details *Beggan and Whaler*, 2008, *Whaler and Beggan*, 2015). Several modelling periods are used, their length ranging from 1 to 9 years, and each terminating at the start of the subsequent forecast period.

Using these fluid flow models, core field forecasts are realised using a first-order Taylor

series of $B_r$. In conjunction with the frozen-flux approximation, and under the assumption that fluid flow modelled over $T$ remains steady over the forecasting period, this series approximates the time evolution of $B_r$ in terms of the flow-related SV contribution explicitly as

$$B_r(t_k) \simeq B_r(t_{k-1}) + (t_k - t_{k-1})\dot{B}_r^u(t_{k-1}), \tag{4.3}$$

with the integer $k$ an index corresponding to the time discretisation. This description allows a field forecast to be computed iteratively, using the field state and the flow contribution to SV at $t_{k-1}$. Additionally, the initial field state at the start of the forecast period (i.e. for $k = 0$) is prescribed by CHAOS-6-x7. For simplicity, the time step over the forecasting period $t_k - t_{k-1}$ is once more set at one month for all $k$.

### 4.2.2 Hybrid forecasts for field advection and diffusion

For the hybrid forecasts, our starting point is the full induction equation, which includes also the diffusive term:

$$\dot{B}_r = -\nabla_H \cdot (\mathbf{u}B_r) + \frac{\eta}{r}\nabla^2(rB_r), \tag{4.4}$$

$$= \dot{B}_r^u + \dot{B}_r^d, \tag{4.5}$$

where $\eta$ is the magnetic diffusivity (assumed uniform). We first apply the methods used for the frozen-flux case described in the previous section to optimise a steady $\mathbf{u}$ over a modelling period of choice. However, this flow model will never describe the SV over $T$ perfectly, and is therefore associated with a nonzero SV residual $\dot{B}_r - \hat{\dot{B}}_r^u$, where the hat denotes a best-fit estimate. To also model magnetic diffusion, motivated by the fact that increasing the complexity of fluid flow beyond a certain amount does not significantly reduce forecast errors (as will be shown later), we subsequently assume that $\dot{B}_r^d = \dot{B}_r - \hat{\dot{B}}_r^u$.

Magnetic diffusion is modelled using the formalism given by *Metman et al.* (2019), who provide a forward solution to the diffusion equation in terms of Galerkin polynomials (see eq. (8) and (15) in their work). While their study considers fitting the time-dependent $B_r$ using this Galerkin solution, their matrix exponential notation allows a straightforward derivation for the time-derivative, which we utilise to write the forward solution

$$\dot{B}_r^d = \sum_{\alpha=1}^{L(L+2)} \frac{\eta l_\alpha(l_\alpha+1)}{r^2}\boldsymbol{\xi}_\alpha^T(r)\mathbf{H}_\alpha \mathrm{expm}\big[\eta\mathbf{H}_\alpha(t-t_0)\big]\mathbf{q}_\alpha Y_\alpha(\theta,\phi), \tag{4.6}$$

where $Y_\alpha$ is the real-valued Schmidt semi-normalised spherical harmonic of degree $1 \leq l_\alpha \leq L$, and order $0 \leq m_\alpha \leq l_\alpha$, which has either azimuthal sine or cosine dependence, and where $L$ is the degree of truncation of the core field (here we set $L = 14$). Moreover, $\theta$ and $\phi$ denote respectively colatitude and longitude, the coefficients $\mathbf{q}_\alpha$ describe the structure of $B_r^d$ throughout the core, and expm$[\cdot]$ is the matrix exponential. The reader is referred to *Metman*

*et al.* (2019) for a detailed description of the vector containing the radial basis functions $\boldsymbol{\xi}_\alpha(r)$ (whose dimension $N$ corresponds to the number of radial modes used to describe $B_r^d$), and that of the associated matrix $\mathbf{H}_\alpha$ relating to the radially dependent part of the Laplacian in eq. (4.4).

Our aim is to best explain the flow residual with diffusion, therefore the optimised coefficients $\hat{\mathbf{q}}_\alpha$ are obtained through the minimisation of the regularised quadratic cost function

$$F = \int_T \int_{\mathrm{CMB}} \left(\dot{B}_r^d - \hat{\dot{B}}_r^d\right)^2 \mathrm{d}S\, \mathrm{d}t + \lambda \int_{\mathbb{R}^3} \hat{\dot{\mathbf{B}}}_0^2 \, \mathrm{d}V. \tag{4.7}$$

This choice of regularisation differs from that of *Metman et al.* (2019), who penalise large magnetic amplitudes throughout of the core. However, such a constraint could still result in high-amplitude SV, therefore we adopt a regularisation norm penalising the time-derivative field (second term on the r.h.s. of the cost function). The norm can also be interpreted as a penalisation of spatial heterogeneity of the modelled structure of $B_r^d$, similar to the norm used by *Bloxham* (1988) to minimise flow heterogeneity. The cost function is expressed in terms of our model coefficients, reducing it to

$$F = (\mathbf{g} - \mathbf{G}\hat{\mathbf{q}})^T \mathbf{W} (\mathbf{g} - \mathbf{G}\hat{\mathbf{q}}) + \lambda \hat{\mathbf{q}}^T \mathbf{H}^T \mathbf{H} \hat{\mathbf{q}}, \tag{4.8}$$

with $\hat{\mathbf{q}} = (\hat{\mathbf{q}}_1, \hat{\mathbf{q}}_2, \ldots, \hat{\mathbf{q}}_{L(L+2)})^T$, $\mathbf{W}$ a diagonal weighting matrix related to Simpson's rule for the numerical integration in time (see Appendix B in *Metman et al.*, 2019), $\mathbf{G} = \mathrm{diag}(\mathbf{G}_1, \mathbf{G}_2, \ldots, \mathbf{G}_{L(L+2)})$ a blockwise-diagonal forward mapping describing purely diffusive SV, where each block is defined as

$$G_{\alpha,ij} = \frac{\eta l_\alpha}{c^2} \left(\frac{c}{a}\right)^{l_\alpha+2} \left(\boldsymbol{\xi}_\alpha^T(c) \mathbf{H}_\alpha \mathrm{expm}[\eta \mathbf{H}_\alpha (t_i - t_0)]\right)_j, \tag{4.9}$$

and $t_k$ is the $k^{\mathrm{th}}$ nodal point in time. The least-squares cost function is then minimised as

$$\hat{\mathbf{q}} = (\mathbf{G}^T \mathbf{W} \mathbf{G} + \lambda \mathbf{H}^T \mathbf{H})^{-1} \mathbf{G}^T \mathbf{W} \dot{\mathbf{g}}^d. \tag{4.10}$$

where $\dot{\mathbf{g}}^d := \dot{\mathbf{g}} - \hat{\dot{\mathbf{g}}}^u$, and $\hat{\dot{\mathbf{g}}}^u$ are the best-fit secular variation coefficients from a flow model.

Having estimated both the fluid flow and magnetic diffusion over the modelling period, we are now in a state to make hybrid forecasts of the core field. This is achieved by using a first-order Taylor series where time evolution of $B_r$ written in terms of both these contributions:

$$B_r(t_k) \simeq B_r(t_{k-1}) + \left(\dot{B}_r^u(t_{k-1}) + \dot{B}_r^d(t_{k-1})\right)(t_k - t_{k-1}), \tag{4.11}$$

where the contributions $\dot{B}_r^u$ and $\dot{B}_r^d$ are computed through forward continuation of their respective descriptions obtained for the modelling period. Like the flow-only forecasts, we use time intervals of one month.

## 4.3 Results

In this section, we use the methods described above to invert the SV described by the time-dependent CHAOS-6-x7 field model (*Finlay et al.*, 2016b) for core fluid flow, or for fluid flow and diffusion, for which several modelling time windows are used. These models are first employed for the computation of hindcasts over 2010.0-2015.0, which allows us to assess the dependency of global and regional forecast errors on the parameter space used to account for core fluid motion and magnetic diffusion. Specifically, we show first for purely flow-based forecasts (obtained with $L_u = 8$ and $L_u = 14$) the RMS error in $\mathbf{B}$ as a function of time. Subsequently, we inspect time-averaged spectra of the RMS forecast error. Moreover, we make a comparison of forecasts based on only fluid flow and those accounting for fluid flow and diffusion, by showing for several $N$ the RMS forecast error as a function of time, time-averaged error spectra, time series of Gauss coefficients, and maps of the unsigned $B_r$ residual at the CMB and at the surface. Subsequently, we present a hybrid forecast for the 2018.0-2025.0 period, which includes the expected evolution of reversed-flux patches, and the predicted movement of the North Magnetic Pole. For comparison, we show also forecasts for which the SV in eq. (4.11) is predicted by a secondary field model, that is the 11th International Geomagnetic Reference Field (IGRF-11) (*Finlay et al.*, 2010) for the 2010.0-2015.0 forecast period, and the out-of-cycle 2015 World Magnetic Model (WMM2015v2) (*Chulliat et al.*, 2019) for the 2018.0-2025.0 period.

### 4.3.1 Purely flow-driven forecasts for 2010.0-2015.0

The global accuracy of our purely flow-driven ($N = 0$) forecasts is given as a function of time in Fig. 4.1, that is in terms of the RMS forecast error in $\mathbf{B}$ with respect to CHAOS-6-x7. These forecasts have been derived with 1, 3, 5, 7, or 9 years of SV data, with $L_u = 8$ (a and c) and $L_u = 14$ (b and d), and are evaluated at either the Earth's surface (a and b) or at the CMB (c and d). Also indicated is the forecast computed with the expected SV as given by IGRF-11 (thick dashed curves). The other line styles correspond to the length of modelling time window. For all forecasts, it can readily be seen that the global error increases monotonically with time, where this error grows more linearly when evaluated at the CMB (Fig. 4.1c and d) than at Earth's surface (Fig. 4.1a and b). Moreover, we find that the choice of modelling time window affects the forecast accuracy more strongly when it is evaluated at the Earth's surface, and that a shorter modelling period generally yields more accurate forecasts. In fact, at the Earth's surface only the 2007.0-2010.0 and 2009.0-2010.0 forecasts are more accurate than the IGRF-11 prediction; at the CMB all flow-based forecasts are more accurate than the IGRF-11 prediction. Additionally, by comparing panels a-b with c-d it can be seen there is no significant error reduction when the spatial flow complexity is increased by changing $L_u = 8$ to $L_u = 14$. The RMS forecast errors at 2015.0 for the flow-only predictions are summarised in Table 4.1 and 4.2.

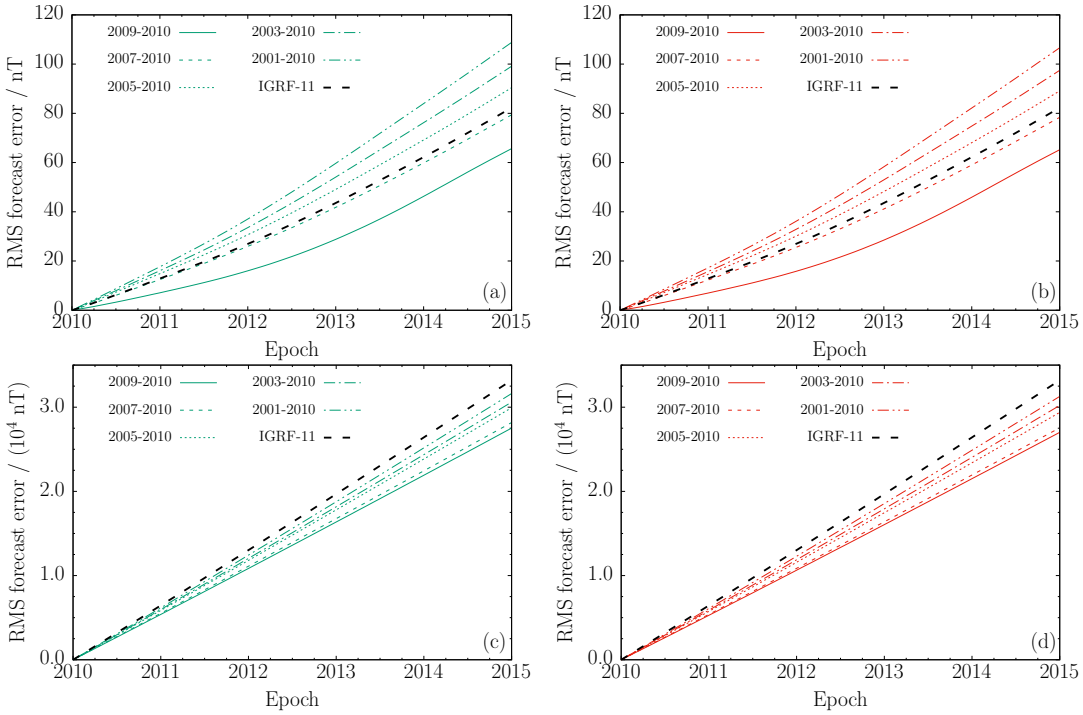


**Figure 4.1:** The RMS forecast error at the Earth's surface (a and b) and the CMB (c and d), for flow-only forecasts with $L_u = 8$ (a and c), with $L_u = 14$ (b and d), or with the SV prescribed by IGRF-11 (a-d). The line styles denote the choice of modelling time window.

| $L_u$ | 2001.0-2010.0 | | 2003.0-2010.0 | | 2005.0-2010.0 | | 2007.0-2010.0 | | 2009.0-2010.0 | |
|---|---|---|---|---|---|---|---|---|---|---|
| | $N=0$ | $N=2$ | $N=0$ | $N=2$ | $N=0$ | $N=2$ | $N=0$ | $N=2$ | $N=0$ | $N=2$ |
| 8 | 109 | 81 | 99 | 78 | 90 | 75 | 79 | 67 | 66 | 62 |
| 14 | 107 | 80 | 97 | 77 | 97 | 77 | 78 | 67 | 65 | 62 |

**Table 4.1:** The RMS forecast error with respect to CHAOS-6-x7 (in nT) at the Earth's surface and at 2015.0, obtained with several modelling periods, with $L_u \in \{8, 14\}$, and with $N \in \{0, 2\}$.

| $L_u$ | 2001.0-2010.0 | | 2003.0-2010.0 | | 2005.0-2010.0 | | 2007.0-2010.0 | | 2009.0-2010.0 | |
|---|---|---|---|---|---|---|---|---|---|---|
| | $N=0$ | $N=2$ | $N=0$ | $N=2$ | $N=0$ | $N=2$ | $N=0$ | $N=2$ | $N=0$ | $N=2$ |
| 8 | 3.2 | 1.2 | 3.1 | 1.1 | 3.0 | 0.92 | 2.8 | 0.69 | 2.8 | 0.62 |
| 14 | 3.1 | 1.2 | 3.0 | 1.1 | 2.9 | 0.92 | 2.8 | 0.69 | 2.7 | 0.62 |

**Table 4.2:** As Table 4.1, but with the error evaluated at the CMB (in $10^4$ nT).

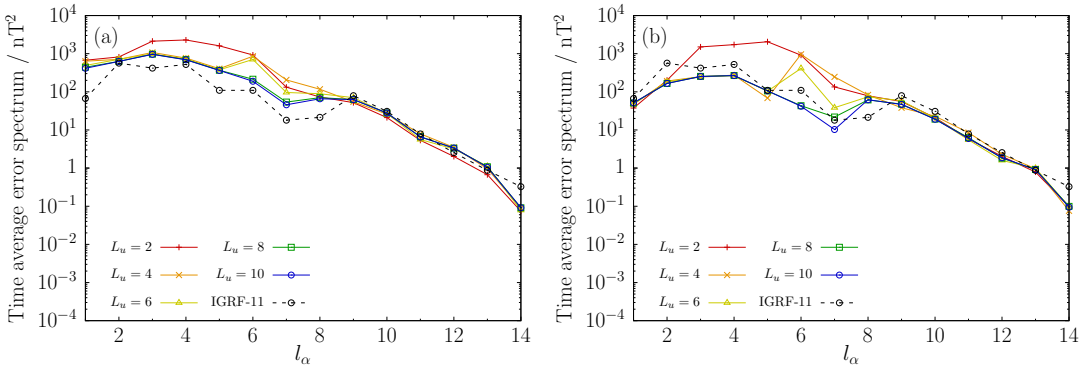


**Figure 4.2:** Power spectra of the RMS flow-only forecast error at Earth's surface, computed with the 2001.0-2010.0 and 2009.0-2010.0 modelling periods (a and b, respectively) and several $L_u$.

These RMS forecast errors may be partitioned in terms of spherical harmonic degree as

$$E(l) = \sum_{m=0}^{l} \frac{(l+1)}{5} \int_{2010.0}^{2015.0} \left(g_l^m(t) - \hat{g}_l^m(t)\right)^2 + \left(h_l^m(t) - \hat{h}_l^m(t)\right)^2 \mathrm{d}t, \tag{4.12}$$

where $g_l^m$ and $h_l^m$ are the time-dependent Gauss coefficients in their canonical representation, and the factor 5 arises from the averaging over a 5-year period. The sum of $E(l_\alpha)$ over $l_\alpha$ is then the squared error in $|\mathbf{B}|$, averaged over the Earth's surface and over the period $T$. These time-averaged error spectra have been computed for $T = [2010.0, 2015.0]$, using the modelling periods 2001.0-2010.0 and 2009.0-2010.0 (Fig. 4.2a and 4.2b, respectively), and several $L_u$; error spectra for the IGRF-11 SV forecast have also been computed. As suggested by Fig. 4.1, these spectra show there is no significant improvement when $L_u$ is increased beyond 8. Additionally, we find that increasing $L_u$ only returns a significant error reduction for field features of degree 7 or lower. For $8 < l_\alpha < 14$, the shape of these error spectra are similar to those for the IGRF-11 SV prediction, whereas for $l_\alpha < 8$ and the 2001.0-2010.0 modelling period it actually performs better than the flow-dependent forecasts. Additionally, for the 2009.0-2010.0 period error amplitudes are relatively small, confirming that a shorter modelling period returns more accurate forecasts.

### 4.3.2 Hybrid forecasts for 2010.0-2015.0

As more spatially complex flows do not necessarily provide more accurate forecasts (increasing $L_u$ beyond 8 does not significantly reduce the RMS forecast error), we now focus attention on forecasts that depend on the sequential estimation of core-fluid flow and magnetic diffusion. To that end, we have adopted the hybrid forecasting scheme (section 4.2.2), for which we have set damping parameters $\lambda$ between $10^{-9}$ and $10^{-8}$ (depending on the modelling time window) to regularise the diffusive solution (eq. 4.10). These values ensure we invert matrices with a (2-norm) condition number $< 10^8$, such that our solutions are computationally tractable when using double precision variables. For the presented hybrid forecasts $N \leq 2$, such that the

degrees of freedom used to model diffusion is always less than or equal to that used to the model the most complex fluid flow considered above (that is less than or equal to 448 when $L_u = 14$). It is true that using such a low number of radial modes ignores diffusion of radially fine-scaled features, and therefore imperfectly captures SV over the modelling period. However, larger $N$ are generally found to return rapid temporal variation of the core field predictions, associated with large forecast residuals. A conservative choice for $N$ is therefore in line with our primary objective of improving geomagnetic forecasts.

Figure 4.3 shows the RMS forecast error for the forecast period 2010.0-2015.0 in $\mathbf{B}$ with respect to CHAOS-6-x7, evaluated at the Earth's surface or at the CMB (a-b and c-d, respectively), and obtained with $L_u = 8$ (a and c) or $L_u = 14$ (b and d); in all cases $N = 2$. Compared to the purely flow-based predictions (Fig. 4.1), we find the hybrid scheme has a smaller global error at all times. The relative improvement made when diffusion is accounted for depends, among other things, on the modelling period used. For example, at the Earth's surface we find for a modelling period of 2001.0-2010.0 and $L_u = 14$ a global forecast error reduction of 25% at 2015.0, while for 2009.0-2010.0 modelling window this reduction is only 5%. The relative overall improvement is much greater at the CMB: for $L_u = 14$ and the 2001.0-2010.0 modelling period the RMS forecast error at 2015.0 is reduced by 61%; using $T = [2009.0, 2010.0]$ instead gives an RMS error reduction in excess of 77% at 2015.0. Lastly, we note that with the hybrid scheme we again find that increasing $L_u$ from 8 to 14 generally yields a negligible reduction in global forecast error, as the relative improvement is typically 1%. The purely flow-based and hybrid RMS forecast errors at 2015.0 are listed in Table 4.1 (at Earth's surface) and 4.2 (at the CMB) for several modelling windows.

Error spectra of the global RMS error at Earth's surface are given in Fig. 4.4, which have been computed with the 2001.0-2010.0 and 2009.0-2010.0 modelling periods (a and b, respectively), $L_u = 14$, and several $N$; the error spectrum associated with the IGRF-11 SV forecast is given as dashed curves. For both modelling periods it can be noted that including magnetic diffusion predominantly results in reduced errors for degrees higher than 8, although for the 2001.0-2010.0 modelling window diffusion also improves forecasts for features of degree 1 to 5 when $N = 2$. Similar to the purely flow-based forecasts we find that the IGRF-11 SV forecast returns rather large residuals for degree 9 and above, whereas for degrees 2 to 8 the $N = 2$ forecasts perform similarly (2001.0-2010.0) or better (2009.0-2010.0); for degree one and the 2001.0-2010.0 time window the IGRF-11 prediction outperforms the other forecasts.

Predicted time series of individual Gauss coefficients also demonstrate how accounting for magnetic diffusion mainly affects the predicted evolution of intermediate to high-degree field features. For example Fig. 4.5 shows time series of the Gauss coefficients $g_1^0$, $g_7^0$, and $g_{14}^0$, as described by CHAOS-6-x7 (solid red). Shown jointly are the Gauss coefficients from the forecasts obtained with the 2009.0-2010.0 modelling period, $L_u = 14$, and either $N = 0$ or $N = 2$ (dashed black and dotted blue, respectively). Additionally, the dot-dashed green curves show the time series from the IGRF-11 SV prediction. Clearly, magnetic diffusion has little effect on the forecast for $g_1^0$, as all predictions exhibit similarly linear, yet overestimated

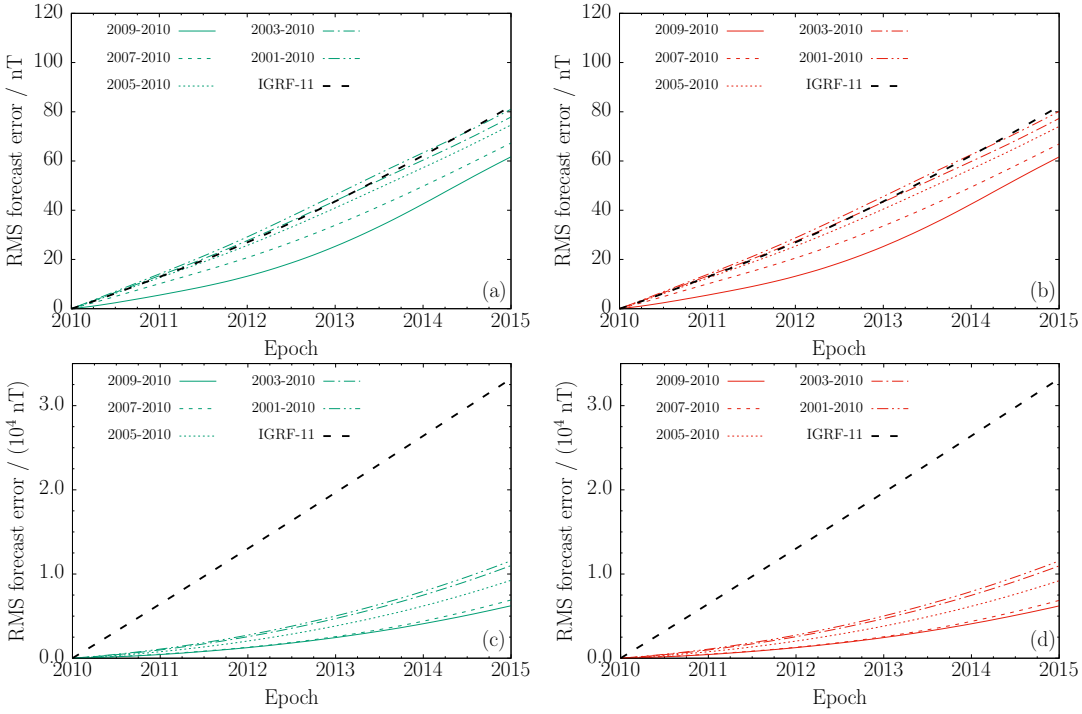


**Figure 4.3:** As Fig. 4.1, but for the hybrid forecasts based on fluid flow and diffusion with $N = 2$.

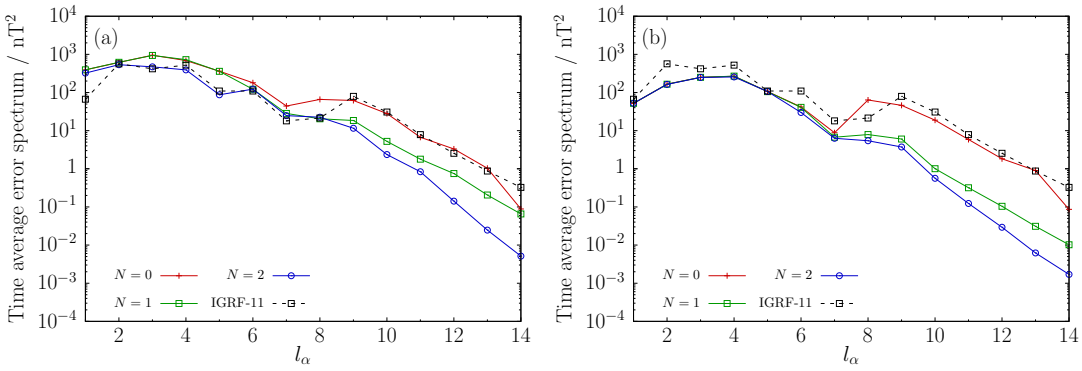


**Figure 4.4:** As Fig. 4.2, but for the hybrid forecasts based on fluid flow and diffusion with $L_u = 14$ and $N \in \{0, 1, 2\}$.

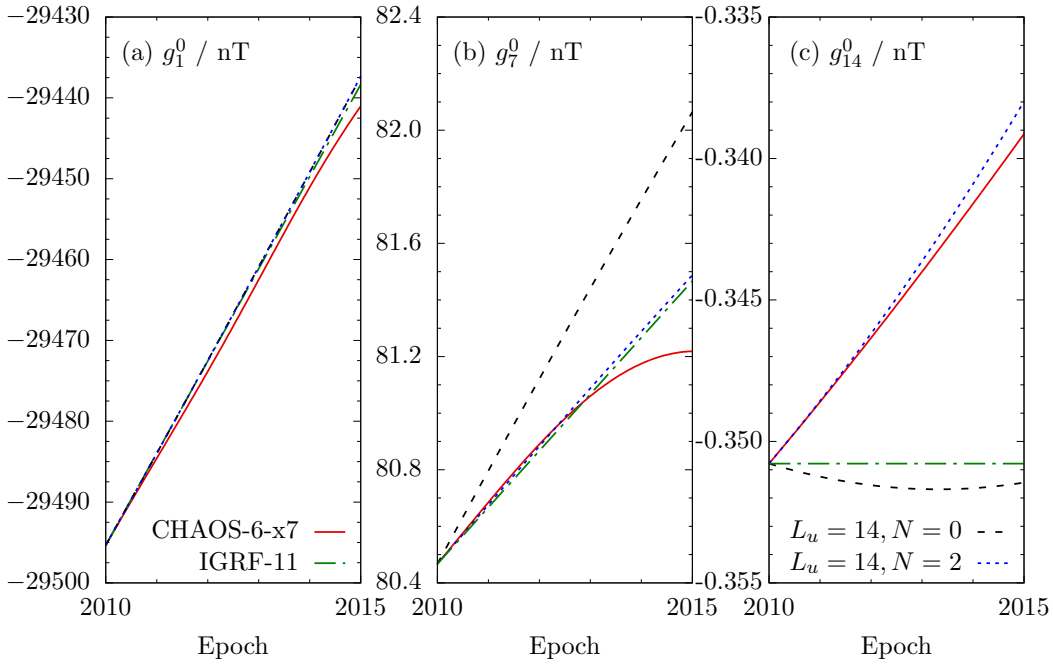


**Figure 4.5:** Time series of selected Gauss coefficients from CHAOS-6-x7 (solid red) and those predicted with $L_u = 14$ and $N = 0$ (dashed black), with $L_u = 14$ and $N = 2$ (dotted blue), and with the SV prescribed by IGRF-11 (dot-dashed green). The 2009.0-2010.0 modelling period was used for the flow and hybrid forecasts.

growth. Moreover, all forecasts show a strengthening in $g_7^0$, although the purely flow-based prediction overestimates the slope, and the hybrid and IGRF-11 forecasts cannot match the decelaration towards the end of the period. This recent behaviour of $g_7^0$ coincides with an obsereved geomagnetic jerk in 2014 (*Torta et al.*, 2015), i.e. a jump change in the secular acceleration. The evolution of $g_{14}^0$ as given by CHAOS-6-x7 is not at all matched by the purely flow-driven and IGRF-11 forecasts, whereas the hybrid forecast is markedly more accurate. However, it should be noted that the IGRF-11 forecast is only for spherical harmonic degree 9 and lower, therefore higher degree coefficients are necessarily assumed constant.

Lastly, we comment on the spatial distribution of forecast errors with respect to CHAOS-6-x7. For example, Figure 4.6 shows the unsigned error in $B_r$ at the CMB and at selected epochs for the forecasts calculated with $L_u = 14$, the 2009.0-2010.0 modelling period, and with either $N = 0$ (a and b) or $N = 2$ (c and d). It is evident that the hybrid forecast produces much reduced errors everywhere (compare Fig. 4.6a and b with c and d), where particularly large error reductions are found below the west of Chile, the South Atlantic, and Central Asia. The largest error amplitudes are found along the $-90°$ and $90°$ meridians and along the $-30°$ circle of latitude, coinciding with the regions where CHAOS-6-x7 has the fastest field change; the smallest forecast errors are generally in the Pacific Hemisphere. Similarly, Fig. 4.7 shows for the same forecast the unsigned $B_r$ error at Earth's surface. Clearly, the error reduction acquired with the hybrid approach is not as significant as at the CMB since it is of small scale. At Earth's surface, we find a hemispherical asymmetry in error distribution, with the largest errors within

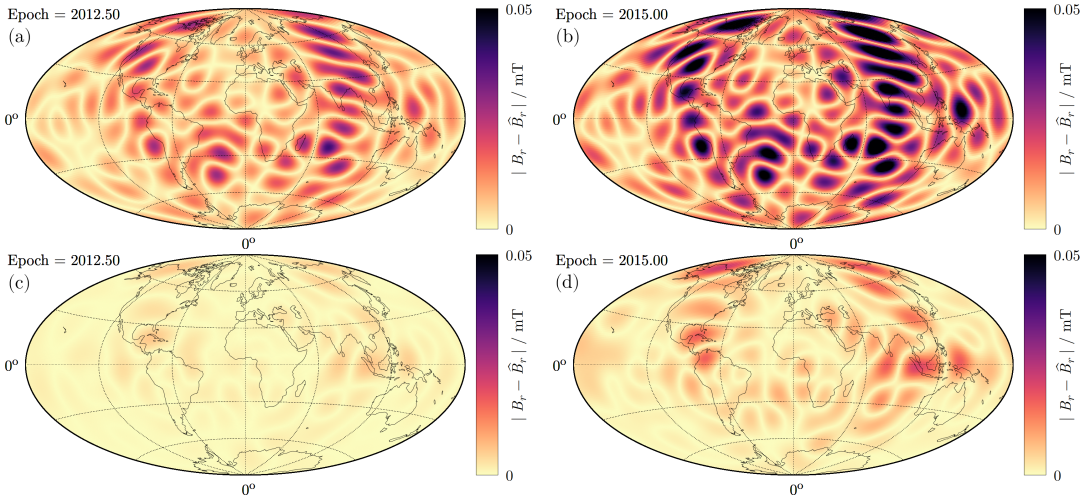


**Figure 4.6:** The unsigned residual $B_r$ at the CMB and at selected epochs, for the forecasts obtained with the 2009.0-2010.0 modelling window, $L_u = 14$, and with either $N = 0$ (a-b) or $N = 2$ (c-d).

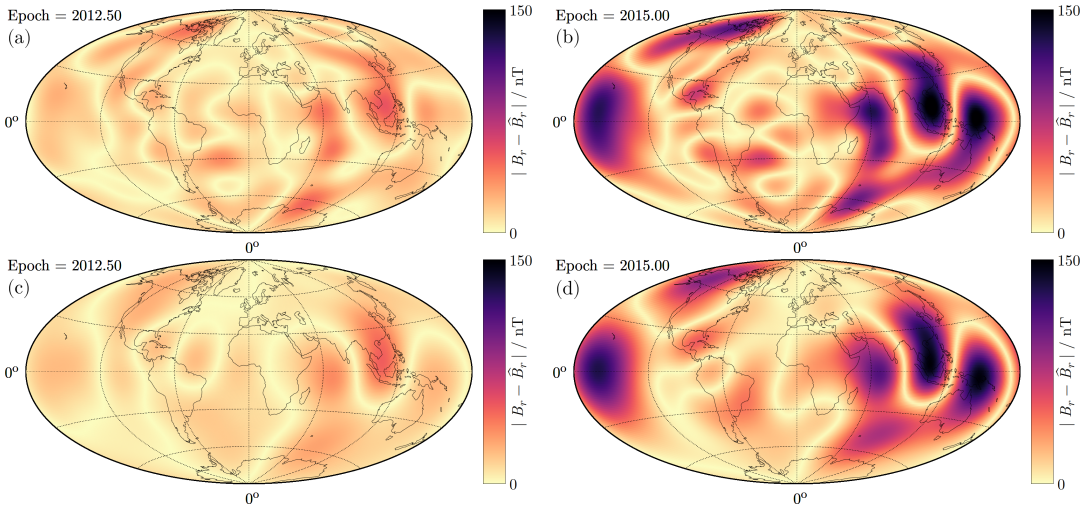


**Figure 4.7:** As Fig. 4.6, but at the Earth's surface. Note the change in colourbar scale.

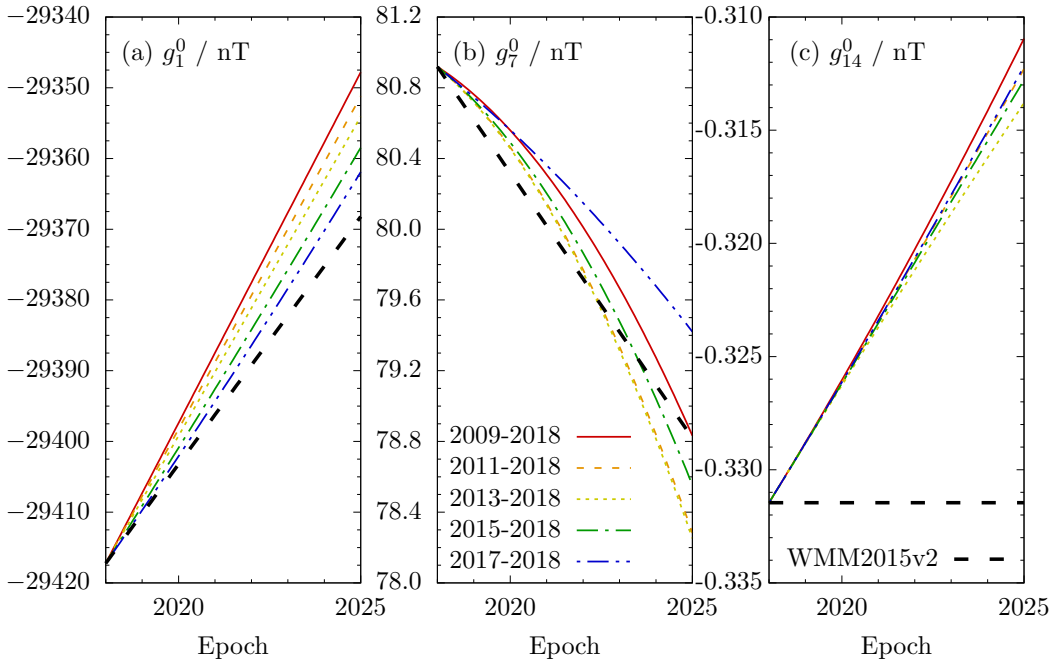


**Figure 4.8:** Predicted evolution of selected Gauss coefficients from the hybrid forecasts (obtained with $L_u = 14$, $N = 2$, and several modelling windows), and with the SV prescribed by WMM2015-v2.

the Indo-Pacific Hemisphere and the smallest in the Atlantic.

### 4.3.3 Hybrid forecasts for 2018.0-2025.0 and IGRF-13 main field candidate

We present now hybrid forecasts of core field evolution for the period 2018.0-2025.0. These predictions have been obtained with $L_u = 14$, $N = 2$, and several modelling time windows ranging from 2009.0-2018.0 to 2017.0-2018.0, which have been sampled monthly. The same $\lambda$-values are used as in the previous section, where the exact choice depends on the length of the modelling time window (e.g. for the 1-year modelling windows 2017.0-2018.0 and 2009.0-2010.0, $\lambda$ is equal). For comparison, we also computed a forecast by substituting in eq. (4.11) the SV prediction from the out-of-cycle World Magnetic Model for 2015-2020 (WMM2015v2) (*Chulliat et al.*, 2019), which goes up to for spherical harmonic degrees 12.

Fig. 4.8 shows predicted time series of selected Gauss coefficients. For $g_1^0$ and $g_{14}^0$ we expect to see continued growth, in agreement with their behaviour over 2010.0-2015.0 (Fig. 4.5). In contrast, $g_7^0$ has strengthened over 2010.0-2015.0 or so (Fig. 4.5), whereas we find for this coefficient accelerated decay up to 2025.0. Since in our formalism flow-related contributions to predicted field evolution are steady (we consider only steady core fluid motion), this increasingly rapid decay exemplifies how magnetic diffusion can provide a significant contribution to the full hybrid forecast. Furthermore, faster axial dipole decay is expected from forecasts computed with longer modelling windows, while for the evolution of $g_7^0$ and $g_{14}^0$ we find no discernible correlation with the modelling windows used. Lastly, we find more disparity between the hybrid and WMM2015v2 forecasts with increasing spherical harmonic degree; this

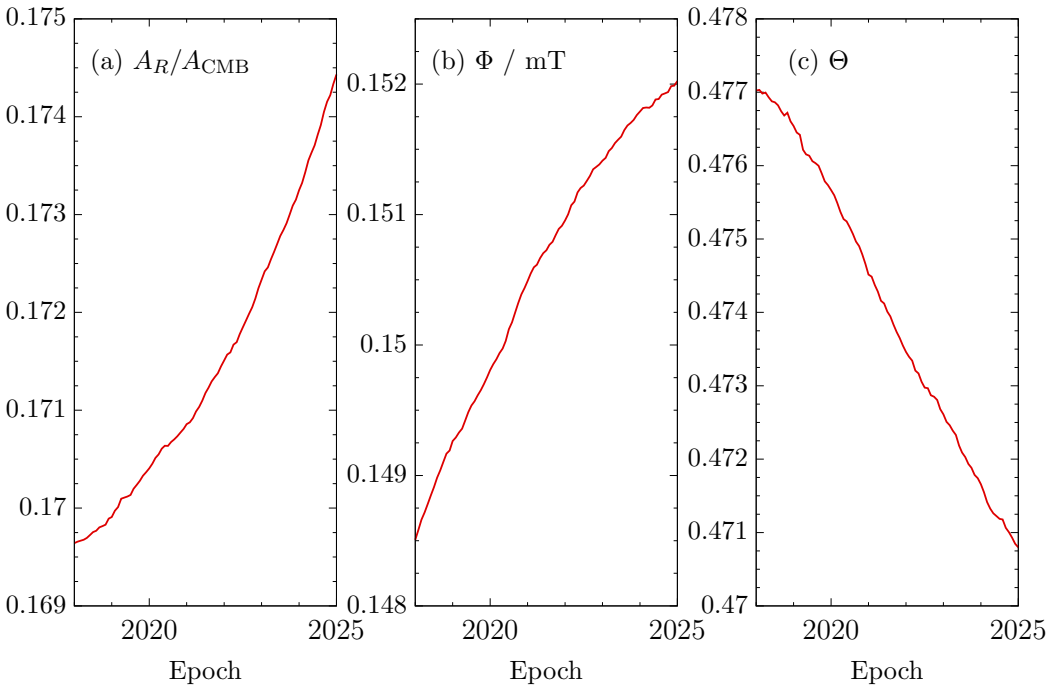


**Figure 4.9:** Predicted evolution of the relative reversed surface area with $A_{\mathrm{CMB}}$ the CMB surface area (a), the average magnetic flux through reversed flux patches (b), and the averaged unsigned latitudinal weighting factor over reversed flux (c).

difference is particularly large for $g_{14}^0$, as the WMM2015v2 SV forecast is constant for degrees 13 and above.

We have also calculated the expected change in several global quantities describing the manifestation of reversed flux on the CMB (Fig. 4.9), motivated by the reduced hybrid forecast errors in the South Atlantic (Fig. 4.6), where these features are particularly prevalent (*Gubbins and Roberts*, 1987, *Terra-Nova et al.*, 2015, *Metman et al.*, 2018). These quantities measure the reversed-flux surface area on the CMB ($A_R$), the average magnetic flux through the reversed surface area ($\Phi$), and a measure of the average latitude of reversed flux ($\Theta \in [0, 1]$, vanishes when reversed flux is concentrated at the equator), defined respectively as

$$A_R(t) = \int_{S_R(t)} \mathrm{d}S, \tag{4.13}$$

$$\Phi(t) = \frac{1}{A_R(t)} \int_{S_R(t)} |B_r(\mathbf{r}, t)| \, \mathrm{d}S, \tag{4.14}$$

$$\Theta(t) = \frac{1}{A_R(t)} \int_{S_R(t)} |\cos\theta| \, \mathrm{d}S, \tag{4.15}$$

where $S_R$ is the combined reversed part of the CMB. These three quantities have all been computed with a degree-3 magnetic equator (see for more details *Metman et al.*, 2018). For the period 2018.0-2025.0, we expect an overall growth and intensification of reversed-flux patches

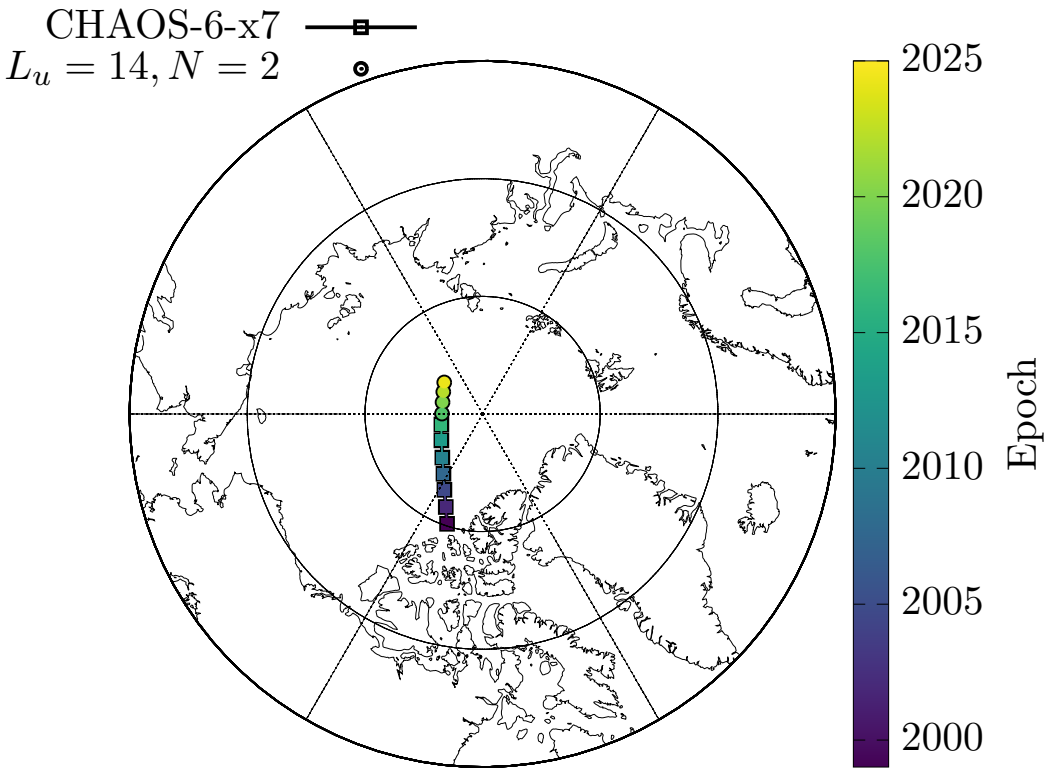


**Figure 4.10:** Predicted movement of the North Magnetic Pole (circles), obtained with $L_u = 14$, $N = 2$, and the 2009-2010 time window. Squares indicate the trajectory described by CHAOS-6-x7.

(Fig. 4.9a and b), and predict these features to migrate towards the equator (Fig 4.9c). This predicted movement contrasts with the overall poleward migration of reversed flux over the 20th century, which has been considered the main cause for the axial dipole decay over that period (*Finlay et al.*, 2016b, *Metman et al.*, 2018). As such, the forecast future decay of the axial dipole (Fig. 4.8), can be attributed only to growth and intensification of the reversed field.

Finally, we comment on the continued movement of the North Magnetic Pole, which has accelerated over the past three decades (*Mandea and Dormy*, 2003). The hybrid $L_u = 14$, $N = 2$, forecast obtained with the 2017.0-2018.0 modelling window, predicts this pole will continue to steadily move towards Russia, and to cross the $180^\circ$ meridian over 2018.0-2025.0, with an time-average velocity of approximately 46 km yr$^{-1}$.

## 4.4 Discussion

We have presented a new, computationally inexpensive method to forecast the short-term evolution of the core magnetic field. With our framework, we combine the work of *Whaler and Beggan* (2015) and *Metman et al.* (2019), by first inverting the SV as given by a time-dependent field model (here chosen to be CHAOS-6-x7) for steady core fluid motion, and subsequently inverting the SV residual generated by this flow to model magnetic diffusion. The associated forecasts are then computed by evaluating the flow and diffusion models at some time of inter-

est, to calculate the associated field change. We find limited reduction in global forecast accuracy when the spatial complexity of fluid flow is increased beyond $L_u = 8$, whereas accounting for diffusion with coarse radial resolution can result in a significant forecast improvement on yearly timescales, in particular for features of high spherical harmonic degree. Therefore, due to the attenuation of the field away from the CMB, the hybrid forecasts (accounting for fluid flow and diffusion) perform particularly well at the CMB (compare e.g. Table 4.1 and 4.2). Moreover, by correcting for diffusion we find relatively large forecast error reductions in the South Atlantic, demonstrating that patches of reversed-flux are captured well with the hybrid scheme. Reversed-flux patches are expected to contribute to axial dipole decay up to 2025.0 through their proliferation and intensification. Lastly, we find persistent rapid movement of the North Magnetic Pole up to 2025.0, with an average velocity of 46 km yr$^{-1}$.

Our flow models have little effect on the prediction of field features characterised by a spherical harmonic degree higher than 8. For these degrees, the purely flow-based forecast error spectra (Fig. 4.2) are independent of the spatial complexity of the flow. Moreover, the $l_\alpha > 8$ part of these error spectra bears a striking resemblance to those of the IGRF SV forecast. SV predictions from the latter model are provided up to degree 8 only (see e.g. Table 2 in *Finlay et al.*, 2010), therefore predictions for higher degree coefficients are made by assuming constant SV (often referred to as a *no-cast*). Since our flow models produce high-degree forecast errors very similar to those obtained with this no-cast (Fig. 4.2), it is seems that our core flows generate little to no high-degree SV. This behaviour is, for example, also observed in Fig. 4.5 for the case of $L_u = 14, N = 0$, which shows little overall temporal change in $g_{14}^0$ compared to other (lower-degree) coefficients. How can we explain the limited SV produced by our modelled high-degree flow? It is likely that this behaviour is due to the regularisation imposed in the flow inversion, which may damp small-wavelength flow to such an extent that it provides a negligible contribution to global field evolution. Further investigation is required to determine if this is a robust feature of our flow-based forecasts, e.g. by considering the effect different damping parameter values, or different means of regularisation (e.g. the use of a kinetic energy norm (*Madden and Le Mouël*, 1982) in place of the 'strong' norm (*Bloxham*, 1988) used here, which will penalise higher degree flow less).

The global forecasting accuracy achieved with our hybrid method is comparable, and occasionally higher, than that reported in previous works. For example, *Beggan and Whaler* (2009), *Aubert* (2015), *Whaler and Beggan* (2015), and *Beggan and Whaler* (2018) already reported forecasts for which the global RMS error steadily increases over yearly time scales (as we demonstrate in Fig. 4.1 and 4.3). In addition, for the modelling periods 2001.0-2010.0, 2005.0-2010.0, and 2007.0-2010.0 our global RMS forecast error at the Earth's surface in 2015.0 is smaller than for the forecasts presented by *Whaler and Beggan* (2015) and *Beggan and Whaler* (2018) (see respectively Table 2 and 1 in these works). When we compare our results with the best performing forecast of *Whaler and Beggan* (2015) (i.e. that obtained with the 2007.0-2010.0 modelling window) the relative difference in the RMS surface error at 2014.5 is slight, approximately 5%. Similarly, *Bärenzung et al.* (2018) report an RMS forecast error at

the Earth's surface of 66 nT at the end of a 2010.0-2015.0 forecasting period, which is roughly 6% higher than our best performing hybrid forecast (Table 4.1). Considering these rather small reductions in forecast error obtained with our hybrid scheme, we emphasise once more that accounting for magnetic diffusion appears useful predominantly for forecasting field evolution at the CMB instead of at the Earth's surface, with the CMB error reductions being proportionally much larger (Table 4.2). Additionally, we note that the RMS error in $|\mathbf{B}|$ describes only how well the field is forecast in an average sense, and other methods may still outperform our hybrid approach regionally or locally.

We note a clear positive correlation between the length of the modelling period and the global forecast error (Fig. 4.1 and 4.3), which is likely due to the steady nature of our modelled core flows. Within a relatively long modelling period (e.g. 2001.0-2010.0), there is an increased amount of short-period fluctuation in the SV, which a steady flow cannot explain. Indeed, the reduction in the RMS surface error achieved with the hybrid scheme is relatively large for long modelling periods (Table 4.1), which may be attributed to diffusion allowing a more accurate description of short-period SV over the modelling period. A better description of short-period SV could also be accomplished by including higher-order terms in eq. (4.11), e.g. by also observations of secular acceleration for fluid flow acceleration (as done by *Whaler and Beggan* (2015)) and/or calculating the secular acceleration generated by diffusion (e.g. by taking a time derivative of eq. (4.6)). As the error of truncation associated with eq. (4.11) is then $\mathcal{O}\big((t_k - t_{k-1})^3\big)$ (for sufficiently short time intervals), such an approach could allow for forecasts of further increased accuracy. Nevertheless, it is of note that our hybrid forecasts generally perform better than those based on fluid flow and flow acceleration (e.g. *Whaler and Beggan*, 2015), suggesting that accounting for diffusion is more advantageous than including higher-order terms in eq. (4.11).

Within our formalism, it is assumed that the SV residual between CHAOS-6-x7 and the steady core-flow models may be fully attributed to magnetic diffusion, while in reality it is uncertain how much diffusion truly contributes to the observed short-term SV. Recent work has shown that magnetic diffusion alone can account almost entirely for core field evolution even over short time windows (*Metman et al.*, 2019), therefore the diffusive contribution to short-term SV need not be small with respect to that of fluid flow. Nevertheless, we consider it more physically realistic to let core fluid flow explain most of the SV, as purely diffusive field evolution is not self-sustainable (e.g. *Gubbins and Roberts*, 1987), and depends on fluid flow to generate the concentrations of the magnetic field that subsequently diffusive (e.g. *Bloxham*, 1986). These considerations are reflected within our approach, by first inverting SV for core fluid flow before correcting for diffusion, and not vice versa, although the induction equation dictates that fluid flow and diffusion occur simultaneously. We find that the diffusion term acts primarily as a correction for high spherical harmonic degrees. This behaviour is certainly physically reasonable as diffusion should operate most rapidly on small magnetic length scales. Our means of accounting for diffusion therefore appears a reasonable method to augment the frozen-flux description, as this approximation should indeed fail for sufficiently small magnetic

length scales.

# References


Aubert, J. (2013), Flow throughout the Earth's core inverted from geomagnetic observations and numerical dynamo models, *Geophysical Journal International*, *192*(2), 537–556. 4.1

Aubert, J. (2015), Geomagnetic forecasts driven by thermal wind dynamics in the Earth's core, *Geophysical Journal International*, *203*(3), 1738–1751. 4.1, 4.4

Bärenzung, J., M. Holschneider, J. Wicht, S. Sanchez, and V. Lesur (2018), Modeling and predicting the short-term evolution of the geomagnetic field, *Journal of Geophysical Research: Solid Earth*, *123*(6), 4539–4560. 4.1, 4.4

Barrois, O., N. Gillet, and J. Aubert (2017), Contributions to the geomagnetic secular variation from a reanalysis of core surface dynamics, *Geophysical Journal International*, *211*(1), 50–68. 4.1

Barrois, O., M. D. Hammer, C. C. Finlay, Y. Martin, and N. Gillet (2018), Assimilation of ground and satellite magnetic measurements: inference of core surface magnetic and velocity field changes, *Geophysical Journal International*, *215*(1), 695–712. 4.1

Beggan, C., and K. Whaler (2008), Core flow modelling assumptions, *Physics of the Earth and Planetary Interiors*, *167*(3), 217 – 222. 4.2.1

Beggan, C. D., and K. A. Whaler (2009), Forecasting change of the magnetic field using core surface flows and ensemble Kalman filtering, *Geophysical Research Letters*, *36*(18). 4.1, 4.4

Beggan, C. D., and K. A. Whaler (2018), Ensemble Kalman filter analysis of magnetic field models during the CHAMP-Swarm gap, *Physics of the Earth and Planetary Interiors*, *281*, 103–110. 4.1, 4.4

Bloxham, J. (1986), The expulsion of magnetic flux from the Earth's core, *Geophysical Journal of the Royal Astronomical Society*, *87*(2), 669–678. 4.4

Bloxham, J. (1988), The determination of fluid flow at the core surface from geomagnetic observations, in *Mathematical Geophysics: A Survey of Recent Developments in Seismology and Geodynamics*, edited by N. J. Vlaar, G. Nolet, M. J. R. Wortel, and S. A. P. L. Cloetingh, pp. 189–208, Springer Netherlands, Dordrecht. 4.1, 4.2.1, 4.2.2, 4.4

Christensen, U. R., J. Aubert, and G. Hulot (2010), Conditions for Earth-like geodynamo models, *Earth and Planetary Science Letters*, *296*(3), 487–496. 4.1

Chulliat, A., W. Brown, P. Alken, S. Macmillan, M. Nair, C. Beggan, A. Woods, B. Hamilton, B. Meyer, and R. Redmon (2019), Out-of-cycle update of the US/UK World Magnetic Model for 2015-2020: Technical note, *National Centers for Environmental Information, NOAA*. 4.3, 4.3.3

Finlay, C. C., B. Langlais, F. J. Lowes, M. Mandea, M. Menvielle, L. Tøffner-Clausen, N. Olsen, A. Tangborn, Z. Wei, C. Manoj, S. Maus, S. McLean, A. W. P. Thomson, B. Hamilton, C. D. Beggan, S. Macmillan, T. A. Chernova, T. I. Zvereva, T. N. Bondar, V. P. Golovkov, A. Chambodut, A. Chulliat, E. Thbault, G. Hulot, H. Lühr, I. Michaelis, I. Wardinski, J. Rauberg, M. Hamoudi, M. Rother, V. Lesur, R. Holme, T. J. Sabaka, and W. Kuang (2010), International Geomagnetic Reference Field: the eleventh generation, *Geophysical Journal International*, *183*(3), 1216–1230. 4.3, 4.4

Finlay, C. C., N. Olsen, S. Kotsiaros, N. Gillet, and L. Tøffner-Clausen (2016a), Recent geomagnetic secular variation from swarm and ground observatories as estimated in the CHAOS-6 geomagnetic field model, *Earth, Planets and Space*, *68*(1), 112. 4.1

Finlay, C. C., J. Aubert, and N. Gillet (2016b), Gyre-driven decay of the Earth's magnetic dipole, *Nature Geoscience*, *7*. 4.2.1, 4.3, 4.3.3

Gillet, N., O. Barrois, and C. C. Finlay (2015), Stochastic forecasting of the geomagnetic field from the COV-OBS.x1 geomagnetic field model, and candidate models for IGRF-12, *Earth, Planets and Space*, *67*(1), 71. 4.1

Gubbins, D., and P. H. Roberts (1987), Magnetohydrodynamics of the Earth's core, in *Geomagnetism*, vol. 2, chap. 1, Academic Press. 4.3.3, 4.4

Hartmann, G. A., and I. G. Pacca (2009), Time evolution of the South Atlantic Magnetic Anomaly, *Anais da Academia Brasileira de Ciências*, *81*, 243 – 255. 4.1

Heirtzler, J. (2002), The future of the South Atlantic anomaly and implications for radiation damage in space, *Journal of Atmospheric and Solar-Terrestrial Physics*, *64*(16), 1701 – 1708. 4.1

Holme, R. (2015), Large-scale flow in the core, in *Treatise on Geophysics*, vol. 8, chap. 4, pp. 91–113, Elsevier. 4.2.1

Jackson, A., and C. Finlay (2015), Geomagnetic secular variation and its applications to the core, in *Treatise on Geophysics*, vol. 5, second ed., chap. 5, Elsevier, Oxford. 4.1

Jackson, A., A. R. T. Jonkers, and M. R. Walker (2000), Four centuries of geomagnetic secular variation from historical records, *Philosophical Transactions of the Royal Society of London. Series A: Mathematical, Physical and Engineering Sciences*, *358*(1768), 957–990. 4.1

Kloss, C., and C. C. Finlay (2019), Time-dependent low-latitude core flow and geomagnetic field acceleration pulses, *Geophysical Journal International*, *217*(1), 140–168. 4.1

Le Mouël, J. (1984), Outer core geostrophic flow and secular variation of Earth's magnetic field, *Nature*, *311*, 734–735. 4.1, 4.2.1

Lesur, V., I. Wardinski, M. Rother, and M. Mandea (2008), GRIMM: The GFZ reference internal magnetic model based on vector satellite and observatory data, *Geophysical Journal International*, *173*(2), 382–394. 4.1

Lesur, V., I. Wardinski, S. Asari, B. Minchev, and M. Mandea (2010), Modelling the Earth's core magnetic field under flow constraints, *Earth, Planets and Space*, *62*(6), 503–516. 4.1

Madden, T., and J. Le Mouël (1982), The recent secular variation and the motions at the core surface, *Philosophical Transactions of the Royal Society of London. Series A, Mathematical and Physical Sciences*, *306*(1492), 271–280. 4.4

Mandea, M., and E. Dormy (2003), Asymmetric behavior of magnetic dip poles, *Earth, Planets and Space*, *55*(3), 153–157. 4.3.3

Metman, M. C., P. W. Livermore, and J. E. Mound (2018), The reversed and normal flux contributions to axial dipole decay for 1880-2015, *Physics of the Earth and Planetary Interiors*, *276*, 106 – 117. 4.3.3, 4.3.3

Metman, M. C., P. W. Livermore, J. E. Mound, and C. D. Beggan (2019), Modelling decadal secular variation with only magnetic diffusion, *Geophysical Journal International*. 4.1, 4.2.2, 4.2.2, 4.2.2, 4.2.2, 4.4

Roberts, P. H., and S. Scott (1965), On analysis of the secular variation, *Journal of Geomagnetism and Geoelectricity*, *17*(2), 137–151. 4.1

Sabaka, T. J., N. Olsen, R. H. Tyler, and A. Kuvshinov (2015), CM5, a pre-Swarm comprehensive geomagnetic field model derived from over 12yr of CHAMP, Ørsted, SAC-C and observatory data, *Geophysical Journal International*, *200*(3), 1596–1626. 4.1

Terra-Nova, F., H. Amit, G. A. Hartmann, and R. I. F. Trindade (2015), The time dependence of reversed archeomagnetic flux patches, *Journal of Geophysical Research: Solid Earth*, *120*(2), 691–704. 4.3.3

Thébault, E., C. C. Finlay, C. D. Beggan, P. Alken, J. Aubert, O. Barrois, F. Bertrand, T. Bondar, A. Boness, L. Brocco, E. Canet, A. Chambodut, A. Chulliat, P. Coïsson, F. Civet, A. Du, A. Fournier, I. Fratter, N. Gillet, B. Hamilton, M. Hamoudi, G. Hulot, T. Jager, M. Korte, W. Kuang, X. Lalanne, B. Langlais, J.-M. Léger, V. Lesur, F. J. Lowes, S. Macmillan, M. Mandea, C. Manoj, S. Maus, N. Olsen, V. Petrov, V. Ridley, M. Rother, T. J. Sabaka, D. Saturnino, R. Schachtschneider, O. Sirol, A. Tangborn, A. Thomson, L. Tøffner-Clausen, P. Vigneron, I. Wardinski, and T. Zvereva (2015), International geomagnetic reference field: the 12th generation, *Earth, Planets and Space*, *67*(1), 79. 4.1

Torta, J. M., F. J. Pavón-Carrasco, S. Marsal, and C. C. Finlay (2015), Evidence for a new geomagnetic jerk in 2014, *Geophysical Research Letters*, *42*(19), 7933–7940. 4.3.2

Vestine, E. H., R. H. Ball, and A. B. Kahle (1967), Nature of surface flow in the Earth's central core, *Journal of Geophysical Research*, *72*(19), 4927–4936, doi:10.1029/JZ072i019p04927. 4.1

Whaler, K. A. (1980), Does the whole of the Earth's core convect?, *Nature*, *287*, 528–530. 4.1, 4.2.1

Whaler, K. A. (1986), Geomagnetic evidence for fluid upwelling at the core-mantle boundary, *Geophysical Journal of the Royal Astronomical Society*, *86*(2), 563–588. 4.2.1

Whaler, K. A., and C. D. Beggan (2015), Derivation and use of core surface flows for forecasting secular variation, *Journal of Geophysical Research: Solid Earth*, *120*(3), 1400–1414. 4.1, 4.2.1, 4.2.1, 4.2.1, 4.4

# Addendum: Chapter 4 — Forecasting secular variation through sequential estimation of core fluid flow and magnetic diffusion

In Chapter 3 we demonstrated how magnetic diffusion alone can reproduce the historical evolution of the core magnetic field described by the COV-OBS.x1 field model, although in the subsequent addendum we discussed several difficulties with this assertion. For example, the conclusions of Chapter 3 rely strongly on the COV-OBS.x1 error budget and may not hold when only the large scale field is considered. Also, from physical considerations, motion of core fluid along the CMB should still be considered dominant with respect to diffusion in the overall SV over yearly/decadal time scales. Therefore, we introduced in Chapter 4 a method to better fit SV over a given period by supplementing core flow models with a models of pure diffusion (and not, for example, vice versa). Using our core flow and diffusive models, we proceeded to forecast core field changes over yearly time scales. Revisiting the results presented in Chapter 4, what added value does diffusion provide for the purposes of forecasting yearly variations in the field?

First of all, we note that although our hybrid forecasts are more accurate than those based on fluid motion alone (compare e.g. Table 4.1 and 4.2), by computing these hybrid predictions we have in fact ignored several difficulties which arise from using our diffusive formalism alongside frozen-flux core flow modelling. More specifically, this hybrid approach is problematic since both end-member models of SV are employed to infer information over different regions of the core. For example, our starting point for the sequential modelling of fluid flow and diffusion is the radial induction equation (eq. 4.4), which is valid only within a thin region just below the CMB where $u_r = 0$. When we adopt the frozen-flux limit ($\eta \to 0$), we may solve the reduced induction equation for core fluid motion within this region only, leaving outside consideration any fluid motion below this boundary region (where $u_r \neq 0$). This creates an inconsistency with our subsequent diffusive modelling, for which we consider full-sphere solutions for the magnetic field over the whole core, while we have not accounted for deeper fluid motion that interacts with the magnetic field to generate SV. However, it is worth reit-

erating that our purely diffusive solutions are sensitive only to approximately the top 1% of the core (as demonstrated in Appendix A.1). As such, our sequential modelling of core flow and diffusion is nevertheless consistent in the sense that both end-member approaches effectively sample roughly the same region of the core, and therefore any errors associated with disregarding deeper flow structures is possibly limited.

A similar issue relates to the fact that our diffusive formalism is based on the assumption of zero toroidal field inside the core (i.e. on setting $T = 0$). Such an approach was motivated by recognising that the field outside the core is strictly poloidal, and therefore the toroidal field inside the core lies completely in the null space. In reality, magnetic diffusion, as represented in the second term in the r.h.s. of eq. 4.6, depends on both the poloidal and toroidal field. However, for the special case that $u_r = 0$ the induction equation for the poloidal field separates, such that poloidal SV (either the inductive or diffusive contributions) depends only on the poloidal field itself (*Bloxham and Jackson*, 1991). Although this result applies to a boundary layer close to the CMB in which radial motion is inhibited, at lower depths time variations due to diffusion has both poloidal and toroidal contributions. Since we consider diffusion over over the whole core, it is therefore plausible that the toroidal field contaminates our (poloidal) diffusive solutions. While these effects are not accounted for within our diffusive formalism, we may nevertheless follow the same reasoning as earlier, and state that since our diffusive models effectively sample only a thin layer just beneath the CMB (in particular for the yearly time windows considered in Chapter 4), contamination from diffusion of the toroidal field is perhaps limited.

Possibly more problematic is the fact that with our sequential approach, we have implicitly assumed that diffusion and fluid flow are separable. This assertion allowed a partitioning of the SV into a frozen-flux and diffusive part, and with that improved geomagnetic forecasts. However, core fluid motion and magnetic diffusion occur jointly and can strictly not be separated. An example of interaction between fluid flow and diffusion is the process of flux expulsion (*Bloxham*, 1986), through which fluid motion enhances field gradients which subsequently diffuse. (Paradoxically, this process is often thought to generate reversed-flux patches and motivated us to study magnetic diffusion in the first place!) An important consequence of this notion is that our partitioning of SV into frozen-flux and diffusive parts is not necessarily meaningful. Therefore, while our method allows for improved core field forecasts, we stress that the reader should exercise caution when interpreting the fluid flow and diffusive models geophysically. Possibly, the interaction between core flow and diffusion can be more realistically modelled in an iterative fashion. For example, one could adopt the following method:

1. For some modelling period, sequentially estimate the core flow and diffusive contributions to SV, as has been done throughout Chapter 4.

2. Substract the estimated diffusive SV from the total SV observed over the modelling period.

3. Re-estimate the core fluid motion using the SV difference computed in step 2.

4. Re-estimate the diffusive SV contribution from the difference between the total and re-estimated frozen-flux SV computed in step 3.

5. Repeat steps 2-4 until some criterion specifying the convergence of the flow and diffusive models has been met.

While there is no *a priori* guarantee that such a method will converge, it could provide a less arbitrary partitioning of the SV into its flow and diffusive parts than is done in Chapter 4, and to some extent takes into account interaction between the two.

Although our hybrid forecasting method may be geophysically inconsistent for the reasons described above, it has nevertheless allowed the production of geomagnetic predictions with increased accuracy. However, a comparison between Table 4.1 and 4.2, and similarly one between Fig. 4.6 and 4.7, demonstrates that the reduction in the global forecast error obtained by accounting for magnetic diffusion is significant only at the CMB. Since geomagnetic measurements are ultimately made at Earth's surface and above, it seems that our hybrid forecasts have only a small advantage over forecasts based on core fluid motion alone, and our hybrid method will likely provide only marginally better estimates of magnetic components or declination there at Earth's surface (for example for the purpose of naval/aerial orientation). On a similar note, we find some improvement near South America, which alludes to a better forecasts of the South Atlantic Anomaly with our hybrid method. The improvement is, however, rather insignificant, and considering this feature will show little change over the yearly periods considered in Chapter 4 (e.g. *Aubert*, 2015), it seems the hybrid method again provides little added value to forecasting the evolution of this anomalous region. That being said, considering the little additional computational overhead our sequential method requires compared to flow-only forecasts (for a single forecast, computing the diffusive contributions takes only seconds), there seems little reason not to model also magnetic diffusion when forecasting yearly field evolution.

Furthermore, Fig. 4.7 clearly demonstrates that at Earth's surface our forecasts produce the largest errors within the Pacific Hemisphere, where data coverage is typically poor. This particular region is also relatively 'quiet', that is to say SV of the radial field is typically of low amplitude there (see e.g. Fig. 3.10 for global maps of $\dot{B}_r$ on the CMB from COV-OBS.x1). This is a rather counter-intuitive result: how could it be more difficult to forecast field evolution for areas in which there is less overall field variation? Most likely, it is not matching the magnitude of the SV that is problematic, but instead its temporal variation, that is the second time derivative of the field or secular acceleration. As such, we suggest our forecasts lack the capacity to match sharp temporal variations in the SV, for example manifest as geomagnetic jerks. Indeed, *Torta et al.* (2015) analysed observatory data and detected a jerk within our testing period of 2010.0-2015.0 (at approximately 2014.0) in all ($X$, $Y$, and $Z$) components of the field. Moreover, they demonstrate a correlation with local (observatory) signatures of this jerk and global maps at Earth's surface of the temporal changes in secular acceleration (a measure of the 'sharpness' of geomagnetic jerks) at 2014.0 from CHAOS-5. Their map showing changes in

the secular acceleration of the $Z$-component (denoted by $\Delta\ddot{Z}$ in Fig. 3 of their work), which in this case is the only relevant component since in Chapter 4 we forecast variations in $B_r$, agrees well with both the flow-only and hybrid forecast errors in $B_r$ at Earth's surface (Fig. 4.7). In other words, our forecast residuals are of high amplitude where jump changes in the secular acceleration are more pronounced, and so there is an indication that our ability to accurately forecast yearly field changes is limited predominantly by the occurrence of geomagnetic jerks. We therefore arrive at a similar conclusion as the one by *Whaler and Beggan* (2015), namely that in order to improve yearly core field forecasts, a better representation of geomagnetic jerks is required. As Fig. 4.7 illustrates, and as already demonstrated in Chapter 3, modelling magnetic diffusion does not eliminate this problem. As such, we need to rely on other aspects of the (magneto)hydrodynamics of Earth's core which could explain jerks, for example torsional oscillations (*Bloxham et al.*, 2002, *Holme and De Viron*, 2013) or Alfèn waves (*Aubert*, 2018, *Aubert and Finlay*, 2019).

# References


Aubert, J. (2015), Geomagnetic forecasts driven by thermal wind dynamics in the Earth's core, *Geophysical Journal International*, *203*(3), 1738–1751. 4.4

Aubert, J. (2018), Geomagnetic acceleration and rapid hydromagnetic wave dynamics in advanced numerical simulations of the geodynamo, *Geophysical Journal International*, *214*(1), 531–547. 4.4

Aubert, J., and C. C. Finlay (2019), Geomagnetic jerks and rapid hydromagnetic waves focusing at Earth's core surface, *Nature Geoscience*, *12*, 393–398. 4.4

Bloxham, J. (1986), The expulsion of magnetic flux from the Earth's core, *Geophysical Journal of the Royal Astronomical Society*, *87*(2), 669–678, doi:10.1111/j.1365-246X.1986.tb06643.x. 4.4

Bloxham, J., and A. Jackson (1991), Fluid flow near the surface of Earth's outer core, *Reviews of Geophysics*, *29*(1), 97–120. 4.4

Bloxham, J., S. Zatman, and M. Dumberry (2002), The origin of geomagnetic jerks, *Nature*, *420*(6911), 65. 4.4

Holme, R., and O. De Viron (2013), Characterization and implications of intradecadal variations in length of day, *Nature*, *499*, 202–204. 4.4

Torta, J. M., F. J. Pavn-Carrasco, S. Marsal, and C. C. Finlay (2015), Evidence for a new geomagnetic jerk in 2014, *Geophysical Research Letters*, *42*(19), 7933–7940. 4.4

Whaler, K. A., and C. D. Beggan (2015), Derivation and use of core surface flows for forecasting secular variation, *Journal of Geophysical Research: Solid Earth*, *120*(3), 1400–1414. 4.4

# Chapter 5

# Discussion and conclusions

*'You've got to get obsessed, and stay obsessed!'*

**'Iowa Bob', in John Irving's *The Hotel New Hampshire***

## 5.1 Discussion

The role of magnetic diffusion in the geomagnetic secular variation has been the main interest of this thesis, a contribution that is neglected in the commonly used frozen-flux assumption. However, observation-based studies suggest that this process has signatures in the secular variation, and is often thought particularly important for the observed emergence of patches of reversed-flux in the radial field on the core-mantle boundary. In chapter 2 we developed a method to identify these features and study their evolution with time-dependent field models, which is based on the magnetic equator defined by the radial core field of spherical harmonic degree 3. With this method we have confirmed that over the 20th century these reversed patches have grown in area, intensified and migrated towards higher latitudes, thereby contributing to the observed weakening of the axial dipole. In a similar fashion, we also find that the non-reversed or normal part of the field has contributed to axial dipole decay, and is accountable for approximately one-third of the total decay since 1880.0.

Combining these results for the reversed and normal partitions, it becomes clear then that the total unsigned radial magnetic flux integrated over the CMB has increased with time, consistent with the observed overall energetic field growth at the CMB (e.g. *Huguet et al.*, 2016). Recall the constraint that when diffusion is a negligible contribution to the SV, the integrated unsigned magnetic flux through the CMB should be conserved (eq. 1.27). Our results from chapter 2 clearly contradict this condition, and with that the frozen-flux assumption that diffusion is restricted to relatively slow, millenial time scales. We therefore have given observation-based indications of magnetic diffusion contributing significantly to SV on shorter, decadal time scales, similar to the work of *Chulliat et al.* (2010a) and *Chulliat and Olsen* (2010).

These trends suggest non-negligible diffusion on relatively short time scales from an observational point of view, but to what extent are they consistent with diffusion from a physical perspective? This is the issue tackled in chapter 3, in which we assumed purely diffusive secular variation in the absence of core fluid motion (i.e. the opposite end-member to the frozen-flux description). Within this end-member regime, we constructed globally optimised models which fit the observation-based and time-dependent field model COV.OBS.x1 (*Gillet et al.*, 2015), by inverting for the initial field structure throughout the core. With this approach, we find that purely-diffusive secular variation is indeed consistent with the emergence, intensification, and movement of reversed flux over the 20th century, as it is in fact with the entire secular variation over several decades. In addition, our purely diffusive models recover other characteristic features of field evolution such as the westward drift and the accelerated movement of the North Magnetic Pole. While the time scale of diffusion is widely assumed to be much longer than that of core fluid motion, we have given direct evidence that this need not be true, and that diffusion can contribute significantly on yearly to decadal time scales. A link between the evolution of reversed flux patches and significant diffusion just below the CMB is therefore certainly plausible.

However, we have shown that diffusion can fit the observed secular variation for only approximately a century (that is, from 1912.0 to 2015.0), whereas reversed-flux growth and intensification may have been ongoing over several centuries (*Terra-Nova et al.*, 2015). Furthermore, our method of modelling pure diffusion does not provide any physical justification for how the initial field states are generated, and diffusion alone is likely incapable of forming the large radial gradients observed in these initial states. These considerations imply that diffusion needs to be accompanied by sufficient radial fluid flow. As radial expulsion of magnetic field (e.g. *Bloxham*, 1986) can enhance magnetic diffusion below the CMB, this mechanism therefore remains a more complete explanation of the emergence of reversed flux. Nevertheless, we have shown that the involvement of diffusion with the time-dependence of reversed-flux patches and the short-term secular variation is viable.

Our purely diffusive formalism was subsequently used in chapter 4 to extend models describing steady core fluid motion by including a contribution from magnetic diffusion, which allowed us to improve forecasts of yearly secular variation. We find that these hybrid forecasts are generally more accurate than those based on fluid flow only, and accounting for diffusion reduces the global forecast error by 5-25% at Earth's surface and at the CMB this error reduction may be in excess of 77%. Additionally, we find that RFP evolution in the South Atlantic is captured particularly well with this hybrid approach. This result is consistent with that by *Gubbins* (1996), who argued that even with a background fluid flow, diffusion is necessary to account for the evolution of patches of RFPs in the South Atlantic. Our hybrid forecasts also indicate that RFPs will continue to contribute to axial dipole decay. However, we find that the end of the 20th century marks a change in the associated governing processes, with poleward migration predicted to actually strengthen the axial dipole, whereas in chapter 2 it is shown that over the 20th century it played a major role in its weakening (consistent with the work

by *Olson and Amit* (2006), *Finlay et al.* (2016a)). Moreover, the total reversed surface area is predicted to grow at an accelerated rate of roughly $18 \times 10^4$ km$^2$ yr$^{-1}$, whereas the characteristic growth rate over the 20th century is approximately $4.5 \times 10^4$ km$^2$ yr$^{-1}$. Although our forecasts have been obtained with use of only one field model series, that of CHAOS-6 (*Finlay et al.*, 2016b), the COV-OBS.x1 model (*Gillet et al.*, 2015) also exhibited reduced poleward migration of reversed flux by the end of the 20th century (Fig. 2.10a). The predicted migration of RFPs towards the equator (Fig. 4.9) is appears therefore a robust feature not associated with differences in the assumptions used to construct these field models.

However, we stress that examining our results requires caution as they rely entirely on the interpretation and/or application of field models unconstrained by frozen flux; however, there are field models that fit geomagnetic observables and obey frozen flux (e.g. *Gubbins*, 1984, *Constable et al.*, 1993, *Lesur et al.*, 2010, *Wardinski and Lesur*, 2012). The overall increase in the unsigned flux found in chapter 2 may therefore only be due to the assumptions used to derive the field models we utilised there, and may not reflect the true secular variation. The use of frozen-flux constrained field models may have led to much reduced overall growth and/or intensification of reversed flux. In such a scenario, it would then have been more difficult to link RFP evolution to magnetic diffusion, although pure diffusion could still fit the global field evolution described in such frozen-flux field models.

*Whaler and Beggan* (2015) report that the accuracy of their purely flow-based forecasts is reduced when geomagnetic jerks occur within the modelling period. Such events have been observed within the periods considered in chapter 4, that is around 2003 (*Olsen and Mandea*, 2007, *Feng et al.*, 2018), 2007 (*Chulliat et al.*, 2010b), and 2014 (*Torta et al.*, 2015). In addition, we noted in chapter 3 the difficulty of using a globally optimised diffusion model to explain jerks, when manifest in a locally measured time series of a field component derivative. It appears therefore unlikely that our sequential estimation of core fluid motion and diffusion as described in chapter 4 is capable of describing these phenomena, and may require a different explanation such as torsional oscillations (*Bloxham et al.*, 2002, *Holme and De Viron*, 2013) or quasi-geostrophic Alfèn waves (*Aubert*, 2018). As a longer modelling time window is more likely to contain such events, this may at least in part explain how the forecast accuracy is generally reduced when the length of the modelling window is increased.

## 5.2 Recommendations for future work

Few observational constraints exist on the magnetic field inside the core. While we have noted that the modelled initial field states in chapter 3 correspond to average field amplitudes consistent with those given by *Buffett* (2010) and *Gillet et al.* (2010), it remains difficult to further ascertain to what extent our model states are physically realistic. As such, a useful extension of the study in chapter 3 would be to compare our three-dimensional diffusive models with those obtained with numerical geodynamo simulations. *Aubert et al.* (2008) and *Peña et al.* (2016) already investigated the magnetic structure within numerical geodynamo simulations;

in this future work we would specifically expand on the presence of large magnetic field gradients, the associated short-term diffusion, and the ratio of the flow and diffusive contributions to field evolution in a region close to the CMB. As our purely diffusive formalism is only able to resolve the field several tens of km below the CMB, focussing attention to such a boundary region would allow us to meaningfully establish any correlations with the magnetic structures obtained in chapter 3, which would aid in determining to what extent our purely diffusive models are physically realistic. Nevertheless, the interpretation of boundary layers within such geodynamo simulations should be interpreted with caution, considering the disparity between the typical parameter space associated with these models and that characteristic for Earth (see e.g. *Glatzmaier*, 2002).

Earlier, we commented on the fact that while magnetic diffusion can fit a time-dependent field model over a considerable time span, such field models are inherently a smoothed representation of the true secular variation. As a result, explaining the local (unsmoothed) field evolution at a specific location with our diffusion models proved to be more difficult (Fig. 3.15). It is therefore possible that the mathematical consistency between pure diffusion and SV described by the field model COV-OBS.x1 (chapter 3) arises partially due to the fact that the latter is a smoothed representation of SV in COV-OBS.x1. We suggest therefore to expand the methods provided in section 3, by fitting instead to local geomagnetic measurements and not the Gauss coefficients provided by field models. Such an extended scheme may result in a nonlinear relation between model coefficients and data (e.g. when declination data are used), therefore the minimisation of the objective function through the explicit solution in eq. (3.24) may no longer be applicable. Fitting geomagnetic data in place of a field model may require a more general iterative optimisation approach, but will more firmly test the consistency between magnetic diffusion and observed secular variation.

Lastly, *Beggan and Whaler* (2009) utilised a sequential approach to data assimilation by means of a Kalman filter, in which the forward prediction steps were made by assuming SV to be governed entirely by steady core fluid motion. In their work, this fluid flow has been estimated by fitting field evolution over a time window preceding the forecasting period, as has been done in chapter 4. However, we have found that accounting for magnetic diffusion in addition to modelling steady core flow fits the observed field evolution better, and thus allows for more accurate field forecasts. As such, it would be worthwhile to further develop the Kalman scheme of *Beggan and Whaler* (2009), by computing the forward field evolution expected from both fluid flow and diffusion (as in chapter 4), which could increase the accuracy of these forecasts and their associated error estimates. While a Kalman filter incorporating the effects of diffusion has already been developed by *Barrois et al.* (2017) and *Barrois et al.* (2018), their formalism relies on statistics derived from geodynamo simulations, and therefore on a parameter space likely unrealistic for Earth's core. It would therefore be valuable to compare their methods with those of *Beggan and Whaler* (2009) (when corrected for diffusion), in particular to determine if the simulation-derived statistical quantities used by *Barrois et al.* (2017) and *Barrois et al.* (2018) produce results that are consistent with the hybrid Kalman

scheme proposed here.

Although magnetic diffusion is commonly assumed to be too slow to contribute significantly to geomagnetic secular variation over yearly to decadal time scales, motivating its omission in the widely adopted frozen-flux approximation, it is often thought important for the observed emergence of RFPs over the 20th century. In this thesis we have shown that diffusion alone can fit global secular variation as described by observation based field models over at least a century, and can reproduce characteristic features such as reversed-flux emergence, the westward drift, and acceleration of the North Magnetic Pole. In addition, we presented a hybrid scheme to compute yearly geomagnetic forecasts based on core fluid motion and diffusion, which is shown to be more accurate than forecasts based on steady core flow only.

# References


Aubert, J. (2018), Geomagnetic acceleration and rapid hydromagnetic wave dynamics in advanced numerical simulations of the geodynamo, *Geophysical Journal International*, *214*(1), 531–547. 5.1

Aubert, J., J. Aurnou, and J. Wicht (2008), The magnetic structure of convection-driven numerical dynamos, *Geophysical Journal International*, *172*(3), 945–956. 5.2

Barrois, O., N. Gillet, and J. Aubert (2017), Contributions to the geomagnetic secular variation from a reanalysis of core surface dynamics, *Geophysical Journal International*, *211*(1), 50–68, doi:10.1093/gji/ggx280. 5.2

Barrois, O., M. D. Hammer, C. C. Finlay, Y. Martin, and N. Gillet (2018), Assimilation of ground and satellite magnetic measurements: inference of core surface magnetic and velocity field changes, *Geophysical Journal International*, *215*(1), 695–712. 5.2

Beggan, C. D., and K. A. Whaler (2009), Forecasting change of the magnetic field using core surface flows and ensemble Kalman filtering, *Geophysical Research Letters*, *36*(18). 5.2

Bloxham, J. (1986), The expulsion of magnetic flux from the Earth's core, *Geophysical Journal International*, *87*(2), 669–678. 5.1

Bloxham, J., S. Zatman, and M. Dumberry (2002), The origin of geomagnetic jerks, *Nature*, *420*(6911), 65. 5.1

Buffett, B. (2010), Tidal dissipation and the strength of the Earth's internal magnetic field, *Nature*, *468*, 952–954. 5.2

Chulliat, A., and N. Olsen (2010), Observation of magnetic diffusion in the Earth's outer core from Magsat, Ørsted, and CHAMP data, *Journal of Geophysical Research: Solid Earth*, *115*(B5). 5.1

Chulliat, A., G. Hulot, and L. R. Newitt (2010a), Magnetic flux expulsion from the core as a possible cause of the unusually large acceleration of the north magnetic pole during the 1990s, *Journal of Geophysical Research: Solid Earth*, *115*(B7), B007,143, doi:10.1029/2009JB007143. 5.1

Chulliat, A., E. Thébault, and G. Hulot (2010b), Core field acceleration pulse as a common cause of the 2003 and 2007 geomagnetic jerks, *Geophysical Research Letters*, *37*(7). 5.1

Constable, C. G., R. L. Parker, and P. B. Stark (1993), Geomagnetic field models incorporating frozen-flux constraints, *Geophysical Journal International*, *113*, 419–433. 5.1

Feng, Y., R. Holme, G. A. Cox, and Y. Jiang (2018), The geomagnetic jerk of 2003.5-characterisation with regional observatory secular variation data, *Physics of the Earth and Planetary Interiors*, *278*, 47 – 58. 5.1

Finlay, C. C., J. Aubert, and N. Gillet (2016a), Gyre-driven decay of the Earth's magnetic dipole, *Nature Communcations*, *7*(10422). 5.1

Finlay, C. C., N. Olsen, S. Kotsiaros, N. Gillet, and L. Tøffner-Clausen (2016b), Recent geomagnetic secular variation from Swarm and ground observatories as estimated in the CHAOS-6 geomagnetic field model, *Earth, Planets and Space*, *68*(1), 112. 5.1

Gillet, N., D. Jault, E. Canet, and A. Fournier (2010), Fast torsional waves and strong magnetic field within the Earth's core, *Nature*, *465*, 74–77. 5.2

Gillet, N., O. Barrois, and C. Finlay (2015), Stochastic forecasting of the geomagnetic field from the COV-OBS.x1 geomagnetic field model, and candidate models for IGRF-12 International Geomagnetic Reference Field - The Twelfth generation, *Earth, Planets and Space*, *67*(1). 5.1

Glatzmaier, G. A. (2002), Geodynamo simulations - how realistic are they?, *Annual Review of Earth and Planetary Sciences*, *30*(1), 237–257. 5.2

Gubbins, D. (1984), Geomagnetic field analysis - II. Secular variation consistent with a perfectly conducting core, *Geophysical Journal of the Royal Astronomical Society*, *77*(3), 753–766. 5.1

Gubbins, D. (1996), A formalism for the inversion of geomagnetic data for core motions with diffusion, *Physics of the Earth and Planetary Interiors*, *98*, 193–206. 5.1

Holme, R., and O. De Viron (2013), Characterization and implications of intradecadal variations in length of day, *Nature*, *499*, 202–204. 5.1

Huguet, L., T. Alboussire, and H. Amit (2016), Magnetic to magnetic and kinetic to magnetic energy transfers at the top of the Earth's core, *Geophysical Journal International*, *207*(2), 934–948. 5.1

Lesur, V., I. Wardinski, S. Asari, B. Minchev, and M. Mandea (2010), Modelling the Earth's core magnetic field under flow constraints, *Earth, Planets and Space*, *62*(6), 503–516. 5.1

Olsen, N., and M. Mandea (2007), Investigation of a secular variation impulse using satellite data: The 2003 geomagnetic jerk, *Earth and Planetary Science Letters*, *255*(1-2), 94–105. 5.1

Olson, P., and H. Amit (2006), Changes in Earth's dipole, *Naturwissenschaften*, *93*(11), 519–542. 5.1

Peña, D., H. Amit, and K. J. Pinheiro (2016), Magnetic field stretching at the top of the shell of numerical dynamos, *Earth, Planets and Space*, *68*(1), 78. 5.2

Terra-Nova, F., H. Amit, G. A. Hartmann, and R. I. F. Trindade (2015), The time dependence of reversed archeomagnetic flux patches, *Journal of Geophysical Research: Solid Earth*, *120*, 691–704. 5.1

Torta, J. M., F. J. Pavón-Carrasco, S. Marsal, and C. C. Finlay (2015), Evidence for a new geomagnetic jerk in 2014, *Geophysical Research Letters*, *42*(19), 7933–7940. 5.1

Wardinski, I., and V. Lesur (2012), An extended version of the $C^3$FM geomagnetic field model: Application of a continuous frozen-flux constraint, *Geophysical Journal International*, *189*(3), 1409–1429. 5.1

Whaler, K. A., and C. D. Beggan (2015), Derivation and use of core surface flows for forecasting secular variation, *Journal of Geophysical Research: Solid Earth*, *120*(3), 1400–1414. 5.1

# Appendix A

# Supplemental material for Chapter 3

## A.1 Depth sensitivity of SV observations

Here, we present our means to determine what region of the core our model of purely diffusive SV is sensitive to, given data on the CMB. We do this by quantifying the diffusive signature on the CMB of delta-function structures at various depths. We use the decay modes presented in section 3.2.1, and define with these functions the initial magnetic anomaly

$$rs_\alpha(r,t_0) = \delta(r-r_0) \simeq \sum_{n=1}^{N} q_\alpha^n r d_{l_\alpha}^n(r,t_0), \tag{A.1}$$

where $\delta(x)$ is the Dirac delta function centred at $r_0 \in (0,c)$. To find the associated coefficients $q_\alpha^n$ we project onto the decay modes using the functional inner product

$$\langle f,g\rangle_{l_\alpha} := \frac{4\pi l_\alpha(l_\alpha+1)}{2l_\alpha+1}\left[\int_0^c \left(\frac{\partial f}{\partial r}\right)\left(\frac{\partial g}{\partial r}\right) + \frac{l_\alpha(l_\alpha+1)}{r^2} fg\,\mathrm{d}r + \frac{l_\alpha}{c} f(c)g(c)\right], \tag{A.2}$$

which for $f = g = rs_\alpha$ corresponds to the magnetic energy over all space defined by $s_\alpha$ (e.g. *Li et al.*, 2018), see also Appendix A.4. The projection then yields the coefficients

$$q_\alpha^n = \frac{\langle \delta(r-r_0), r d_{l_\alpha}^n(r,t_0)\rangle_{l_\alpha}}{\langle r d_{l_\alpha}^n(r,t_0), r d_{l_\alpha}^n(r,t_0)\rangle_{l_\alpha}} = \frac{2r_0 d_{l_\alpha}^n(r_0,t_0)}{c^3 j_{l_\alpha+1}^2(k_{l_\alpha}^n)} \tag{A.3}$$

(see appendix A.5). With these coefficients, we may compute for all $l_\alpha$ a diffusive response $[rs_\alpha(c,t)]_{t_0}^{t_1}$, that is the amplitude of the anomaly at the CMB after $t_1 - t_0$ years of diffusion. To determine how sensitive CMB observations are to different depths inside the core, we vary the radius $r_0$ at which the initial anomaly is centred.

Figure A.1 shows the amplitude of three different resultant anomalies for each $l_\alpha \in \{1, 8, 14\}$ after 175 years of diffusion (matching the full COV-OBS.x1 period), which are centred at $r_0 \in \{c/4, c/2, 0.95c\}$. These have been computed with $N = 200$, which ensures numerical convergence, as integration over $[0, c]$ of the decay mode representation of the delta

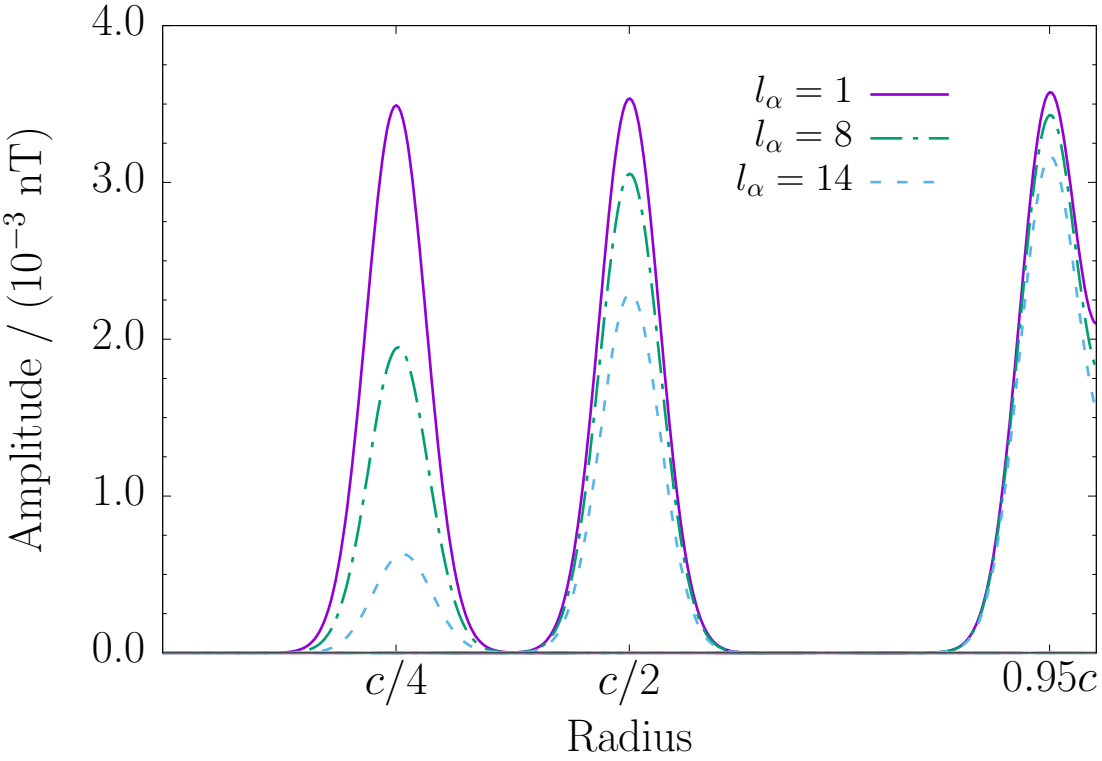


**Figure A.1:** Amplitude of the degree 1, 8, and 14 magnetic anomalies, centred at three different depths: $(c/4, c/2, 0.95c)$ after 175 years of diffusion.

function is within one percent of unity. While all anomalies assume similar curvature, the decay of these features is noticeably faster for higher degrees, with this separation being more pronounced at greater depth. Additionally, the anomalies at $0.95c$ are spatially less symmetric compared to those at greater depth, due to the imposed matching condition at $r = c$ (*Gubbins and Roberts*, 1987; Eq. 3.56). This figure confirms that the diffusive evolution of deep magnetic structures is unobservable at the CMB after 175 years, since the amplitude of the relatively deep $r_0 = c/4$ anomaly is negligible beyond $c/2$. Conversely, the diffusion of shallow features, such as the $r_0 = 0.95$ anomaly, has a clear signature at the CMB.

Figure A.2 highlights this depth sensitivity in more detail, by showing for all degrees the diffusive response at the CMB as a function of the central radius $r_0$, for 10 and 175 years of diffusion (a and b, respectively). In both figures, the response is weaker for features of increasing degree, and this discrepancy is more striking when the time window is lengthened. Most importantly, these response functions demonstrate that for pure diffusion the CMB field evolution can only constrain the magnetic structure within the uppermost core, that is the upper 80 km when one decade of diffusion is considered (Fig. A.2a); for 175 years of diffusion the CMB field evolution is sensitive to roughly the upper 400 km (Fig. A.2b).

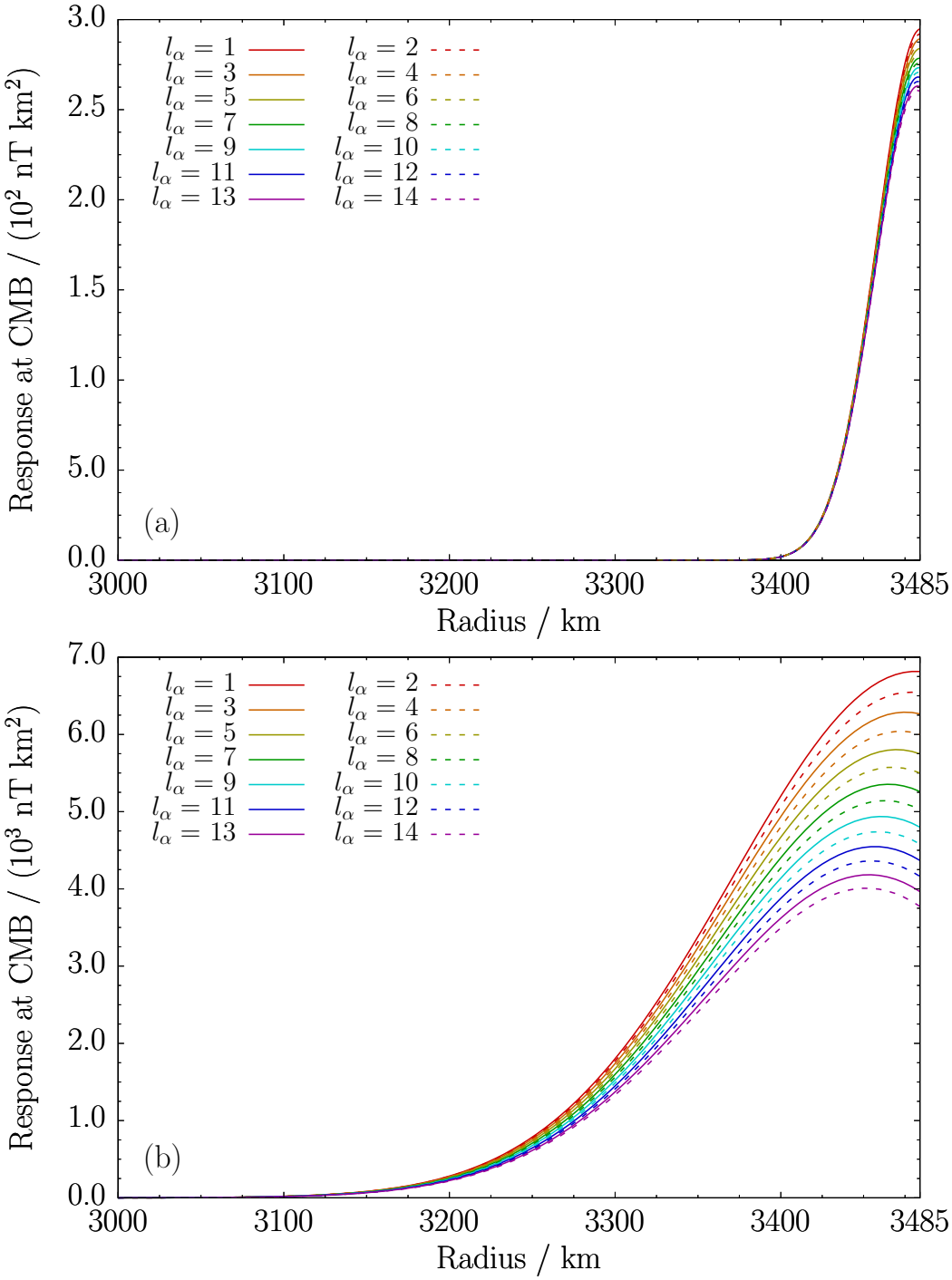


**Figure A.2:** The diffusive response at the CMB of the magnetic impulse anomaly as a function of the radius at which the anomaly is centred, after 10 years (a) and 175 years (b).

## A.2 Derivation of the diffusive least-squares residual

In this paper, there are two representations of the magnetic field. The first is the poloidal field defined within the electrically conducting core (e.g. *Gubbins and Roberts*, 1987), and the second is geomagnetic field model defined as a potential field. Respectively these are given by

$$B_r(\mathbf{r},t) = \begin{cases} \frac{1}{r}\sum_{\alpha=1}^{L(L+2)} l_\alpha(l_\alpha+1)s_\alpha(r,t)Y_\alpha(\theta,\phi), & r \le c \\ \sum_{\alpha=1}^{L(L+2)}(l_\alpha+1)\left(\frac{a}{r}\right)^{l_\alpha+2} g_\alpha(t)Y_\alpha(\theta,\phi), & r \ge c \end{cases} \tag{A.4}$$

Constructing the residual on $r = c$ then leads to

$$(B_r - \hat{B}_r)|_{r=c} = \sum_{\alpha=1}^{L(L+2)} (l_\alpha+1)\left(\frac{a}{c}\right)^{l_\alpha+2}\left[g_\alpha(t) - \frac{l_\alpha}{c}\left(\frac{c}{a}\right)^{l_\alpha+2}\hat{s}_\alpha(c,t)\right]Y_\alpha(\theta,\phi), \tag{A.5}$$

where the hat denotes our modelled field. It then follows from the orthogonality of the spherical harmonics that:

$$\int_{\mathrm{CMB}} (B_r - \hat{B}_r)^2 \,\mathrm{d}\Omega = 4\pi c^2 \sum_{\alpha=1}^{L(L+2)} \frac{(l_\alpha+1)^2}{2l_\alpha+1}\left(\frac{a}{c}\right)^{2l_\alpha+4}\left[g_\alpha(t) - \frac{l_\alpha}{c}\left(\frac{c}{a}\right)^{l_\alpha+2}\hat{s}_\alpha(c,t)\right]^2. \tag{A.6}$$

We may substitute the Galerkin approximation for the poloidal coefficients (Eq. 3.15), and write the coefficients $g_\alpha(t_k)$ and $\hat{s}_\alpha(t_k)$ as $g_{\alpha,k}$ and $\hat{s}_{\alpha,k}$ respectively. Time integration of this residual then yields:

$$\int_T \int_{\mathrm{CMB}} (B_r - \hat{B}_r)^2 \,\mathrm{d}\Omega \simeq 4\pi c^2 \sum_{\alpha=1}^{L(L+2)} \frac{(l_\alpha+1)^2}{2l_\alpha+1}\left(\frac{a}{c}\right)^{2l_\alpha+4} (\mathbf{g}_\alpha - \mathbf{D}_\alpha\hat{\mathbf{q}}_\alpha)^T\mathbf{T}(\mathbf{g}_\alpha - \mathbf{D}_\alpha\hat{\mathbf{q}}_\alpha) \tag{A.7}$$

where $D_{\alpha,ij} = \frac{l_\alpha}{c^2}\left(\frac{c}{a}\right)^{l_\alpha+2}\left(\boldsymbol{\xi}_\alpha(c)^T \mathrm{expm}[\mathbf{H}_\alpha(t_i - t_0)]\right)_j$, and $\mathbf{T}$ a diagonal weighting matrix corresponding to the numerical temporal integration scheme used. Here we use Simpson's rule, in which case:

$$T_{ij} = \begin{cases} \delta t/3\,\delta_{ij} & i = 1 \quad \text{or} \quad i = K \\ 4\delta t/3\,\delta_{ij} & i \text{ even} \quad \text{and} \quad 1 < i < K \\ 2\delta t/3\,\delta_{ij} & i \text{ odd} \quad \text{and} \quad 1 < i < K \end{cases} \tag{A.8}$$

with $\delta t$ the interval length between time points, and $K$ the number of time points (see appendix A.6). If we define the quantities: $\mathbf{q} = (\mathbf{q}_1, \mathbf{q}_2, \ldots, \mathbf{q}_{L(L+2)})^T$, $\mathbf{g} = (\mathbf{g}_1, \mathbf{g}_2, \ldots, \mathbf{g}_{L(L+2)})^T$, $\mathbf{D} = \mathrm{diag}(\mathbf{D}_1, \mathbf{D}_2, \ldots, \mathbf{D}_{L(L+2)})$, $\mathbf{W}_\alpha = 4\pi c^2 \frac{(l_\alpha+1)^2}{2l_\alpha+1}\left(\frac{a}{c}\right)^{2l_\alpha+4}\mathbf{T}$, and $\mathbf{W} = \mathrm{diag}(\mathbf{W}_1, \mathbf{W}_2, \ldots, \mathbf{W}_{L(L+2)})$ we may further simplify the residual and show that it

corresponds to a weighted least-squares problem:

$$\int_T \int_{\mathrm{CMB}} (B_r - \hat{B}_r)^2 \, \mathrm{d}\Omega \, \mathrm{d}t = (\mathbf{g} - \mathbf{D}\mathbf{q})^T \mathbf{W} (\mathbf{g} - \mathbf{D}\mathbf{q}) \tag{A.9}$$

with the solution minimising this residual:

$$\hat{\mathbf{q}} = (\mathbf{D}^T \mathbf{W} \mathbf{D})^{-1} \mathbf{D}^T \mathbf{W} \mathbf{g} \tag{A.10}$$

## A.3 Numerical convergence

The least-squares solution (Eq. 3.18) relies on several approximations, namely the use of a finite radial truncation $N$ and a discretised numerical time integration with $K$ abscissae: here we use Simpson's rule. We test what values of $N$ and $k$ are needed for an accurate and numerically converged solution.

Firstly, consider Fig. A.3 showing a normalised objective function $R_{\mathrm{unreg}}$, that is the RMS error in $B_r$, against the number of basis functions $N$ used for the inversion. These solutions have been obtained using sextuple (256-digit) precision and the mean COV-OBS.x1 field model (*Gillet et al.*, 2015) over the period 1840-2015, with either $K = 103$ or $K = 203$ time points (purple crosses and green circles, respectively). It can be seen that the residual decreases monotonically with $N$; for $N > 21$ there is a regime in which this decay is more gradual. As such, increasing $N$ beyond 30 can be expected to return a much reduced increase in accuracy — the relative difference between the $N = 29$ and $N = 30$ residuals is already only about 1%. We therefore consider the solution to be sufficiently converged for $N = 30$. For this choice of $N$, the figure also shows that $K = 103$ and $K = 203$ produce almost the same result.

Secondly, Fig. A.4 shows the normalised $R_{\mathrm{unreg}}$ as a function of the number of time points used, acquired with the same field model and floating-point precision as for Fig. A.3, and for either 2 or 30 basis functions (purple crosses and green circles, respectively). The rate of convergence appears rather sensitive to the number of basis functions, as a converged solution for $N = 30$ requires significantly more time points compared to the $N = 2$ case. However, for both choices the relative change in the residual when increasing $K$ beyond 203 is less than 1%, so we consider this number of time points to be sufficient.

The requirements in terms of truncation parameters for both $N$ and $K$ follow similarly for the regularised cases.

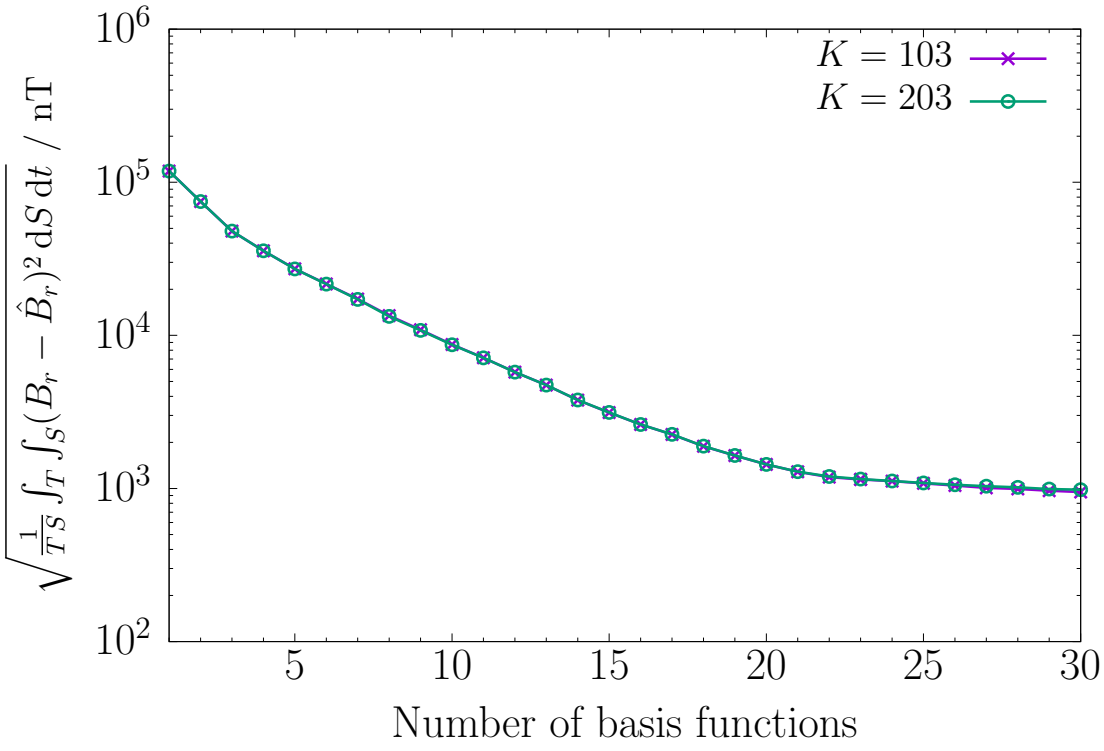


**Figure A.3:** Dependence of the unregularised objective function $R_{\mathrm{unreg}}$, normalised to represent an RMS residual in space and time, on the number of basis functions used for the inversion. Purple crosses and green circles correspond to the use of 103 or 203 time points, respectively.

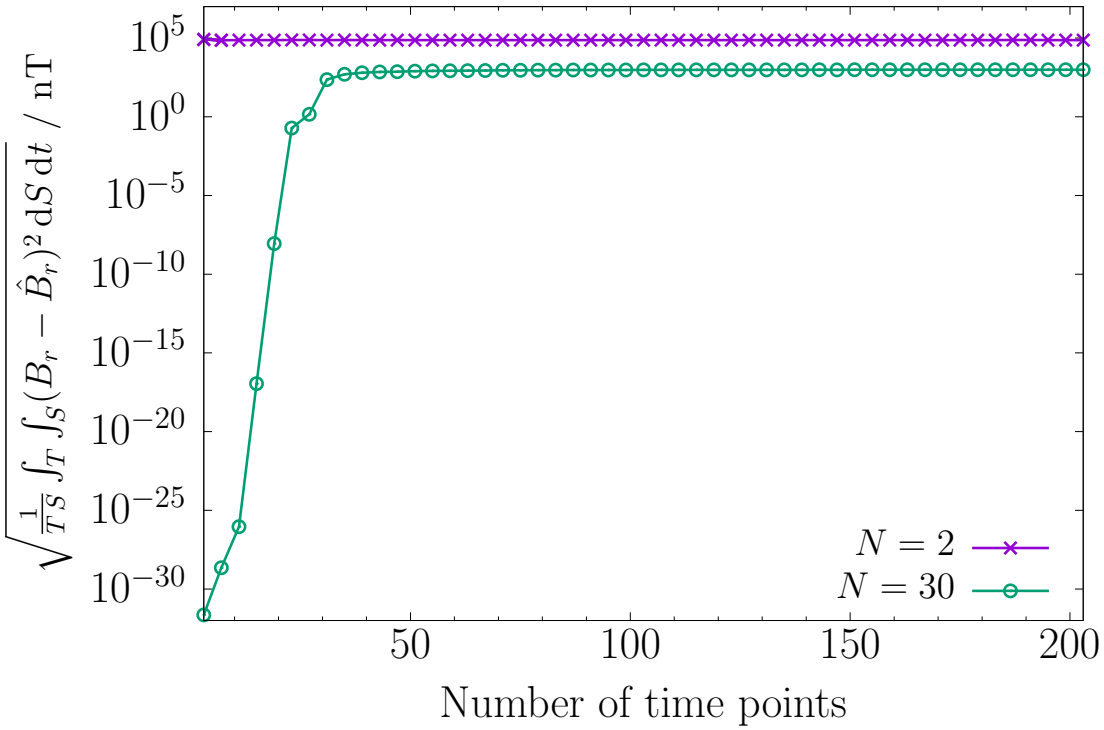


**Figure A.4:** Dependence of the unregularised objective function $R_{\mathrm{unreg}}$, normalised to represent an RMS residual in space and time, on the number of time points used for the inversion. Purple crossed and green circles correspond to the use of 2 or 30 basis functions, respectively.

## A.4 Derivation of the magnetic energy regularisation term

To incorporate the energy term into our inverse problem, we need to express it in terms of our model coefficients. To do so we first partition all magnetic energy into internal an external partsas

$$\int_{\mathbb{R}^3} \hat{\mathbf{B}}_0^2 \, \mathrm{d}V = \int_{V_{\text{int}}} \hat{\mathbf{B}}_0^2 \, \mathrm{d}V + \int_{V_{\text{ext}}} \hat{\mathbf{B}}_0^2 \, \mathrm{d}V, \tag{A.11}$$

where $V_{\text{int}}$ is the core volume and $V_{\text{ext}}$ is the space outside the core. To derive an expression for the field exterior to the core, we use the approximation of no electrical currents for $r \geq c$. Then, $\nabla \times \mathbf{B} = \mathbf{0}$ outside the core, from which it follows that (*Gubbins and Roberts*, 1987)

$$T = 0, \qquad r \geq c, \tag{A.12}$$

$$\nabla^2 S = 0, \qquad r \geq c. \tag{A.13}$$

Since $S$ is a potential field outside the core, it permits solutions in the form of spherical harmonics (excluding external sources):

$$S = \sum_{\alpha=1}^{L(L+2)} s_\alpha(c) \left(\frac{c}{r}\right)^{l_\alpha+1} Y_\alpha(\theta, \phi), \qquad r \geq c. \tag{A.14}$$

As $T = 0$, the external field $\mathbf{B}_{\text{ext}}$ is purely poloidal and fully constrained by the poloidal field inside the core, and we can derive (using eq. 3.3)

$$\mathbf{B}_{\text{ext}} = \nabla \left( \frac{\partial (rS)}{\partial r} \right) = -\nabla V. \tag{A.15}$$

The external field is then

$$\mathbf{B}_{\text{ext}}(\mathbf{r}) = - \sum_{\alpha=1}^{L(L+2)} l_\alpha s_\alpha(c) \nabla \left[ \left(\frac{c}{r}\right)^{l_\alpha+1} Y_\alpha(\theta, \phi) \right]. \tag{A.16}$$

Therefore, we may write

$$\int_{V_{\text{ext}}} \hat{\mathbf{B}}_0^2 \, \mathrm{d}V = 4\pi c \sum_{\alpha=1}^{L(L+2)} \frac{l_\alpha^2 (l_\alpha + 1)}{2l_\alpha + 1} \hat{s}_\alpha^2(c). \tag{A.17}$$

Besides some algebra, deriving the above requires the identity

$$\int_{\Omega(1)} \frac{\partial Y_\alpha}{\partial \theta} \frac{\partial Y_\beta}{\partial \theta} + \frac{1}{\sin^2 \theta} \frac{\partial Y_\alpha}{\partial \phi} \frac{\partial Y_\beta}{\partial \phi} \, \mathrm{d}S = \frac{4\pi l_\alpha (l_\alpha + 1)}{2l_\alpha + 1} \delta_{\alpha\beta}, \tag{A.18}$$

where $\Omega(1)$ is the surface of the unit sphere. This identity can be obtained by considering a

surface gradient operator $\nabla_S = (r\nabla - \mathbf{r}\partial_r) = (0, \partial_\theta, \frac{1}{\sin\theta}\partial_\phi)^T$ and the associated surface analogue of the divergence theorem (*Backus et al.*, 1996)

$$\int_S \nabla_S \cdot \mathbf{v}\, \mathrm{d}S = \int_{\partial S} \mathbf{v} \cdot \mathrm{d}\mathbf{l}, \tag{A.19}$$

where $S \subseteq \Omega(1)$ is some spherical surface, $\partial S$ its boundary over the solid angle, $\mathrm{d}\mathbf{l}$ a line element, and $\mathbf{v}$ some vector. We may then write the l.h.s. of eq. (A.18) as

$$\begin{aligned} \int_{\Omega(1)} (\nabla_S Y_\alpha) \cdot (\nabla_S Y_\beta)\, \mathrm{d}S &= \int_{\Omega(1)} \nabla_S \cdot (Y_\alpha \nabla_S Y_\beta) - Y_\alpha \nabla_S^2 Y_\beta\, \mathrm{d}S, & \text{(A.20)} \\ &= \int_{\Omega(1)} Y_\alpha \mathrm{L}^2 Y_\beta\, \mathrm{d}S, & \text{(A.21)} \end{aligned}$$

which follows from eq. (A.19) and the fact that $\partial\Omega(1) = \emptyset$, and where $\mathrm{L}^2 = \frac{1}{\sin\theta}(\frac{\partial}{\partial\theta}\sin\theta\frac{\partial}{\partial\theta} + \frac{1}{\sin\theta}\frac{\partial^2}{\partial\phi^2})$. Finally, by recognising the eigenproperty $\mathrm{L}^2 Y_\alpha = l_\alpha(l_\alpha+1)Y_\alpha$, and by adopting Schmidt semi-normalisation of the $Y_\alpha$, one arrives at eq. (A.18).

Our modelled internal model field is also poloidal, and by using eq. (A.18) again we can derive:

$$\int_{V_{\mathrm{int}}} \hat{\mathbf{B}}_0^2\, \mathrm{d}V = 4\pi \sum_{\alpha=1}^{L(L+2)} \frac{l_\alpha(l_\alpha+1)}{2l_\alpha+1} \int_0^c \frac{l_\alpha(l_\alpha+1)}{r^2}(r\hat{s}_\alpha)^2 + \left(\frac{\partial(r\hat{s}_\alpha)}{\partial r}\right)^2 \mathrm{d}r \tag{A.22}$$

Adding the internal and external contributions we obtain:

$$\int_{\mathbb{R}^3} \hat{\mathbf{B}}_0^2 = 4\pi \sum_{\alpha=1}^{L(L+2)} \frac{l_\alpha(l_\alpha+1)}{2l_\alpha+1} \left[ \int_0^c \frac{l_\alpha(l_\alpha+1)}{r^2}(r\hat{s}_\alpha)^2 + \left(\frac{\partial(r\hat{s}_\alpha)}{\partial r}\right)^2 \mathrm{d}r + c l_\alpha \hat{s}_\alpha^2(c) \right] \tag{A.23}$$

We apply the Galerkin approximation $r s_\alpha(r, t_0) = \sum_n^N q_n^\alpha \xi_n^\alpha(r)$:

$$\int_{\mathbb{R}^3} \hat{\mathbf{B}}_0^2 = \sum_{\alpha=1}^{L(L+2)} \sum_{n=1}^{N} \sum_{j=1}^{N} \hat{q}_n^\alpha \langle \xi_n^\alpha, \xi_j^\alpha \rangle_{l_\alpha} \hat{q}_j^\alpha$$

By definition $\langle \xi_n^\alpha, \xi_j^\alpha \rangle_{l_\alpha} = \delta_{nj}$, so that

$$\int_{\mathbb{R}^3} \hat{\mathbf{B}}_0^2 = \sum_{\alpha=1}^{L(L+2)} \mathbf{q}_\alpha^T \mathbf{q}_\alpha = \hat{\mathbf{q}}^T \hat{\mathbf{q}} \tag{A.24}$$

## A.5 Orthogonality of spherical Bessel functions of the second kind

### A.5.1 Alternative orthogonality

The spherical Bessel functions of the second kind $j_l(z)$ obey the orthogonality

$$\int_0^1 r^2 j_l(k_{nl}r) j_l(k_{ml}r)\,\mathrm{d}r = \frac{1}{2}[j_{l+1}(k_{nl})]^2 \delta_{mn}, \tag{A.25}$$

where $k_{nl}$ is the $n^{\text{th}}$ root of $j_l(z)$. We will show here that an alternative but similar relation holds, that of

$$\int_0^1 r^2 j_{l+1}(k_{nl}r) j_{l+1}(k_{ml}r)\,\mathrm{d}r = \frac{1}{2}[j_{l+1}(k_{nl})]^2 \delta_{mn}. \tag{A.26}$$

For simplicity, we first introduce the abbreviation $j_l^m := j_l(k_{ml}r)$. Similarly, $j_l^{m\prime}$ will denote $\mathrm{d}j_l^m/\,\mathrm{d}r$. We start our derivation from the recursion relation

$$j_l'(kr) - \frac{l}{r} j_l(kr) = -k j_{l+1}(kr) \tag{A.27}$$

(see *Abramowitz and Stegun*, 1964; eqn. 10.1.22). Substituting this in Eq. (A.26) yields

$$\begin{aligned}\int_0^1 r^2 j_{l+1}(k_{nl}r) j_{l+1}(k_{ml}r)\,\mathrm{d}r \quad &= \quad \frac{1}{k_{lm}k_{ln}} \int_0^1 l^2 j_l^m j_l^n + j_l^{m\prime} j_l^{m\prime} \\ &\qquad -lr\frac{\mathrm{d}}{\mathrm{d}r}\left(j_l^m j_l^n\right)\mathrm{d}r\end{aligned} \tag{A.28}$$

Integration by parts of the last term then gives

$$\int_0^1 r^2 j_{l+1}(k_{nl}r) j_{l+1}(k_{ml}r)\,\mathrm{d}r = \frac{1}{k_{lm}k_{ln}} \int_0^1 l(l+1) j_l^m j_l^n + r^2 j_l^{m\prime} j_l^{m\prime}\,\mathrm{d}r, \tag{A.29}$$

as by definition $j_l(k_{ml}) = 0$. Next, we use the derivative identity

$$\frac{\mathrm{d}}{\mathrm{d}r}\left(f(r)\frac{\mathrm{d}}{\mathrm{d}r}g(r)\right) = \left(\frac{\mathrm{d}}{\mathrm{d}r}f(r)\right)\left(\frac{\mathrm{d}}{\mathrm{d}r}g(r)\right) + f(r)\frac{\mathrm{d}^2}{\mathrm{d}r^2}g(r), \tag{A.30}$$

which gives

$$\begin{aligned}\int_0^1 r^2 j_{l+1}(k_{nl}r) j_{l+1}(k_{ml}r)\,\mathrm{d}r = \frac{1}{k_{lm}k_{ln}} \int_0^1 &l(l+1) j_l^m j_l^n + r^2 \frac{\mathrm{d}}{\mathrm{d}r}\left(j_l^m \frac{\mathrm{d}}{\mathrm{d}r} j_l^n\right) \\ &- r^2 j_l^m \frac{\mathrm{d}^2}{\mathrm{d}r^2} j_l^n\,\mathrm{d}r.\end{aligned} \tag{A.31}$$

Another identity is that of

$$\frac{\mathrm{d}^2}{\mathrm{d}r^2} r f(r) = 2f'(r) + r f''(r), \tag{A.32}$$

which subsequently implies that

$$\int_0^1 r^2 j_{l+1}(k_{nl} r) j_{l+1}(k_{ml} r)\,\mathrm{d}r = \frac{1}{k_{lm} k_{ln}} \int_0^1 l(l+1) j_l^m j_l^n + r^2 \frac{\mathrm{d}}{\mathrm{d}r}\left( j_l^m \frac{\mathrm{d}}{\mathrm{d}r} j_l^n \right) - r j_l^m \frac{\mathrm{d}^2}{\mathrm{d}r^2}\left( r j_l^n \right) + 2 r j_l^m j_l^{n\prime}\,\mathrm{d}r. \tag{A.33}$$

Conveniently, integration by parts of the second term on the r.h.s. lets it cancel against the rightmost one, therefore we may omit these terms. Moreover, the $j_l(z)$ obey the eigenfunction property

$$\frac{\mathrm{d}^2}{\mathrm{d}r^2} r j_l^n = -k_{ln}^2 r j_l^n + \frac{l(l+1)}{r^2} r j_l^n, \tag{A.34}$$

which reduces eq. (A.33) to

$$\int_0^1 r^2 j_{l+1}(k_{nl} r) j_{l+1}(k_{ml} r)\,\mathrm{d}r = \int_0^1 r^2 j_l(k_{lm}) j_l(k_{ln})\,\mathrm{d}r. \tag{A.35}$$

Therefore the orthogonalities in eq. (A.25) and eq. (A.26) are equivalent.

### A.5.2 Application to the energy norm

Consider the functional inner product of the form

$$\langle f, g \rangle_l := \int_0^1 \frac{\partial f}{\partial r} \frac{\partial g}{\partial r} + \frac{l(l+1)}{r^2} f g\,\mathrm{d}r + l f(1) g(1), \tag{A.36}$$

which is used widely throughout this work. Here, we demonstrate that this norm relates to the alternative orthogonality given above through

$$\langle r j_{l+1}^m, r j_{l+1}^n \rangle_l = k_{nl}^2 \int_0^1 r^2 j_{l+1}^m j_{l+1}^n\,\mathrm{d}r = \frac{1}{2}\big(k_{nl}\, j_{l+1}(k_{nl})\big)^2 \delta_{mn}. \tag{A.37}$$

To derive this we first use integration by parts, and for the leftmost term of the integrand in Eq. (A.36) doing so yields

$$\int_0^1 \left( \frac{\partial}{\partial r} r j_{l+1}^m \right)\left( \frac{\partial}{\partial r} r j_{l+1}^n \right)\mathrm{d}r = \left[ r j_{l+1}^m \left( \frac{\partial}{\partial r} r j_{l+1}^n \right) \right]_0^1 - \int_0^1 r j_{l+1}^m \left( \frac{\partial^2}{\partial r^2} r j_{l+1}^n \right)\mathrm{d}r. \tag{A.38}$$

There is the recursion relationship

$$\left(\frac{\partial}{\partial r} j_l(kr)\right) + \frac{l+1}{r} j_l(kr) = k j_{l-1}(kr) \tag{A.39}$$

(see Abramowitz and Stegun, 1964, Eq. 10.1.21), and substitution for the boundary term gives

$$\begin{aligned} \int_0^1 \left(\frac{\partial}{\partial r} r j_{l+1}^m\right)\left(\frac{\partial}{\partial r} r j_{l+1}^n\right) \mathrm{d}r &= -l j_{l+1}(k_{ml}) j_{l+1}(k_{nl}) \\ &\quad - \int_0^1 r j_{l+1}^m \left(\frac{\partial^2}{\partial r^2} r j_{l+1}^n\right) \mathrm{d}r \end{aligned} \tag{A.40}$$

The remaining integral may be simplified using the eigenfuntion relation (Eq. A.34):

$$\begin{aligned} \int_0^1 \left(\frac{\partial}{\partial r} r j_{l+1}^m\right)\left(\frac{\partial}{\partial r} r j_{l+1}^n\right) \mathrm{d}r &= -l j_{l+1}(k_{ml}) j_{l+1}(k_{nl}) + \int_0^1 k_{nl}^2 r^2 j_{l+1}^m j_{l+1}^n \\ &\quad - l(l+1) j_{l+1}^m j_{l+1}^n \, \mathrm{d}r. \end{aligned} \tag{A.41}$$

Clearly, there is cancellation against the other terms in eq. (A.36) — all that remains is

$$\langle r j_{l+1}^m, r j_{l+1}^n \rangle_l = k_{nl}^2 \int_0^1 r^2 j_{l+1}^m j_{l+1}^n \, \mathrm{d}r = \frac{1}{2}\big(k_{nl}\, j_{l+1}(k_{nl})\big)^2 \delta_{mn}. \tag{A.42}$$

## A.6 Numerical integration

While many functions representing physical quantities are continuous in a mathematical sense, often these must unavoidably be represented as a discrete sequence, for example because the associated quantity can only be sampled at a finite rate. Any operations on such a sampled function, such as integration, must then also be treated discretely.

We consider a continuous function $f : \mathbb{R} \to \mathbb{R}$ and its discrete analogue $f_k$ with the integer $k \in [0, K]$. In other words, we know the function $f$ at $K + 1$ grid points $x_k$. Consider also the domain $I \subseteq \mathbb{R}$, partitioned into $N$ intervals such that
$I = \cup_{n=0}^{N} I_n = \{[a_0, a_1], [a_1, a_2], \ldots, [a_{N-1}, a_N]\}$. The strategy for the approximate (numerical) integration of $f$ is to represent it by a different interpolating polynomial for every interval $I_n$. Then, the sum of the integrals of all $I_n$ will approximate the complete integral of $f$ over $I$.

### A.6.1 Lagrange interpolating polynomials

While there exist various types of interpolating functions we consider here only Lagrange interpolating polynomials, which approximate $f$ as

$$f(x) \simeq P_M(x) := \sum_{m=0}^{M} C_m(x) f(x_m), \tag{A.43}$$

where $C_m$ are called the *cardinal functions* or *basis polynomials*. For Lagrange polynomials these are defined as

$$C_m(x) = \prod_{\substack{j=0,\\ j \neq m}}^{M} \frac{x - x_j}{x_m - x_j}, \tag{A.44}$$

which have the property: $C_m(x_k) = \delta_{mk}$, therefore $P_N$ fits the interpolating values $f(x_k)$ exactly. Note that the number of interpolating points determines the degree of the interpolating polynomial: a polynomial of degree $K$ requires $K+1$ interpolating points. By varying the order $M$ of the interpolating polynomials one can obtain several numerical interpolation methods, and we will discuss several choices below.

### A.6.2 Rectangle rule ($M = 0$)

Let us apply these interpolating functions to the integration over $I_n$ for the case $M = 0$. First, we arrange our grid points so that $x_n \in I_n$. This implies there is only one interpolating point (i.e. $x_n$) for every $I_n$, and the interpolant for that interval is then simply $P_N = f(x_n)$ (the evaluation of the basis polynomials returns the empty product, so $C_0 = 1$). It follows then that,

$$\int_{I_n} f(x)\,\mathrm{d}x \simeq \int_{I_n} P_0(x_n)\,\mathrm{d}x = f(x_n) h_n, \tag{A.45}$$

where $h_n = a_{n+1} - a_n$ is the length of the $n^{\text{th}}$ interval. However, we have not yet specified where $x_n$ is placed in $I_n$. Typical choices are $x_n = a_n$ (left rectangular), $x_n = a_{n+1}$ (right rectangular), or $x_n = (a_n + a_{n+1})/2$ (midpoint rectangular). Here we consider only the midpoint rectangular integration. Applying this to the full domain $I$ gives

$$\int_I f(x)\,\mathrm{d}x = \sum_{n=0}^{N} \int_{I_n} f(x)\,\mathrm{d}x \simeq \sum_{n=0}^{N} f(x_n) h_n \tag{A.46}$$

### A.6.3 Trapezium rule ($M = 1$)

We now arrange our grid to have two interpolation points for every $I_n$. More specifically, we set $x_n = a_n$, so that the grid points align with the boundaries of $I_n$. The local interpolating polynomial is now of degree 1, such that

$$P_1(x) = \frac{x - x_{n+1}}{x_n - x_{n+1}} f(x_n) + \frac{x - x_n}{x_{n+1} - x_n} f(x_{n+1}). \tag{A.47}$$

Integrating this function yields

$$\int_{I_n} P_1\,\mathrm{d}x = \big(f(x_{n+1}) + f(x_n)\big)\frac{h_n}{2}. \tag{A.48}$$

Therefore,

$$\int_I f(x)\,\mathrm{d}x \simeq \frac{1}{2}\sum_{n=0}^{N} \big(f(x_{n+1}) + f(x_n)\big) h_n \tag{A.49}$$

This type of numerical integration is known as the *trapezium rule*.

### A.6.4 Simpson's rule ($M = 2$)

For our final case, consider three equally spaced grid points $x_k$ in $I_n$, i.e. $x_{2n} = a_n$, $x_{2n+1} = (a_{n+1} + a_n)/2$ and $x_{2n+2} = a_{n+1}$. With three interpolating points the local interpolant becomes:

$$\begin{aligned} P_2(x) = {} & \frac{(x - x_{2n+1})(x - x_{2n+2})}{(x_{2n} - x_{2n+1})(x_{2n} - x_{2n+2})} f(x_{2n}) + \frac{(x - x_{2n})(x - x_{2n+2})}{(x_{2n+1} - x_{2n})(x_{2n+1} - x_{2n+2})} f(x_{2n+1}) \\ & + \frac{(x - x_{2n})(x - x_{2n+1})}{(x_{2n+2} - x_{2n})(x_{2n+2} - x_{2n+1})} f(x_{2n+2}) \end{aligned} \tag{A.50}$$

Again, we integrate over $I_n$:

$$\int_{I_n} P_2(x)\,\mathrm{d}x = \frac{h}{3}\bigg(f(x_{2n}) + 4f(x_{2n+1}) + f(x_{2n+2})\bigg), \tag{A.51}$$

where $h = x_{2n+1} - x_{2n} = x_{2n+2} - x_{2n+1} = (x_{2n+2} - x_{2n})/2$. It follows then that

$$\int_I f(x)\,\mathrm{d}x \simeq \frac{h}{3}\sum_{n=0}^{N}\Big(f(x_{2n}) + 4f(x_{2n+1}) + f(x_{2n+2})\Big) \tag{A.52}$$

This is Simpson's rule for numerical integration. Note that this type of integration requires that $K = 2N + 1$, i.e. the number of interpolation points must be odd.

### A.6.5 Application to least squares minimisation

Consider the total squared residual

$$\phi = \int_I \big(f(t) - \hat{f}(t)\big)^2\,\mathrm{d}t, \tag{A.53}$$

where $f(t)$ and $\hat{f}(t)$ are respectively a continuous function and its best-fit estimate. Applying the rectangle approximation to the integration above we obtain

$$\phi \simeq \delta t\sum_{k=0}^{K}\big(f(t_k) - \hat{f}(t_k)\big)^2, \tag{A.54}$$

where we have assumed the uniform interval length $h_k = \delta t$. By letting $f(t_k) = f_k$ and $\mathbf{f} = (f_0, f_1, \ldots, f_K)^T$, we may write the above as

$$\phi = (\mathbf{f} - \hat{\mathbf{f}})^T\mathbf{W}(\mathbf{f} - \hat{\mathbf{f}}), \tag{A.55}$$

where in this case $\mathbf{W} = \delta t\mathbf{I}$ and represents the weights provided by the integration scheme. Thus, the rectangular integration of time series residual yields a discrete unweighted least-squares residual. This is not true for example for the trapezium rule, in which case

$$\phi \simeq \frac{\delta t}{2}\sum_{k=0}^{K}(f_k - \hat{f}_k)^2 + (f_{k+1} - \hat{f}_{k+1})^2. \tag{A.56}$$

Now, we find some overlap in the summation. That is, the endpoints $f_0$ and $f_K$ have only one term in the above equation, and the weight of these terms is half that of all other terms. We may therefore write the above in the form given by Eq. (A.55), where

$$\mathbf{W} = \delta t\begin{pmatrix} \frac{1}{2} & 0 & \cdots & 0 & 0 \\ 0 & 1 & \cdots & 0 & 0 \\ \vdots & \vdots & \ddots & \vdots & \vdots \\ 0 & 0 & \cdots & 1 & 0 \\ 0 & 0 & \cdots & 0 & \frac{1}{2} \end{pmatrix} \tag{A.57}$$

In a similar fashion, we may derive for Simpson's rule the integration weights as

$$W_{ij} = \begin{cases} \delta_{ij}\delta t/3, & i = 1 \quad \text{or} \quad i = K+1 \\ 4\delta_{ij}\delta t/3, & 1 < i < K+1 \quad \text{and} \quad i \text{ even} \\ 2\delta_{ij}\delta t/3, & 1 < i < K+1 \quad \text{and} \quad i \text{ odd} \end{cases} \tag{A.58}$$

with $\delta_{ij}$ the Kronecker delta.

# References


Abramowitz, M., and I. A. Stegun (1964), *Handbook of Mathematical Functions: With Formulas, Graphs and Mathematical Tables*, National Bureau of Standards. A.5.1

Backus, G., R. Parker, and C. Constable (1996), *Foundations of Geomagnetism*, Cambridge University Press, Cambridge. A.4

Gillet, N., O. Barrois, and C. C. Finlay (2015), Stochastic forecasting of the geomagnetic field from the COV-OBS.x1 geomagnetic field model, and candidate models for IGRF-12, *Earth, Planets and Space*, *67*(1), 71. A.3

Gubbins, D., and P. H. Roberts (1987), Magnetohydrodynamics of the Earth's Core, in *Geomagnetism*, vol. 2, chap. 1, Academic Press. A.1, A.2, A.4

Li, K., A. Jackson, and P. W. Livermore (2018), Taylor state dynamos found by optimal control: axisymmetric examples, *Journal of Fluid Mechanics*, *853*, 647697. A.1